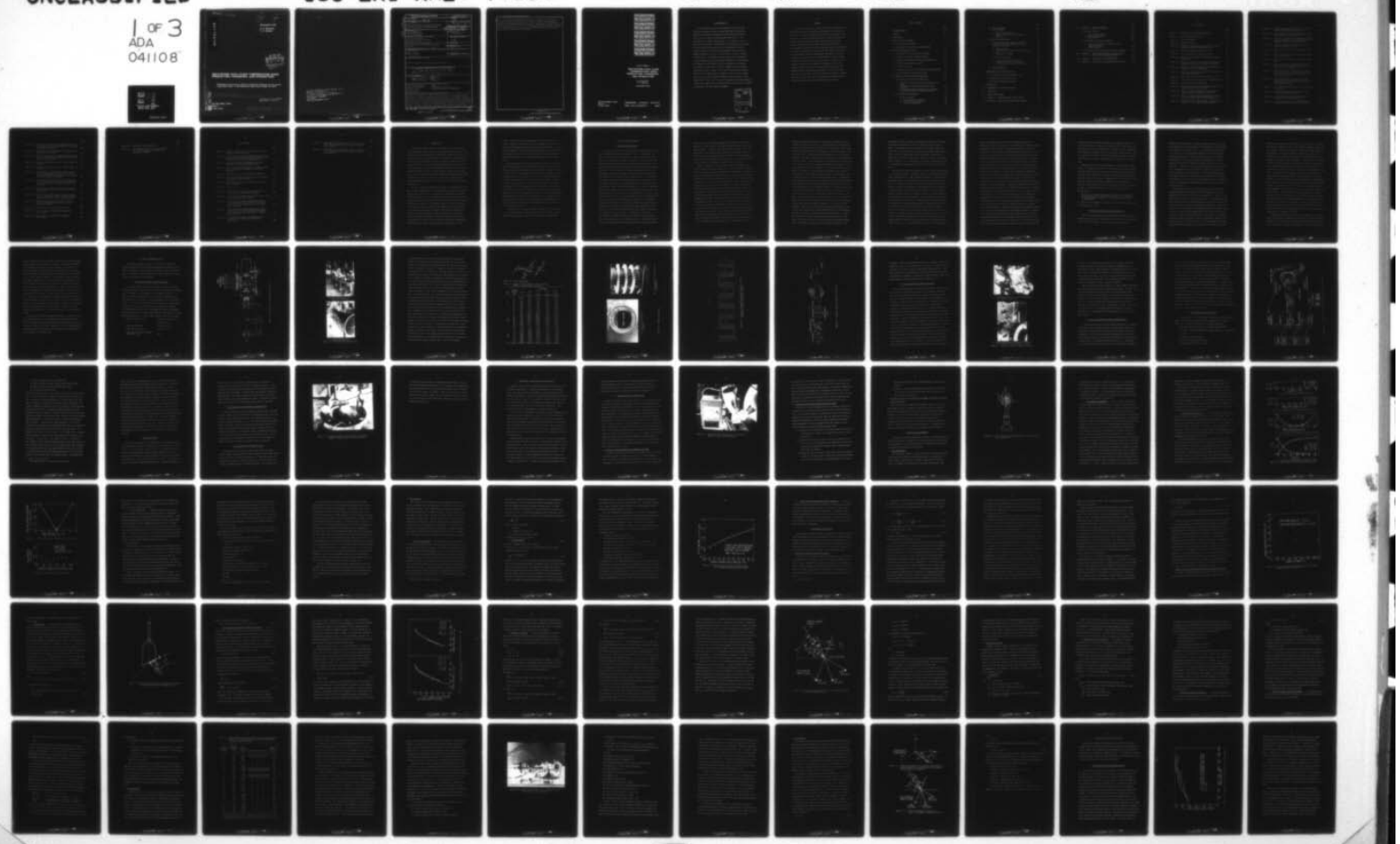
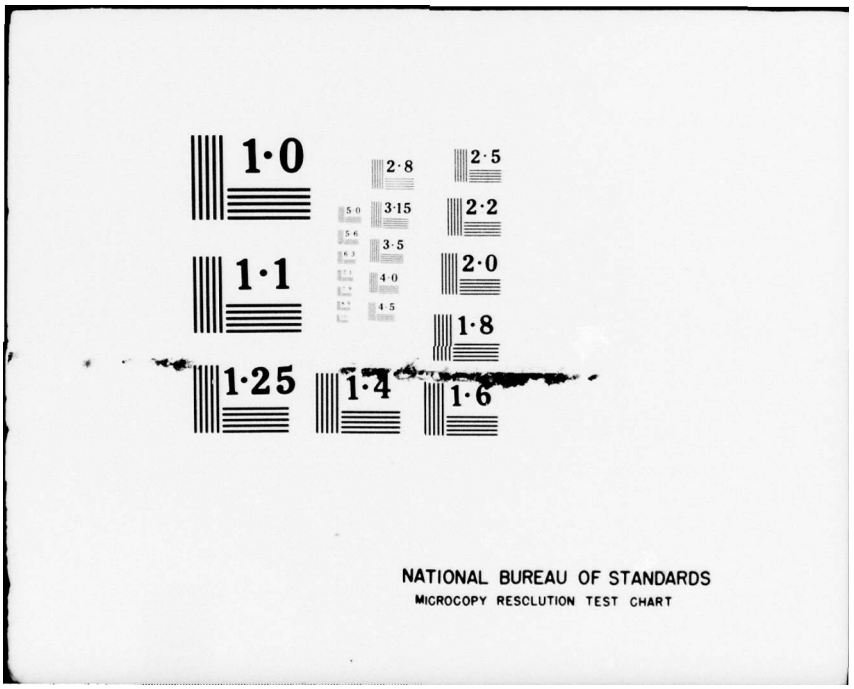
AD-A041 108 IOWA STATE UNIV AMES ENGINEERING RESEARCH INST F/G 13/7
MULTISTAGE AXIAL-FLOW TURBOMACHINERY WAKE PRODUCTION, TRANSPORT--ETC(U)
NOV 76 D P SCHMIDT, T H OKIISHI AF-AFOSR-2916-76
UNCLASSIFIED ISU-ERI-AMES-77130 AFOSR-TR-77-0720 NL

1 OF 3
ADA
041108




1·0
1·1
1·25
1·4
1·6
1·8
2·0
2·2
2·5
2·8
3·15
3·5
4·0
4·5
5·0
5·6
NATIONAL BUREAU OF STANDARDS
MICROCOPY RESCLUTION TEST CHART

AFOSR-TR- 77-0720

AD A041108

November 1976

D. P. Schmidt
T. H. Okiishi

DDC
RECEIVED
JUL 1 1977
A

MULTISTAGE AXIAL-FLOW TURBOMACHINE WAKE PRODUCTION, TRANSPORT, AND INTERACTION

Presented to the Air Force Office of Scientific Research for the period 1 September 1975 to 30 September 1976, Grant AFOSR 76-2916

DDC FILE COPY

TURBOMACHINERY
COMPONENTS RESEARCH PROGRAM

Approved for public release;
distribution unlimited.

ISU-ERI-AMES -77130
TCRL-7
Project 1204

ENGINEERING RESEARCH INSTITUTE
IOWA STATE UNIVERSITY
AMES, IOWA 50010 USA

AIR FORCE OFFICE OF SCIENTIFIC RESEARCH (AFSC)
NOTICE OF TRANSMITTAL TO DDC
This technical report has been reviewed and is
approved for public release IAW AFR 190-12 (7b).
Distribution is unlimited.
A. D. BLOSE
Technical Information Officer

SECURITY CLASSIFICATION OF THIS PAGE (When Data Entered)

REPORT DOCUMENTATION PAGE

READ INSTRUCTIONS BEFORE COMPLETING FORM

1. REPORT NUMBER: AFOSR-TR-77-0720	2. GOVT ACCESSION NO.
3. RECIPIENT'S CATALOG NUMBER	
4. TITLE (and Subtitle): MULTISTAGE AXIAL-FLOW TURBOMACHINERY WAKE PRODUCTION, TRANSPORT, AND INTERACTION	5. TYPE OF REPORT & PERIOD COVERED: INTERIM 1 Sept. 1 Sep 75 - 30 Sep 76
	6. PERFORMING ORG. REPORT NUMBER: ISU-ERI-AMES-77130
7. AUTHOR(s): DOUGLAS P. SCHMIDT, THEODORE H. OKIISHI	8. CONTRACT OR GRANT NUMBER(s): F44620-76-C-0007, AFOSR 76-2916
9. PERFORMING ORGANIZATION NAME AND ADDRESS: IOWA STATE UNIVERSITY, ENGINEERING RESEARCH INSTITUTE, AMES, IOWA 50010	10. PROGRAM ELEMENT, PROJECT, TASK AREA & WORK UNIT NUMBERS: 2307A4, 61102F
11. CONTROLLING OFFICE NAME AND ADDRESS: AIR FORCE OFFICE OF SCIENTIFIC RESEARCH/NA, BLDG 410, BOLLING AIR FORCE BASE, D C 20332	12. REPORT DATE: Nov 76
	13. NUMBER OF PAGES: 234
14. MONITORING AGENCY NAME & ADDRESS (if different from Controlling Office): 234 p.	15. SECURITY CLASS. (of this report): UNCLASSIFIED
	15a. DECLASSIFICATION/DOWNGRADING SCHEDULE

16. DISTRIBUTION STATEMENT (of this Report)

Approved for public release; distribution unlimited.

17. DISTRIBUTION STATEMENT (of the abstract entered in Block 20, if different from Report)

AF-AFOSR-2916-76

18. SUPPLEMENTARY NOTES: 2307 A1

19. KEY WORDS (Continue on reverse side if necessary and identify by block number)

AXIAL-FLOW COMPRESSOR
AXIAL-FLOW TURBOMACHINE
AXIAL-FLOW FAN
AXIAL-FLOW BLOWER
AXIAL-FLOW PUMP
WAKE
TURBOMACHINE FLUID FLOW
MULTISTAGE AXIAL-FLOW TURBOMACHINE

20. ABSTRACT (Continue on reverse side if necessary and identify by block number)

The first year results of a study of multistage axial-flow turbomachine wake production, transport and interaction are described in this report. Evidence indicating how the noise level measured at the inlet of a low speed, multistage, axial-flow research compressor was found to vary appreciably with inlet guide vane and stator row relative circumferential positioning with the largest amount of noise reduction occurring at the blade passing frequency is presented. The results of detailed slow- (cobra probe and surface pressure taps) and fast-response (hot-wire) measurements made within the research compressor flow field

DD FORM 1 JAN 73 1473 EDITION OF 1 NOV 65 IS OBSOLETE

404 418

UNCLASSIFIED

SECURITY CLASSIFICATION OF THIS PAGE (When Data Entered)

to aid in understanding the physics involved are shown in scalar and vector plots and tables. Significant local changes in blade-section aerodynamic performance and flow field appearance with variation in stationary blade row placement were observed although corresponding improvement of overall efficiency could not be ascertained. Several interesting periodically unsteady aspects of the flow field and its measurement are demonstrated and some conclusions about blade row interaction are proposed.

ENGINEERING RESEARCH

ENGINEERING RESEARCH
ENGINEERING RESEARCH
ENGINEERING RESEARCH
ENGINEERING RESEARCH

Interim Report

MULTISTAGE AXIAL-FLOW TURBOMACHINE WAKE PRODUCTION, TRANSPORT, AND INTERACTION

D. P. Schmidt
T. H. Okiishi

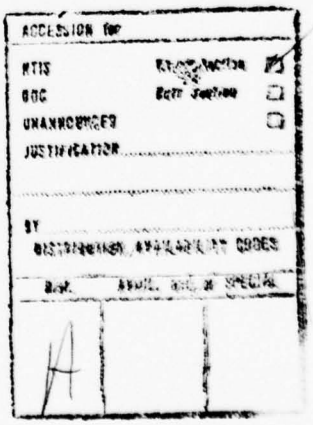
November 1976

ISU-ERI-AMES-77130
TCRL-7
Project 1204

ENGINEERING RESEARCH INSTITUTE
IOWA STATE UNIVERSITY AMES

ACKNOWLEDGMENTS

The work reported herein was accomplished in the Iowa State University Engineering Research Institute/Mechanical Engineering Department Turbomachinery Components Research Laboratory under Air Force Office of Scientific Research Grant AFOSR 76-2916. The encouragement of AFOSR Program Manager Lt. Col. Robert C. Smith is gratefully acknowledged. Additionally, the cost sharing participated in and the staff help provided by the ISU Engineering Research Institute and Mechanical Engineering Department and the personal support extended by Dr. Paul W. Peterson and Dr. Arthur E. Bergles are appreciated. The equipment grants received from the National Science Foundation and the ISU Research Foundation are acknowledged. The authors are also indebted to their colleagues, in particular, Dr. George K. Serovy and Dr. George H. Junkhan for their valuable comments, Mr. Joel H. Wagner for his help in obtaining and reducing data, Mr. Del D. Whitmer and Mr. Stephen Lee Wells for their superb solution of the many electronic problems we gave them, and Mr. Leon Girard and Mr. Lloyd R. Wasson for their dispatch of related machining. Finally, the authors wish to thank Mary Mishele Schmidt for her numerous contributions and loyal support throughout.



SUMMARY

The first year results of a study of multistage axial-flow turbomachine wake production, transport and interaction are described in this report. Evidence indicating how the noise level measured at the inlet of a low speed, multistage, axial-flow research compressor was found to vary appreciably with inlet guide vane and stator row relative circumferential positioning with the largest amount of noise reduction occurring at the blade passing frequency is presented. The results of detailed slow- (cobra probe and surface pressure taps) and fast-response (hot-wire) measurements made within the research compressor flow field to aid in understanding the physics involved are shown in scalar and vector plots and tables. Significant local changes in blade-section aerodynamic performance and flow field appearance with variation in stationary blade row placement were observed although corresponding improvement of overall efficiency could not be ascertained. Several interesting periodically unsteady aspects of the flow field and its measurement are demonstrated and some conclusions about blade row interaction are proposed.

TABLE OF CONTENTS

		Page
	ACKNOWLEDGEMENTS	ii
	SUMMARY	iii
I.	INTRODUCTION	1
II.	DIRECTLY RELATED RESEARCH	3
	A. Blade Interaction Effects	3
	B. Experimental Procedures and Instrumentation	8
III.	RESEARCH COMPRESSOR FACILITY	12
	A. Multistage Axial-Flow Research Compressor	12
	B. Probe and Stationary Blade-Row Actuators	20
	C. Pressure and Temperature Sensing Instrumentation	22
	D. Fast-Response Measurement System	23
	E. Calibration Nozzle	26
	F. Sound-Pressure Level (SPL) Measurement Instrumentation	27
	G. Data Acquisition and Reduction System	27
IV.	EXPERIMENTAL PROCEDURES AND DATA REDUCTION	30
	A. Sound-Pressure Level (SPL) Measurements	31
	1. Testing for noise variation over compressor rpm range	31
	2. Determining the minimum and maximum sound settings	33
	3. Obtaining detailed SPL measurements at minimum and maximum sound-level blade-row settings	34
	B. Slow-Response Measurements	34
	1. Probe calibration	34
	a. Total pressure calibration	36
	b. Probe yaw-angle calibration	37
	c. Kiel probe comparison	40

		Page
	2. Data acquisition	40
	3. Data reduction	43
	a. Flow-field parameters	43
	b. Rotor, stator, and stage performance parameters	47
C.	Fast-Response Measurements	47
	1. Periodic sampling and averaging technique	47
	2. Single hot-wire three-dimensional velocity measurement technique	51
	a. Probe geometry	53
	b. Effective cooling velocity/actual velocity ratio	55
	c. Measurement technique	58
	3. Calibration procedure	63
	a. Linearizer velocity calibration	64
	b. Second order velocity calibration	65
	c. Effective cooling velocity calibration	66
	4. Data acquisition	68
	5. Data reduction	75
V.	PRESENTATION AND DISCUSSION OF DATA	78
A.	Sound-Pressure Level Measurement Results	78
B.	Slow-Response Measurement Results	84
C.	Fast-Response Measurement Results	126
VI.	CONCLUSIONS	155
VII.	RECOMMENDATIONS FOR FUTURE RESEARCH	158
VIII.	BIBLIOGRAPHY	161
IX.	SYMBOLS AND NOTATION	164
X.	APPENDIX A: PERIODIC-SAMPLING CIRCUIT DESIGN	169
XI.	APPENDIX B: CALCULATOR PROGRAMS AND DATA STORAGE	174

		Page
XII.	APPENDIX C: PARAMETER EQUATIONS	176
	A. General Parameters	176
	1. Basic fluid properties	176
	2. Blade-element quantity	178
	3. Miscellaneous	178
	B. Slow-Response Instrument Parameters	178
	1. Point and circumferential-average blade-element quantities	178
	2. Global parameters	182
	C. Three-Dimensional Fast-Response Hot-Wire Parameters	183
XIII.	APPENDIX D: LEAST SQUARES EMPIRICAL CORRELATION FOR EFFECTIVE COOLING VELOCITY RATIO	185
XIV.	APPENDIX E: TABULATION OF SLOW-RESPONSE DATA	188
XV.	APPENDIX F: TABULATION OF FAST-RESPONSE HOT-WIRE DATA	210

LIST OF FIGURES

		Page
Figure 3.1.	Driving motor and research compressor.	13
Figure 3.2.	The axial-flow compressor rig.	14
Figure 3.3.	Blade nomenclature.	16
Figure 3.4.	Compressor blading.	17
Figure 3.5.	Schematic diagram showing axial location of probe measurement stations (dimensions in mm).	18
Figure 3.6.	Research compressor apparatus side view.	19
Figure 3.7.	Probe and stationary blade-row actuators.	21
Figure 3.8.	Schematic setup diagram of fast-response measurement system.	24
Figure 3.9.	Calibration nozzle, probe positioner, and optical alignment telescope used for probe calibration.	28
Figure 4.1.	Sound-level meter and position of microphone for compressor inlet noise measurement.	32
Figure 4.2.	Total-pressure and flow-yaw-angle cobra probe and probe angle nomenclature.	35
Figure 4.3.	Cobra probe total-pressure calibration curves.	38
Figure 4.4.	Cobra probe yaw angle sensitivity calibration curve.	39
Figure 4.5.	Cobra and Kiel probe comparison.	39
Figure 4.6.	Static-pressure radial equilibrium solution for the compressor behind the third stator.	46
Figure 4.7.	Percent variation coefficient of the periodic-sample averages for different values of N.	52
Figure 4.8.	Hot-wire configuration relating velocity vector $\vec{V}$ to hot-wire sensor and probe coordinates x, y, z.	54
Figure 4.9.	Typical effective cooling velocity calibration results for a 35.35 degree inclined hot-wire.	57

Page

Figure 4.10. Hot-wire measurement positions and nomenclature, viewed from above along probe axis. 61

Figure 4.11. Probe actuator positioned at calibration nozzle for hot-wire velocity calibration. 72

Figure 4.12. Compressor coordinate system showing nomenclature and sign convention for three-dimensional fast-response velocity and angle parameters. 76

Figure 4.13. Hot-wire measurement positions with respect to compressor coordinates Y and Z. 76

Figure 5.1. Compressor inlet noise level over compressor rpm range. 79

Figure 5.2. Required noise reductions for subjective improvement from Sofrin (11). 82

Figure 5.3. Compressor inlet noise spectrum (1% filter bandwidth). 83

Figure 5.4. Blade-to-blade plane, time-average, velocity vector plot for first stator at mid-span (constructed from slow-response data). 85

Figure 5.5. Blade-to-blade plane, time-average, velocity vector plots at constant passage height for the minimum sound blade-row schedule; constructed from slow-response data. 87

Figure 5.6. Blade-to-blade plane, time-average, velocity vector plots at constant passage height for the maximum sound blade-row schedule; constructed from slow-response data. 96

Figure 5.7. Circumferential-average axial velocity blade span distribution. 107

Figure 5.8. Circumferential-average absolute tangential velocity blade span distribution. 108

Figure 5.9. Circumferential-average absolute tangential flow angle blade span distribution. 109

Figure 5.10. Blade span distribution of total-head-loss coefficient for rotor and stator blade rows. 110

		Page
Figure 5.11.	Blade span distribution of incidence and deviation blade angles, rotor and stage head-rise coefficient and hydraulic efficiency.	113
Figure 5.12.	Comparison of slow-response and fast-response data behind the first stator.	128
Figure 5.13.	Mid-span slow-response instrument averaged velocity vector variation for first stator with inlet guide vane wake streets shown.	129
Figure 5.14.	Multiple oscilloscope traces of hot-wire signal for location A.	131
Figure 5.15.	Multiple oscilloscope traces of hot-wire signal for location B.	132
Figure 5.16.	Circumferential distribution of periodic-average flow field parameters behind the first rotor at 50% passage height for locations A and B, obtained with rotor-passing survey method.	133
Figure 5.17.	Circumferential distribution of periodic-average flow field parameters obtained at different rotor positions with frozen rotor-blade flow-field survey method.	135
Figure 5.18.	Blade-to-blade velocity vector plots obtained at different rotor positions with frozen rotor-blade survey method.	141
Figure 5.19.	Circumferential distribution of periodic-average flow field parameters obtained at different radial positions with frozen rotor-blade survey method.	150
Figure 5.20.	Blade-to-blade velocity vector plots obtained at different radial positions with frozen rotor-blade survey method.	152
Figure 10.1.	Block diagram of periodic-sampling circuit.	166
Figure 10.2.	Circuit diagram of triggering and sample-and-hold circuits.	167
Figure 10.3.	Power supply for triggering and sample-and-hold circuits.	168

Page

Figure 10.4. Interfacing cable connections. 169

Figure 12.1. Sketch showing nomenclature, sign convention, and velocity triangles for slow-response instrument parameters. 177

LIST OF TABLES

		Page
Table 3.1.	Geometric blade details for IGV, rotors and stators at several radial locations.	16
Table 4.1.	Specifications for periodic-average hot-wire circumferential surveys, all measurements were made at the minimum sound stationary blade-row schedule.	69
Table 5.1.	Stationary blade-row circumferential placement schedules for minimum and maximum sound.	81
Table 5.2.	Overall and octave band analyses of compressor inlet noise for minimum and maximum noise blade-row schedules.	81
Table 5.3.	Uncertainty levels of slow-response parameters.	121
Table 5.4.	Flow rate comparison between venturi and integrated measurement station flow rates.	122
Table 5.5.	Uncertainty and scatter of periodic-average flow field parameters.	127
Table 13.1.	Equation 13.14.	187
Table 14.1.	Point-by-point circumferential distributions of total head for minimum noise condition.	189
Table 14.2.	Point-by-point circumferential distribution of total head for maximum noise condition.	197
Table 14.3.	Blade-to-blade circumferential-average values of total head, static head, tangential flow angle, and incidence and deviation angles for minimum noise condition.	205
Table 14.4.	Blade-to-blade circumferential-average values of total head, static head, tangential flow angle, and incidence and deviation angles for maximum noise condition.	207
Table 14.5.	Circumferential-average outer-annulus-surface static head for minimum and maximum noise conditions.	209

Page

Table 15.1. Fast-response circumferential survey data obtained with frozen rotor-blade survey method at minimum noise condition. 211

Table 15.2. Fast-response circumferential survey data obtained with passing rotor-blade survey method at minimum noise condition. 221

I. INTRODUCTION

Although most modern multistage turbomachine design procedures are very sophisticated in many respects, they remain incomplete because of our present inability to consistently determine some important details of the complicated fluid flow field involved. For example, the general calculation of spatial and unsteady (periodic and random) changes of the turbomachine flow field and blade response with enough detail and precision to avoid undesirable acoustic and aeromechanical performance is still a major unresolved problem. Further, the total-pressure losses and flow turning angles precisely required by all modern computer based turbomachine design procedures are often very difficult to predict well, especially under off-design operation conditions. At best, limited empirical correlations are relied on.

One way to improve the design and reliability of turbomachines is to gain a better understanding of the fluid mechanics involved via fundamental laboratory experiments. In particular, an understanding of the unsteady interaction that occurs between moving and stationary blade rows via viscous wake and potential flow effects would provide valuable design information with respect to aeroelastic stability and noise generation. The details of blade wake production and transport are important aspects of the viscous wake interaction process. This kind of information is, however, not readily available in the open literature. For example, little is published concerning the effects of relative circumferential positioning of the blade rows in an axial-flow multistage turbomachine on the aerodynamic, acoustic, and aeromechanical characteristics of the

machine. Work in this area indicates that the rotor and stator flow fields in multistage turbomachines can be considerably influenced by the relative circumferential position of the stationary blade rows. In the research compressor used in the present investigation, the sound level at the compressor inlet could be varied significantly by adjusting the circumferential positions of the stationary blade rows relative to each other.

The primary purpose of the present research project was to experimentally investigate the three-dimensional, unsteady fluid flow field within a low-speed, three-stage, axial-flow research compressor in order to develop a better understanding of the fluid physics involved. To gain an appreciation for the unsteady flow effects of blade wake production, transport, and interaction, slow-response and fast-response instrument data were obtained between the blade rows of the research compressor. Time-average flow field measurements were obtained with a slow-response pressure and flow-angle probe throughout the compressor at two distinct stationary blade row circumferential placement schedules corresponding to minimum and maximum compressor inlet noise levels. In addition, a hot-wire measurement technique was developed and three-dimensional periodic-average measurements were made of the unsteady flow field to obtain further details of the flow.

Although some of the specific results obtained to date are peculiar to the research compressor configuration involved, the general concepts developed are applicable to all multistage axial-flow turbomachines.

II. DIRECTLY RELATED RESEARCH

A. Blade Interaction Effects

The effects and importance of the interaction between blade rows have been considered by numerous individuals. (See for example Meyer (1), Smith (2), Kerrebrock and Mikolajczak (3), Parker and Watson (4), Walker and Oliver (5), Kiock (6), Lockhart and Walker (7), and Mikolajczak (8).) Blade row interaction appears to be of particular importance when turbomachine performance and blade vibration and noise generation improvements are sought. It is also possible that blade interaction effects could significantly influence cavitation occurrence in hydraulic turbomachines and blade surface heat transfer rates in gas turbines. The interaction can involve blade rows several stages apart (2,4) as well as those that are adjacent to each other. Basically, there are two recognized types of interaction, a viscous wake one which primarily is a result of downstream blades cutting through the wakes of upstream blades, and a potential flow one which would be present even if the working fluid was inviscid. Both types of blade interaction can play important roles in the development of the unsteady flow field and subsequent consequences in a turbomachine. Data presented by Fincher (9) and Doak and Vaidya (10) suggest that the importance of potential flow interaction becomes insignificant in comparison to viscous wake interaction when the axial blade row spacing is 30% or greater of the blade chord. As indicated by Sofrin (11), the interaction phenomena involve periodic events at blade passing frequency and harmonics as well as random occurrences. According to Evans (12) and Raj and Lakshminarayana (13), periodic and random unsteadiness

values are of the same order of magnitude near design point operation. Evans (12) further concluded that random unsteadiness becomes most important near stall. As pointed out by Horlock (14), the work of Tyler and Sofrin (15) on the rotating adjacent blade row interaction pressure pattern is an outstanding accomplishment of the past. Their conclusion relating the speed of spinning acoustic patterns to duct sound propagation is well accepted and is applied in present design procedures.

Blade row interaction is obviously related to the manner in which fluid is transported through a blade row. Several individuals including Smith (2), Walker and Oliver (5), Okapuu (16), and Lockhart and Walker (7) have found experimentally that the rotor exit flow can be significantly influenced by a periodic flow pattern at the rotor inlet from an upstream stationary blade row such as inlet guide vanes, stators or nozzles. Stationary periodic flow patterns were observed to propagate through the rotor row, and considerable viscous wake interactions were identified in some instances. Smith (2) offered a qualitative description of the wake interaction phenomenon between an upstream stationary blade row and a downstream rotor blade row, and provided a means for calculating some of the geometrical aspects of the flow. He proposed that as the wakes from the upstream stationary blade row move through the rotor row, they are affected not only by viscous action but also by dispersive wake chopping and uneven energy addition. The chopping action results from the rotor blades cutting through and reorienting the upstream flow disturbance, while the uneven energy addition results from the wake fluid residing in the rotor longer than the freestream fluid. Qualitative hot-wire

anemometer measurements obtained in a four-stage, low-speed, axial-flow compressor behind the first rotor at the mean diameter were displayed by Smith (2) to illustrate how the rotor exit flow field varies with circumferential position because of the influence of the IGV blade wakes on the rotor exit flow. In addition, Smith (2) observed that the flow pattern behind the third rotor could be altered significantly by circumferentially moving the IGV row. Savell and Wells (17) have shown that the attenuation of a stationary periodic flow variation (produced, for example, by an upstream stationary blade row) through a rotor blade probably depends upon a number of variables including distortion wave length and rotor design characteristics (chord length, solidity, loading, flow Mach number levels and angles, blade angle, and flow passage annulus shape). Measurements made by Walker and Oliver (5) on a single-stage (IGV-rotor-stator combination), low-speed axial-flow compressor with the same number of IGV and stator blades showed that considerable reduction of compressor inlet noise (at blade passing frequency) could be achieved with appropriate circumferential positioning of the IGV and stator blade rows relative to each other. They claimed that the noise reduction was due to a combination of blade section pressure fluctuation reduction and sound wave interference. Further measurements by Lockhart and Walker (7) in the same research compressor, indicate that the mean velocity, apparent turbulence levels, and rotor wake decay rate all varied periodically in the circumferential direction as a result of the IGV and rotor wake interaction. A simple physical model of the wake interaction process was proposed by these authors on the basis of their slow and fast response instrument measurements. Kerrebrock and Mikolajczak (3) offered an explanation of the

experimentally observed stagnation temperature variations in the tangential direction downstream of stators in high Mach number compressor stages. They proposed that the transport of rotor wakes through the stator row is the cause of this phenomenon and presented a wake transport theory. While the experimental evidence presented by the authors in support of their theory is convincing, Lockhart and Walker (7) concluded that the analysis is not appropriate in a multistage turbomachine because of the significant wake-to-wake interactions that can occur upstream of a stator.

Also related to blade row interaction are the detailed characteristics of rotor and stator wakes. Important research on this aspect includes the works of Whitfield et al. (18), Lockhart and Walker (7), Evans (12), Raj and Lakshminarayana (13), Thompkins and Kerrebrock (19), and Hirsch and Kool (20). Lockhart and Walker (7) concluded that because rotor wake apparent turbulence level decay can vary significantly with circumferential position, the rotor wake should not be modeled by the wake decay behind an isolated airfoil or a single cascade as is commonly assumed in current blade row interaction theories. In one instance, they observed that rotor wake turbulence level increased instead of decayed with distance downstream. Raj and Lakshminarayana (13) compared isolated rotor wake decay data with those for an isolated airfoil and a cascade of aerofoils, and found that the rotor wake velocity defect, turbulence intensities, and Reynolds stresses decayed much faster. Further, they found that the anisotropy, the magnitude of turbulence intensities, and the Reynolds stresses associated with an isolated rotor blade wake are much higher than those of a cascade blade wake. Based on their measurements,

Raj and Lakshminarayana (13) developed an approximate quasi-three-dimensional turbulent wake model for a turbomachine rotor blade. Lieblein and Roudebush (21) found that the downstream variations of turbulent cascade and isolated airfoil wake characteristics (minimum velocity, form factor, full thickness, and total pressure loss) were generally similar. Parker and Watson (4) indicate that preliminary comparisons of uncambered C4 airfoil cascade velocity defect decay data and isolated airfoil wake data calculated after Silverstein et al. (22) do not compare favorably. Raj and Lakshminarayana (13) concluded that a cascade blade wake differs from that of a cylinder, a flat plate and an isolated and symmetrical airfoil at zero incidence in several ways. Several researchers (see Refs. 13, 18, 19, 20) noted that the radial velocities in rotor wakes are significant due to an imbalance of centrifugal and pressure forces inside the wakes. Further, substantial variations in downstream stator incidence angle were observed by Evans (12). Thompkins and Kerrebrock (19) claimed that large static pressure variations can occur in rotor wakes. The data of Whitfield et al. (18), Raj and Lakshminarayana (13), Thompkins and Kerrebrock (19), and Hirsch and Kool (20) indicated that substantial variations may occur in rotor wake characteristics in the spanwise direction. Raj and Lakshminarayana (13) showed the variation of wake half-width decay with radius. Thompkins and Kerrebrock (19) presented numerous rotor exit flow field contour plots illustrating radial and circumferential variations of total pressure, static pressure, radial, axial, and tangential Mach numbers, total temperature, and entropy rise at 0.1 and 1.0 chord downstream of the rotor. Whitfield et al. (18) and Hirsch and Kool (20) showed three-dimensional velocity vector plots as well as more

conventional scalar graphs which demonstrate the spanwise variations in rotor wake velocities. Additionally, Whitfield et al. (18) offered rotor blade row exit flow field contour plots to display radial and circumferential variations of absolute velocity, swirl angle, and pitch angle. Kiock (6), Evans (12), and Hirsch and Kool (20) presented limited data showing the variation of rotor wake characteristics with changes in flow coefficient.

While much has already been accomplished in the past, more remains to be done. For example, data related to the variation of periodic-average rotor wake shape with frozen rotor section circumferential position when the rotor flow is unsteady in all frames of reference do not appear to be available in the open literature. Detailed slow- and fast-response instrument data related to multistage turbomachine blade wake production, transport, and interaction as well as data showing the results of particular blade row placement schedules are scarce. As noted recently by Mikolajczak (8),

> The state of the art in turbomachinery technology has advanced to the point where further significant improvements will come from the understanding and control of the unsteady flows which exist in turbomachines.

The present work is intended as a modest contribution to the growing body of literature in this area.

B. Experimental Procedures and Instrumentation

Because modern turbomachine flow measurement techniques can involve complicated procedures and instruments, a brief review of related research on this topic area follows. A good overview of state-of-the-art

turbomachine flow measurement techniques including the use of slow- and fast response probes and transducers, flow visualization, and laser based optical methods is available in Ref. 23. As pointed out by Whitfield et al. (18), most of the measurements made prior to 1971 were obtained upstream and downstream of blade rows using stationary slow-response instrumentation. These tests provided much information on the time-average flow field and the overall performance characteristics of the blade rows. In the case of rotor row exit flow, however, very little if any, circumferential survey information was available until recently. Detailed unsteady flow data were scarce. Rotating instrumentation and fast-response stationary instrumentation were developed by a few early investigators (24,25), but none of these methods were used to measure the complete three-dimensional, time-dependent flow field involved behind a rotating blade row.

Of particular relevance to the present research are the hot-wire anemometer measurement techniques developed by Whitfield et al. (18), Lakshminarayana and Poncet (26), Lockhart and Walker (7), Evans (12), Raj and Lakshminarayana (13), and Hirsch and Kool (20). In all instances cited above, a means of phase locking the measurement with the rotor motion was used and some form of ensemble averaging was accomplished. Lockhart and Walker (7) used a single-wire probe aligned radially while Evans (12) used a single wire probe aligned perpendicular to the radius as well as an X-type probe. In both cases, radial velocities were ignored. A technique involving a single-wire sensor inclined 54.7 degrees with respect to the probe axis was used by Whitfield et al. (18) for measurement of the three-dimensional, periodic-average flow field behind an isolated rotor. The

slant wire was rotated about the probe axis at increments of 120 degrees and data were obtained for each of three mutually orthogonal orientations of the sensor. A relatively simple set of equations (simple because of the geometry of the probe and the measurement positions selected) were used to relate the readings at the three wire orientations to the axial, tangential, and radial velocity components. Hirsch and Kool (20) further developed this general single-wire technique, and through a more complex set of reduction equations extended the method so that probes of any inclined wire angle could be used with any three wire measurement orientations. To demonstrate this technique, they presented (20) periodic-average velocity measurements of the flow field behind a rotor with an upstream IGV row in a low-speed, axial-flow turbomachine. Lakshminarayana and his students (13,26,27) have developed some three-dimensional, hot-wire anemometry procedures which utilize stationary and rotating probes with three orthogonally directed sensors. Raj (13) obtained three-dimensional, periodic-sample, circumferential blade-to-blade profiles of velocity, turbulence intensity, and Reynolds stress behind an isolated axial-flow fan rotor while Gorton (27) made measurements within a pump inducer rotor and Poncet (26) obtained data downstream of a pump inducer rotor. Although experimental data are not yet available, Hardin (see Ref. 28) developed a triaxial hot-wire technique which has been used to make on-rotor measurements of a compressor rotor wake.

In comparing the single-wire and three-wire systems, the three-wire system seems especially advantageous for measuring the three-dimensional components of turbulence intensity (random unsteadiness) since the three sensor readings can be obtained simultaneously. However, as pointed out

by Hirsch and Kool (20), the three-wire system can have several disadvantages including: (1) poor spatial resolution, (2) increased possibility of encountering probe prong interference effects, (3) difficulty of securing optimum wire positions for all flow situations, (4) increased work in obtaining a complete and accurate calibration, and (5) increased cost of initial system and repairs. The three-wire systems developed to date could be improved further by optimizing the relative positions of the three wires and deriving a more general set of reduction equations which would apply for any wire configuration. Hirsch and Kool (20) note that the advantages of a single-wire system include: (1) better spatial resolution since the sensor is rotated about the probe centerline, (2) less calibration effort required, (3) greater possibility for optimization of wire measurement positions, and (4) smaller cost of initial system and repairs. On the other hand, the time required to obtain a set of measurements is much greater, and it is more difficult to acquire the three-dimensional flow quantities of turbulence intensity with the single-wire system.

The distinction between measurements made with a stationary hot-wire probe and those made with a circumferentially traversing probe moved ahead of or behind a periodically frozen rotor blade row has not yet been seriously considered in the open literature. For a rotor operating under unsteady relative flow conditions, the difference can be significant as will be shown in the present report.

III. RESEARCH COMPRESSOR FACILITY

The research compressor facility of the Iowa State University Engineering Research Institute/Mechanical Engineering Department Turbomachinery Components Research Laboratory was used in this research program. A description of the compressor and related equipment and instrumentation is presented in this section.

A. Multistage Axial-Flow Research Compressor

The low Mach number, three-stage, axial-flow research compressor, shown schematically in Figure 3.1, was used in the experimental investigation. Photographs of the compressor rig are shown in Figure 3.2. A smooth gradually contracting inlet to the compressor guided the flow entering the inlet guide vanes and three subsequent sets of rotor-stator stages. The compressor flow path involved constant hub and tip diameters of .285 m (11.2 in.) and .406 m (16.0 in.), respectively, resulting in a hub/tip radius ratio of 0.7. The blades were made up of British C4 sections reflecting a free vortex design and were constructed of a plastic (Monsanto ABS) material. Overall blade characteristics are as follows:

Number of blades per row	IGV and stator rows - 37 rotor rows - 38
Blade span (constant)	6.10 cm (2.4 in.)
Blade chord (constant), c	3.05 cm (1.2 in.)
Blade section maximum thickness/ chord ratio, t_{max}	10%

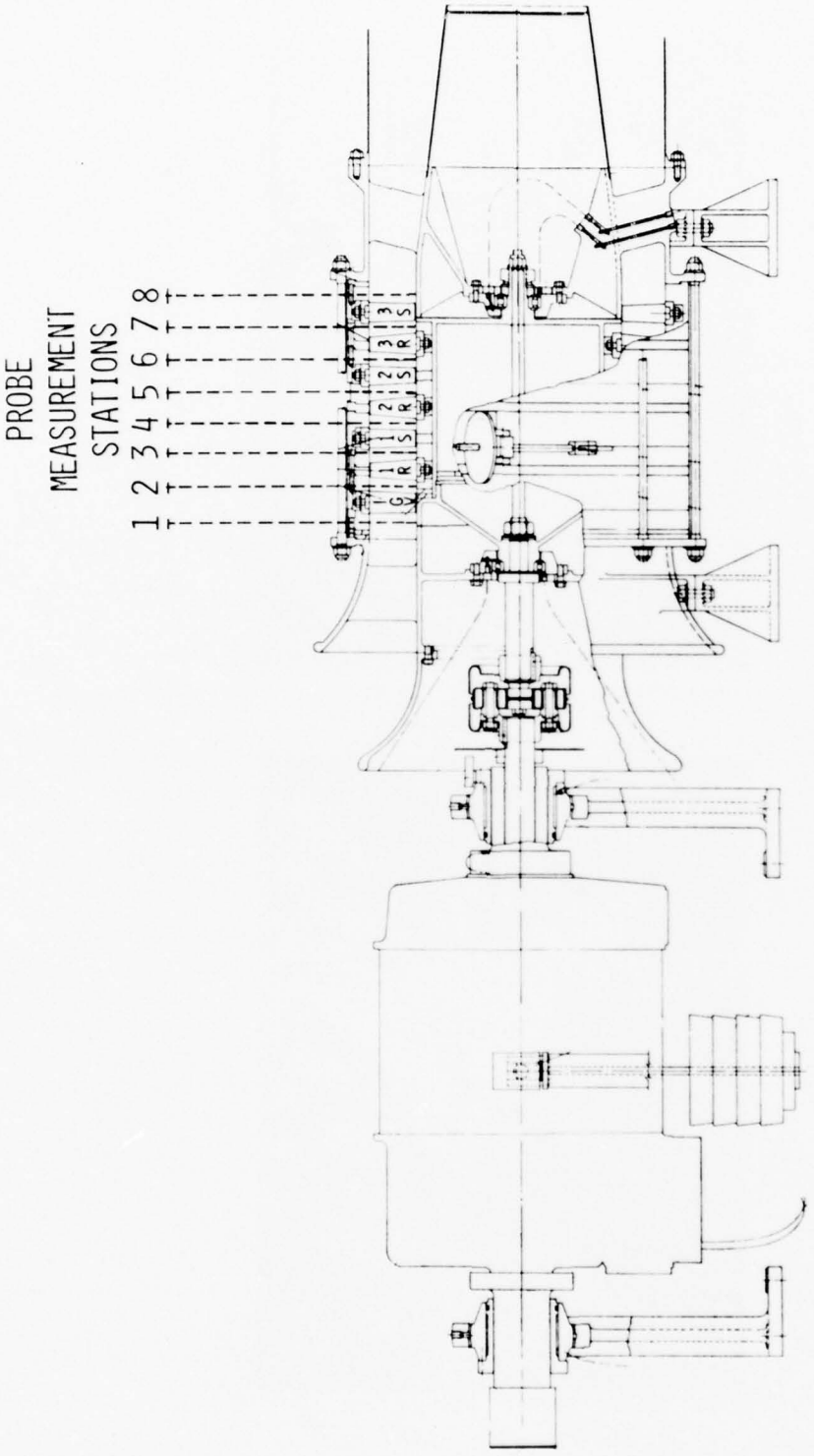
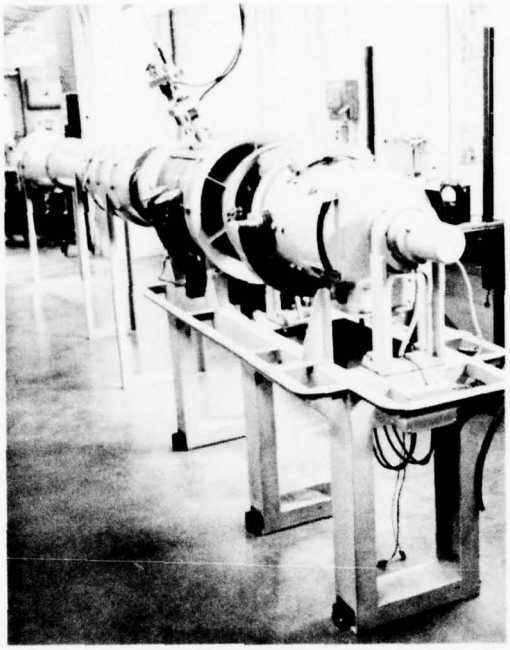
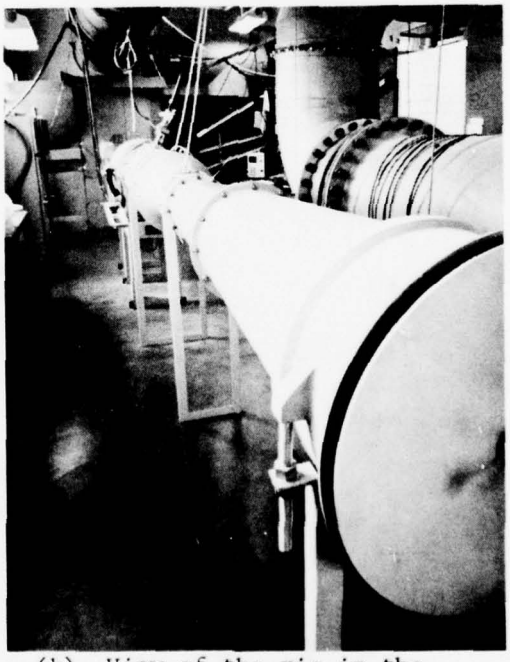


Figure 3.1. Driving motor and research compressor.



(a) View of the rig in the downstream direction.



(b) View of the rig in the upstream direction.

Figure 3.2. The axial-flow compressor rig.

The three rotor-stator stages were identical repeating stages, and the number of IGV blades and stator blades per row were the same. Further geometric blade details are tabulated in Table 3.1, and associated nomenclature is described in Figure 3.3. Figure 3.4 shows the arrangement of the stationary and rotor blade rows. Each blade row was in the form of an independent ring assembly which permitted rapid disassembly and reassembly of the compressor flow path and adjustment of the blade setting angles as well as the axial spacing between rows which was set for approximately 0.7 chord length (see Figure 3.5). The four stationary blade-row supporting rings were mounted in circular tracks in the outer-annulus casing to permit independent rotation of each stationary blade row about the machine axis. The stationary blade rows could be rotated during tests by means of a circumferential motion actuator which was mechanically linked to each stationary blade-row mounting ring as described in more detail later in the probe and stationary blade-row actuators section. For the present study, the three rotor-blade-row rings were positioned during assembly so that corresponding blade stacking axes for each rotor row were in line when viewed along the compressor axis. Probe-traversing measurement stations were aligned axially upstream and downstream approximately midway between each blade row, the exact axial location of each probe measurement station is shown in Figure 3.5. The compressor discharged into a downstream duct, as shown in Figure 3.6, which included an air straightening section, a venturi flow rate meter, a diffuser section, and a variable outlet-throttle plate. The compressor was driven by an 11 kW thyristor controlled variable speed (300-3000 rpm) motor mounted on air bearings to facilitate shaft torque measurement with a lever arm and weights

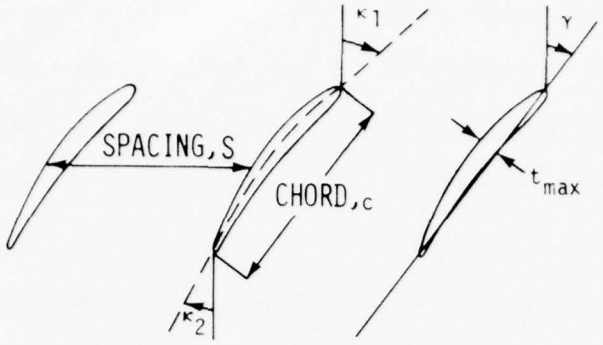
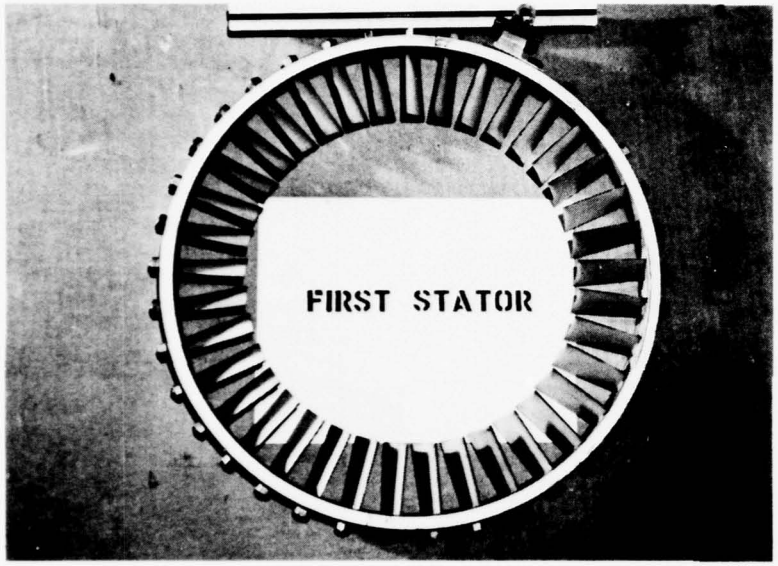


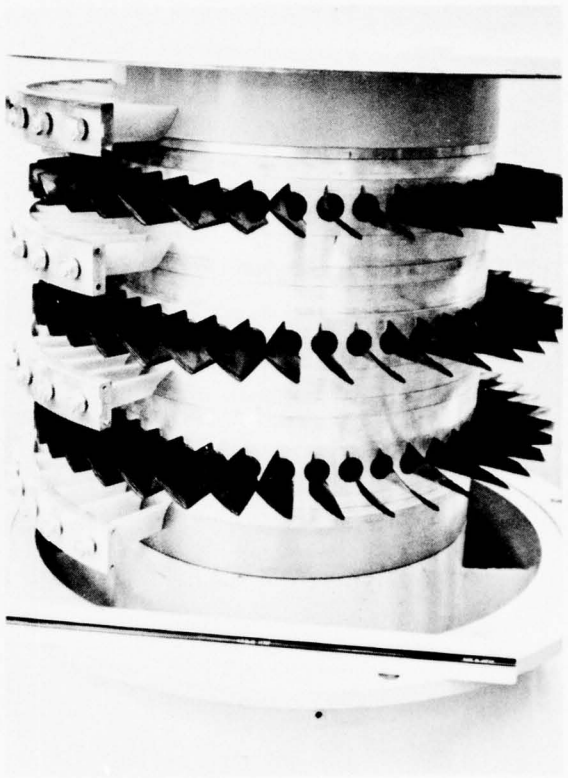
Figure 3.3. Blade nomenclature.

Table 3.1. Geometric blade details for IGV, rotors and stators at several radial locations.

Blade Row	Percent Passage Ht. From Hub PHH	Solidity c/S	Blade Angles: Stagger γ degrees	Inlet κ_1 degrees	Outlet κ_2 degrees	Camber $\kappa_1 - \kappa_2$ degrees
IGV	0	1.263	20.35	0.00	42.10	-42.10
	10	1.211	20.05	0.00	40.77	-40.77
	20	1.164	19.69	0.00	39.47	-39.47
	30	1.121	19.25	0.00	38.23	-38.23
	40	1.080	18.65	0.00	37.08	-37.08
	50	1.041	18.15	0.00	36.05	-36.05
	60	1.004	17.63	0.00	35.02	-35.02
	70	0.971	17.05	0.00	33.93	-33.93
	80	0.940	16.45	0.00	32.92	-32.92
	90	0.913	15.65	0.00	32.10	-32.10
	100	0.887	14.15	0.00	31.40	-31.40
Rotor	0	1.299	-20.54	-42.40	3.90	-46.30
	10	1.250	-24.39	-44.76	- 2.84	-41.92
	20	1.205	-28.11	-46.85	- 9.51	-37.34
	30	1.164	-31.70	-48.53	-15.96	-32.57
	40	1.123	-35.15	-49.82	-21.88	-27.94
	50	1.078	-38.47	-50.81	-27.06	-23.75
	60	1.035	-41.66	-51.77	-31.64	-20.13
	70	0.999	-44.71	-52.90	-35.78	-17.12
	80	0.968	-47.63	-53.98	-39.26	-14.72
	90	0.939	-50.41	-54.82	-41.91	-12.91
	100	0.909	-53.07	-55.50	-44.10	-11.40
Stator	0	1.263	40.24	54.80	26.70	28.10
	10	1.211	39.32	53.48	25.67	27.81
	20	1.164	38.39	52.36	24.68	27.68
	30	1.121	37.46	51.43	23.74	27.69
	40	1.080	36.54	50.25	22.77	27.48
	50	1.041	35.61	48.56	21.72	27.84
	60	1.004	34.68	47.13	20.76	26.37
	70	0.971	33.75	46.65	20.01	26.64
	80	0.940	32.83	46.36	19.34	27.02
	90	0.913	31.90	45.59	18.62	26.97
	100	0.887	30.97	44.50	17.85	26.65



(a) First stator blade-row assembly.



(b) Stationary and rotor blade-row arrangement.

Figure 3.4. Compressor blading.

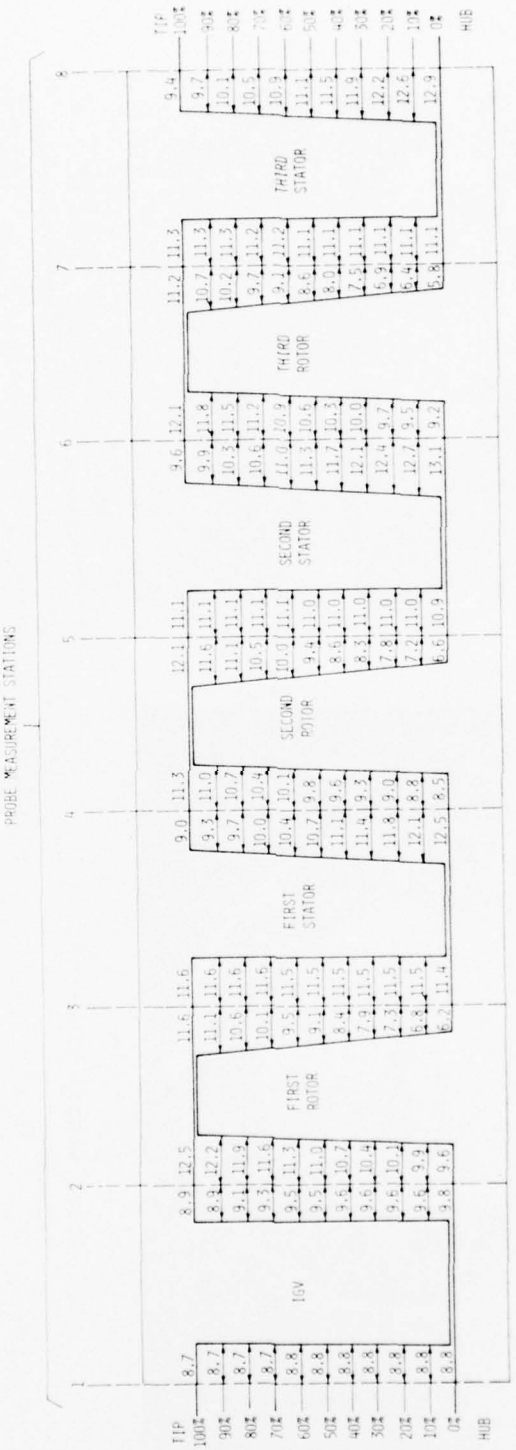


Figure 3.5. Schematic diagram showing axial location of probe measurement stations (dimensions in mm).

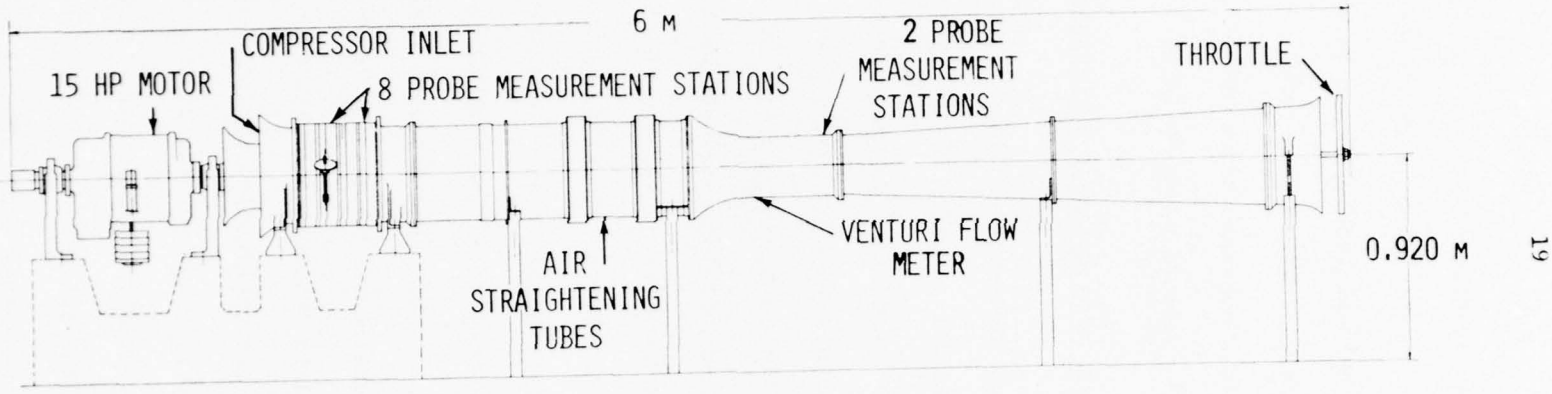
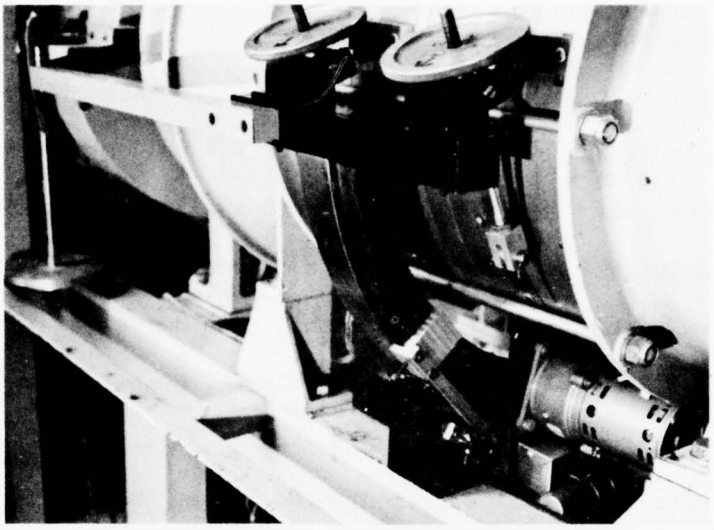


Figure 3.6. Research compressor apparatus side view.

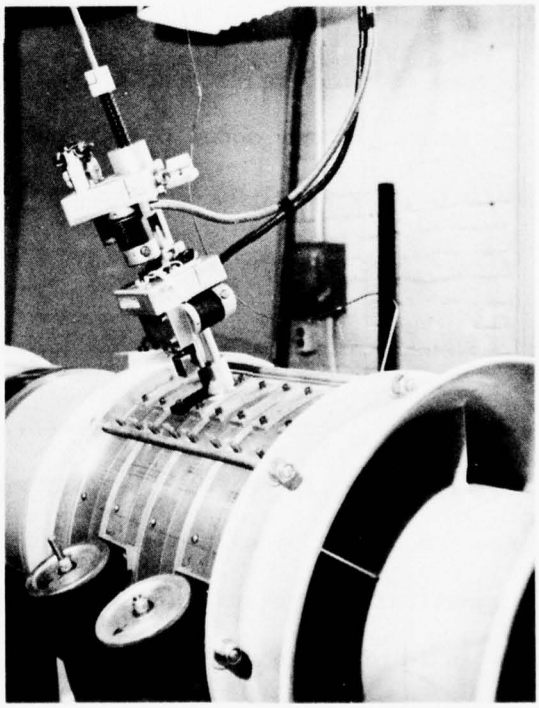
arrangement. Shaft rpm measurement was made with a frequency counter and a magnetic pickup off a 60-toothed gear on the shaft. The motor speed was controlled by a multiturn helical potentiometer balanced against a feedback voltage from a dc tachogenerator which rotated with the motor shaft. It was possible to maintain a constant rotor speed to within ±1 rpm. More details about the research compressor may be found in Ref. 29.

B. Probe and Stationary Blade-Row Actuators

The circumferential motion actuator system, shown in Figure 3.7a, was used to set the circumferential position of the stationary blade rows. The actuator was basically composed of a semicircular dovetail slide driven by a gearmotor through a rack and pinion gear arrangement. The actuator was connected to each stationary blade-row mounting ring through an adjustable hand-screw link, making possible the simultaneous or individual circumferential movement of all the stationary blade rows. The circumferential positions of the individual stationary blade rows were determined with four circumferential blade-row scales (one for each blade row) marked in degrees and mounted on the compressor outer casing. The scales were designed so that angle readings were positive in the direction of rotor rotation, and a reading of 0.0 degrees corresponded to a position where the blade stacking axis was in axial alignment with the probe-traversing stations. The circumferential position of the actuator slide could be recorded by monitoring the voltage of a linear potentiometer geared to the slide. The potentiometer output voltage was correlated to the incremental motion of the actuator by a linear least squares fit. When the stationary blade rows were moved jointly with the actuator, the



(a) Circumferential motion actuator connected to the stationary blade rows.



(b) Probe immersion and angle actuator mounted at a probe-traversing measurement station.

Figure 3.7. Probe and stationary blade-row actuators.

positions of the blade rows were specified by recording Y, the circumferential position of the actuator in degrees as determined from the potentiometer voltage, and by knowing the circumferential position of each blade row when Y was equal to zero (Y0). The values of Y0 for the stationary blade rows ($Y0_{IGV}$, $Y0_{1S}$, $Y0_{2S}$ and $Y0_{3S}$) were determined from the circumferential blade row scales. The actuator system could be used to position the stationary blades to within 0.05 degrees.

Figure 3.7b shows the probe actuator (L. C. Smith Company model 6180) which was used for probe angle and immersion positioning. The probe angle and radial positions were each monitored by both mechanical digital counters and by linear potentiometers. The potentiometer voltages were correlated to their respective movements by a linear least squares fit and were used to record the probe angle and immersion positions with an accuracy of 0.05 degrees and 0.15 mm, respectively. A probe actuator control indicator (L. C. Smith Company model DI-3R) and probe actuator switchbox (L. C. Smith Company model DI-4R-SB) were used to control the probe actuator.

C. Pressure and Temperature Sensing Instrumentation

A scanning valve system (Scanivalve Company model 48D3-1) including a strain-gage pressure transducer (Scanivalve Company model PDCR22) and a bridge circuit (Endevco model 4470) were used for qualitative pressure measurements. All quantitative pressure measurements were made using various precision water in glass manometers (Meriam type Incl.) which were calibrated with a micromanometer (Meriam type Micro.). A conventional pitot tube (United Sensor type PC) was used as a calibration standard for

fluid velocity measurement. Several types of pressure probes, including Kiel, cobra, wedge, and sphere, were tested for suitability in the compressor. A cobra probe (United Sensor type CA), capable of measuring total pressure and flow yaw angle, proved most appropriate for use in the compressor and was used for almost all slow-response measurement tests. An outer-annulus wall static pressure tap was provided at each axial location corresponding to a probe-traversing station. In addition, a hub static pressure tap was installed behind the third stator row where the hub was stationary. Several wall pressure static taps were also located at the inlet and throat of the flow rate venturi meter. Mercury in glass thermometers were used to measure room air temperature while copper-constantan thermocouples and a precision millivolt potentiometer (Leeds and Northrup Company model 8686) were used to measure flowing fluid temperatures. A mercury in glass barometer (Princo Instruments, Inc. Model B-222) was used to measure atmospheric pressure.

D. Fast-Response Measurement System

A setup diagram of the fast-response measurement system used to make periodic-average, three-dimensional velocity measurements is shown in Figure 3.8. The system consisted of the following components:

(1) Single slant hot-wire probe (Disa model 55P02 Modified)

(2) Constant temperature anemometer (Thermo-Systems, Inc. (TSI) model 1010A)

(3) Linearizer (TSI model 1072)

(4) Periodic sample-and-hold circuit

(5) Photoelectric triggering circuit

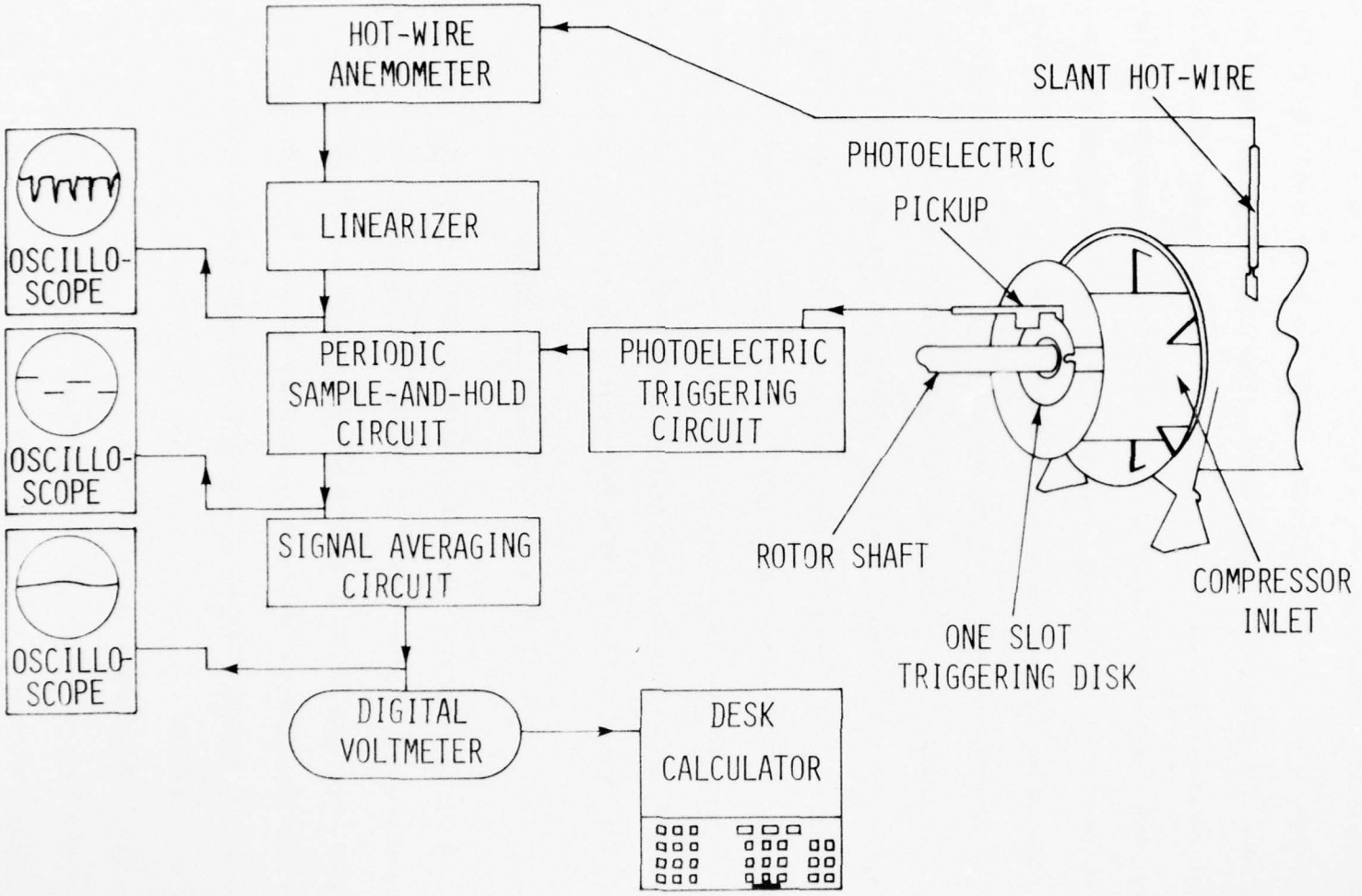


Figure 3.8. Schematic setup diagram of fast-response measurement system.

(6) Signal averaging circuit (TSI model 1047)

(7) Digital scanning voltmeter (Hewlett-Packard model 3480D)

(8) Desk-top calculator (Hewlett-Packard model 9821A)

(9) Oscilloscopes (Tektronix Inc.)

The hot-wire probe involved a 5 μm diameter platinum-plated tungsten wire with a 1.25 mm sensitive wire length and copper and gold plating at the ends. One wire was slanted with respect to a plane normal to the probe axis at an angle of 35 degrees while the other was at 45 degrees. The constant temperature anemometer was used in conjunction with a polynomial analog-signal linearizer. The periodic sample-and-hold circuit was designed and built on campus in cooperation with the Iowa State University Engineering Research Electronic Shop staff. Details on the circuit design appear in Appendix A. The circuit was used to obtain periodic-average flow field data. A photoelectric pickup triggered by a one slot per revolution disk rotating with the compressor shaft was used to synchronize the periodic sample-and-hold circuit activity and rotor motion. The sampling circuit was designed to obtain a 5 μsec[1] sample of the linearized hot-wire anemometer output-voltage signal during each revolution of the rotor shaft. Each time the 5 μsec sample was taken, a stroboscope was also triggered and the periodic-sampling position of the rotor blades and shaft could be visually observed. The time delay between the triggering of the photoelectric pickup and sample-and-hold circuit could be varied to permit control of the periodic-sampling position of the rotor blades relative to the hot-wire probe and stationary blades. The photoelectric

---

[1]The typical period of the rotor wake was 1.1 msec.

pickup could be moved circumferentially to also vary the rotor periodic-sampling position, and the movement could be recorded from a circumferential degree scale attached to the photoelectric pickup. Two scribe marks, one on the rotor shaft surface locating the stacking axis position of a rotor blade and the other on the stationary hub surface corresponding to the position of the probe measurement stations, were used in conjunction with the photoelectric pickup circumferential scale to ascertain the circumferential location of the rotor blade periodic-sampling position. The photoelectric pickup motion could be mechanically linked to the stationary blade-row circumferential actuator in order to provide effective circumferential traversing of the hot-wire probe past the stationary blade rows and periodically frozen rotor blade rows. The periodic-sampling signal from the sample-and-hold circuit was electronically smoothed using a signal averaging circuit which acted like a simple low-pass filter with time constant adjustment from 1 to 100 sec. Finally, the signal from the averaging circuit was digitized by the voltmeter and recorded by the calculator.

E. Calibration Nozzle

An air nozzle was used for the calibration of slow-response pressure probes and hot-wire sensors. The nozzle had a throat diameter of 25.4 mm (1.0 in.) and a contraction ratio of 144 to 1. No measurable difference between the plenum pressure and total pressure measured with a pitot-static probe positioned 0.25 throat diameters from the exit of the nozzle was detected over a velocity range from 0.0 to 50.0 m/s. The flow at the nozzle exit involved a uniform velocity profile. Regulated compressed air

provided the air supply, and the air temperature was controlled by a variable-current heater, blower, and heat exchanger arrangement. Figure 3.9 shows the probe holder which allowed probe stream immersion and yaw and pitch angle positioning. The probe holder was designed to permit the sensing portion of the probe to remain in the same position in the flow while the probe yaw and pitch angles were varied. The telescope, shown in Figure 3.9, was used to initially align hot-wire probes in the flow.

F. Sound Pressure Level Measurement Instrumentation

A precision sound-level meter and analyzer (General Radio type 1933) was used to make overall sound-pressure level measurements and octave band analyses of the compressor inlet noise. The instrument included a 1 in. electret condenser microphone, A, B, C, and flat weighting characteristics and ten octave band filters with band center frequencies from 31.5 Hz to 16 kHz. The sound-level meter was also used as a preamplifier for a narrow band pass (down to 1%) frequency analyzer (Brüel and Kjaer model 2121) for obtaining spectrum analyses of the compressor noise. The frequency analyzer was combined with a related level recorder (Brüel and Kjaer model 2305) for automatic recording of the noise spectrum.

G. Data Acquisition and Reduction System

A desk-top calculator (Hewlett-Packard model 9821A) and related multiple channel scanning digital voltmeter (Hewlett-Packard 3480D, 3458D) were used for data collection and reduction. An interface between the calculator and voltmeter allowed the calculator to read any one of ten voltmeter channels and store the reading in memory. The calculator had

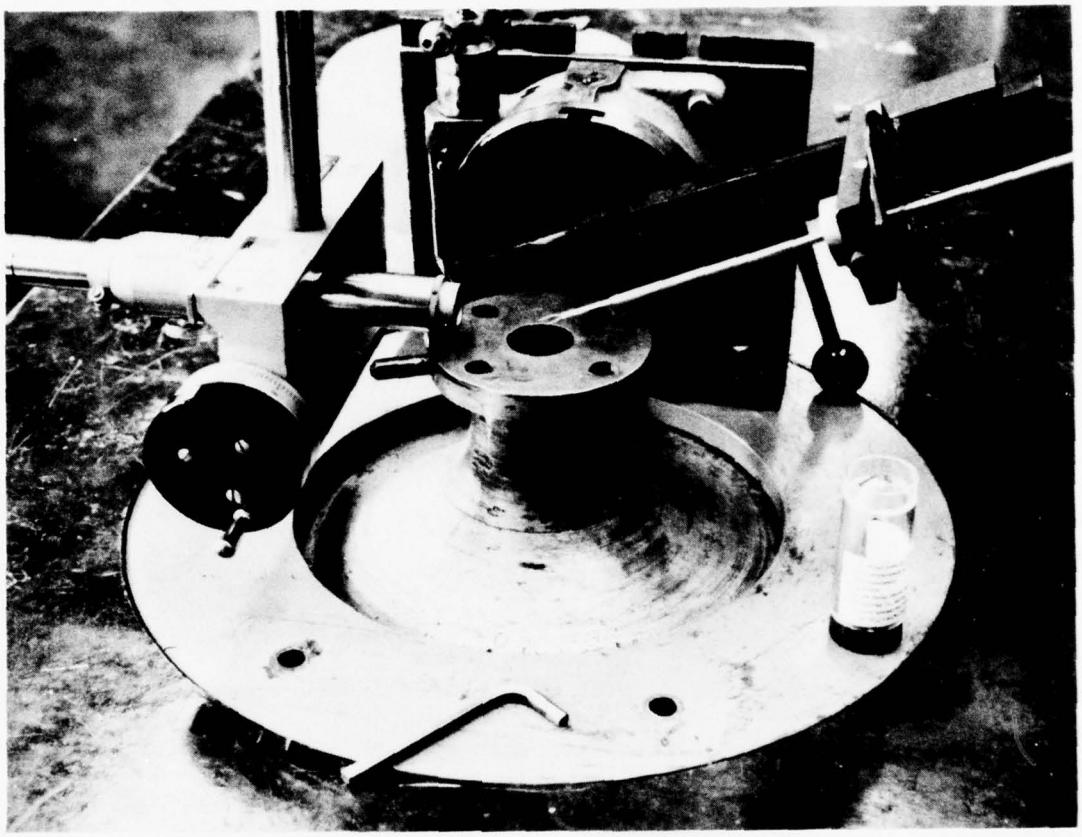


Figure 3.9. Calibration nozzle, probe positioner, and optical alignment telescope used for probe calibration.

423 available memory registers for program and data storage. The data storage and programming capabilities of the calculator were expanded by a tape cassette built into the calculator which could be used to load and record data and programs from memory. Since the calculator had limited printing and no plotting capabilities, the Iowa State University Computation Center computing system (IBM 360/65, 370/158) was utilized for data tabulation and plotting.

IV. EXPERIMENTAL PROCEDURES AND DATA REDUCTION

Basically, three types of measurements were involved during the experimental investigation. Included were sound-pressure level measurements, slow-response pressure measurements, and fast-response hot-wire anemometer measurements. One set of sound-level measurements was obtained over the entire rpm range of the compressor at constant flow coefficient. All other data were taken with the compressor speed and flow rate set at 1400 rpm and 0.94 kg/s (0.42 flow coefficient), respectively. This operating condition was near maximum efficiency for 1400 rpm.

The pitot tube, micromanometer, and mercury in-glass thermometer were respectively used as standards for velocity, pressure, and temperature calibration and measurement. Calibration of all electronic components used in this experimental investigation were performed in the Iowa State University Engineering Research Institute Electronic Shop. Before each test, sufficient time was allowed for the electronic instrumentation to warm up and for the laboratory and compressor fluid temperatures to reach equilibrium values.

Data acquisition programs were written for the desk-top programable calculator (Hewlett-Packard) to control the step-by-step procedures of the experimental tests. Data were either typed into the calculator or read by the calculator through the interface from the digital voltmeter as specified by the program. The data acquisition programs were used to (1) store data in memory, (2) make preliminary calculations, (3) print out data and preliminary results, and (4) record data and preliminary results on magnetic cassette tape. In addition, data reduction programs for the

calculator were written to accept the data and preliminary results recorded on magnetic tape and to perform the required manipulations to obtain the final results. A list and brief description of the data acquisition and reduction programs are presented in Appendix B.

A. Sound-Pressure Level Measurements

During early stages of the research project, it was noticed that the inlet noise produced by the compressor could be varied significantly by changing the circumferential positions of the inlet guide vane and stator blade rows relative to each other. As a result, sound-pressure level (SPL) measurements of the compressor inlet noise were made with the stationary blade rows set at different circumferential position schedules. The microphone of the sound-level meter was positioned at the compressor inlet as shown in Figure 4.1. Three categories of sound-level tests were made: (1) testing for compressor inlet noise variation by changing the IGV row circumferential position at several points over the compressor rpm range for a fixed flow coefficient of 0.42, (2) determining the stationary blade-row circumferential settings for minimum and maximum sound at a speed of 1400 rpm and a flow coefficient of 0.42, and (3) obtaining detailed SPL measurements at the minimum and maximum noise blade-row settings found from test (2) above.

1. Testing for noise variation over compressor rpm range

In order to determine the influence of stationary blade row circumferential placement on compressor inlet noise at various compressor speeds, overall SPL measurements were obtained over the rpm range of the compressor at a constant flow coefficient of 0.42. Only the circumferen-



Figure 4.1. Sound-level meter and position of microphone for compressor inlet noise measurement.

tial position of the IGV row was varied; the positions of the three stator rows were set so that the stacking axis of one stator blade in each row was in line with the probe traversing stations. Overall SPL readings were taken at minimum and maximum noise circumferential positions of the IGV row at fifteen rpm settings over the rpm range from 200 to 2700. The flow coefficient, determined from the venturi mass flow rate indication, was maintained constant at 0.42 by adjusting the outlet throttle plate.

2. Determining the minimum and maximum sound settings

For this test and all remaining tests, the compressor operating conditions were set for a rotor speed of 1400 rpm and a flow coefficient of 0.42. The stationary blade-row circumferential settings for minimum and maximum noise at the above compressor operating conditions were uniquely obtained by monitoring the overall SPL while adjusting the circumferential positions of the four stationary blade rows relative to each other by using the iterative procedure outlined below:

(1) Holding the IGV row stationary, the three stator rows were moved circumferentially together until minimum (maximum) inlet noise was observed.

(2) Holding the IGV and first stator (first stator position determined in step 1) rows stationary, the remaining two stator rows were moved circumferentially together until minimum (maximum) inlet noise was observed.

(3) Holding the IGV, first stator (first stator position determined in step 1), and second stator (second stator position determined in step 2) rows stationary, the remaining third stator row was

moved circumferentially until minimum (maximum) inlet noise was observed.

(4) Steps 1, 2, and 3 were repeated until the relative circumferential positions of the stationary blade rows were identical for two consecutive repetitions.

3. Obtaining detailed SPL measurements at minimum and maximum sound-level blade-row settings

Once the blade-row circumferential placement schedules for minimum and maximum noise were determined, overall, octave band, and spectrum analyses SPL measurements were made at the two circumferential blade-row settings. Ten octave band measurements with center frequencies from 31.5 Hz to 16 kHz were taken with the sound-level meter, and a 1% band-pass spectrum analysis was obtained over the frequency range from 200 Hz to 2000 Hz with the sound-level meter used as a preamplifier connected to the narrow band-pass frequency analyzer and level recorder.

B. Slow-Response Measurements

Slow-response pressure measurements were taken to obtain detailed and overall time-average information of the flow field between the blade rows of the compressor. The details involved in obtaining and reducing these measurements are described in this section.

1. Probe calibration

The cobra probe sketched in Figure 4.2 was used to obtain nearly all total-pressure and flow-angle slow-response data in the compressor. In order to better understand the measurement capabilities of the cobra probe, an extensive total-pressure and flow-angle calibration of the

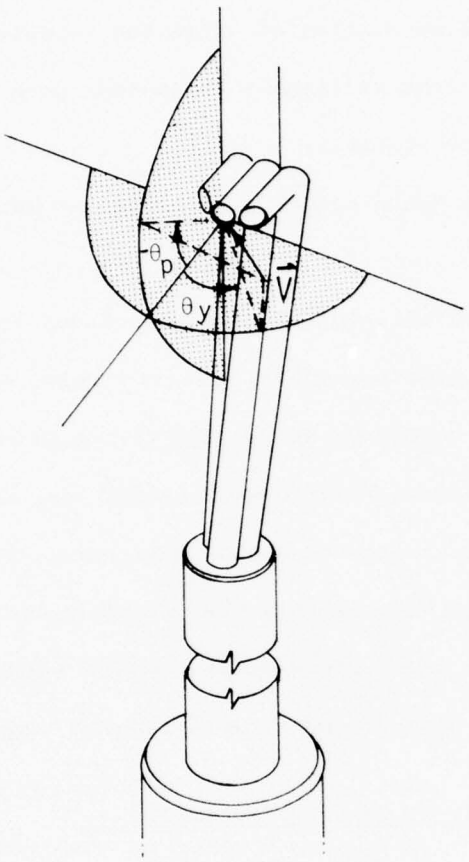


Figure 4.2. Total-pressure and flow-yaw-angle cobra probe and probe angle nomenclature.

probe was made utilizing the calibration nozzle. For all calibrations, the probe was positioned 0.25 nozzle orifice diameters from the nozzle exit. The total pressure at this point was determined by measurement of the plenum wall pressure. The micromanometer was used to measure all differential pressures. The probe pitch angle, θ_p, and probe yaw angle, θ_y, were defined as indicated in Figure 4.2.

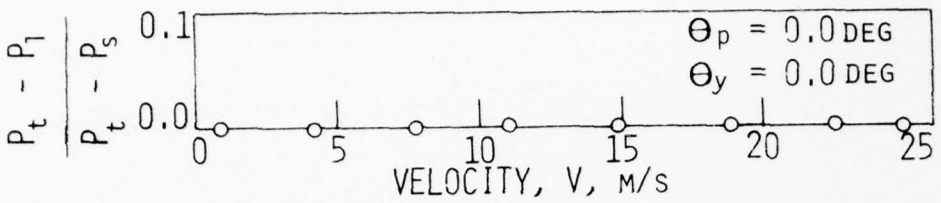
a. Total pressure calibration A total pressure calibration of the cobra probe with respect to velocity, probe pitch angle, probe yaw angle, and probe time-response was made. In order to calibrate for total-pressure velocity effect, the probe was aligned in the flow with zero pitch angle and rotated about the probe axis until the two probe side-tube pressures, P_2 and P_3, were equal (U-tube manometer balance). The pressure difference between the plenum pressure, P_t, and the probe indicated total pressure, P_1, was observed over the velocity range anticipated in the compressor (0.0 to 25.0 m/s). Next, the flow-angle and time-response total pressure calibrations were conducted at a constant velocity of 18.7 m/s (typical average velocity in the compressor). The effect of pitch angle on probe indicated total pressure was determined by measuring the difference between P_t and P_1 at different pitch angles over the range from -4.0 to 5.5 degrees with the probe yaw angle set at zero. The total pressure calibration of yaw angle effect was made by obtaining the difference between P_t and P_1 at 18 yaw angle positions from -24 to 24 degrees at a pitch angle of zero. The probe total-pressure time-response characteristics were determined with the total-pressure probe tap connected to the inclined manometer actually used for compressor flow field total pressure measurement. To suddenly change the pressure at the probe total-pressure

sensing tube, a plate was temporarily placed ahead of the probe. The indicated total pressure, P_1, was read from the manometer every 5 sec.

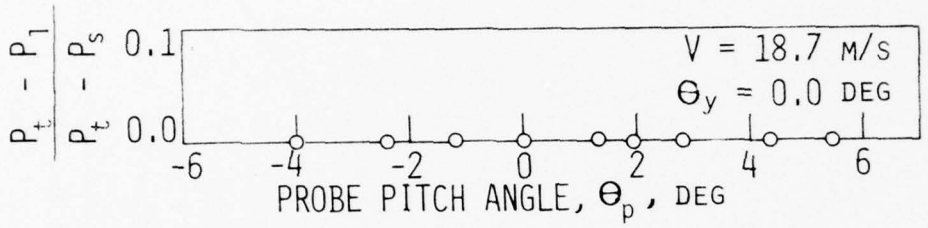
The results for the velocity, pitch angle, yaw angle, and time-response portions of the total pressure calibration are shown in Figure 4.3. No measurable difference between the nozzle plenum total pressure and the probe indicated total pressure was detected over the velocity and pitch angle measurement ranges. Also, the probe indicated total pressure was insensitive to yaw angle over the range from -5.0 to 5.0 degrees. The total-pressure time-response curves were used as guidelines for the time span needed between total-pressure readings.

b. Probe yaw-angle calibration A probe yaw-angle calibration was made to determine the yaw-angle sensitivity of the cobra probe. The pressure difference between the probe side-tube pressures, P_2 and P_3, was measured at 19 yaw-angle settings over a range from -5.0 to 5.0 degrees at a constant velocity of 18.7 m/s. The results of this test, shown in Figure 4.4, indicate that under the steady uniform flow conditions of the calibration nozzle, the cobra probe yaw-angle measurement uncertainty was approximately 0.1 degrees (20 to 1 odds).

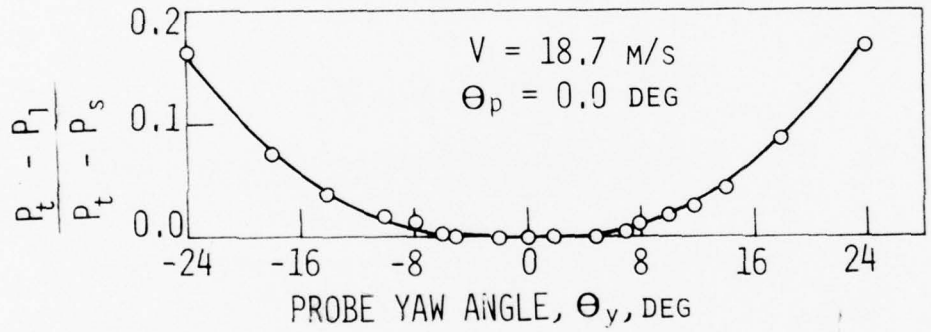
The flow angle indicated by the cobra probe when the side-tube pressures are balanced in the flow, is largely affected by hole-to-hole velocity gradients. In regions of high velocity gradients, large flow-angle errors result due to the physical distance between the side-tube pressure holes. Since there was no calibration method available to account for this effect, precautions were taken when making flow-angle measurements in the compressor. Flow-angle measurements behind stationary blade rows were made only in the freestream where the velocity gradients



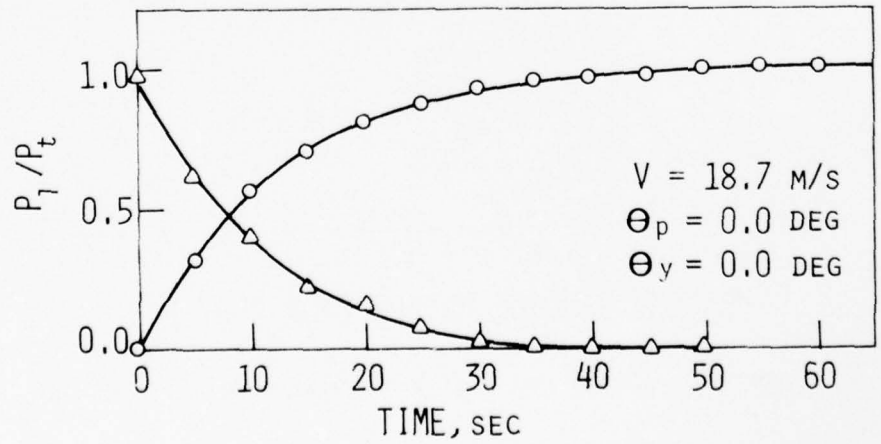
(a) Velocity total-pressure calibration curve.



(b) Probe pitch-angle total-pressure calibration curve.



(c) Probe yaw-angle total-pressure calibration curve.



(d) Time-response total-pressure calibration curve.

Figure 4.3. Cobra probe total-pressure calibration curves.

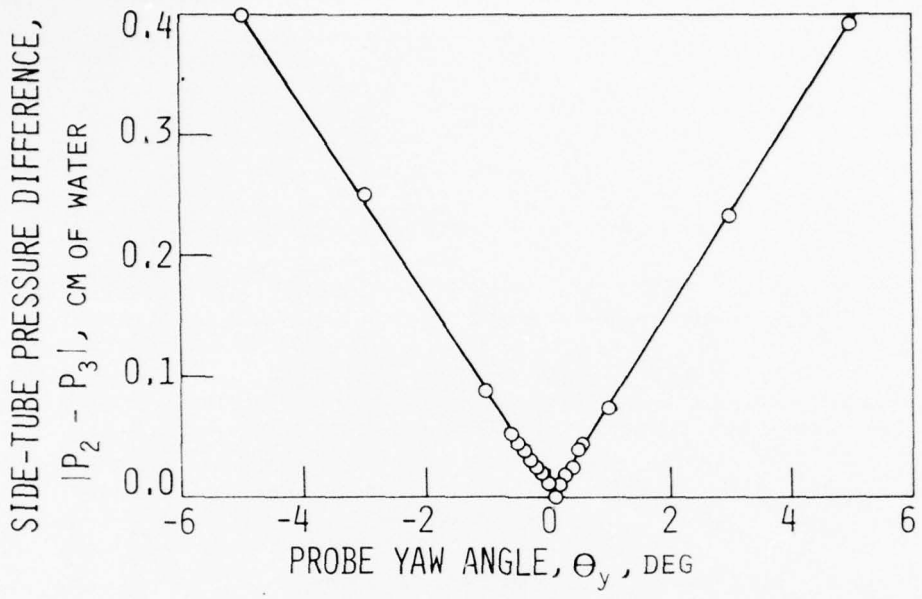


Figure 4.4. Cobra probe yaw-angle sensitivity calibration curve.

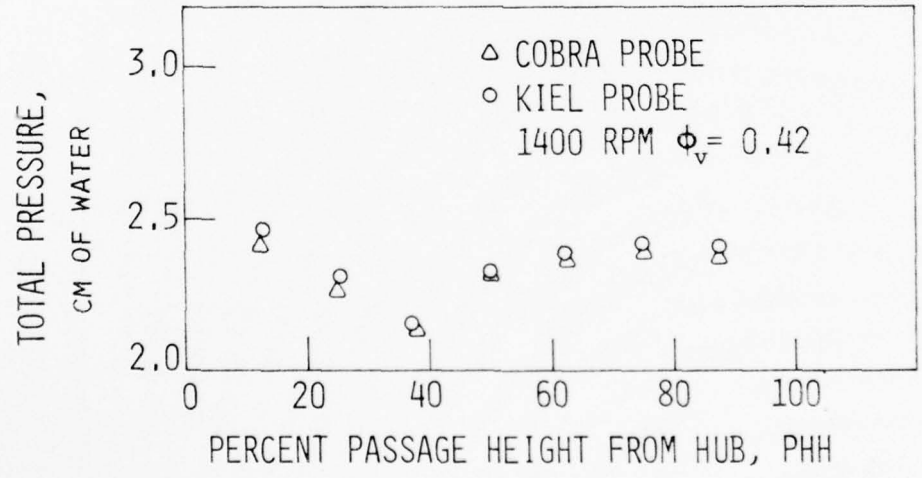


Figure 4.5. Cobra and Kiel probe comparison.

were small. The probe angle was set approximately at the average free-stream value for total-pressure measurements in and near the blade wake where the velocity gradients were high.

c. Kiel probe comparison A radial direction survey of total-pressure variation behind the first rotor at a speed of 1400 rpm and a flow coefficient of 0.42 was made with the cobra and Kiel probes. Total-pressure measurements were made by both probes at the same eight radial locations from 12.5 to 87.5% passage height from the hub. The cobra probe was aligned in the flow by balancing the side-tube pressures, and the indicated flow angle was used to set the angular position of the Kiel probe. The results (see Figure 4.5) show that the total pressures indicated by the two probes were equal at mid-span height and deviated only slightly (0.6 mm of water maximum) toward the hub and tip.

2. Data acquisition

Slow-response total-pressure and flow-angle circumferential direction surveys of the compressor flow field were obtained with the cobra probe at nine passage height locations of 10, 20, 30, 40, 50, 60, 70, 80, and 90% from the hub ahead and behind each of the rotating and stationary blade rows for both minimum and maximum noise conditions. In addition, outer-annulus wall static-pressure circumferential surveys were made at each probe traversing axial location for minimum and maximum noise. The steps followed to obtain this data are described below.

Prior to testing, several preliminary setups were required. The cobra probe was mounted in the probe actuator at the calibration nozzle. The probe angle zero was ascertained by balancing the probe side-tube pressures, and the probe immersion was zeroed by using a depth micrometer.

The voltages from the stationary blade-row circumferential motion, probe immersion, and probe flow-yaw-angle potentiometers were correlated with their respective motions with a linear least squares correlation. The circumferential positions of the stationary blade rows were set to either the minimum or maximum sound schedules (refer to Table 5.1). Before each test, the scales on the inclined and U-tube manometers were zeroed, and the bridge balance and gain adjustments on the Endevco pressure-transducer bridge circuit were set.

Once the preliminary setup procedures were completed, the following miscellaneous data were recorded so that the measurement conditions were always completely specified:

(1) Probe traversing station number, see Figure 3.1

(2) Stationary blade position settings, YO_{IGV}, YO_{1S}, YO_{2S} and YO_{3S}, degrees

(3) Barometric pressure,[1] inches of Hg

(4) Barometer ambient temperature,[1] °F

(5) Room temperature,[1] °F

(6) Compressor rpm

(7) Compressor rpm variation

(8) Differential pressure across venturi, inches of water

(9) Station pressure at venturi throat, inches of water

(10) Temperature at venturi throat, millivolts

(11) Date

(12) Time[1]

---

[1] Taken at beginning and end of each circumferential survey.

The circumferential direction surveys were made with the probe actuator mounted at one of the probe-traversing stations with the probe immersed to the specified radial position. A qualitative trace of the circumferential variation of total pressure with the probe set at the approximate average flow yaw angle was made on an X-Y storage oscilloscope from the electrical signals of the strain-gage pressure transducer and the circumferential motion potentiometer. The trace was used to select the positions of the flow-field measurement points. For each circumferential direction survey, measurements were obtained over one circumferential stationary blade pitch, eleven measurement points behind each rotor blade row and between fourteen and seventeen points behind each stationary blade row. The cobra probe side-tube pressures were balanced with the aid of a U-tube manometer at every flow-field measurement point behind a rotor blade row and at measurement points in the freestream behind a stationary blade row. The probe angle and the circumferential position Y were recorded at each point along with the total pressure measured with the inclined water manometer. After the last measurement point of each circumferential survey was taken, the miscellaneous and flow-field data were printed out and recorded on magnetic tape for reduction at a later time.

Once the total-pressure and flow-angle circumferential surveys were completed for all radial positions at one axial probe station, a circumferential survey over one blade pitch was made of the outer-annulus wall static pressure with the wall tap at the axial location of the probe station.

3. Data reduction

The first step in the reduction of the slow-response data was to determine the primary flow-field quantities of total head, static head, and tangential flow angle. Once these primary values were obtained, other flow-field parameters such as absolute velocity, relative velocity, incidence angle, deviation angle, etc. were calculated along with their circumferential average values. Finally, overall rotor, stator, and stage parameters were determined. Since the velocities in the compressor were all less than that corresponding to a Mach number of 0.2, the flow was assumed to be incompressible for all calculations. Integrated averages were computed using a spline-fit integration (see Ref. 30). A complete list of all equations used in reducing the data is presented in Appendix C.

a. Flow-field parameters The total head[1], H, was determined for each flow-field measurement point from the measured total pressure, and a circumferential integrated average was calculated for each radial position at every probe-traversing measurement station. The tangential flow angle, β_y, was assumed to be circumferentially constant and a circumferentially integrated average value was determined for each radial position at every measurement station. All circumferential averages except for flow angle averages behind stationary blade rows were determined by integrating over one stator blade pitch. The average flow angle behind a stationary blade row at each radial position was obtained by integrating only over the freestream portion. The static head[1], h, was also assumed to be circum-

[1]With respect to atmospheric pressure.

ferentially constant, and the radial distribution of h was determined at each measurement station by solving the radial equilibrium equation. Since the compressor involved cylindrical annulus walls, the radial velocities between the blade rows at the probe traversing stations were assumed to be zero. By making this assumption and by neglecting viscous effects locally, the equation of motion in the radial direction reduces to

$$g_c \frac{dh}{dr} = \frac{V_y^2}{r} \tag{4.1}$$

where h = static head, Nm/kg

r = radius, m

V_y = tangential velocity, m/s

g_c = gravitational constant, kgm/Ns^2

The tangential velocity is equal to

$$V_y = \sqrt{2g_c(H-h)\sin\beta_y} \tag{4.2}$$

where β_y = tangential flow angle, degrees.

Substituting the expression for V_y into Equation (4.1), the radial equilibrium equation becomes

$$\frac{dh}{dr} = \frac{2\sin^2(\beta_y)(H-h)}{r} \tag{4.3}$$

Equation (4.3) is a first order ordinary differential equation and was solved by the Runge-Kutta numerical technique (see Ref. 31) for the radial distribution of static head. The solution was obtained by using the average outer-annulus static wall pressure as an initial value and by marching radially toward the hub at increments of 5% of passage height. The radial distributions of H and β_y required for the solution were obtained by a second order Lagrange interpolation of the known circumferen-

tial average values. A typical static-pressure radial equilibrium solution behind the third stator is shown in Figure 4.6. The radial distribution of static pressure from the solution is in good agreement with the measured static wall pressure at the hub.

With the circumferential distributions of H and the circumferential average values of β_y and h determined, the circumferential variation and integrated average of absolute velocity, V, were calculated for each radius at every probe measurement station. From the circumferential average velocity and tangential flow angle, the following circumferential average quantities were computed for all nine radial positions at each measurement station:

(1) Axial velocity, m/s, Eq. 12.16

(2) Tangential velocity, m/s, Eq. 12.18

(3) Blade incidence angle, degrees, Eqs. 12.24, 12.26, and 12.28

(4) Blade deviation angle, degrees, Eqs. 12.25, 12.27, and 12.29

(5) Flow coefficient, Eq. 12.30

(6) Relative velocity, m/s, Eq. 12.22

(7) Relative tangential velocity, m/s, Eq. 12.20

(8) Relative flow angle, degrees, Eqs. 12.23

In addition, an overall integrated flow rate and flow coefficient at each probe-traversing station was computed and compared with the flow rate and flow coefficient obtained from the flow rate venturi meter data. In order to determine the integrated flow rate at the probe stations, the flow near the hub and tip in the passage height regions beyond 10% and 90% was estimated by extrapolating the axial velocity variation with a straight line.

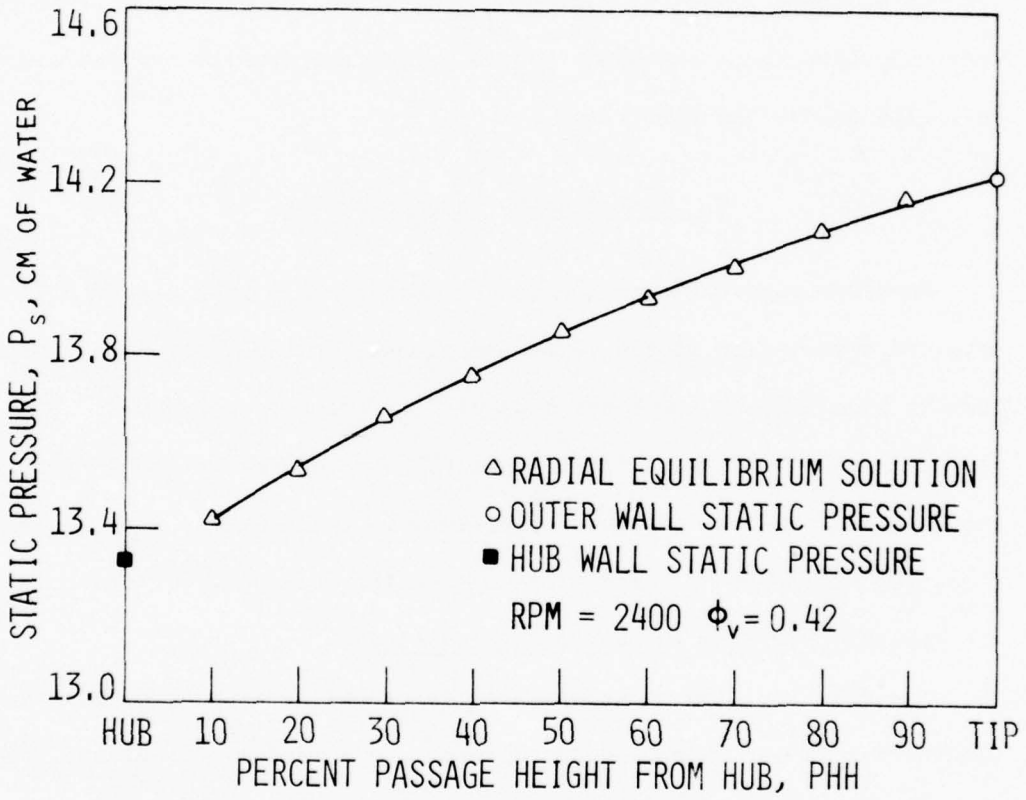


Figure 4.6. Static-pressure radial equilibrium solution for the compressor behind the third stator.

b. Rotor, stator, and stage performance parameters The actual and ideal head-rise coefficients and hydraulic efficiency were calculated at the nine radial positions for each of the three rotor rows, three rotor-stator stages, and the overall compressor. In addition, blade-section total-head-loss coefficients for each rotor and stator blade row were determined. Finally, the mechanical power and mechanical efficiency were calculated from the motor torque-meter measurements and the overall head rise across the compressor.

C. Fast-Response Measurements

Fast-response hot-wire anemometer measurements were taken to obtain a detailed description of the three-dimensional, periodic-average, instantaneous flow between the blade rows of the research compressor. The periodic-average hot-wire measurement technique is described in the first two sections, and the procedures involved in calibration, data acquisition, and data reduction are presented in the remaining sections.

1. Periodic sampling and averaging technique

The flow field in a turbomachine is generally made up of two types of fluctuating flows: a periodic component and a random (turbulent) component. When a stationary fast-response instrument such as a hot-wire probe is used to measure the flow, the hot-wire signal $s(t)$ will be composed of a periodic signal $p(t)$ with known period T in phase with the blade passing frequency of the moving blade row and a random signal $n(t)$; hence

$$s(t) = p(t) + n(t) \tag{4.4}$$

The periodic component p(t) can be obtained by periodically sampling s(t) with period T and averaging arithmetically. As shown by Hirsch and Kool (20), the periodic-average signal $\tilde{s}(t)$ can be expressed as follows:

$$\tilde{s}(t) = \frac{1}{N} \sum_{k=1}^{N} s(t + kT) \tag{4.5}$$

or

$$\tilde{s}(t) = \frac{1}{N} \sum_{k=1}^{N} p(t + kT) + \frac{1}{N} \sum_{k=1}^{N} n(t + kT) \tag{4.6}$$

If N is made large enough, the last term of Equation 4.6 will be zero due to its random character. Thus,

$$\tilde{s}(t) = p(t) \tag{4.7}$$

and the periodic component p(t) can be obtained from s(t) by using a periodic-sampling and averaging technique.

The hot-wire anemometer system and periodic-sampling and averaging circuits described earlier (see Figure 3.8) were used to procure periodic-average velocity data of the flow between blade rows in the compressor. A periodic average of the linearized anemometer signal for each distinct position and orientation of the hot-wire probe was obtained by taking approximately 1200 periodic samples (one sample each revolution) and averaging both electronically and arithmetically. The electronic averaging was accomplished with the signal averaging circuit (low-pass filter) set for a time constant of 1.0 sec. The electronically averaged signal was subsequently sampled 180 times (equivalent to approximately 1200 hot-wire signal samples) once every 0.17 sec by the calculator through the digital voltmeter interface after which an arithmetic average was calculated. Two types of periodic-average circumferential surveys were made:

(1) frozen rotor-blade flow-field surveys made by effectively traversing the hot-wire probe circumferentially relative to stationary IGV, stator, and periodically frozen and sampled rotor blades and (2) passing rotor-blade flow-field surveys made with a stationary hot-wire probe sampling the passing rotor blade flow.

Measurements made by the first method yield the periodic component of the flow field at an instant in time with the rotor blades periodically frozen in one position with respect to the stationary blades. Results obtained with the frozen rotor-blade survey method include the stationary periodicity produced by the stationary blade rows. With this method it is possible to obtain both periodic-frozen rotor and stator blade wake profiles. Frozen rotor-blade surveys were obtained by mechanically locking the photoelectric pickup motion (periodic-frozen rotor blade circumferential motion) with the circumferential movement of the stationary blade rows. Jointly moving the periodic-frozen rotor and stationary blades past the stationary probe results in the effective circumferential traversing by the probe. Since a frozen rotor-blade flow-field probe survey is representative of the blade exit flow field at only one instant of time, information must be obtained for several instants of time as the rotor blade passes in stop action sequence by the stator blade in order to obtain a more complete picture of the blade exit flow field. This was done by making frozen rotor-blade flow-field surveys for several periodic-frozen rotor blade positions relative to the position of the stationary blades. These varying frozen rotor blade/stator blade relative position schedules were attained by simply shifting the photoelectric pickup with

respect to the stationary blades. Most of the hot-wire data were obtained using this method.

Periodic-average circumferential surveys made by the second method represent the flow field as seen by a stationary observer (e.g., stator blade or stationary probe) as the rotor blade passes by during a finite length of time. The passing rotor-blade survey method disregards the stationary periodicity produced by the stationary blade rows. A passing rotor-blade survey behind a stationary blade row lends little information with regard to the overall wakes produced by the upstream stationary blade row. Passing rotor-blade flow-field surveys were obtained by moving only the photoelectric pickup, maintaining the stationary blade rows motionless while hot-wire data were collected. This is similar to the methods used by Evans (12), Raj and Lakshminarayana (13), Whitfield et al. (18), and Hirsch and Kool (20). The frozen rotor-blade and passing rotor-blade measurement techniques should yield the same results when the rotor flow is steady in the relative (rotating) reference frame, for example, in the case of isolated rotor measurements.

The accuracy of the periodic-sampling and averaging technique is largely dependent on N, the number of samples. If N is small, the random component term in Equation 4.6 will be significant, and an accurate average of the periodic component will not be obtained. The accuracy is also dependent on the magnitude of the random fluctuations about the mean value. The accuracy decreases as the magnitude of the random fluctuations increase. Hirsch and Kool (20) present a relation between σ, the standard deviation of the periodic-sample average, and σ_n, the standard deviation

of the random fluctuations, which is dependent on N, the number of samples. This relationship

$$\sigma^2 = \frac{1}{N} \sigma_n^2 \tag{4.8}$$

shows that as N is increased, σ is reduced as the square root of N. This relation is valid when the periodic-sample averaging is done arithmetically.

In order to obtain a relationship between σ and N when the averaging of the periodic samples is performed using the electronic and arithmetic technique described previously, an experiment was conducted with a hot wire positioned in the axial direction behind the second rotor of the compressor at 50% passage height with the compressor at typical operating conditions of 1400 rpm and 0.42 flow coefficient. The linearized anemometer signal was sampled at periodic rotor positions corresponding to the hot-wire positioned in and out of the rotor wake. A set of ten periodic-average velocity values was obtained for several values of N over a range from 4 to 1556 samples at both periodic-sampling rotor-blade positions. The variation coefficient of the ten values within each set was then calculated and plotted against the corresponding value of N. The results in Figure 4.7 show that as N increases, σ decreases rapidly at first and then tapers off until increasing N has little further effect on σ because of gradual variations in temperature and rpm.

2. Single hot-wire three-dimensional velocity measurement technique

A hot-wire measurement technique involving a single inclined hot-wire sensor was used to measure the periodic-average, three-dimensional flow

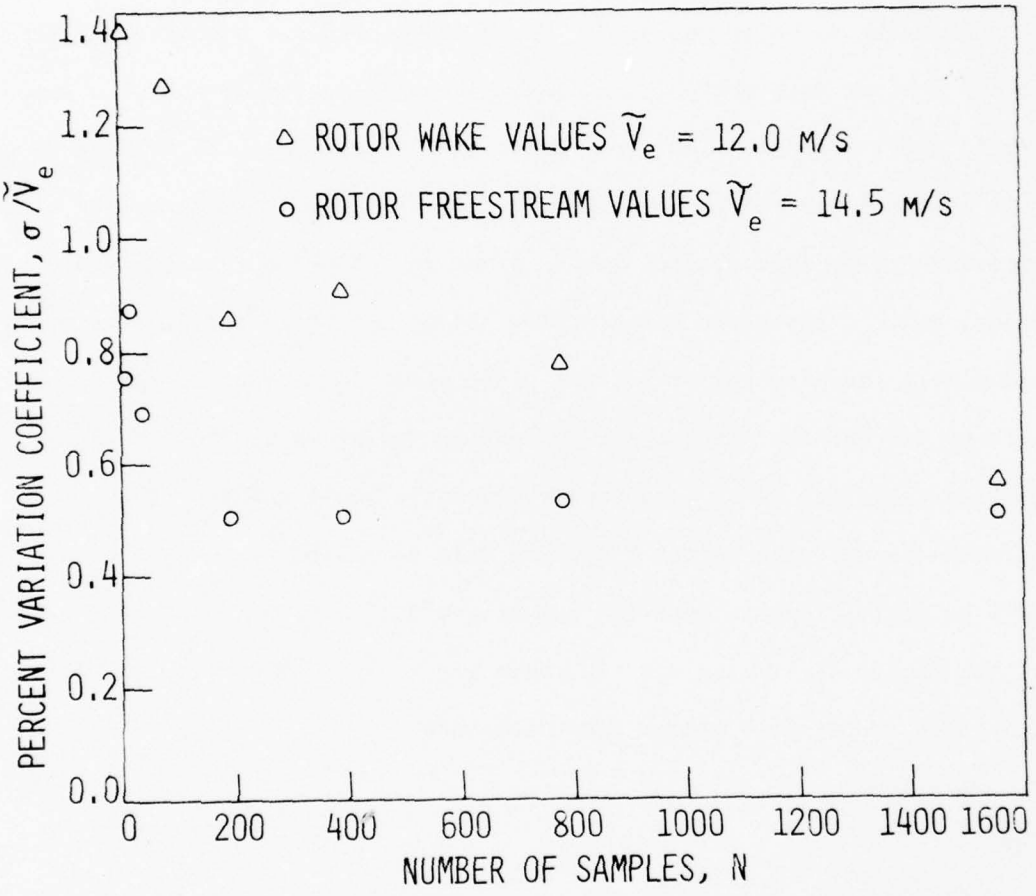


Figure 4.7. Percent variation coefficient of the periodic-sample averages for different values of N.

field in the compressor. The details related to this technique are described below.

a. Probe geometry The hot-wire probe configuration shown in Figure 4.8 relates the hot-wire sensor to the probe coordinates x, y, and z and to the velocity vector $\vec{V}$. The z coordinate was placed along the hot-wire probe axis while the x coordinate was located so that the sensor lay in the x-z plane. The wire sensor is represented in Figure 4.8 by the unit vector $\vec{A}$ slanted at the angle θ_o to the x axis. The direction of the velocity vector with respect to the probe is defined by θ_y, the probe yaw angle, and θ_p, the probe pitch angle. Since the probe coordinates x, y, and z were fixed to the probe, the probe angle θ_y changed by the amount of turning whereas the pitch angle θ_p remained constant as the probe was rotated about its axis. The sensor yaw angle α was defined as the angle between the velocity vector $\vec{V}$ and the axis to the hot-wire sensor. It will be useful to note that the sensor yaw angle can be expressed in terms of the angles θ_o, θ_p, and θ_y. The unit vector $\vec{A}$ and the velocity vector $\vec{V}$ expressed in terms of vector components are

$$\vec{A} = \cos \theta_o \vec{i} + \sin \theta_o \vec{k} \tag{4.9}$$

and

$$\vec{V} = -V \cos \theta_p \cos \theta_y \vec{i} - V \cos \theta_p \sin \theta_y \vec{j} - V \sin \theta_p \vec{k} \tag{4.10}$$

The dot product of $\vec{A}$ and $\vec{V}$ is

$$\vec{A}\cdot\vec{V} = |\vec{A}||\vec{V}| \cos(180 - \alpha) = -|\vec{V}| \cos \theta_o \cos \theta_p \cos \theta_y - |\vec{V}| \sin \theta_o \sin \theta_p \tag{4.11}$$

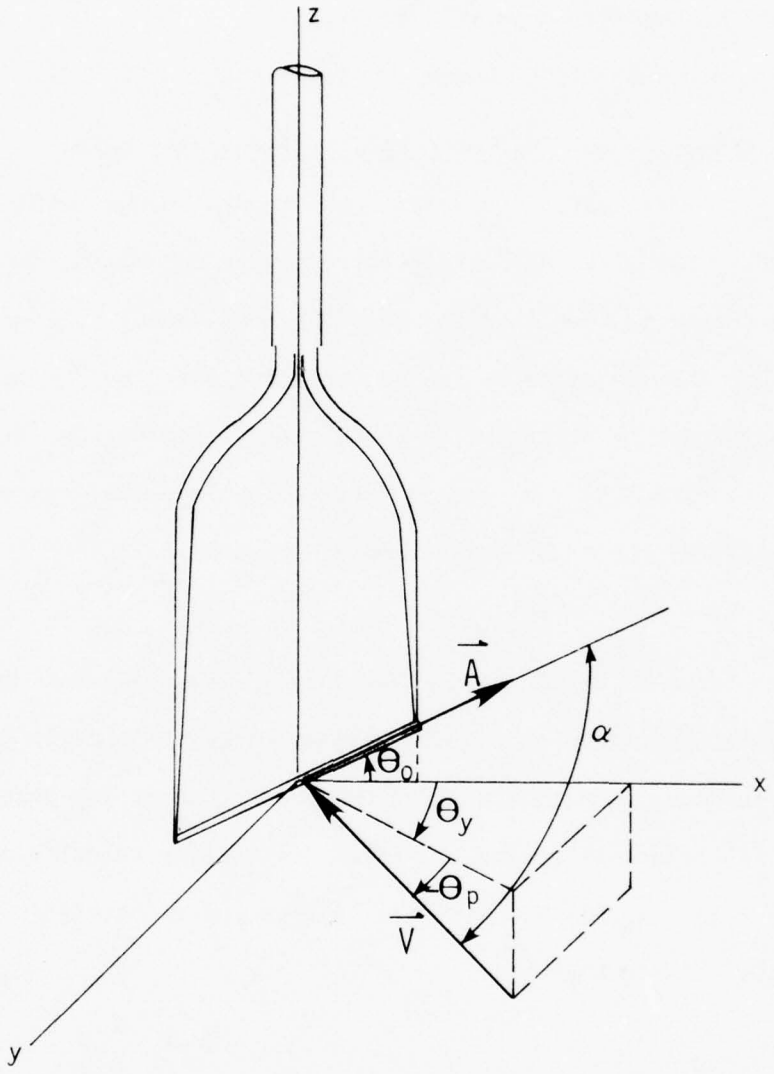


Figure 4.8. Hot-wire configuration relating velocity vector $\vec{V}$ to hot-wire sensor and probe coordinates x, y, z.

Hence, the sensor yaw angle relationship is

$$\cos \alpha = \cos \theta_o \cos \theta_p \cos \theta_y + \sin \theta_o \sin \theta_p \tag{4.12}$$

b. Effective cooling velocity/actual velocity ratio If a hot-wire velocity calibration is made in the typical manner with the sensor yaw angle, α, equal to 90 degrees (wire sensor normal to the flow) and the hot-wire sensor is then used for velocity measurement at a sensor yaw angle other than 90 degrees, the velocity indicated by the sensor will not equal the actual velocity and is therefore defined as the "effective cooling velocity," V_e. V_e was related to the linearized anemometer bridge voltage, E_ℓ, by the empirical second order equation

$$V_e = K_1 + K_2 E_\ell + K_3 E_\ell^2 \tag{4.13}$$

where the three coefficients K_1, K_2, and K_3 were determined from a velocity calibration with the wire sensor normal to the flow. The hot-wire measurement technique used in the present study was based on knowing the precise relationship for the effective cooling velocity/actual velocity ratio, V_e/V. The sine law is a useful relationship for sensor yaw angles near 90 degrees:

$$\frac{V_e}{V} = \sin \alpha \tag{4.14}$$

Another commonly used relationship is

$$\left(\frac{V_e}{V}\right)^2 = \sin^2\alpha + k^2\cos^2\alpha \tag{4.15}$$

where k is claimed to be dependent on the sensor type and length-to-diameter ratio. The latter relationship attributed to Champagne et al. (32) takes into consideration the residual velocity sensitivity when the velocity vector is parallel to the sensor due to the finite

length and nonuniform temperature of the sensor. For this experimental investigation, both the sine law and the Champagne, Sleicher, and Wehrmann relationship were judged as being inadequate for the inclined hot-wire probe and the measurement conditions involved. The sine law was not appropriate since sensor yaw angles as small as 40 degrees were encountered. Experimentally determined values of k for the Champagne, Sleicher, and Wehrmann relationship for the slant wire probe were found to vary considerably depending on sensor yaw angle and pitch angle.

Experiments showed that V_e/V was strongly dependent on sensor yaw angle, weakly dependent on pitch angle, and only very slightly dependent on velocity level. The dependence of V_e/V on sensor yaw angle was determined for several combinations of velocities and pitch angles with the calibration nozzle. Typical results for a 35.35-degree slant hot-wire sensor are shown in Figure 4.9. A second order empirical correlation was used to express the effective cooling velocity ratio as a function of sensor yaw angle, pitch angle, and velocity as follows:

$$\frac{V_e}{V} = b_0 + b_1\alpha + b_2\theta_p + b_3V + b_4\alpha^2 + b_5\theta_p^2 + b_5V^2 + b_7\alpha\theta_p + b_8\alpha V + b_9\theta_p V \qquad (4.16)$$

The coefficients b_0 through b_9 were determined with a least squares fit of effective cooling velocity calibration data as described in the calibration procedure section. Since the sensor yaw angle, α, and the probe yaw angle, θ_y, are geometrically related (Equation 4.12), either angle could have been selected as one of the independent variables in Equation 4.16. However, the sensor yaw angle was chosen since the dependence of V_e/V with

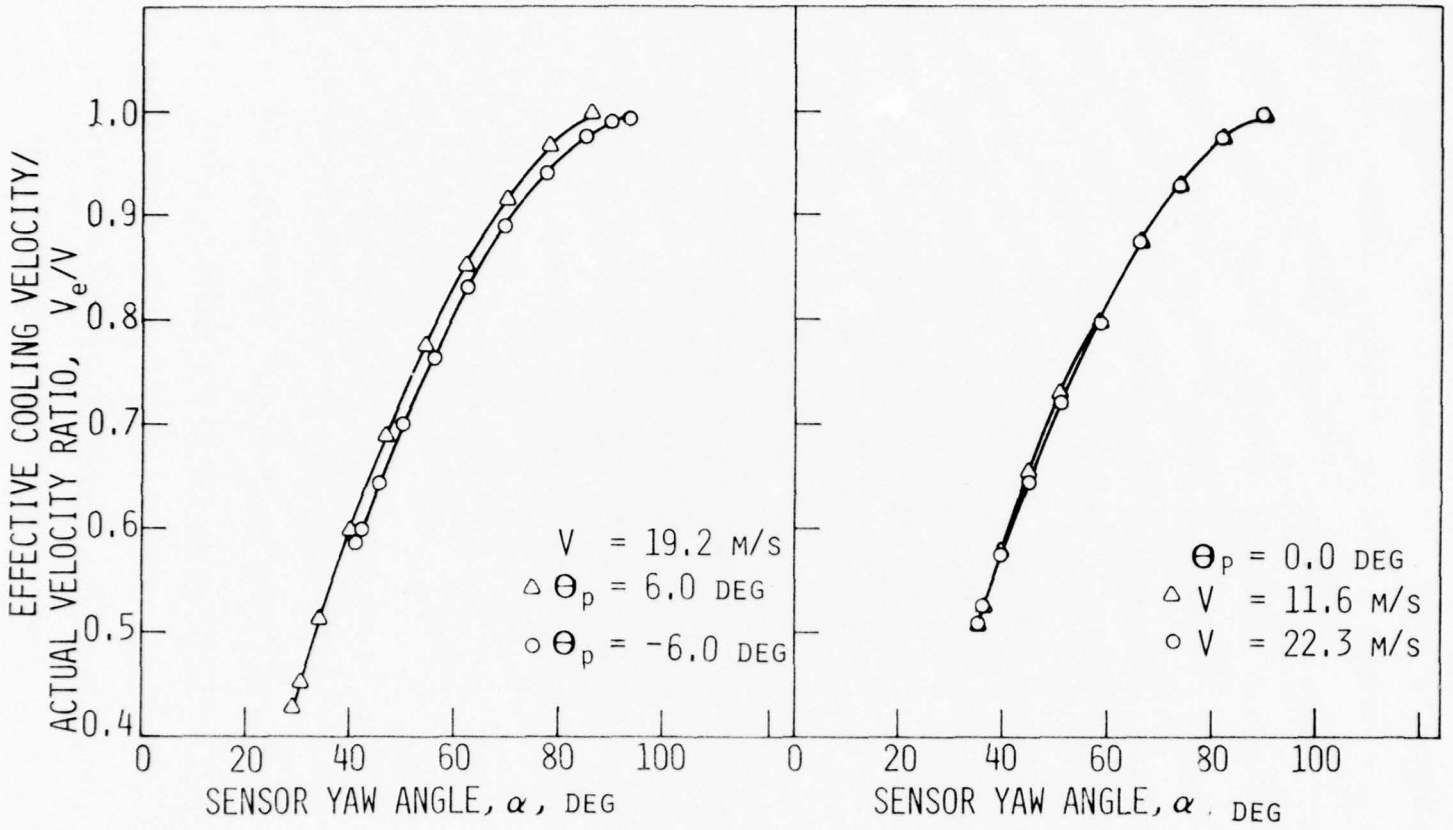


Figure 4.9. Typical effective cooling velocity calibration results for a 35-degree inclined hot wire.

respect to α facilitated correlation with a second order empirical type fit. Since hot-wire sensor behavior was not symmetrical about the axis of the probe, two sets of coefficients were used, one for each of the probe yaw angle θ_y ranges 0 to 90 degrees and 0 to -90 degrees.

c. Measurement technique Hot-wire measurements were made at compressor flow-field measurement points by positioning the hot-wire sensor and recording data at each of three probe angle orientations (a, b, and c) corresponding to probe yaw angles of $\theta_{y,a}$, $\theta_{y,b}$, and $\theta_{y,c}$ which equal:

$$\theta_{y,a} = \theta_y \tag{4.17}$$

$$\theta_{y,b} = \theta_y - m_b \tag{4.18}$$

$$\theta_{y,c} = \theta_y - m_c \tag{4.19}$$

where m_b and m_c are constant probe turning angle increments. For each wire orientation a geometric relationship similar to Equation 4.12 could be expressed and an effective cooling velocity relationship similar to Equation 4.16 applied. The resulting six equations are:

For position a

$$\frac{V_{e,a}}{V} = b_{0a} + b_{1a}\alpha_a + b_{2a}\theta_p + b_{3a}V + b_{4a}\alpha_a{}^2 + b_{5a}\theta_p{}^2 + b_{6a}V^2 + b_{7a}\alpha_a\theta_p + b_{8a}\alpha_a V + b_{9a}\theta_p V \tag{4.20}$$

$$\cos \alpha_a = \cos \theta_0 \cos \theta_p \cos \theta_y + \sin \theta_0 \sin \theta_p \tag{4.21}$$

For position b

$$\frac{V_{e,b}}{V} = b_{0b} + b_{1b}\alpha_b + b_{2b}\theta_p + b_{3b}V + b_{4b}\alpha_b{}^2 + b_{5b}\theta_p{}^2 + b_{6b}V^2 + b_{7b}\alpha_b\theta_p + b_{8b}\alpha_b V + b_{9b}\theta_p V \tag{4.22}$$

$$\cos\alpha_b = \cos\theta_0 \cos\theta_p \cos(\theta_y - m_b) + \sin\theta_0 \sin\theta_p \tag{4.23}$$

For position c

$$\frac{V_{e,c}}{V} = b_{0c} + b_{1c}\alpha_c + b_{2c}\theta_p + b_{3c}V + b_{4c}\alpha_c^2 + b_{5c}\theta_p^2 + b_{6c}V^2 +$$

$$b_{7c}\alpha_c\theta_p + b_{8c}\alpha_c V + b_{9c}\theta_p V \tag{4.24}$$

$$\cos\alpha_c = \cos\theta_0 \cos\theta_p \cos(\theta_y - m_c) + \sin\theta_0 \sin\theta_p \tag{4.25}$$

The coefficients (b_0, b_1, b_2 ... b_9) in Equations 4.20, 4.22, and 4.24 were known by empirical fitting of calibration data and selected depending on whether the respective probe measurement angle ($\theta_{y,a}$, $\theta_{y,b}$, $\theta_{y,c}$) for each orientation was within the probe yaw angle calibration range of 0 to 90 or 0 to -90. Since the effective velocities $V_{e,a}$, $V_{e,b}$, and $V_{e,c}$ were measured values, six unknown variables (α_a, α_b, α_c, θ_p, θ_y, V) remained, and the six nonlinear equations (Equations 4.20 through 4.25) could be solved simultaneously by using the Newton-Raphson numerical method. With V, θ_p, θ_y determined, the velocity vector is completely specified with respect to the probe coordinate system. The velocity vector with respect to compressor coordinates is determined by accounting for the rotation of the probe coordinate system about the compressor coordinate system. More will be said about the method of solution and transformation to compressor coordinates in the section on data reduction.

The precision of this measurement technique was largely dependent on the selection of the three probe measurement angles $\theta_{y,a}$, $\theta_{y,b}$, and $\theta_{y,c}$. It was important to select the measurement angles in regions of high sensor yaw angle sensitivity for best resolution. As can be seen from Figure 4.9, the sensor yaw angle region near 90 degrees was unfavorable

since large variations in α (5 degrees) could result from small changes of effective cooling velocity ratio. Therefore, in this region, substantial measurement errors were likely to occur. In fact, if the sensor yaw angle was near 90 degrees at any one of the three probe angle measurement positions, the solution would not converge. In addition, sensor yaw angles near 90 degrees were also avoided since this position was most susceptible to velocity gradients along the sensor. Since the effective cooling velocity ratio was calibrated over the two distinct probe angle regions 0 to 90 and 0 to -90, probe angle measurement positions were selected to insure that the varying sensor yaw angle caused by the random variation of the velocity direction at the measurement point always remained in one of these two regions. To avoid probe prong interference, the shorter prong was always positioned into the flow upstream of the longer prong.

Figure 4.10 is a view of the three probe angle measurement positions looking along the axis of the probe. To insure acceptable probe angle measurement positions at each flow-field measurement point, the periodic-average tangential flow angle was approximately determined (within 5 degrees), and appropriate measurement positions were selected. This was done by determining the angle corresponding to minimum effective cooling velocity, β_{mv}, (see Figure 4.10) while rotating the probe about its axis. The three sensor measurement positions were then located by rotating the probe from the angle β_{mv} according to the off-set angles $\theta_{a,off}$, $\theta_{b,off}$, and $\theta_{c,off}$. Where the off-set angles were equal to:

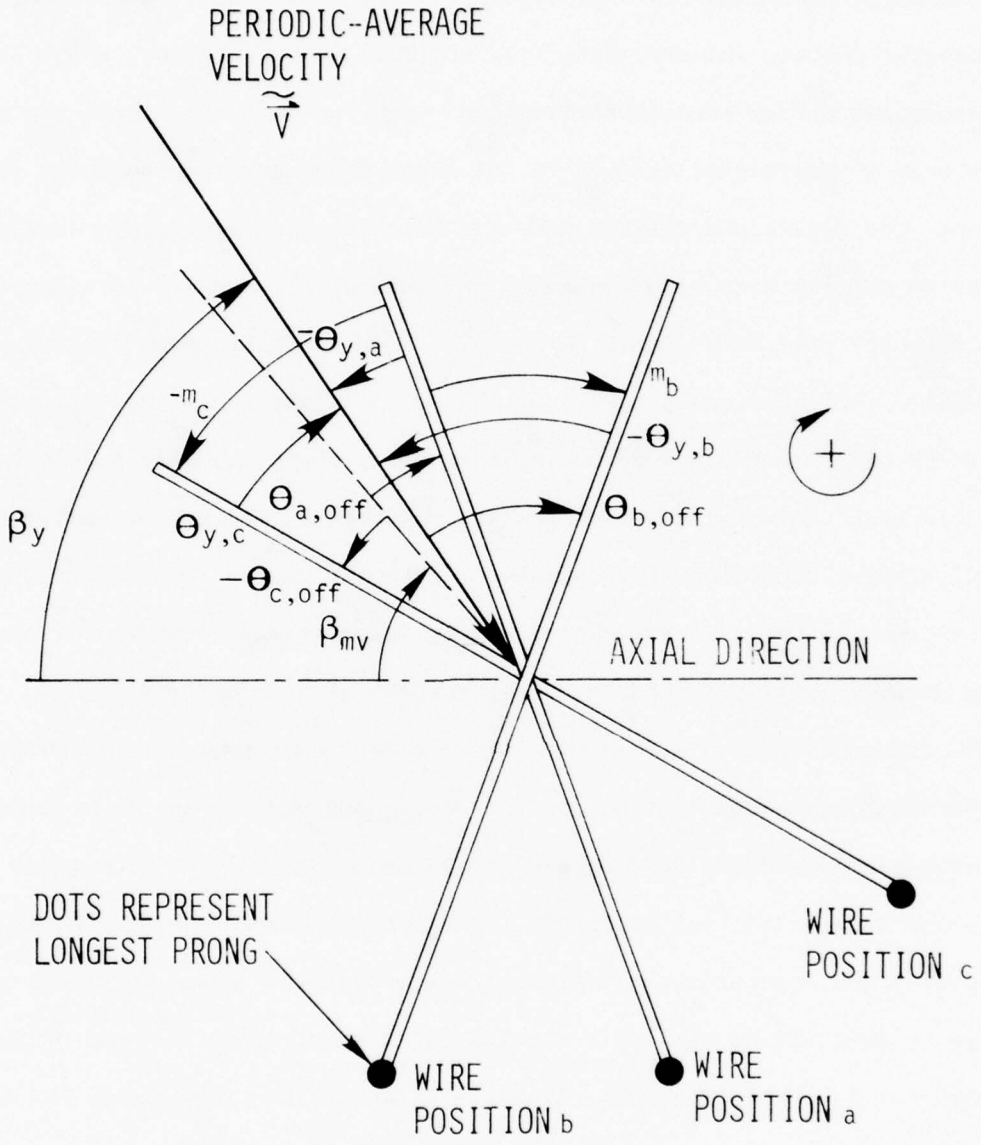


Figure 4.10. Hot-wire measurement positions and nomenclature, viewed from above along probe axis.

$$\theta_{a,off} = 20 \text{ degrees}$$

$$\theta_{b,off} = 60 \text{ degrees}$$

$$\theta_{c,off} = -20 \text{ degrees}$$

and therefore, as can be seen from Figure 4.10

$$\theta_{y,a} = \theta_y \approx -20 \text{ degrees}$$

$$\theta_{y,b} = \theta_y - m_b \approx -60 \text{ degrees}$$

$$\theta_{y,c} = \theta_y - m_c \approx 20 \text{ degrees}$$

and

$$m_b = 40 \text{ degrees}$$

$$m_c = -40 \text{ degrees}$$

This method of positioning the sensor at each flow-field measurement point was necessary since the periodic-average tangential flow angle varied as much as 20 degrees over the circumferential traverse range.

The angle of wire inclination, θ_0, is also an important factor in the measurement technique since it affects the sensitivity and uniqueness of solution. The measurement sensitivity to tangential and radial angles increases as θ_0 is decreased. The lower limit of θ_0 is governed by the value of the radial angle and the selection of the probe angle measurement positions. Hirsch and Kool (20) state that in order to obtain a unique solution, the pitch angle θ_p must be smaller than the value computed from

$$\tan \theta_p = \frac{\tan \theta_0}{\cos \theta_y} \tag{4.26}$$

which is dependent on the wire angle and probe measurement yaw angle. In addition, if θ_0 is too small, unsteady probe prong interference effects

could cause large errors for probe measurement angles near 0.0 degrees. Of the two hot-wire probes used (θ_0 of 45 and 35 degrees), the results obtained from the 35-degree probe were more consistent and judged to be more accurate. For this reason, the majority of the measurements were made with the 35-degree probe. Possibly, the accuracy can be slightly increased by further optimization of the wire angle for the measurement conditions involved.

3. Calibration procedure

A complete velocity sensing calibration of the hot wire was made employing the calibration nozzle. The probe was positioned at 0.25 nozzle orifice diameters from the nozzle exit, and at this location the static pressure was assumed to be atmospheric, and the total pressure was equal to the plenum wall static pressure over the velocity range involved. The compressor and hence calibration nozzle flow-velocity range consisted of Mach numbers less than 0.2, thus permitting the assumption of incompressible flow conditions. The nozzle jet velocity was calculated by the following equation:

$$V = \sqrt{\frac{2g_c \gamma_{H_2O} \Delta P_n}{\rho}} \tag{4.27}$$

where V = velocity, m/s

g_c = gravitational constant, 1.0 kgm/Ns^2

γ_{H_2O} = specific weight of manometer fluid, N/m^3

ρ = density of air, kg/m^3

ΔP_n = differential pressure between plenum pressure and atmospheric pressure, m of water

Before actual calibration took place, sufficient warm-up time was allowed for the nozzle stream temperature to reach its equilibrium state. It was possible to maintain the nozzle stream temperature to within 0.15 ^{o}K over a calibration period. Three types of hot-wire velocity sensing calibrations were made: linearizer velocity calibration, second order velocity calibration, and effective cooling velocity calibration.

a. Linearizer velocity calibration The anemometer linearizer approximated the hot-wire curve of effective cooling velocity versus bridge voltage with a fourth order polynomial curve. The "zero" degree polynomial term was set equal to zero, and the four polynomial coefficient values were determined with a fourth order least squares curve fit of calibration nozzle data obtained as explained below.

The hot-wire sensor was positioned in the nozzle jet stream normal to the flow by optical alignment with a telescope. The cold resistance of the sensor was measured and the anemometer resistance deck was set corresponding to an overheat ratio (operating sensor resistance/cold sensor resistance) of 1.8 using the relationship

$$R_{s,op,d} = 1.8(R_{s,c,d} - R_{cb} - R_{ph} - R_{pl}) + R_{cb} + R_{ph} + R_{pl} \qquad (4.28)$$

where

$R_{s,op,d}$ = sensor operating resistance deck setting, ohms

$R_{s,c,d}$ = cold resistance read off anemometer resistance deck, ohms

R_{cb} = cable resistance, ohms

R_{ph} = probe holder resistance, ohms

R_{pl} = probe lead resistance, ohms

The cable and probe holder resistances were measured using an impedance bridge and a shorting probe while the probe lead resistance was specified by the manufacturer of the hot-wire probe. The following parameters were recorded at the beginning and end of the calibration run:

(1) Barometric pressure, inches of Hg

(2) Barometer ambient temperature, °F

(3) Room temperature, °F

(4) Nozzle stream temperature, millivolts

(5) Anemometer standby voltage, volts

Anemometer voltage and plenum pressure readings were taken at 16 velocity level values over a range of 0.0 to 23 m/s. After the last calibration point was recorded, a calculator program proceeded to reduce the data and to determine the polynomial coefficients. In addition, the percent error each data point between the actual nozzle jet velocity determined with Equation 4.27 and the velocity predicted by the polynomial relationship was calculated. The majority of errors were within 0.25% and none were larger than 1.0%. The coefficient potentiometers of the linearizer were then adjusted to reflect the four calculated polynomial coefficients, and the zero suppression and input gain of the linearizer were adjusted (see Ref. 33). The linearizer velocity calibration was performed initially for each hot-wire probe and thereafter approximately every 40 hours of actual running time.

b. Second order velocity calibration As mentioned previously, a second order relationship between the linearized anemometer bridge voltage and the effective cooling velocity with the form

$$V_e = K_1 + K_2 E_\ell + K_3 E_\ell^2 \qquad (4.13)$$

where

V_e = effective cooling velocity, m/s

E_ℓ = anemometer linearizer output voltage, volts

K_1, K_2, and K_3 = least square coefficients

was used to determine the effective cooling velocity from the measured linearized anemometer bridge voltage. A velocity calibration was made to determine the three coefficients K_1, K_2, and K_3 by a least squares fit of calibration nozzle data.

For this calibration, the position of the sensor was also aligned normal to the flow, and an overheat ratio of 1.8 was used. The barometric pressure, barometer ambient temperature, room temperature, and nozzle stream temperature were taken before and after the calibration test. The anemometer linearizer output voltage and the plenum pressure were recorded at 14 points over a velocity range from 4 to 23 m/s. The three coefficients and the percent error at each calibration point were then computed by the calculator calibration program. The error between the actual calibration velocity and the predicted velocity from the second order equation was almost always within 1% or better. This second order velocity calibration was made before each circumferential blade-to-blade survey in the compressor, and was also used in the calibration of effective cooling velocity described in the next section.

c. Effective cooling velocity calibration A comprehensive calibration procedure was followed to determine the coefficients involved in the previously presented V_e/V relationship

$$\frac{V_e}{V} = b_0 + b_1\alpha + b_2\theta_p + b_3V + b_4\alpha^2 + b_5\theta_p{}^2 + b_6V^2 + b_7\alpha\theta_p + b_8\alpha V + b_9\theta_pV \qquad (4.16)$$

The effective cooling velocity calibration was made over the entire velocity, probe yaw angle θ_y, and pitch angle θ_p measurement ranges expected in the compressor. The coefficients were obtained and spot checked approximately every 30 hrs of running time and the calibration was repeated when the drift was discerned to be greater than 2.0 to 3.0%.

The slant hot-wire probe was mounted near the calibration nozzle exit in a manual actuator which allowed both probe yaw angle and pitch angle variation (see Figure 3.9). The hot-wire sensor was zeroed in the actuator with the optical telescope and was positioned so that the center of the sensor remained at the same point in the nozzle flow stream for various θ_y and θ_p. A second order velocity calibration of the linearized anemometer voltage was first made to determine the coefficients K_1, K_2, and K_3 in Equation 4.13. The nozzle stream and atmospheric conditions were recorded and the effective cooling velocity calibration involving the following velocity, pitch angle, and probe yaw angle levels was begun:

Velocity	11.6, 15.2, 19.2, 22.3, m/s
Pitch angle	-9 to 6, degrees, in increments of 3 degrees
Probe yaw angle	0 to 90, degrees, in increments of 5 degrees 0 to -90, degrees, in increments of 5 degrees

The probe yaw angle was varied over each range for each pitch angle setting and each velocity level. At every probe yaw angle position, the probe yaw angle was recorded along with the linearized anemometer voltage, and the calculator was used to perform the following preliminary calcula-

tions and steps:

(1) The actual velocity was calculated from nozzle data with Equation 4.27.

(2) The effective cooling velocity was determined from the linearized anemometer voltage with the second order velocity relationship, Equation 4.13.

(3) The sensor yaw angle α was calculated using Equation 4.12.

(4) V_e/V was calculated.

After all the calibration data were taken, the ten coefficients in Equation 4.16 were determined with a least squares method (see Appendix D), one set for the probe yaw angle range 0 to 90 degrees and another set for the angle range 0 to -90 degrees. In order to inspect the accuracy of the V_e/V relationship, the percent error between the measured velocity and the predicted velocity ratio from Equation 4.16 was calculated. The majority of errors were within 0.80% and no errors were greater than 2.0%.

4. Data acquisition

Three-dimensional, periodic-average, compressor flow-field velocity measurements were made with the periodic-sampling-and-averaging method and the slant hot-wire measurement technique. Circumferential traversing surveys of velocity were made between the blade rows over the first two stages of the compressor with the stationary blade rows set for minimum sound. The measurement location, rotor blade setting position YO_R, and periodic-sampling circumferential survey method (frozen rotor-blade type or passing rotor-blade type) for each survey are summarized in Table 4.1. The rotor setting position YO_R, is the periodic-sampling position of the

Table 4.1. Specifications for periodic-average hot-wire circumferential surveys, all measurements were made at the minimum sound stationary blade-row schedule.

Probe Measurement Station	Percent Passage Ht. from Hub PHH	Rotor Position YO_R/S_R	Periodic-Sampling Method	Probe Wire Angle θ_0 degrees
3	10	0.0	Frozen rotor-blade survey	35
3	20	0.0	" " "	35
3	30	0.0	" " "	45
3	40	0.0	" " "	35
3	50	0.0	" " "	35
3	50	0.17	" " "	35
3	50	0.28	" " "	35
3	50	0.28	Passing rotor-blade survey[a]	35
3	50	0.50	Frozen rotor-blade survey	35
3	50	0.69	" " "	35
3	50	0.69	Passing rotor-blade survey[b]	35
3	50	0.83	Frozen rotor-blade survey	35
3	60	0.0	" " "	35
3	70	0.0	" " "	45
3	80	0.0	" " "	45
3	90	0.0	" " "	35
4	50	0.0	" " "	35
4	50	0.17	" " "	35
4	50	0.34	" " "	35
4	50	0.50	" " "	35
4	50	0.69	" " "	35
4	50	0.83	" " "	35
5	50	0.0	" " "	35
5	50	0.17	" " "	35
5	50	0.34	" " "	35
5	50	0.50	" " "	35
5	50	0.67	" " "	35
5	50	0.83	" " "	35
6	50	0.00	" " "	35
6	50	0.34	" " "	35
6	50	0.67	" " "	35

[a] Circumferential position of stationary blade rows set at Y = 3.50.

[b] Circumferential position of stationary blade rows set at Y = 0.00.

first rotor blade in each rotor row, when the circumferential traversing position Y is equal to zero. YO_R is measured as the angular circumferential distance from the probe-traversing measurement stations to the periodic-sampling position of the rotor blade stacking axis, and is positive in the direction of rotor rotation. Measurement errors due to temperature variation and dirt accumulation on the hot-wire sensor were minimized by maintaining the room and compressor flow passage temperatures constant at their respective values to within 0.5 ^{o}K for the duration of a test and by frequent calibration of the hot-wire sensor. The remaining portion of this section is a detailed description of the data procurement procedure.

Several preliminary steps were required before measurements were made in the compressor. The alignment telescope was used to position the slant hot-wire sensor in the probe actuator so that the hot-wire probe prongs were in line with the compressor axis with the shortest prong forward when the actuator angle indicator read 0.0 degrees. After the initial warm up, the instruments were electronically zeroed and the linearizer coefficient adjustments were made. The voltages from the circumferential motion actuator potentiometer and the probe actuator yaw angle motion potentiometer were correlated to their respective motions using a linear least squares correlation. The circumferential position of the stationary blade rows relative to each other were set corresponding to the minimum sound placement schedule (see Table 5.1). The stationary blade rows were connected to the circumferential motion actuator for periodic-average frozen rotor-blade flow-field surveys. For the passing rotor-blade flow-field

surveys, the stationary blade rows were moved jointly to a circumferential position Y specified for the test with the minimum sound schedule maintained, but the blade rows were not connected to the circumferential motion actuator. For either type of periodic-average survey, the periodic-sampling rotor blade position YO_R was set to the desired value for each test by moving the photoelectric pickup to the appropriate position and subsequently locking its movement to the circumferential motion actuator.

Immediately before each circumferential traversing survey, a second order hot-wire velocity calibration was performed with the sensor positioned at the calibration nozzle normal to the flow (see Figure 4.11) and with the linearized anemometer signal routed through the periodic-sampling and averaging circuits. The sensor operating resistance was set corresponding to an overheat ratio of 1.8. The temperature of the fluid flowing through the calibration nozzle was maintained to within 0.5 ^{o}K of the compressor fluid temperature. From the calibration, the three coefficients K_1, K_2, and K_3 of Equation 4.13 were determined as described previously. After calibration, the probe actuator was positioned at a compressor probe traversing station and the radial position of the hot-wire sensor was set.

The following miscellaneous parameters were recorded in order to completely specify the measurement conditions:

(1) Probe traversing station number, see Figure 3.1

(2) Passage height position from hub, inches

(3) Periodic-sampling rotor position setting YO_R, degrees

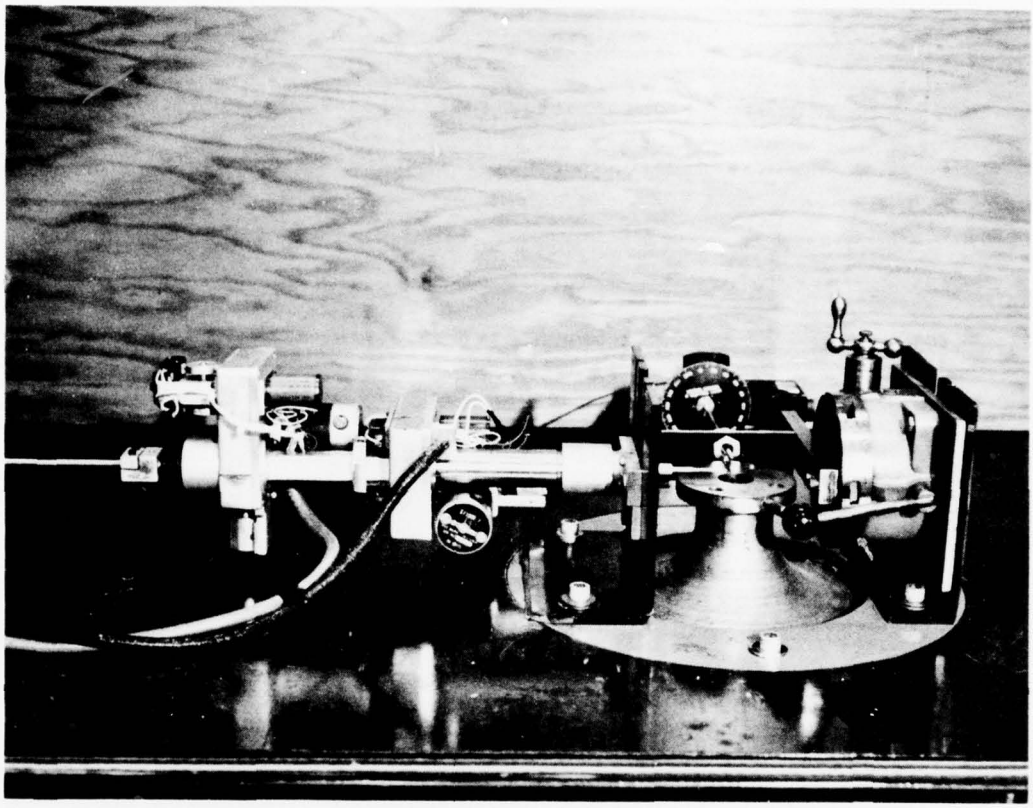


Figure 4.11. Probe actuator positioned at calibration nozzle for hot-wire velocity calibration.

(4) Stationary blade position settings YO_{IGV}, YO_{1S}, YO_{2S}, YO_{3S}, degrees

(5) Measurement offset angles $\theta_{a,off}$, $\theta_{b,off}$, $\theta_{c,off}$, degrees

(6) Actuator linear correlation coefficients, for immersion, probe yaw angle, and circumferential traversing movements

(7) Date

(8) Barometric pressure, inches of Hg

(9) Barometer ambient temperature, °F

(10) Differential pressure across venturi, inches of water

(11) Temperature at venturi throat, millivolts

(12) Room temperature, °F

(13) Compressor flow passage temperature, millivolts

(14) Compressor rpm

(15) Compressor rpm variation

(16) Hot-wire sensor angle θ_0, degrees

(17) Calculator sampling and averaging number related to N

(18) Sensor resistance overheat ratio R_{oh}

(19) Sensor operating resistance $R_{s,op}$, ohms

(20) Sensor cold resistance $R_{s,c}$, ohms

(21) Anemometer bridge standby voltage, volts

In order to insure the same compressor operating conditions for each test, the flow coefficient was calculated preceding the test using flow rate venturi meter data. Before activating the hot-wire anemometer, the anemometer bridge standby voltage was checked against the recorded calibration value, and the sensor operating resistance was set according to the

value used during calibration. A four channel time-base oscilloscope was used to observe the behavior and to detect any anomalies of the output signals from the triggering circuit, anemometer linearizer, sample-and-hold circuit, and electronic averaging circuit. Two X-Y channel storage oscilloscopes were used to display the periodic-average voltage signal from the electronic averaging circuit, one as a function of probe yaw angle position and the other as a function of circumferential traversing position Y. A qualitative trace on the oscilloscope was made of the circumferential varying velocity profile to determine the best circumferential distribution of flow-field measurement points.

A series of repetitive steps were then taken to obtain the hot-wire data. First, the circumferential position Y was set by adjusting the position of the circumferential motion actuator and was recorded by the calculator. Next, the approximate tangential flow angle β_{mv} was determined, and the hot-wire sensor was positioned at the three measurement orientations in the manner described previously. For each orientation, the effective cooling velocity was measured and recorded using the periodic-sampling-and-averaging technique. This point-by-point measurement procedure was repeated for each of 30 flow-field measurement points over one stator blade spacing.

After the last circumferential point, the data were printed on thermal sensitive paper and recorded on magnetic tape for reduction at a later time. If time remained, the second order hot-wire velocity calibration was repeated and another circumferential survey was made.

5. Data reduction

The reduction of the hot-wire data involved solving the six nonlinear simultaneous equations (Equations 4.20 through 4.25) at each flow-field measurement point and expressing the solution in terms of the compressor coordinate system. The Newton-Raphson method which is a general technique for finding real roots of simultaneous transcendental equations (see Ref. 31) was used to solve these six equations. The solution convergence rate was typically about 5 iterations but never greater than 100 iterations per solution point. The convergence rate seemed to be dependent on the selection of the probe angle measurement positions, the initial guess of the unknowns, and the accuracy required of the solution.

The compressor coordinate system is shown in Figure 4.12. The Z and R coordinates are respectively directed along the machine axis and radius of the compressor, while the Y axis is in the direction of rotor rotation. The direction of the velocity vector with respect to the compressor is completely specified by the absolute tangential angle β_y and the radial angle β_r. The sign convention for β_y, β_r and the velocity components V_z, V_y, and V_r (axial, tangential, and radial) are shown in the figure. Since the probe was immersed radially into the compressor, the probe coordinate axis z and compressor coordinate axis R were coincident. As the probe was rotated about its axis, the probe coordinate system (x, y, z) rotated about the compressor coordinate system with Y and Z, and x and y axes always in the same plane. The pitch angle and the radial angle could be related by

$$\beta_r = -\theta_p \tag{4.29}$$

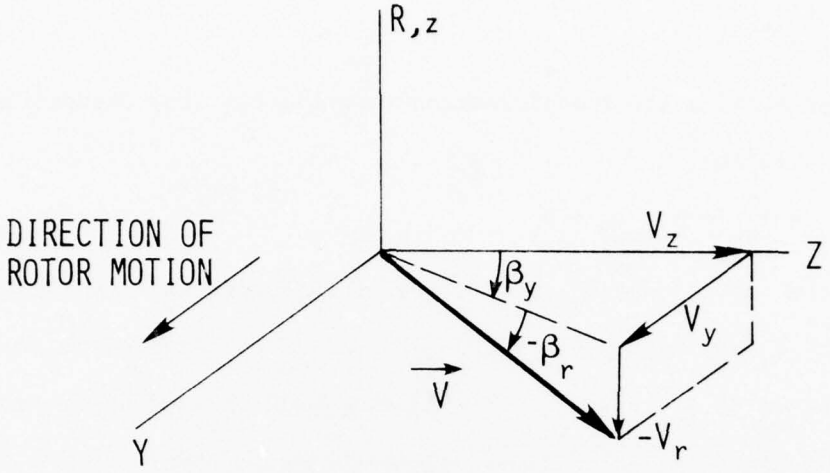


Figure 4.12. Compressor coordinate system showing nomenclature and sign convention for three-dimensional fast-response velocity and angle parameters.

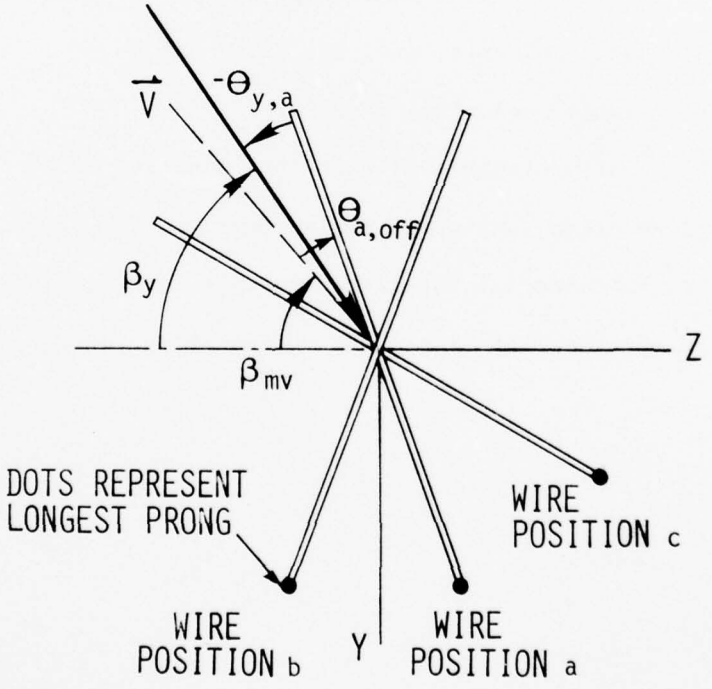


Figure 4.13. Hot-wire measurement positions with respect to compressor coordinates Y and Z.

Since

$$\theta_{y,a} = \theta_y \tag{4.30}$$

The tangential angle transformation relationship from inspection of Figure 4.13 is

$$\beta_y = \beta_{mv} + \theta_{a,off} + \theta_y \tag{4.31}$$

The values of β_{mv} and $\theta_{a,off}$ were recorded during data acquisition, and the value of θ_y was determined solving the six simultaneous equations. In addition to V, β_y, and β_r, the following velocity and angle parameters were calculated at each flow-field measurement point:

(1) Axial velocity, m/s, Eq. 12.55

(2) Absolute tangential velocity, m/s, Eq. 12.56

(3) Radial velocity, m/s, Eq. 12.57

(4) Relative velocity, m/s, Eq. 12.59

(5) Relative tangential velocity, m/s, Eq. 12.58

(6) Relative tangential angle, degrees, Eq. 12.60

A circumferential integrated average for each parameter was also computed. A complete listing of the equations used appears in Appendix C.

V. PRESENTATION AND DISCUSSION OF DATA

The results involving the sound pressure level (SPL) data, slow-response data, and fast-response hot-wire data are presented and discussed in this section. The primary flow field parameters for the slow and fast response data are tabulated in Appendices E and F. In graphing the results, all data variation curves were drawn through the actual data points; statistical curve fitting of the data was not attempted.

A. Sound-Pressure Level Measurement Results

The variation of overall SPL measured at the compressor inlet over the rpm range of the compressor at a constant flow coefficient of 0.42 is shown in Figure 5.1 for each of the two cases obtained by adjusting the circumferential position of the IGV blade row (the stator blade rows were not moved) for minimum and maximum noise. It should be noted that varying the IGV row circumferential position resulted in significant changes of the compressor inlet noise level at rotor speeds greater than 700 rpm. At rotor speeds below 600 rpm, moving the IGV row had little if any effect on the noise level detected at the compressor inlet. The spinning mode "cut-off" rotor speed (see Tyler and Sofrin (15)) required for the propagation of blade-row interaction noise established by the number of rotor and stator blades per row in the research compressor was independently estimated as being about 610 rpm. These results seem to indicate that the level of discrete frequency noise due to adjacent blade row interaction can be influenced by stationary blade-row circumferential positioning at rotor speeds greater than the "cut-off" amount. The varying amounts of

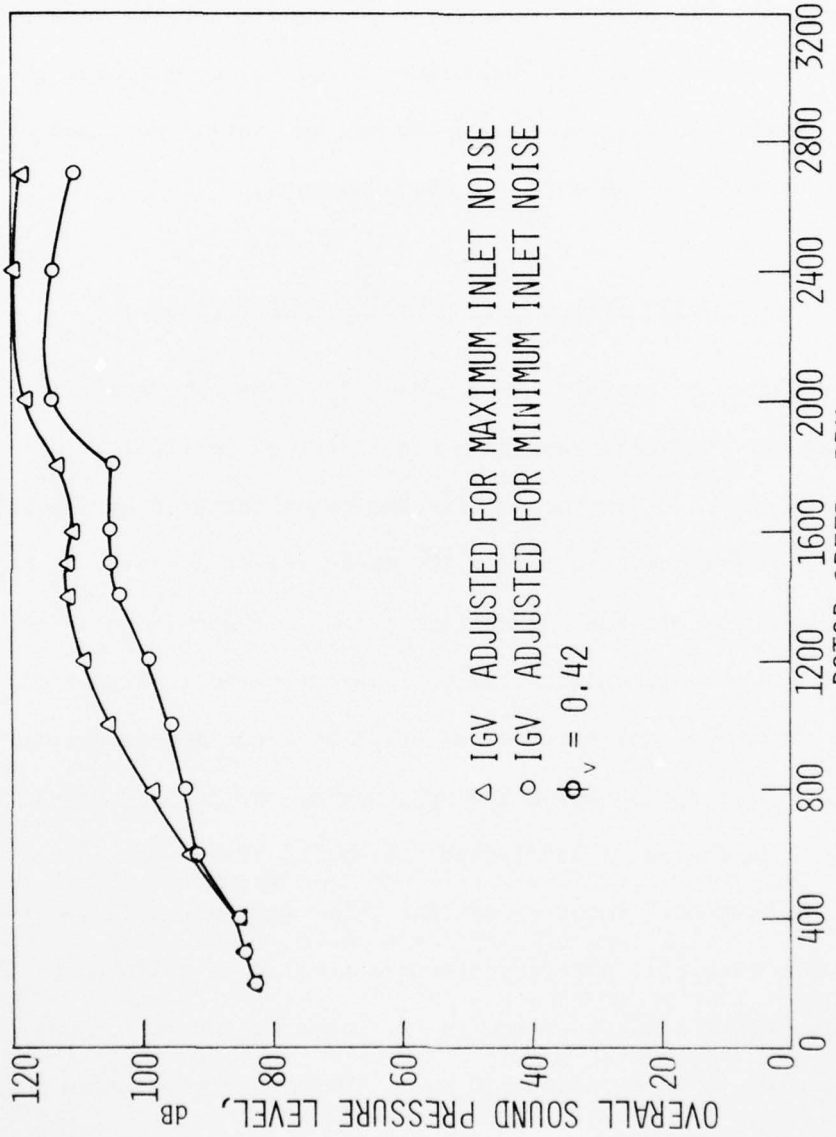


Figure 5.1. Compressor inlet noise level over compressor rpm range.

compressor inlet noise reduction possible at the different rotor speeds may be related to the proportions of noise reduction attributable to wake cancellation and sound wave interference. As pointed out by Walker and Oliver (5), a combination of these phenomena is the probable cause of noise variation with circumferential placement of stationary blade rows. It appears as if more sound-pressure level data at various rotor speeds are required before this aspect of noise reduction is understood.

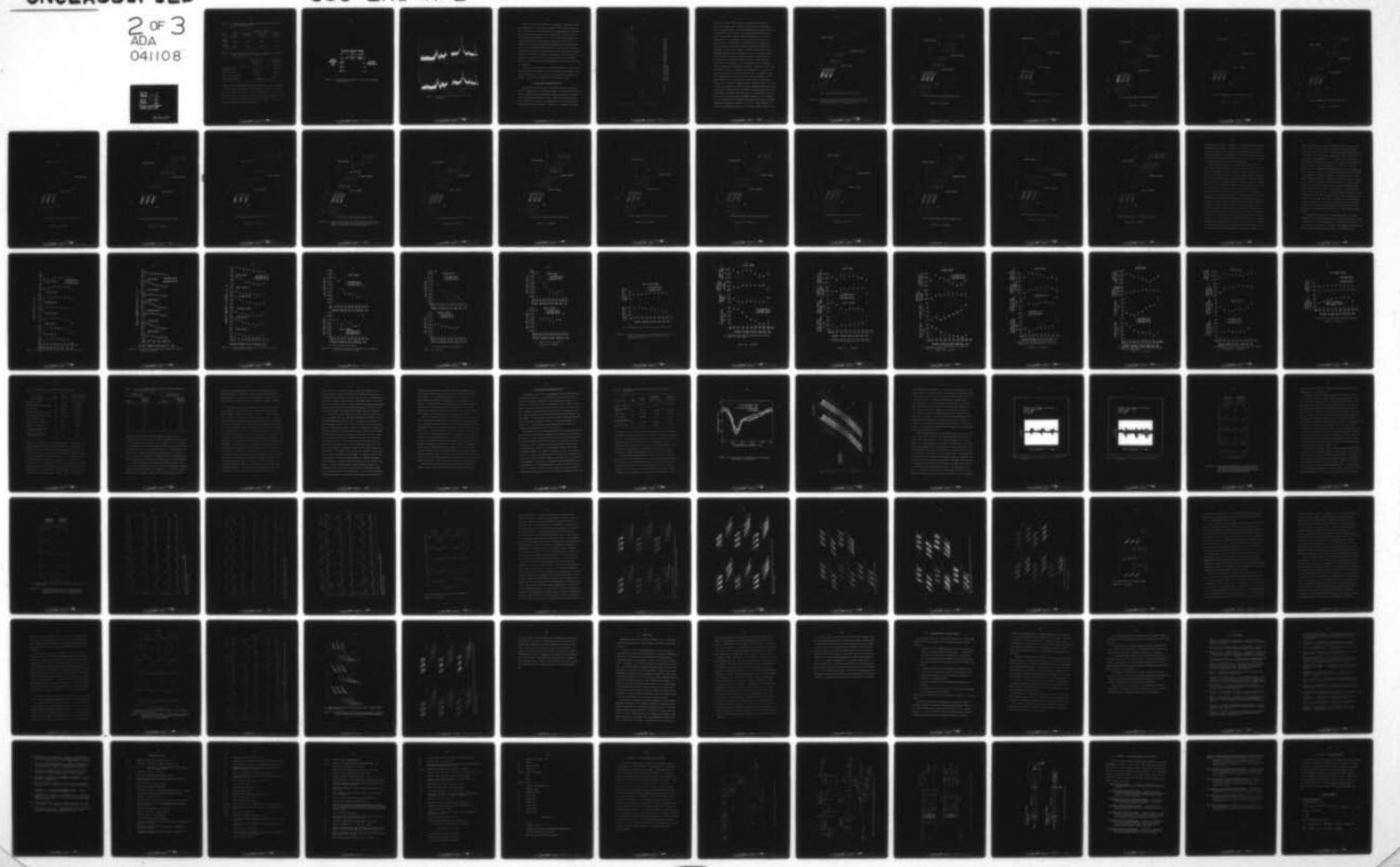
The stationary blade-row circumferential settings (all of the stationary blade rows were set) for minimum and maximum noise at a rotor speed of 1400 rpm and a flow coefficient of 0.42 are presented in Table 5.1. These circumferential position schedules were each found to be distinct and uniquely obtainable on a repeatable basis. The circumferential positioning of the IGV, first stator, and second stator blade rows was critical, whereas the placement of the third stator row had little effect on the overall sound level (1 dB variation range) perceived at the inlet.

Overall SPL and octave band SPL analyses of the compressor inlet noise at the minimum and maximum noise blade-row schedules (specified in Table 5.1) are presented in Table 5.2. A difference in the overall SPL of 11.5 dB was measured, and in terms of the perceived sound this is equivalent to about a 1/2 reduction in relative annoyance as defined by Sofrin (see Figure 5.2). The SPL octave band analyses were found to differ for the two cases within the 500 and 1000 Hz bands only, which are nearest to the rotor blade passing frequency of 887 Hz. A narrow band spectrum analysis for each of both minimum and maximum noise conditions (see

AD-A041 108 IOWA STATE UNIV AMES ENGINEERING RESEARCH INST F/G 13/7
MULTISTAGE AXIAL-FLOW TURBOMACHINERY WAKE PRODUCTION, TRANSPORT--ETC(U)
NOV 76 D P SCHMIDT, T H OKIISHI AF-AFOSR-2916-76

UNCLASSIFIED ISU-ERI-AMES-77130 AFOSR-TR-77-0720 NL

2 OF 3
ADA
041108



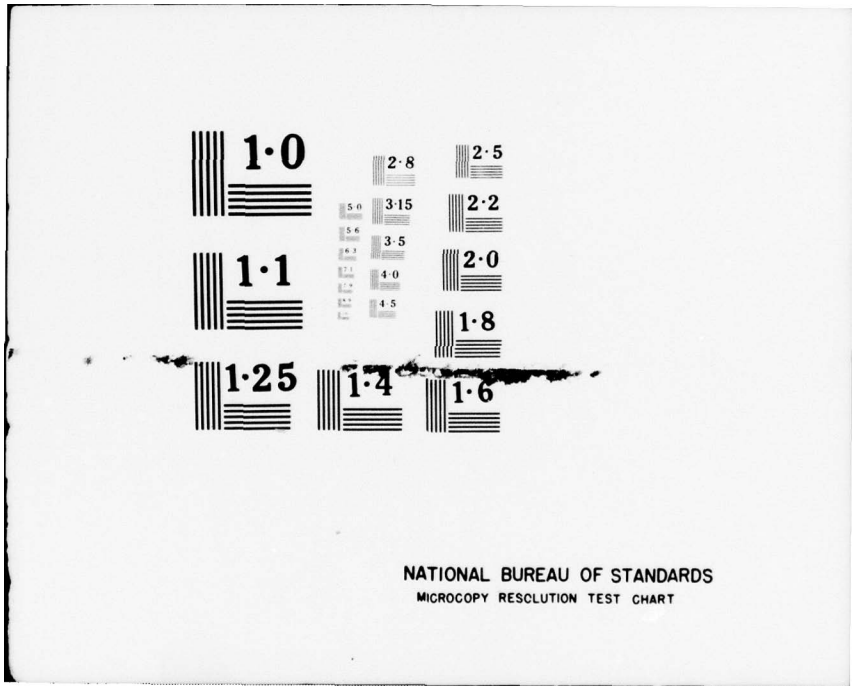

1·0
1·1
1·25
1·4
1·6
1·8
2·0
2·2
2·5
2·8
3·15
3·5
4·0
4·5
5·0
5·6
6·3
7·1
8·0
9·0
NATIONAL BUREAU OF STANDARDS
MICROCOPY RESOLUTION TEST CHART

Table 5.1. Stationary blade-row circumferential placement schedules for minimum and maximum sound.

Noise Level	Blade-Row Schedule			
	IGV YO_{IGV}/S_S	First Stator YO_{1S}/S_S	Second Stator YO_{2S}/S_S	Third Stator YO_{3S}/S_S
Minimum sound	0.000	0.1285	0.5601	-0.2261
Maximum sound	0.000	0.5447	0.1439	0.1490

Table 5.2. Overall and octave band analyses of compressor inlet noise for minimum and maximum noise blade-row schedules.

	Minimum Noise Blade-Row Schedule	Maximum Noise Blade-Row Schedule
Overall SPL (flat)	101.0 dB	112.5 dB
500 Hz octave band SPL	92.5 dB	98.5 dB
1000 Hz octave band SPL	96.5 dB	112.8 dB
Other octave band SPL	Insignificant difference	

Figure 5.3) shows large and distinct discrete frequency noise level peaks at the first and second harmonics of blade passing frequency. Also shown are some broadband noise peaks. The spectrum analyses point out that the reduction in noise level obtained by proper circumferential positioning of the stationary blade rows involved the discrete frequency noise only. No change in broadband noise could be discerned.

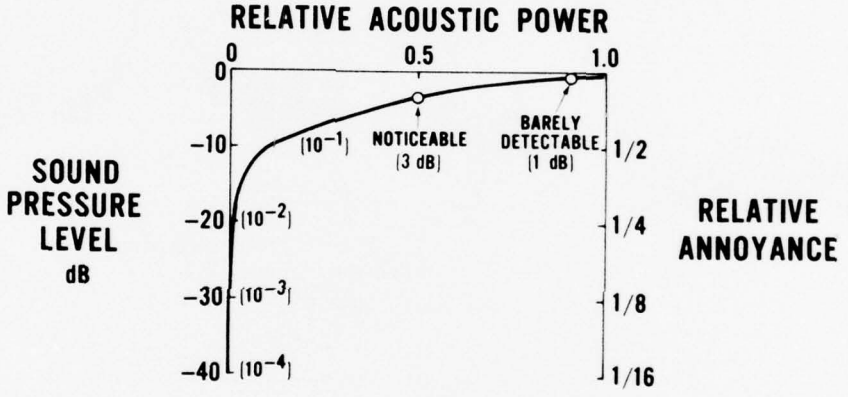


Figure 5.2. Required noise reduction for subjective improvement from Sofrin (11).

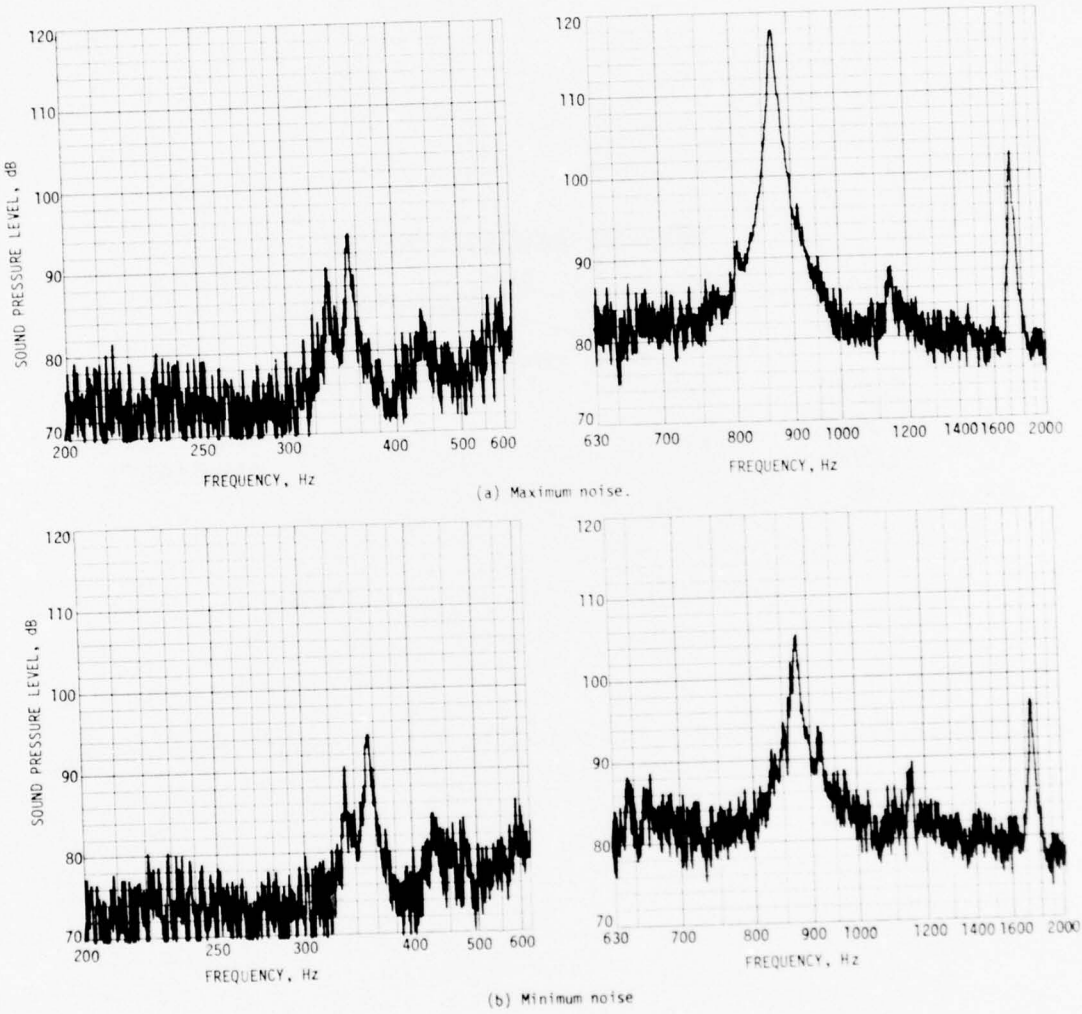


Figure 5.3. Compressor inlet noise spectrum (1% filter bandwidth).

A similar noise level reduction in a low-speed, single-stage, axial-flow compressor also with identical numbers of IGV and stator blades per row was obtained by Walker and Oliver (5) through appropriate circumferential positioning of the IGV and stator blade rows. Variations in SPL at the first and second harmonics of the rotor blade passing frequency were achieved by varying the circumferential position of the IGV row. The difference in SPL between the maximum and minimum IGV row positions was chiefly at the rotor blade passing frequency. Although inlet noise level reduction was attributed to wake cancelling (stator blade section pressure fluctuation reduction) and sound wave interference, Walker and Oliver (5) concluded, on the basis of a test involving removal of the downstream stator row, that wake cancelling eliminates much of the noise generated by the stator row.

In order to further explain the inlet noise reduction achieved in the Iowa State University research compressor with appropriate positioning of stationary blade rows, detailed slow- and fast-response measurements were obtained. These data are discussed in the following sections.

B. Slow-Response Measurement Results

The results of the slow-response measurements were used to obtain a physical description of the time-average fluid flow field ahead and behind each of the blade rows of the research compressor for each of the conditions of minimum and maximum inlet noise. Blade-to-blade plane velocity vector plots were constructed to graphically depict the circumferentially varying average fluid flow field. In Figure 5.4, an example of one such

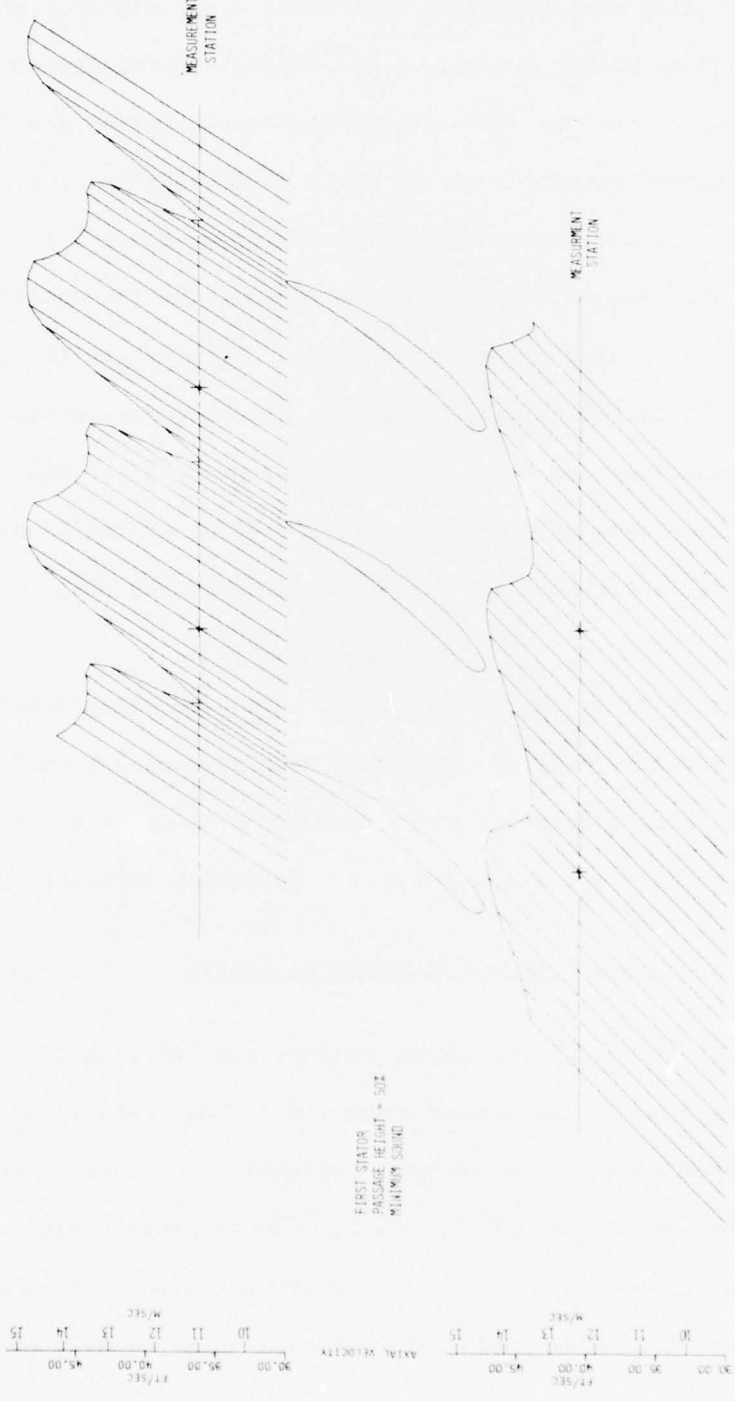
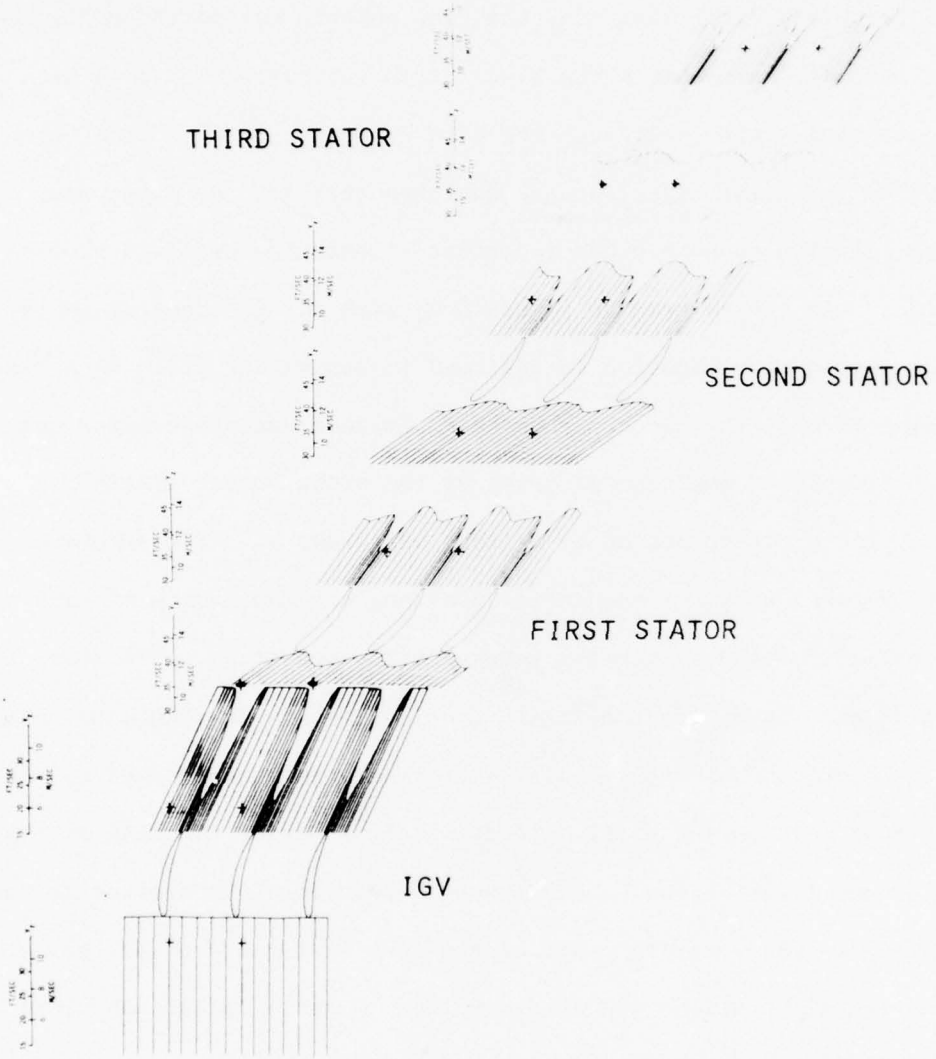


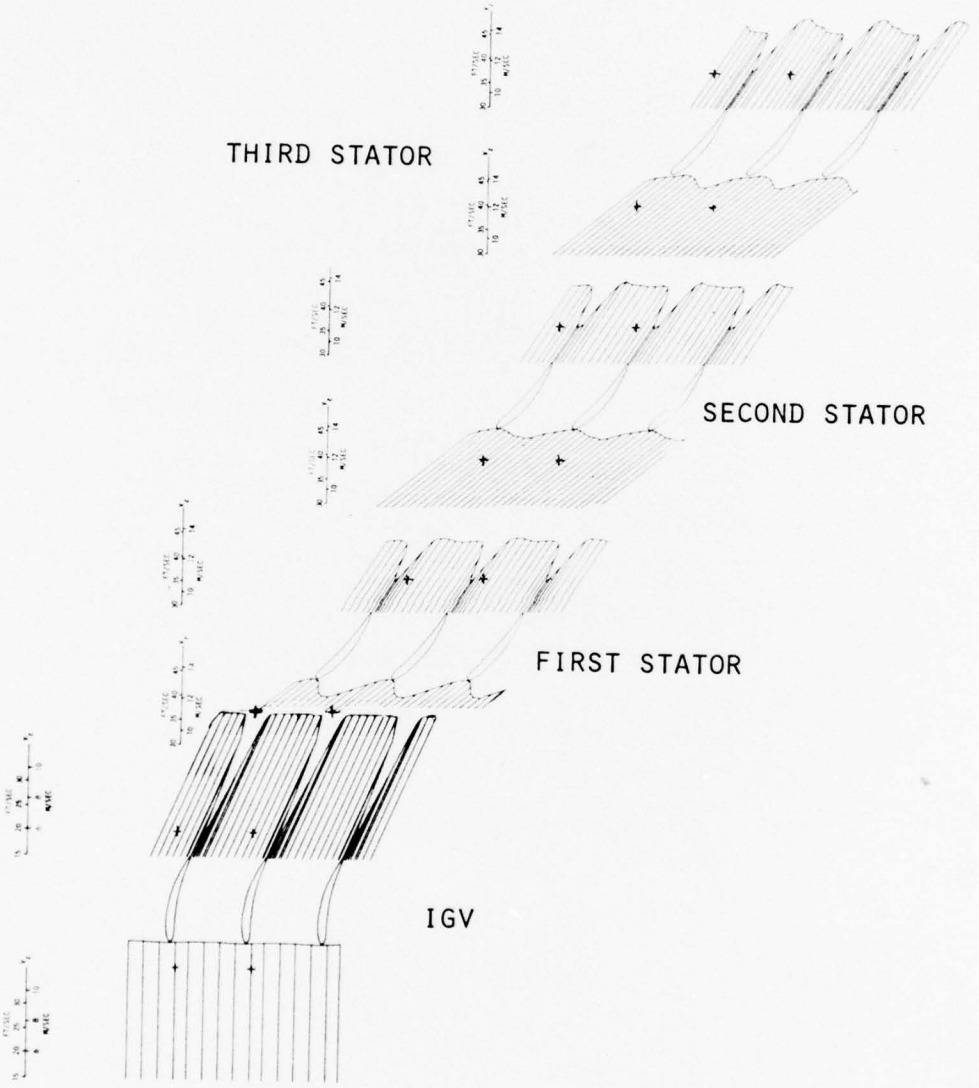
Figure 5.4. Blade-to-blade plane, time-average, velocity vector plot for first stator at mid-span (constructed from slow-response data).

vector plot is shown. This particular illustration represents the velocity flow field ahead and behind the first stator at 50% passage height for minimum sound. Although measurements were obtained over only one stator blade pitch distance, the flow pattern was periodically repeated over approximately three blade pitch intervals to aid in data interpretation. Also, although the data were obtained "in line" with respect to the axial direction as mentioned earlier, the plots were shifted relative to each other to better illustrate the fluid flow development. As can be seen in Figure 5.4, each circumferential survey measurement station location is depicted in the vector plots by a line extending through the two cross marks positioned one blade pitch apart. At each flow-field measurement point at the probe survey station, a velocity vector (represented by a line) was drawn at the circumferentially averaged absolute tangential flow angle. The length of each vector (or line) is related to the absolute velocity magnitude. The left-hand velocity scale specifies the axial velocity level. It should be noted that the magnitude of the velocity vectors are zero suppressed by the amount indicated on the axial velocity scale in order to amply display velocity level variations. Blade-to-blade vector plots similar to the one in Figure 5.4 were made for each of the four stationary blade rows at each of nine radial positions and were combined to represent the absolute time-average flow field through the three stages of the compressor at each of the nine constant passage height measurement locations. These combined velocity vector plots for the minimum and maximum noise blade-row position schedules are presented in Figures 5.5 and 5.6. In these figures, the axial and circumferential positions of the blade profiles as well as the



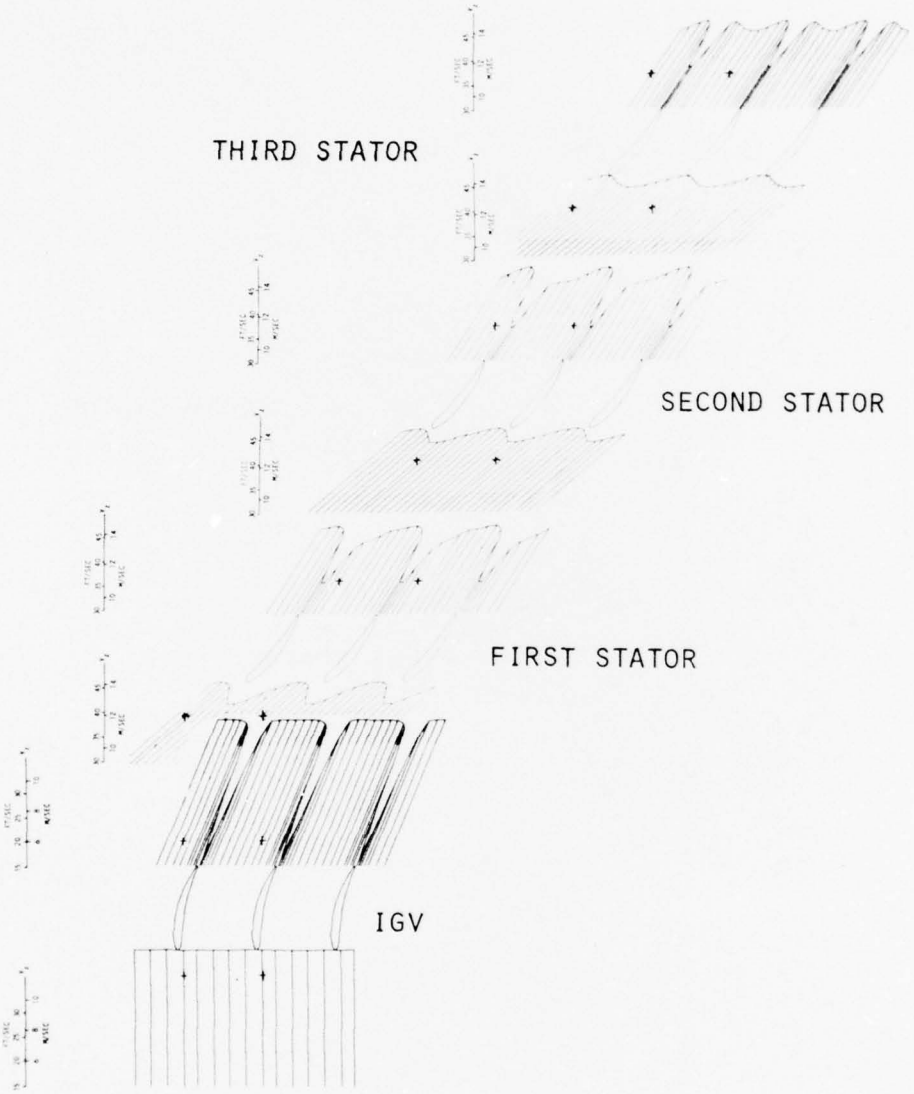
(a) 10% passage height from hub; minimum sound.

Figure 5.5. Blade-to-blade plane, time-average, velocity vector plots at constant passage height for the minimum sound blade-row schedule; constructed from slow-response data.



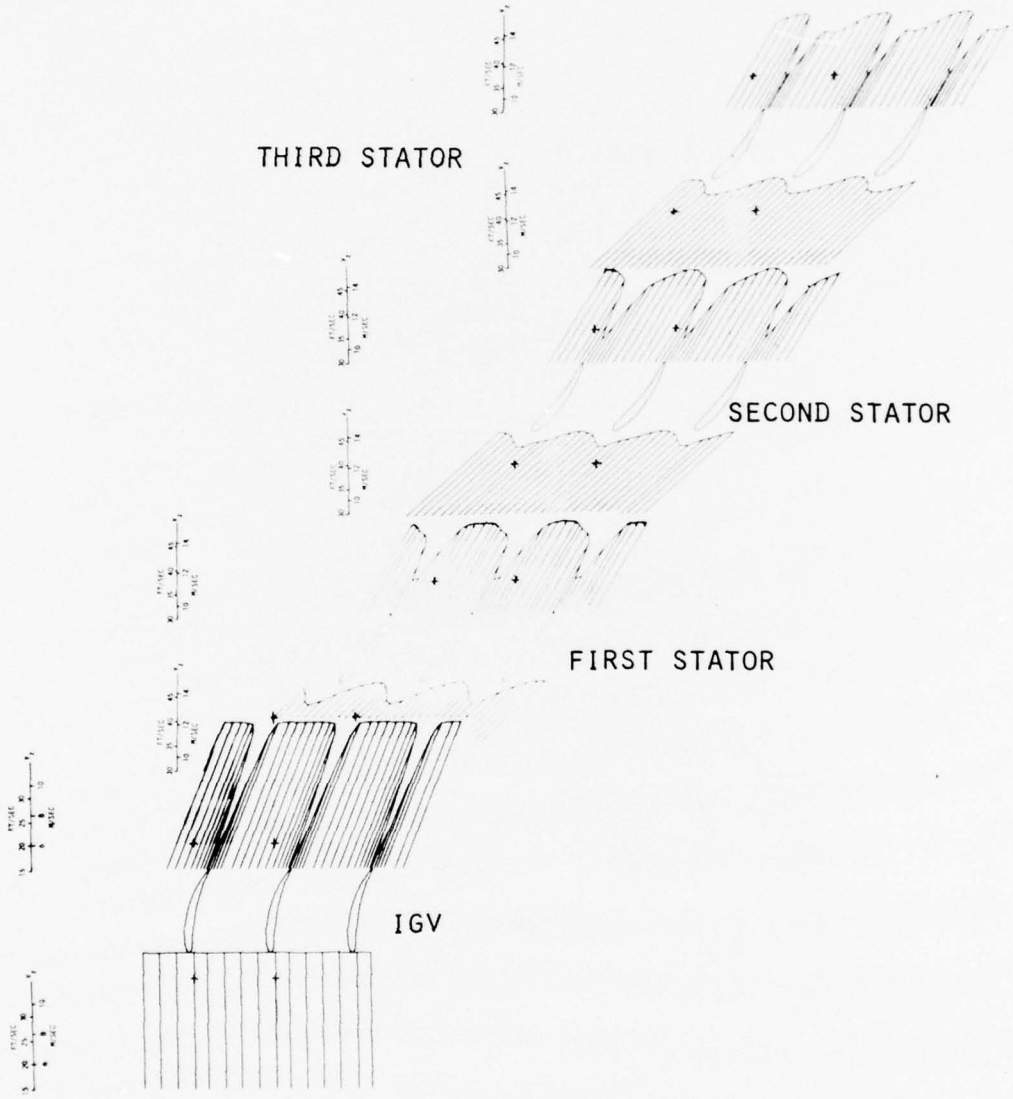
(b) 20% passage height from hub; minimum sound.

Figure 5.5. Continued.



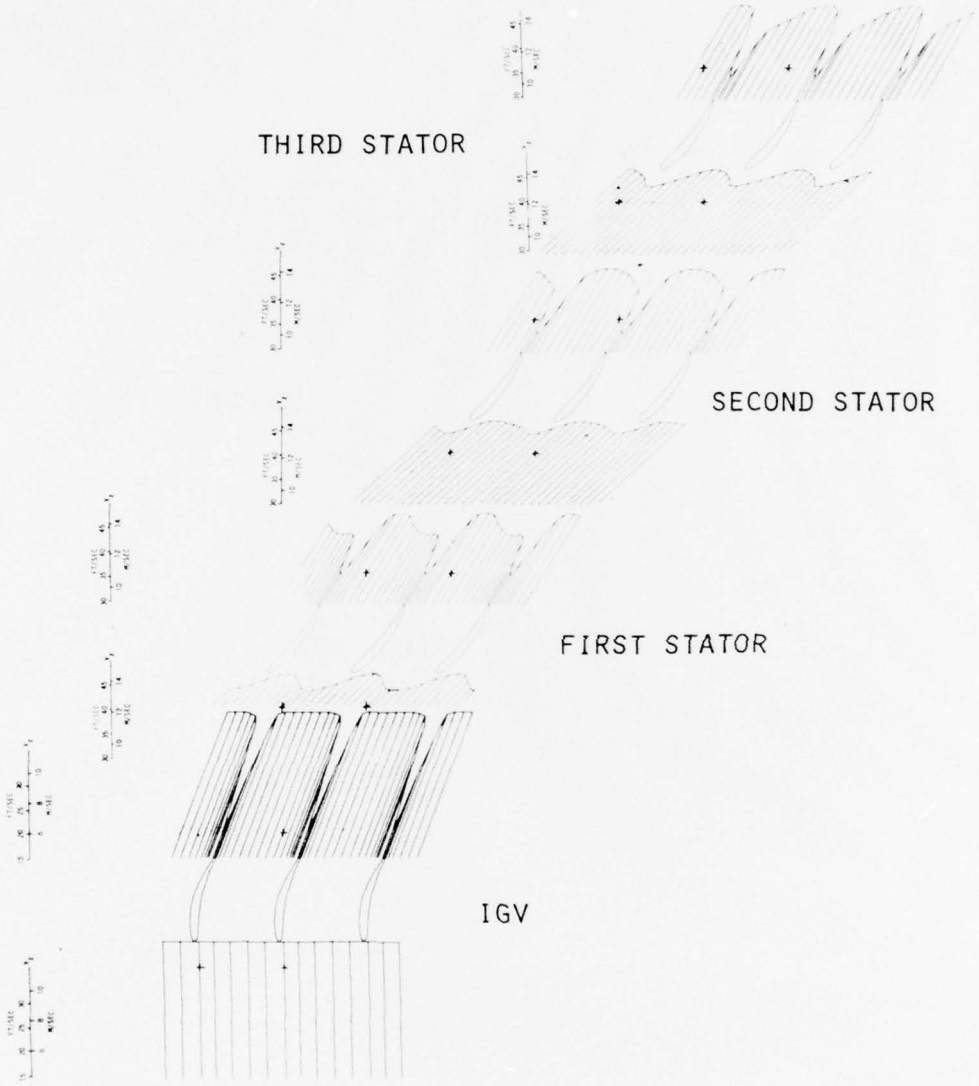
(c) 30% passage height from hub; minimum sound.

Figure 5.5. Continued.



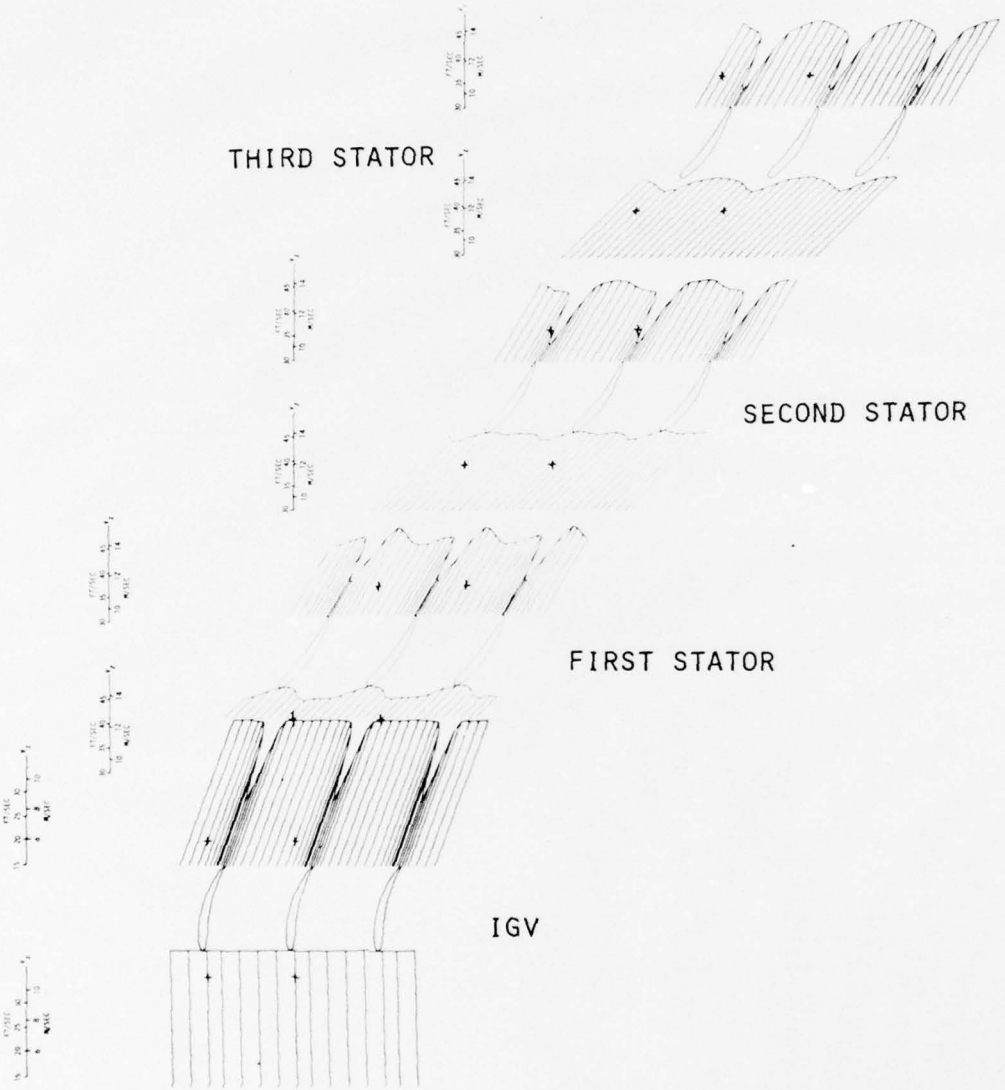
(d) 40% passage height from hub; minimum sound.

Figure 5.5. Continued.



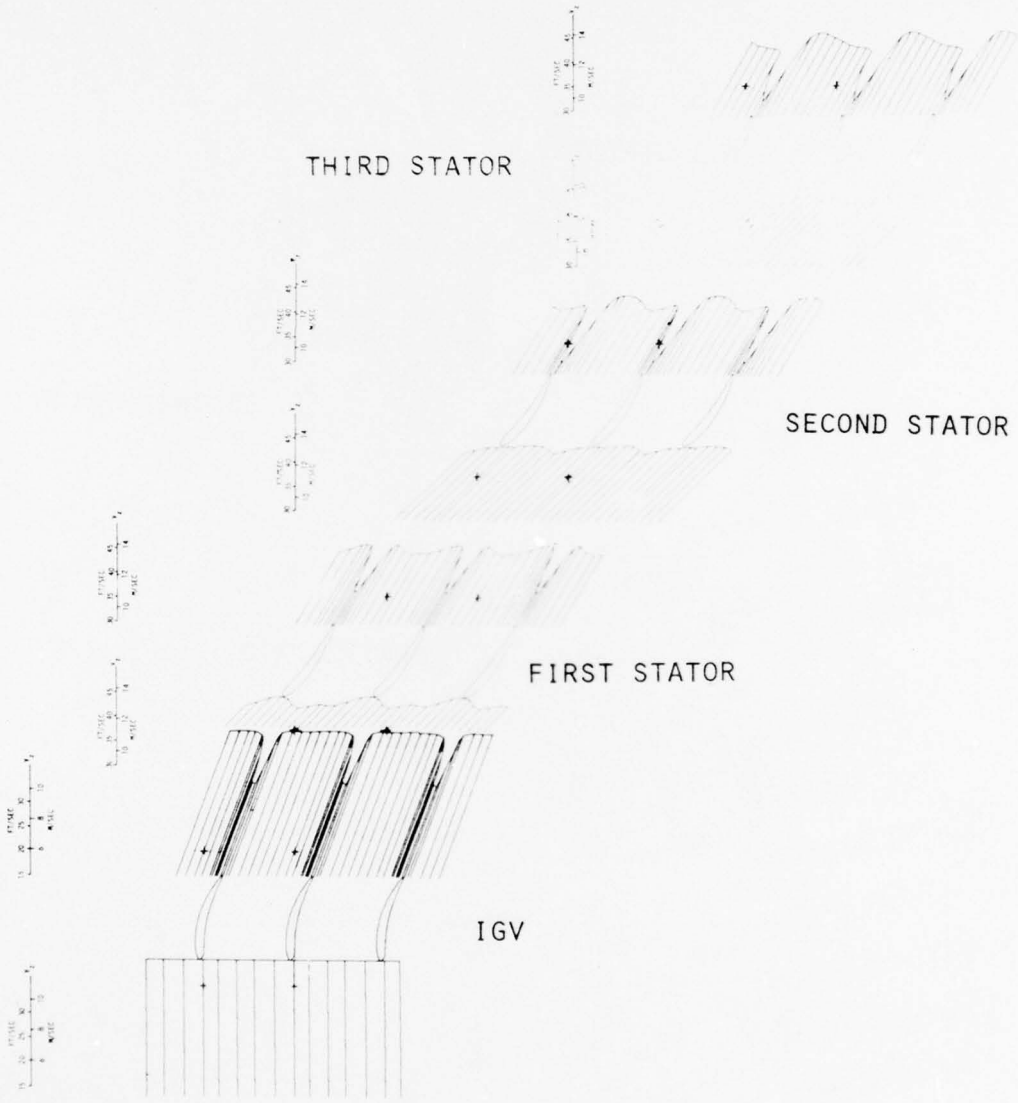
(e) 50% passage height from hub; minimum sound.

Figure 5.5. Continued.



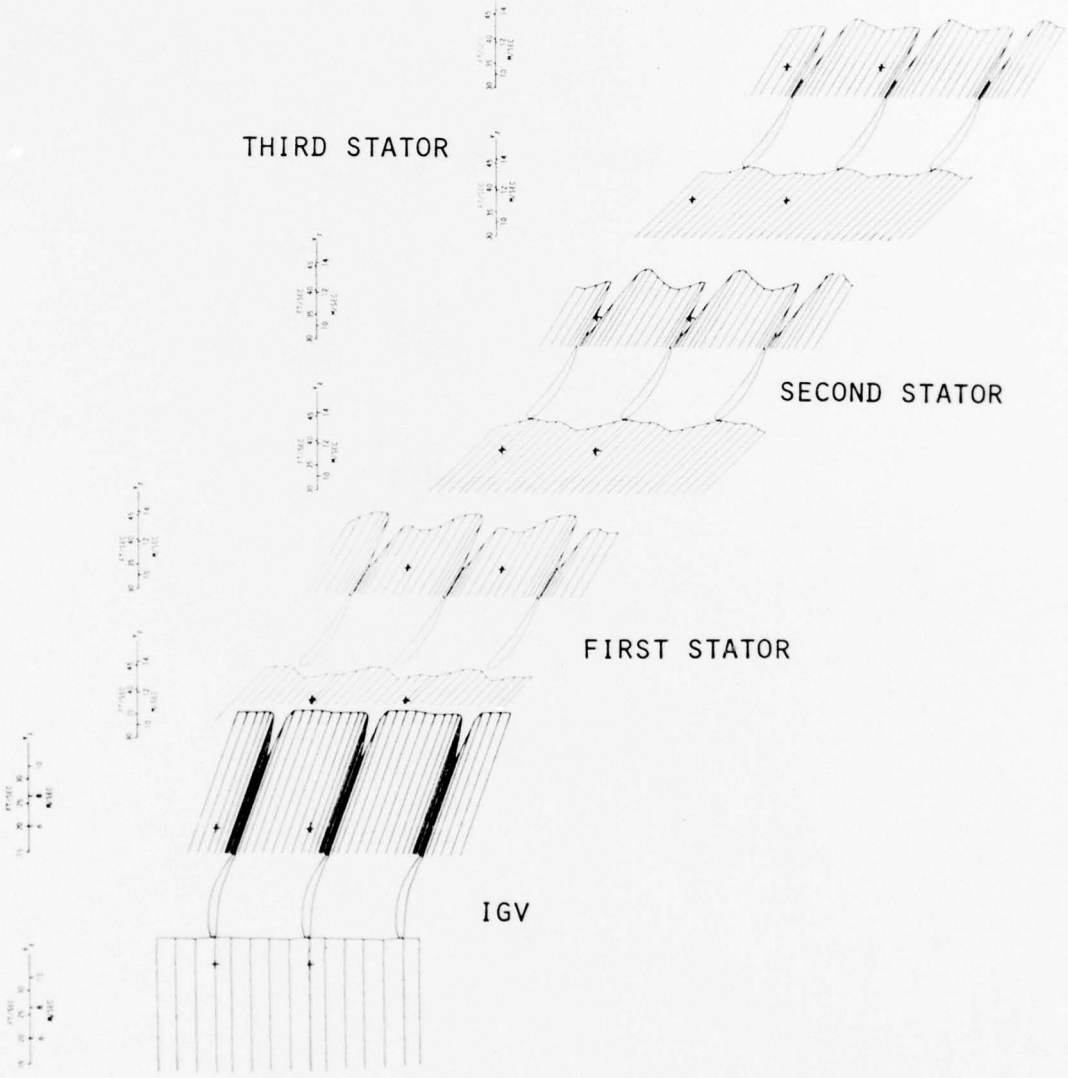
(f) 60% passage height from hub; minimum sound.

Figure 5.5. Continued.



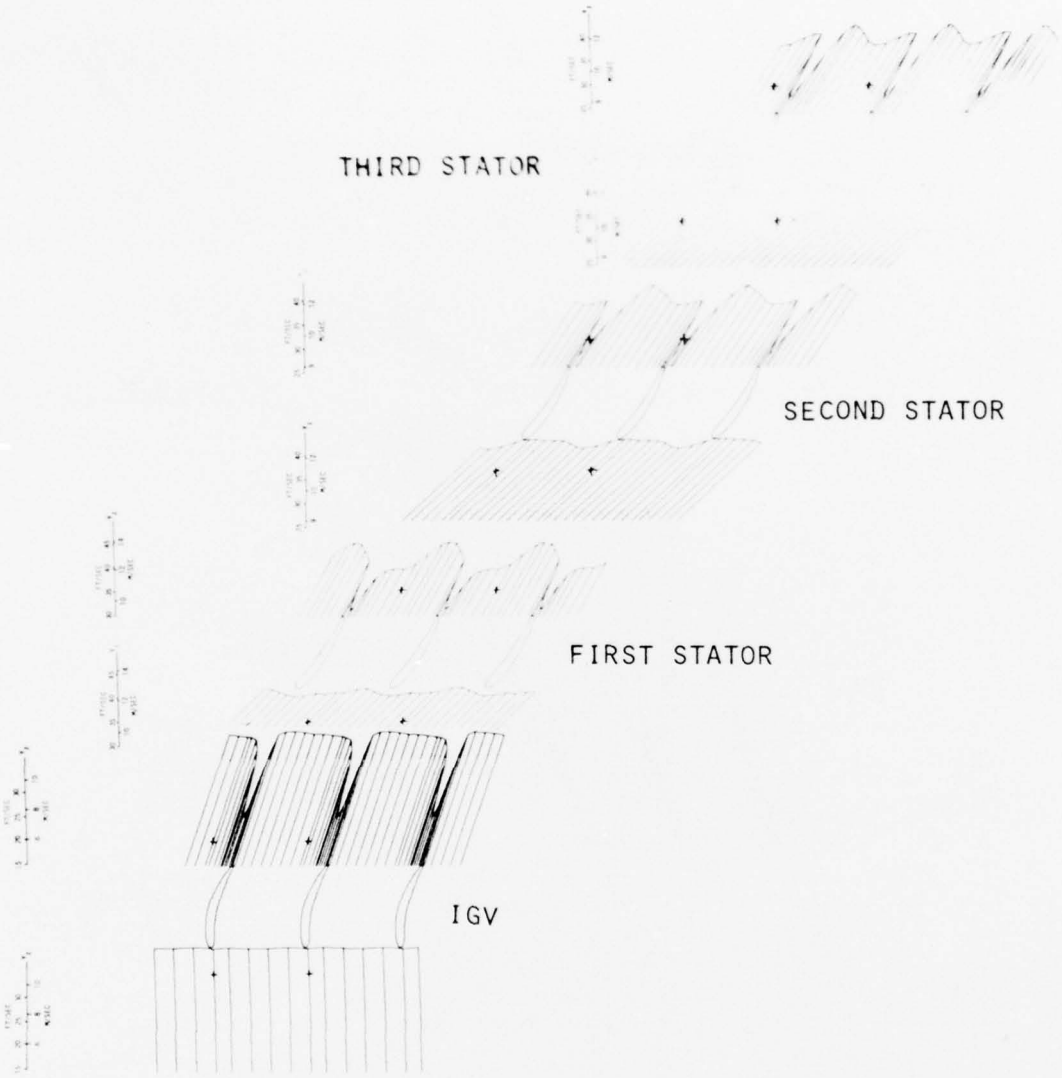
(g) 70% passage height from hub; minimum sound.

Figure 5.5. Continued.



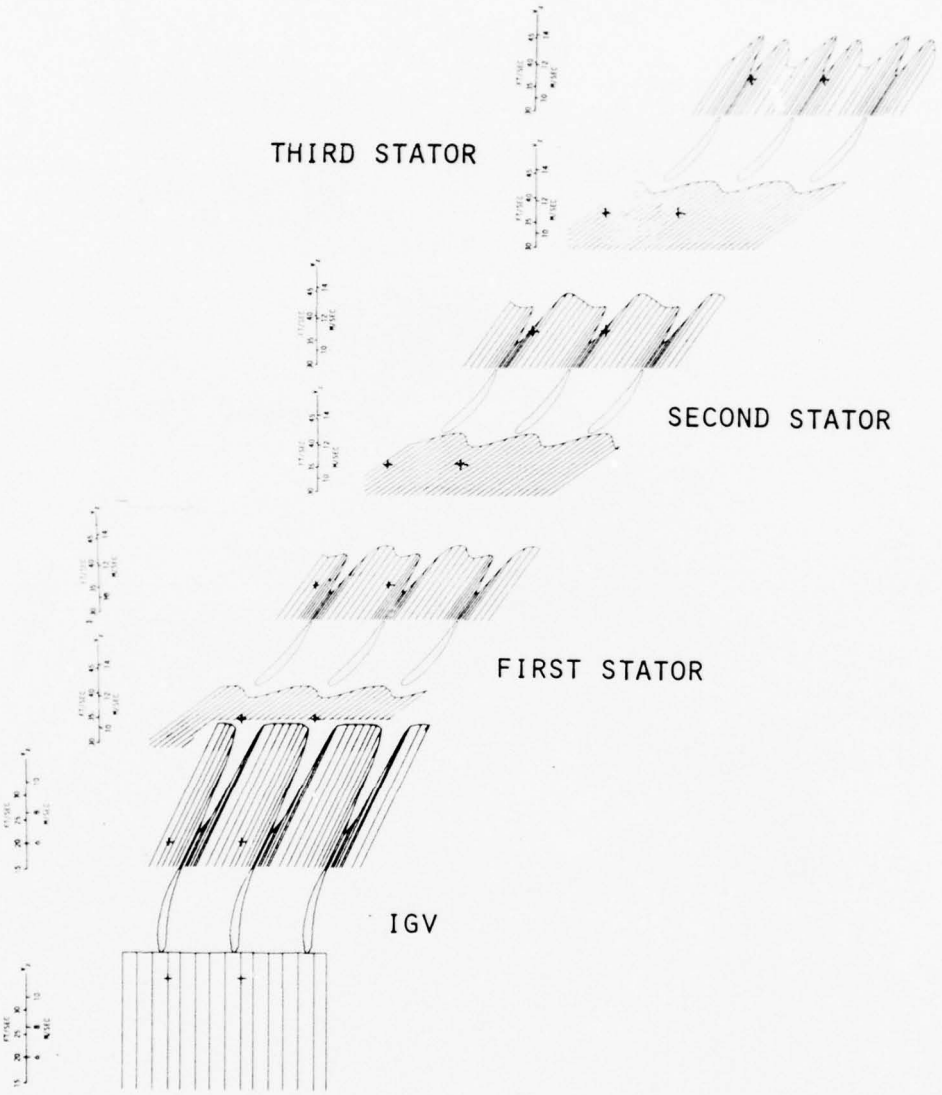
(h) 80% passage height from hub; minimum sound.

Figure 5.5. Continued.



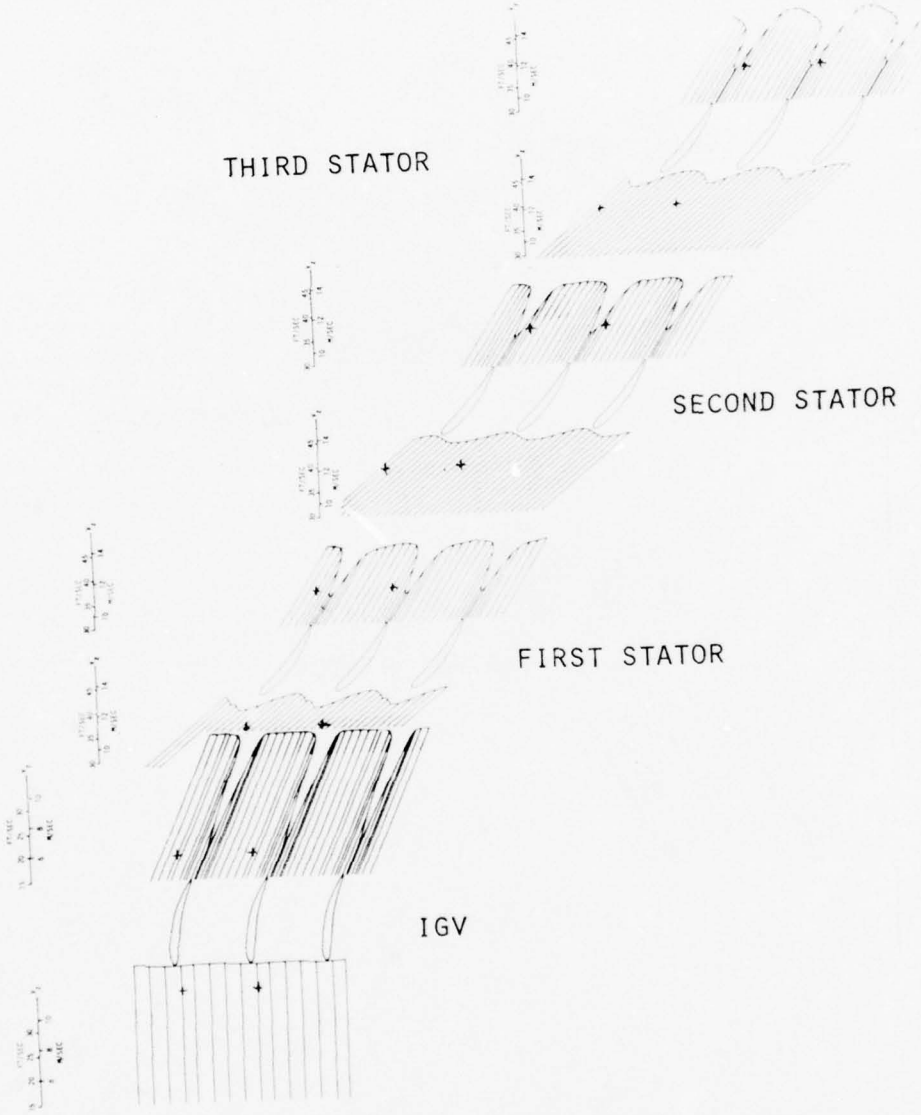
(i) 90% passage height from hub; minimum sound.

Figure 5.5. Concluded.



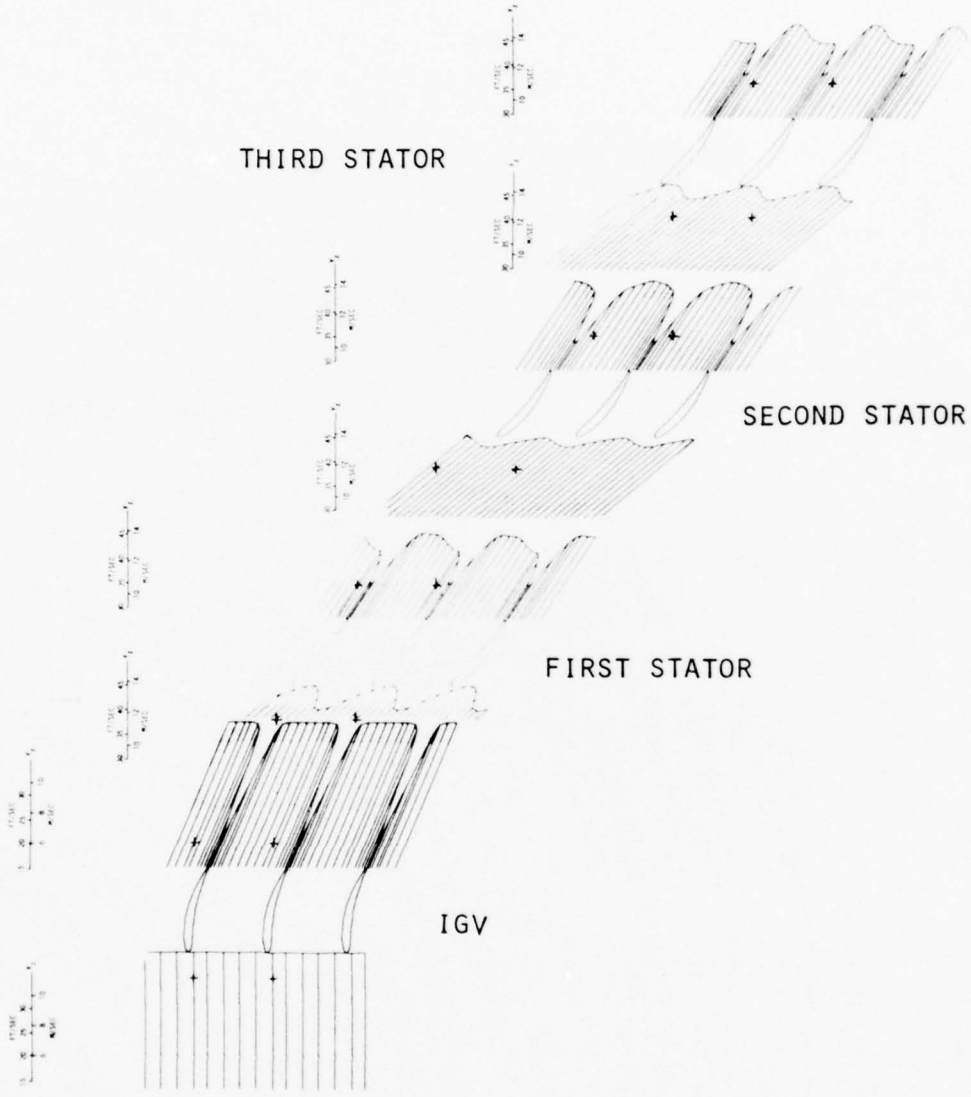
(a) 10% passage height from hub; maximum sound.

Figure 5.6. Blade-to-blade plane, time-average, velocity vector plots at constant passage height for the maximum sound blade-row schedule; constructed from slow-response data.



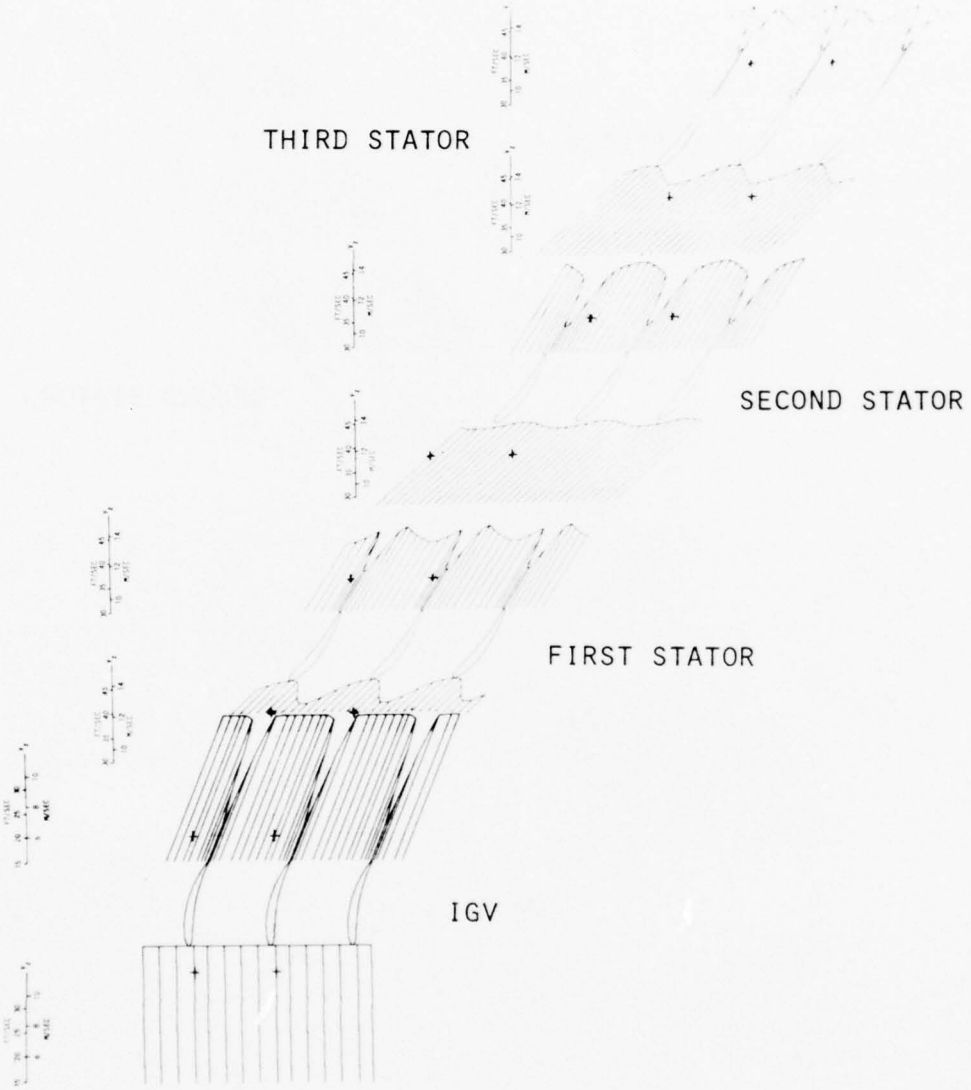
(b) 20% passage height from hub; maximum sound.

Figure 5.6. Continued.



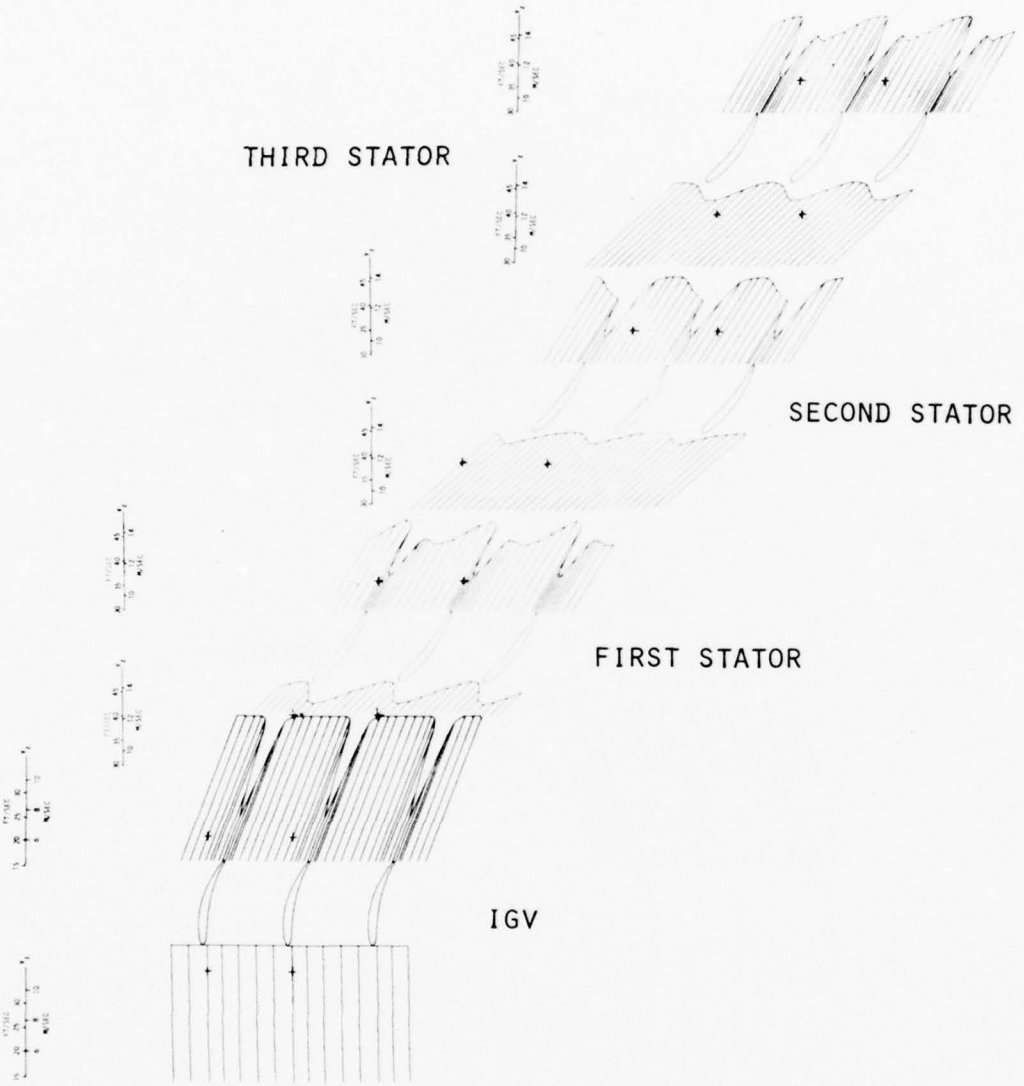
(c) 30% passage height from hub; maximum sound.

Figure 5.6. Continued.



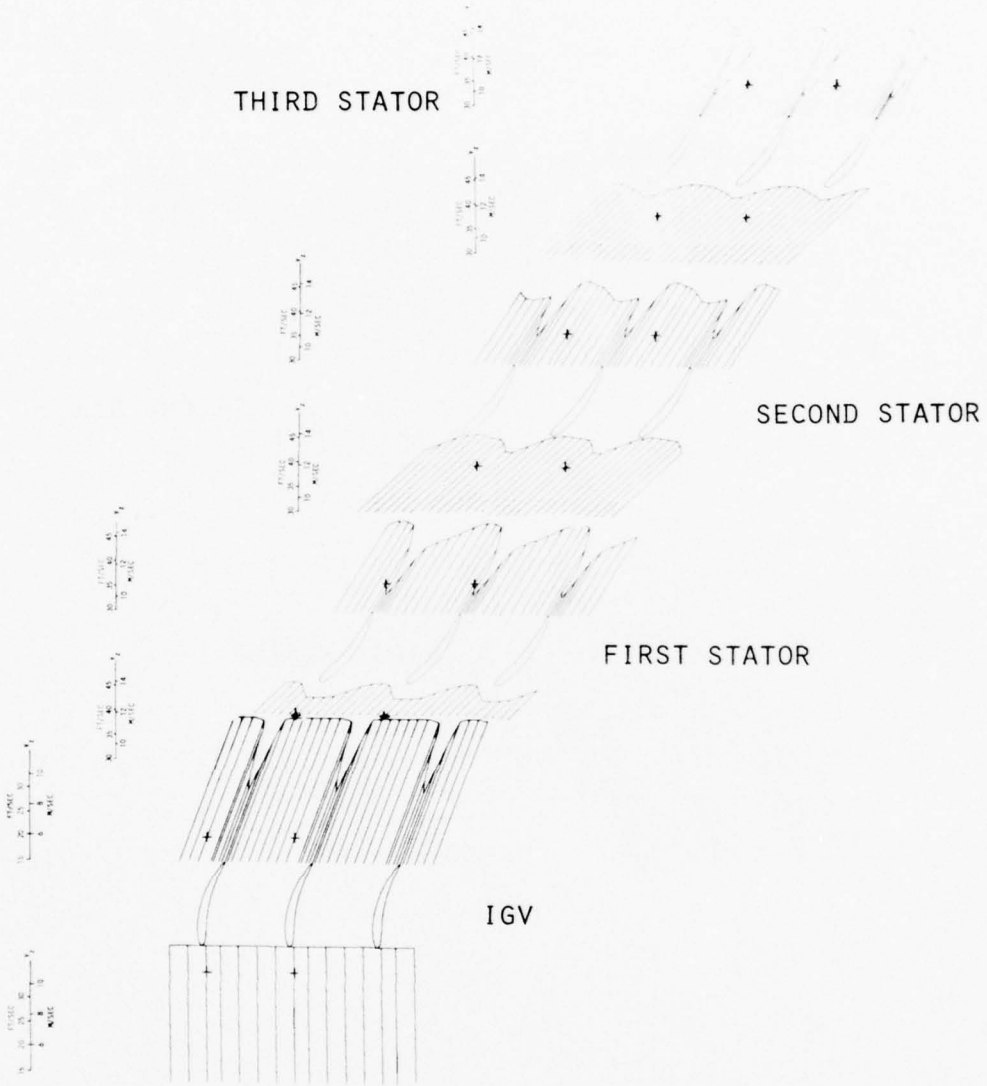
(d) 40% passage height from hub; maximum sound.

Figure 5.6. Continued.



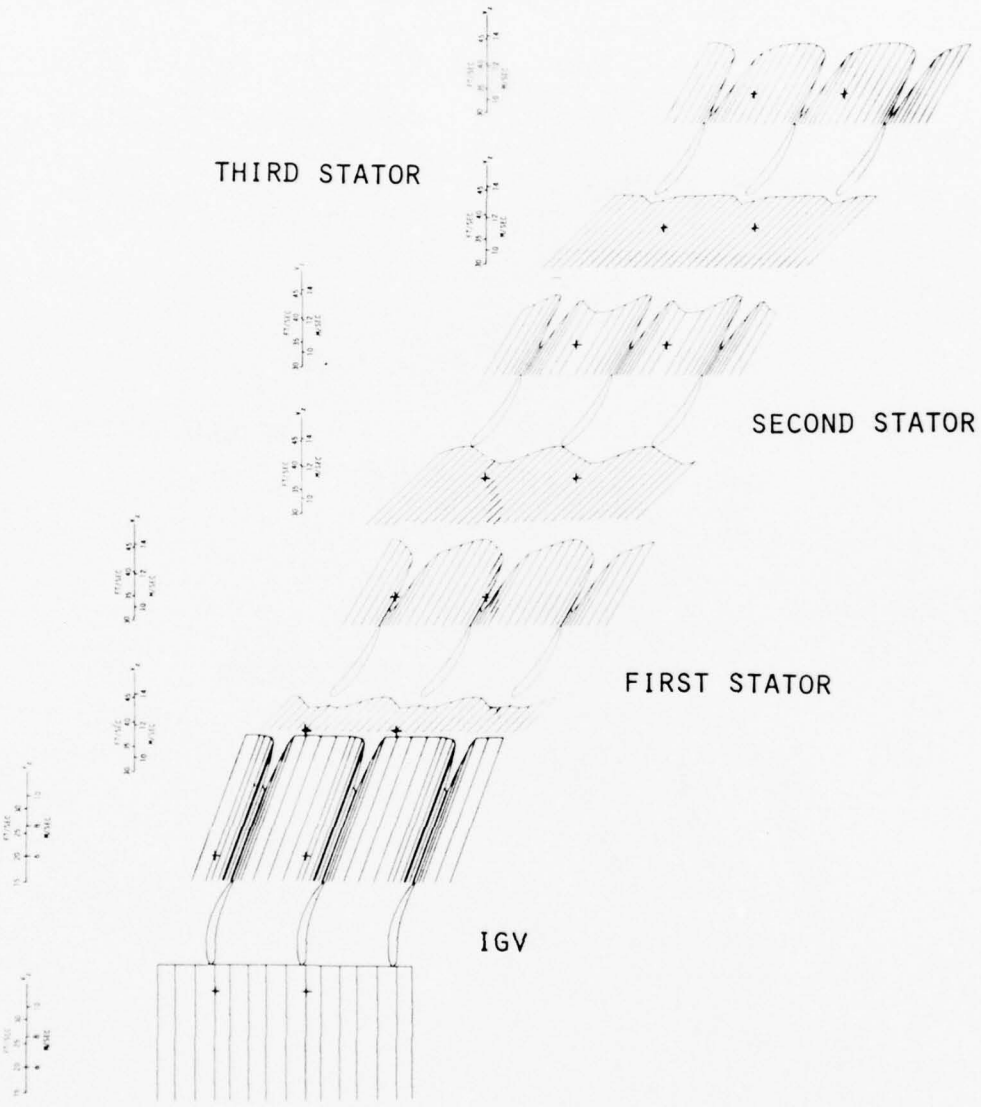
(e) 50% passage height from hub; maximum sound.

Figure 5.6. Continued.



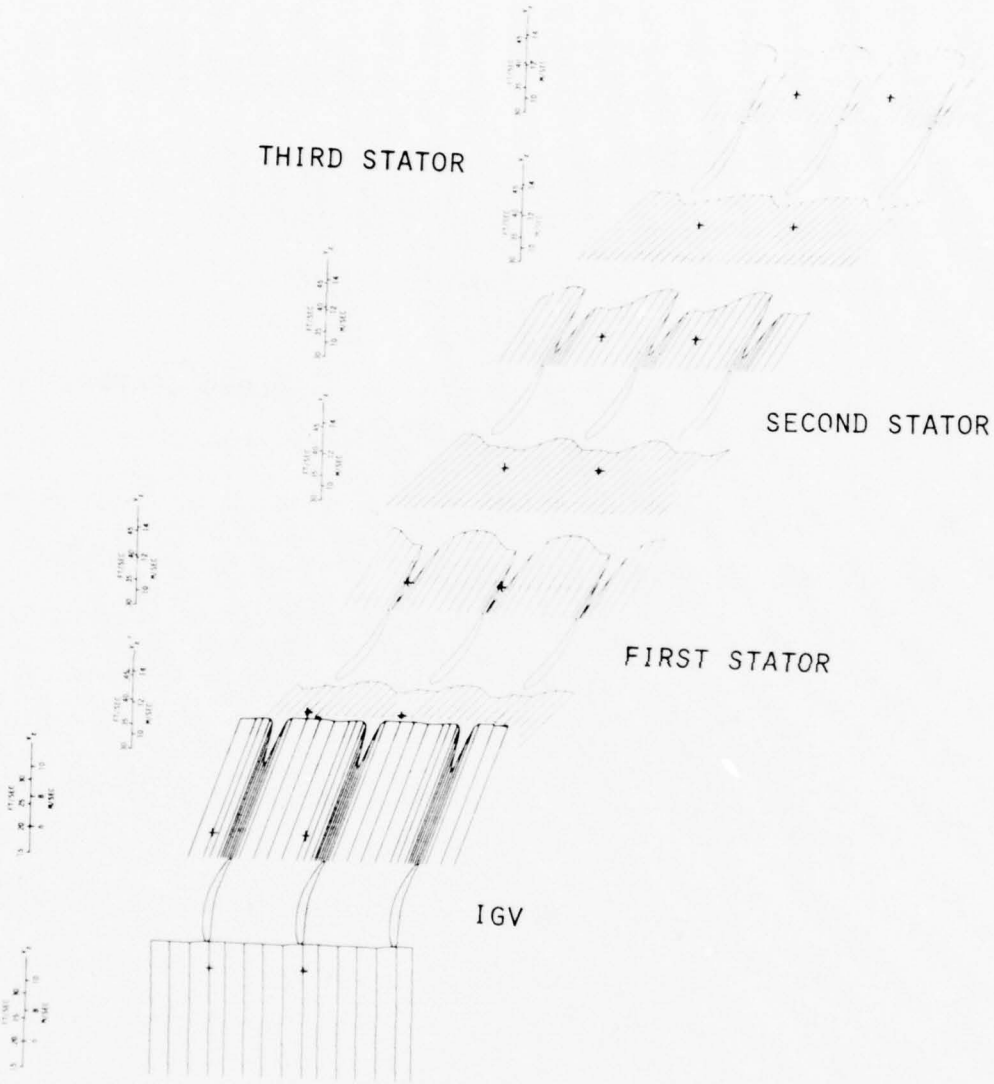
(f) 60% passage height from hub; maximum sound.

Figure 5.6. Continued.



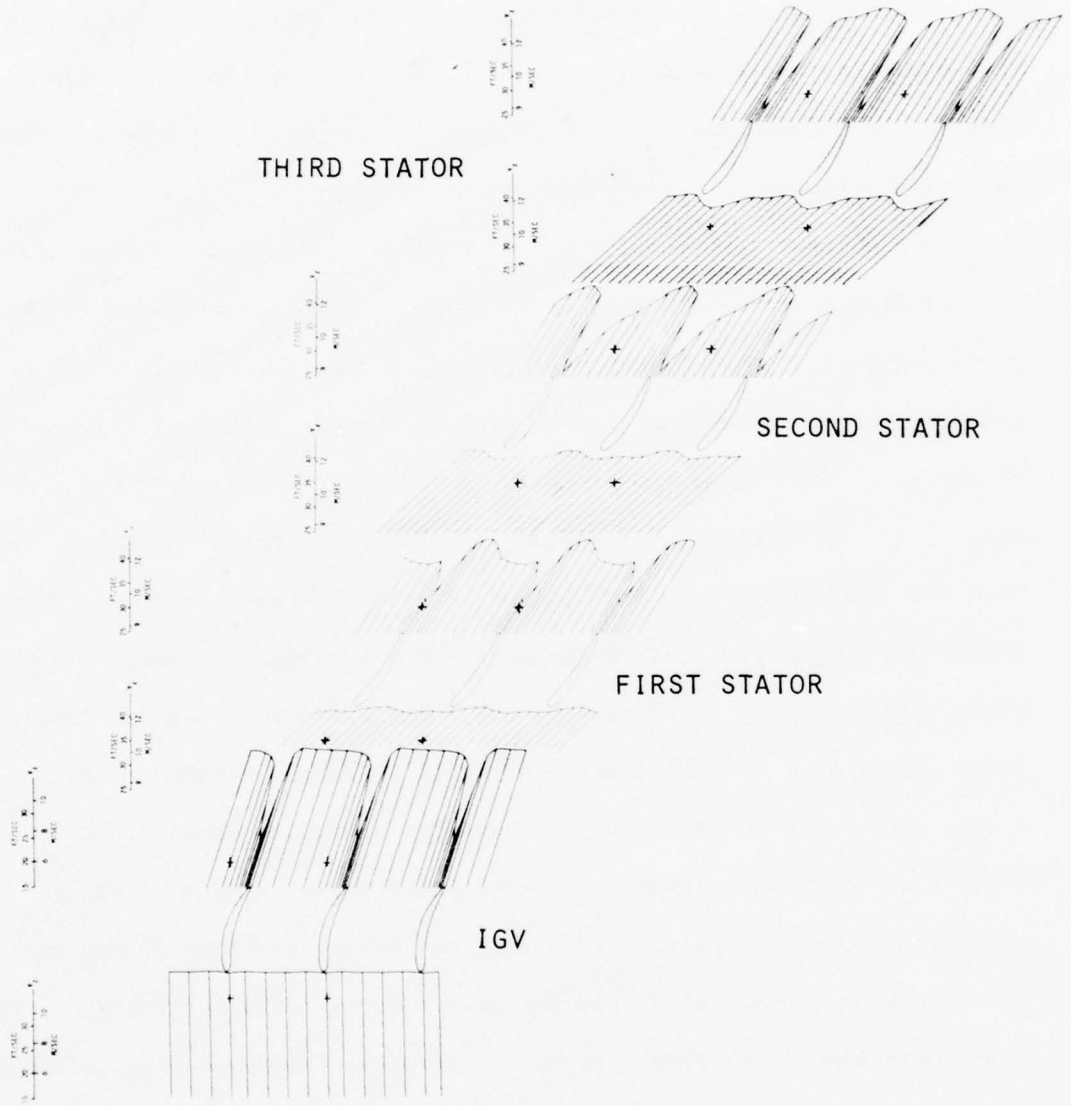
(g) 70% passage height from hub; maximum sound.

Figure 5.6. Continued.



(h) 80% passage height from hub; maximum sound.

Figure 5.6. Continued.



(i) 90% passage height from hub; maximum sound.

Figure 5.6. Concluded.

blade section size, shape, and angles are in scale with the actual blade configuration of the research compressor. Although the rotor blade profiles are not shown, the axial spacings between measurement stations are also scaled correctly. As indicated by the crosses, the vector plots were shifted circumferentially by one or more stator pitch distance increments to increase the effectiveness of the combined plots.

Some observations about the slow-response instrument average stationary flow patterns are apparent from the blade-to-blade velocity vector plots. The stationary flow pattern could be changed appreciably in regions of the compressor annulus by varying the circumferential positions of the stationary blade rows relative to each other. Figures 5.5 and 5.6 show that throughout a large portion of the compressor annulus, the wakes from the stationary blade rows influenced the flow downstream of the next rotor even though the stationary blade row wakes were attenuated to a large extent as they moved through the rotor blade row. As observed by Smith (2), this substantial attenuation is expected because of the unequal energy addition and the dispersive chopping action involved within the rotor rows. Further, these stationary blade row wake streets exiting from the rotors were attenuated very little as they passed through the next downstream stationary blade row and were a discernable influence on the stationary blade exit flow. In most instances, the shape of a stator exit flow field was dependent on the position of that stator blade leading edge relative to the incoming stationary periodic flow pattern, as can be seen, for example, when comparing the first stator exit flow fields in Figures 5.5d and 5.6d (40% span). In general, if a stator blade leading edge was positioned within the incoming stationary wake street, identified as the

region of lower velocity (see for example the first stator flow in Fig. 5.5c), that stator blade produced a deeper velocity wake ("wakes together" type profile) than if the stator blade leading edge was moved out of the wake street ("wakes apart" type profile). When a stator blade leading edge was positioned out of the incoming wake street region (see for example the first stator flow in Figure 5.6d), the velocity deficit at that stator inlet could be identified in the stator exit freestream region. Also, by changing the circumferential position of one blade row, the flow pattern could in some instances be modified more than one blade row downstream. For example, comparison of Figures 5.5f and 5.6f indicates a change in the flow field behind the second rotor due to a change in the relative circumferential position between the IGV and first stator blade rows. Further, this change in the flow field behind the second rotor affected the flow field of the second stator. The data also make evident the fact that stationary interaction patterns changed with radius. For example, the stationary circumferential position of the wake street at a rotor exit varied with blade span. In general, the circumferentially periodic flow patterns at the inlet to a stator row were in circumferential phase at two span locations resulting in similar stator exit flow profiles at those two spanwise positions (e.g., compare Figures 5.5b and 5.5g).

The spanwise distribution of circumferential-average flow field parameters ahead of and behind each of the blade rows are shown in Figures 5.7 through 5.11. These results should be interpreted with the uncertainty levels listed in Table 5.3 in mind. The parameter precision bounds were based on the uncertainties associated with determining total

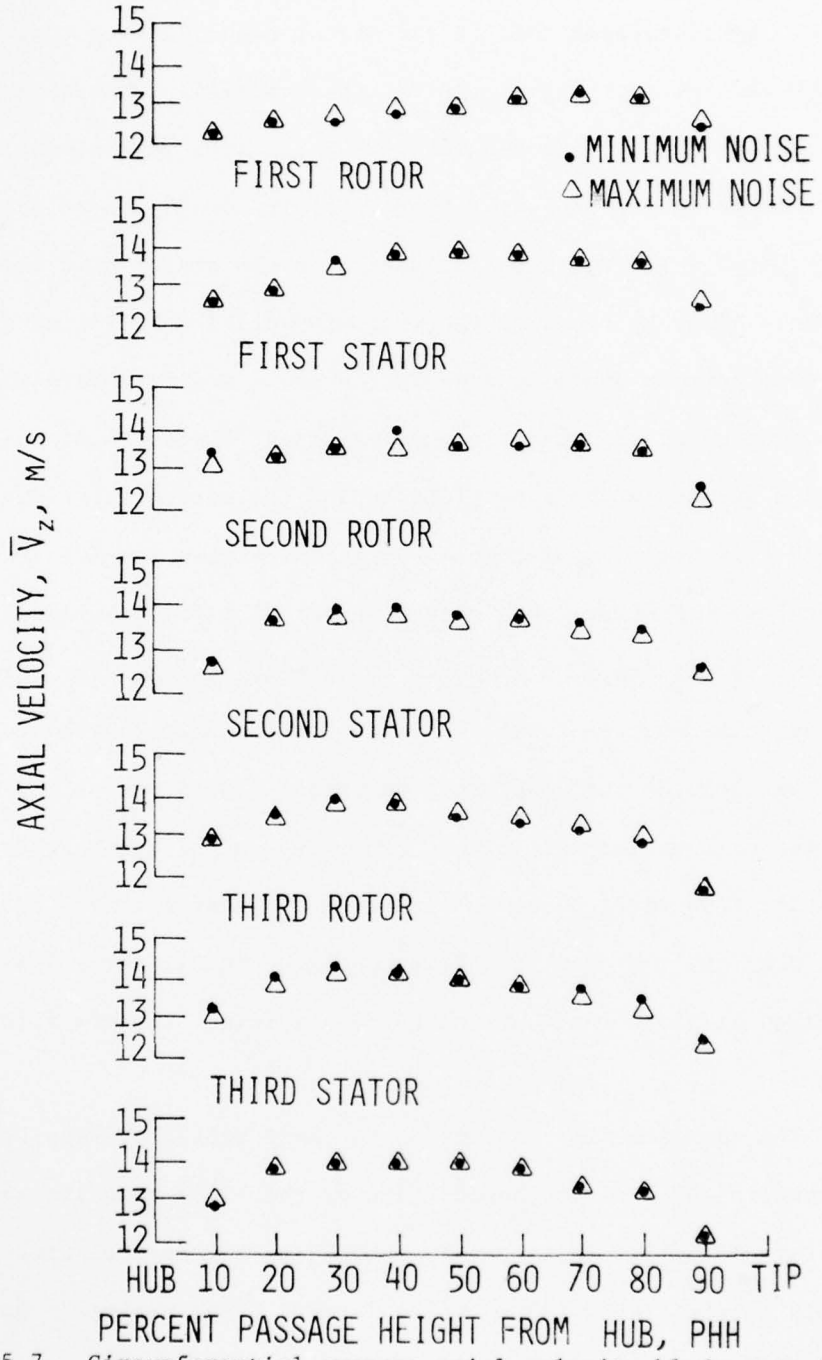


Figure 5.7. Circumferential-average axial velocity blade span distribution.

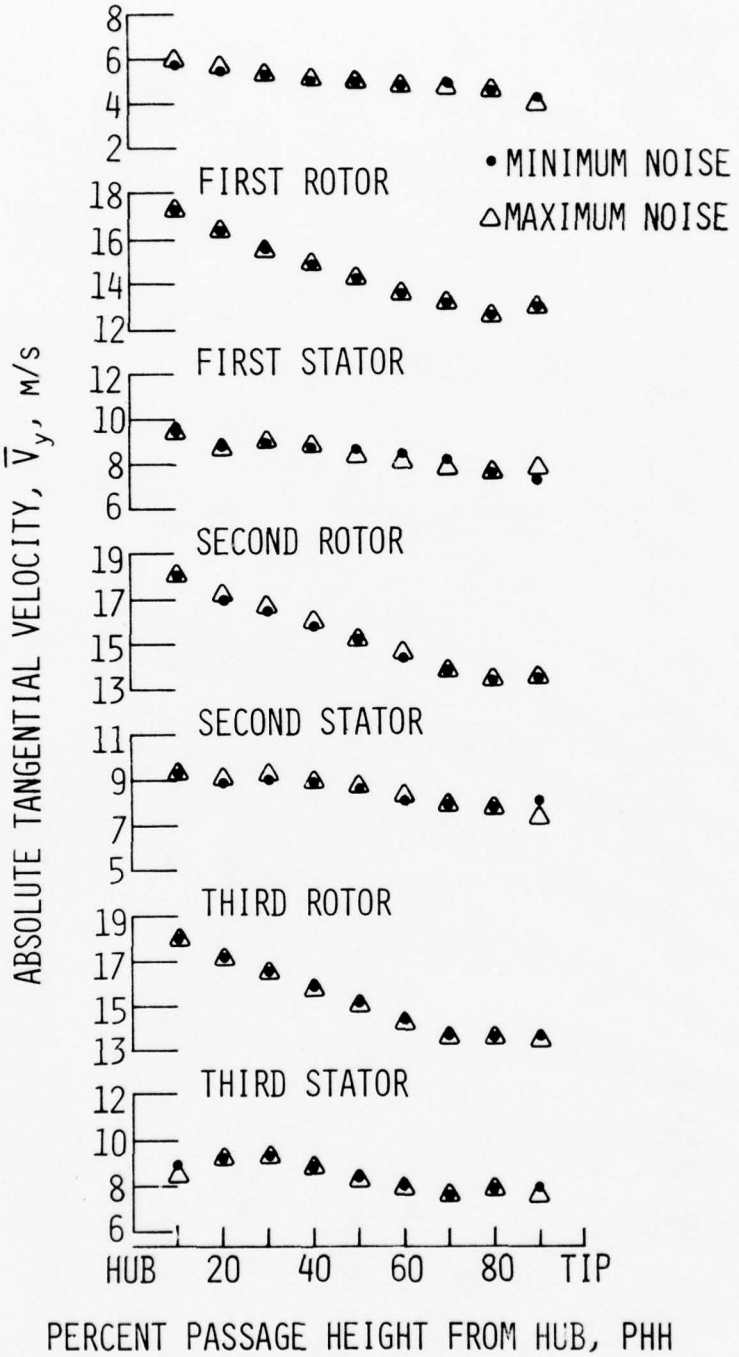


Figure 5.8. Circumferential-average absolute tangential velocity blade span distribution.

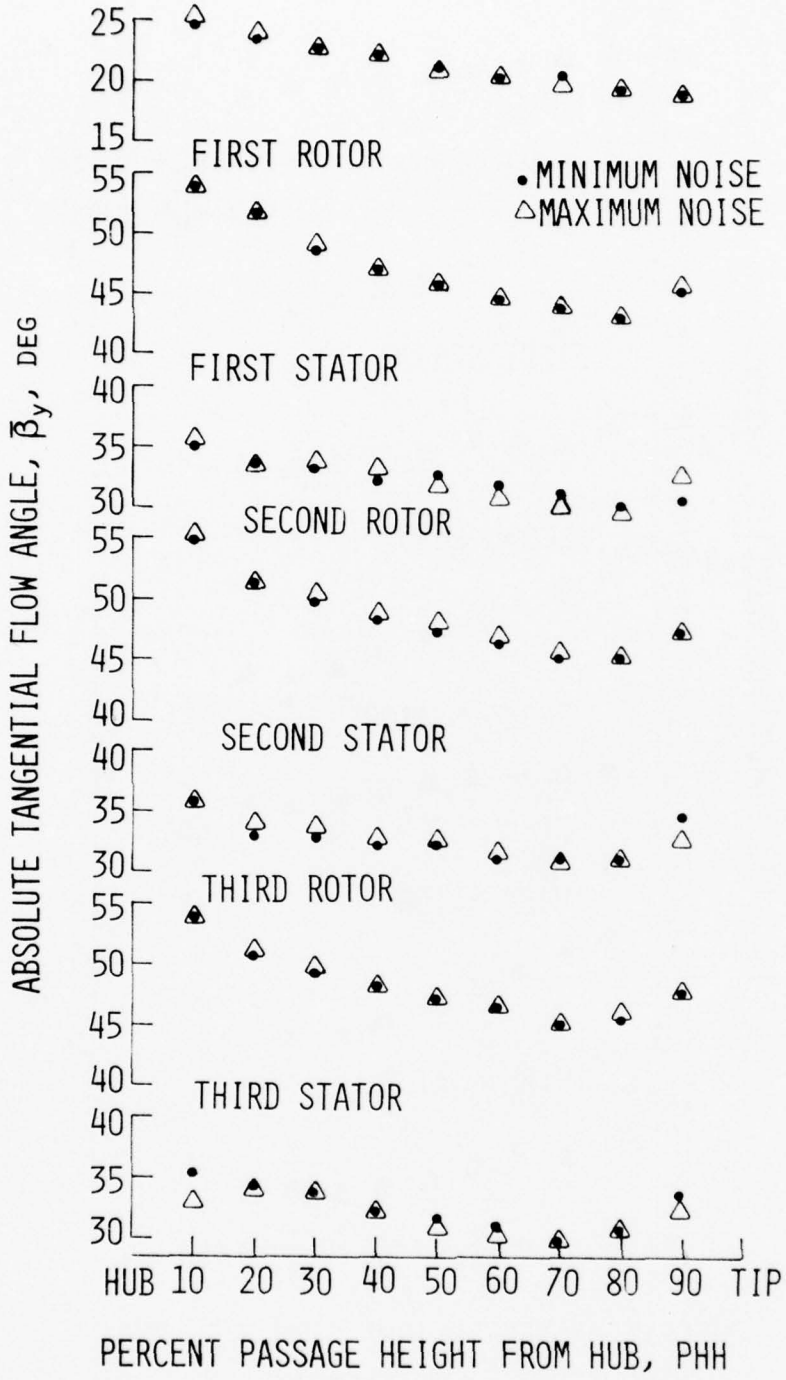
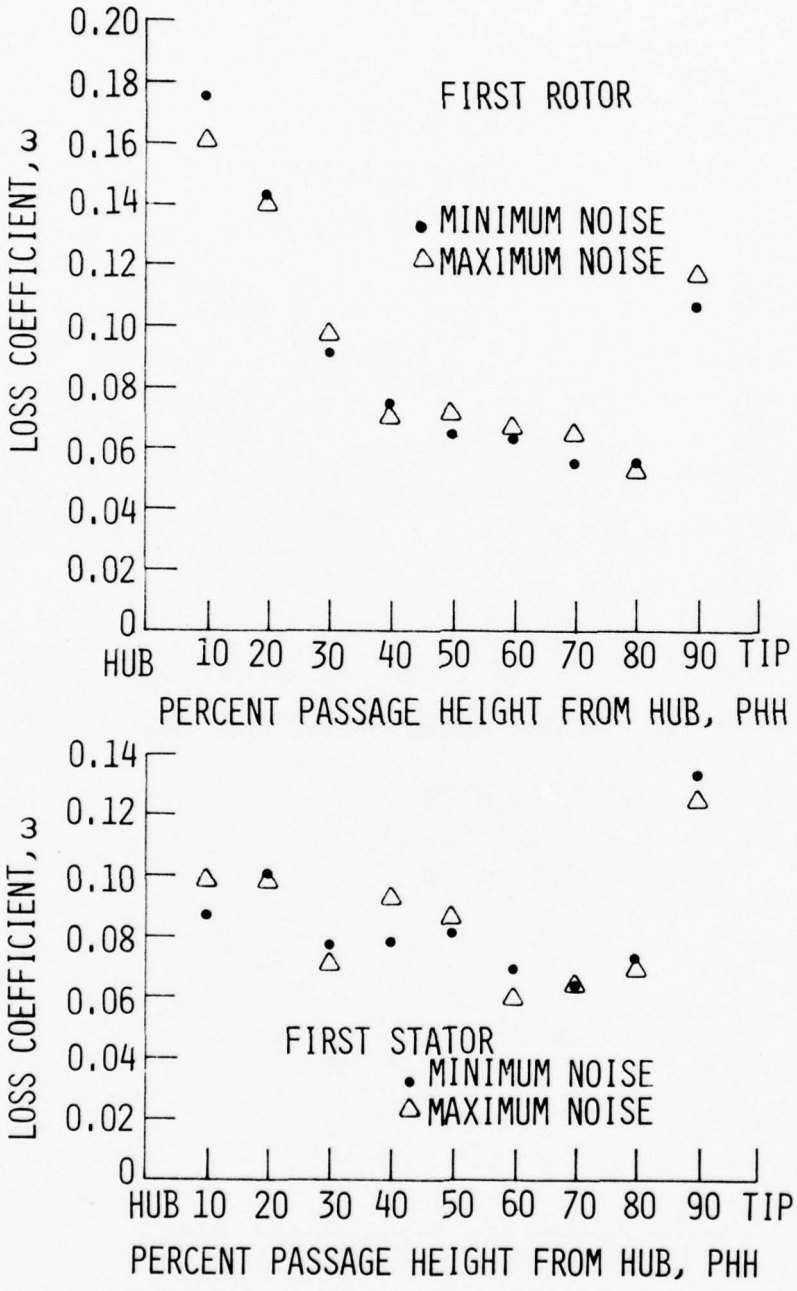
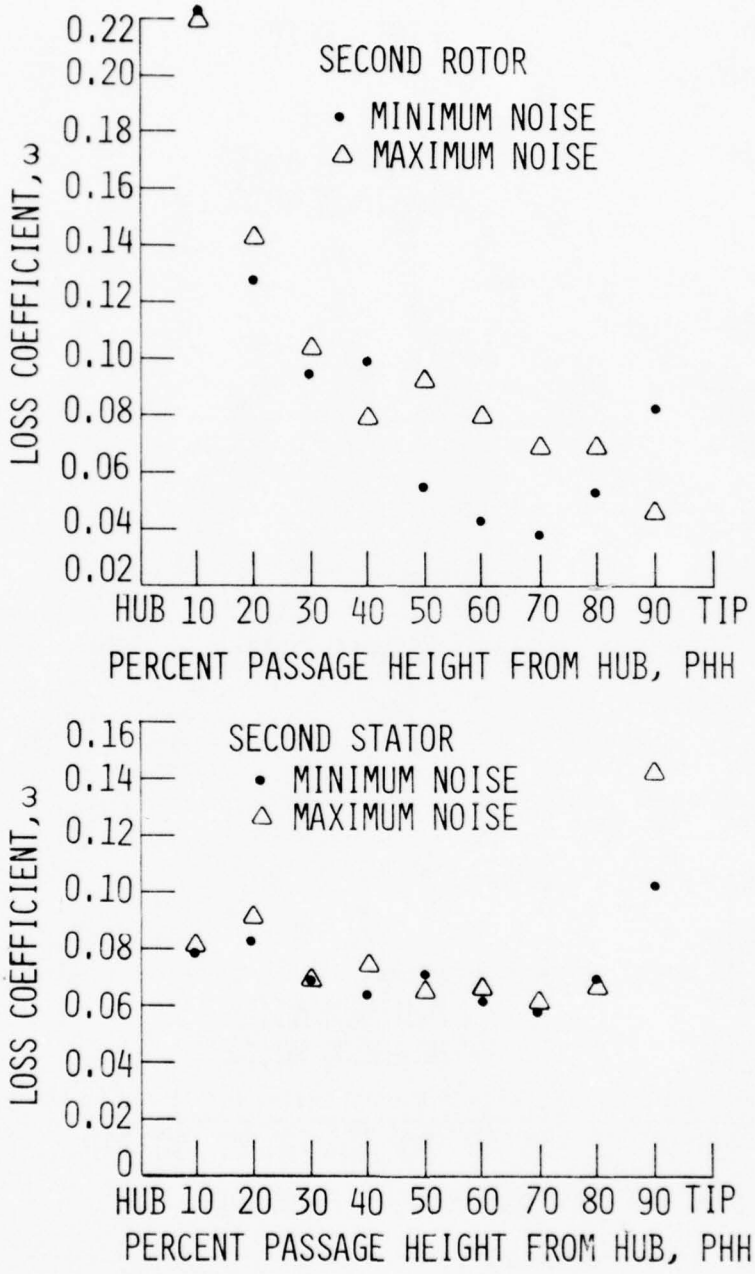


Figure 5.9. Circumferential-average absolute tangential flow angle blade span distribution.



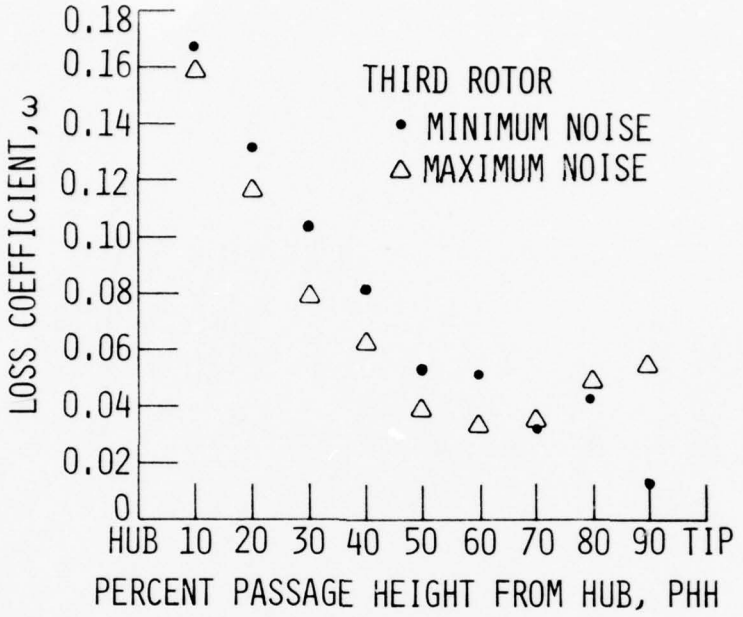
(a) First rotor and first stator.

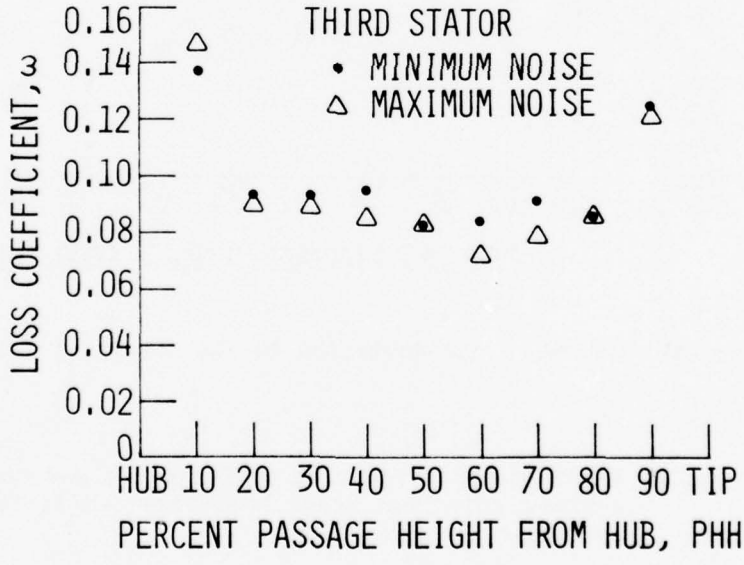
Figure 5.10. Blade span distribution of total-head loss coefficient for rotor and stator blade rows.



(b) Second rotor and second stator.

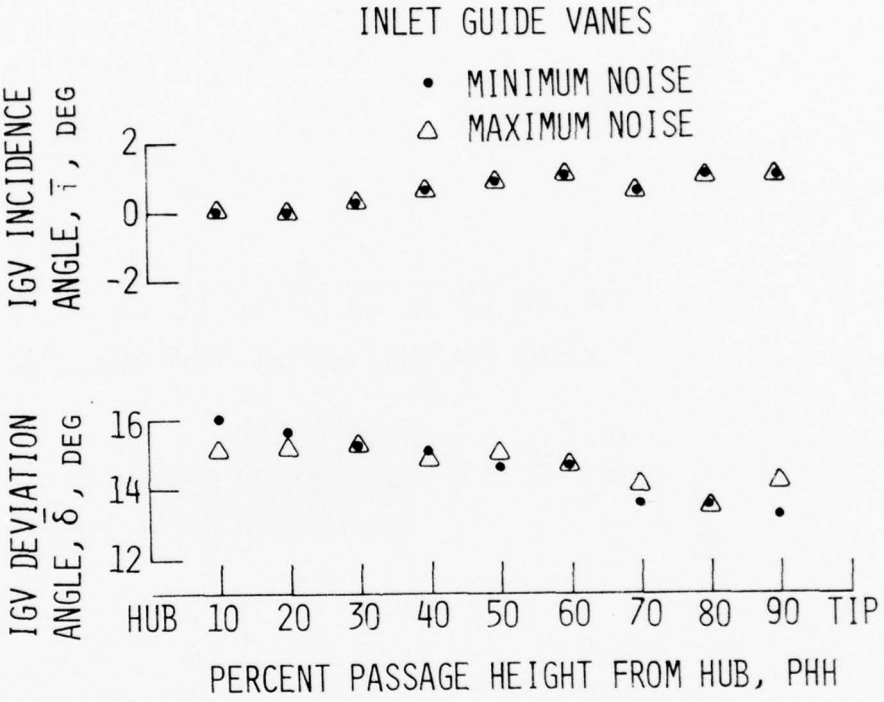
Figure 5.10. Continued.





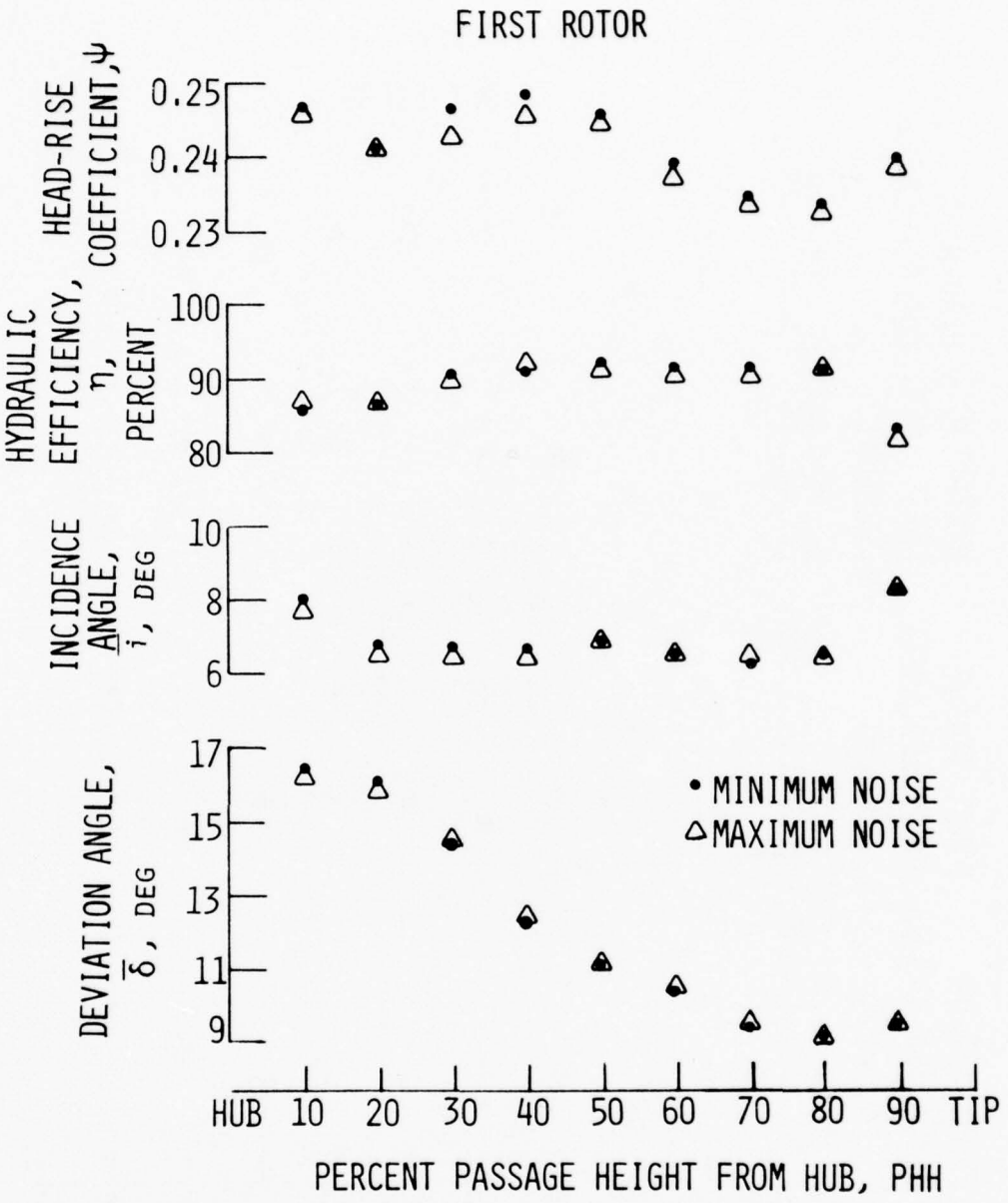
(c) Third rotor and third stator.

Figure 5.10. Concluded.



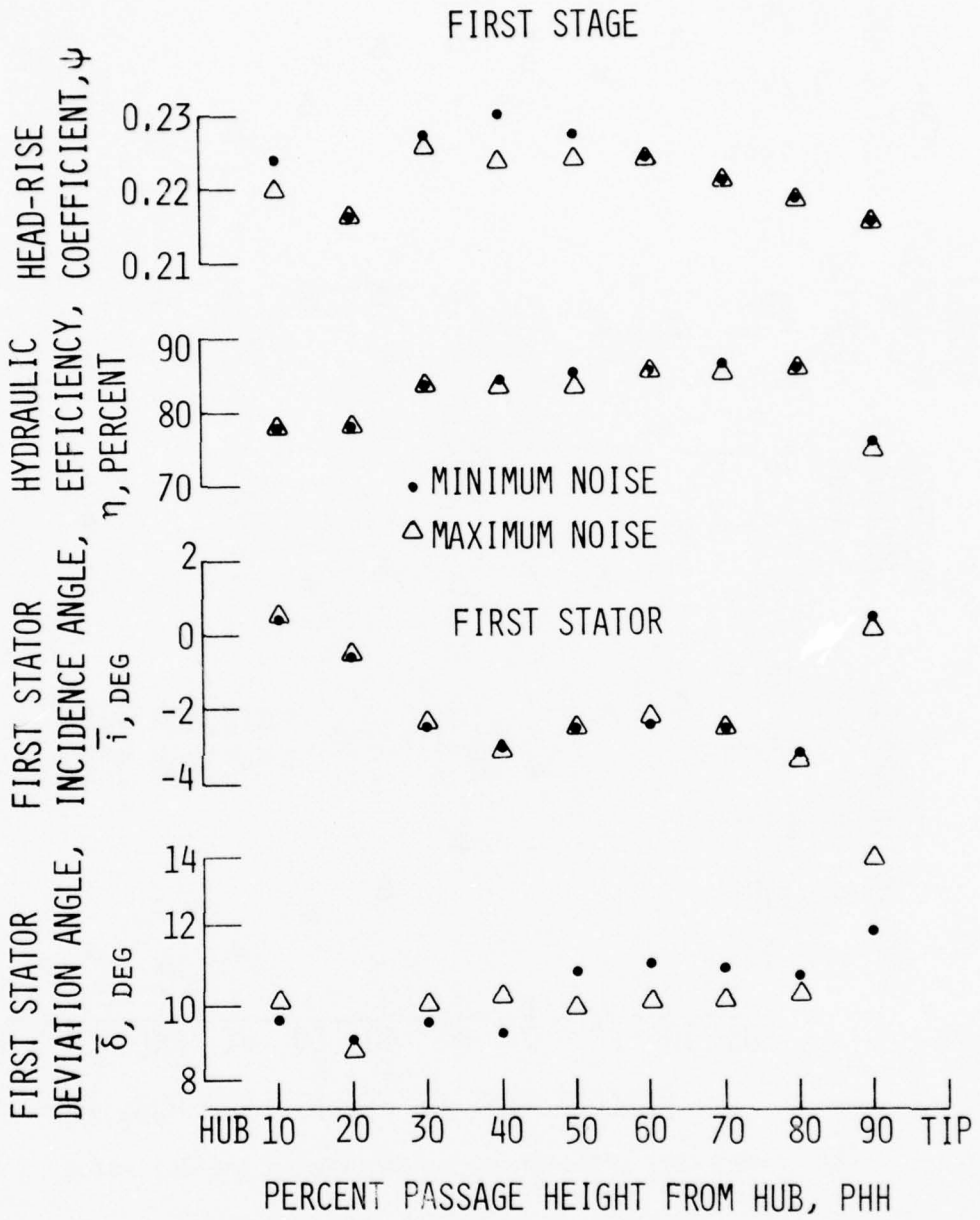
(a) Incidence and deviation angles for inlet guide vanes.

Figure 5.11. Blade span distribution of incidence and deviation blade angles, rotor and stage head-rise coefficient and hydraulic efficiency.



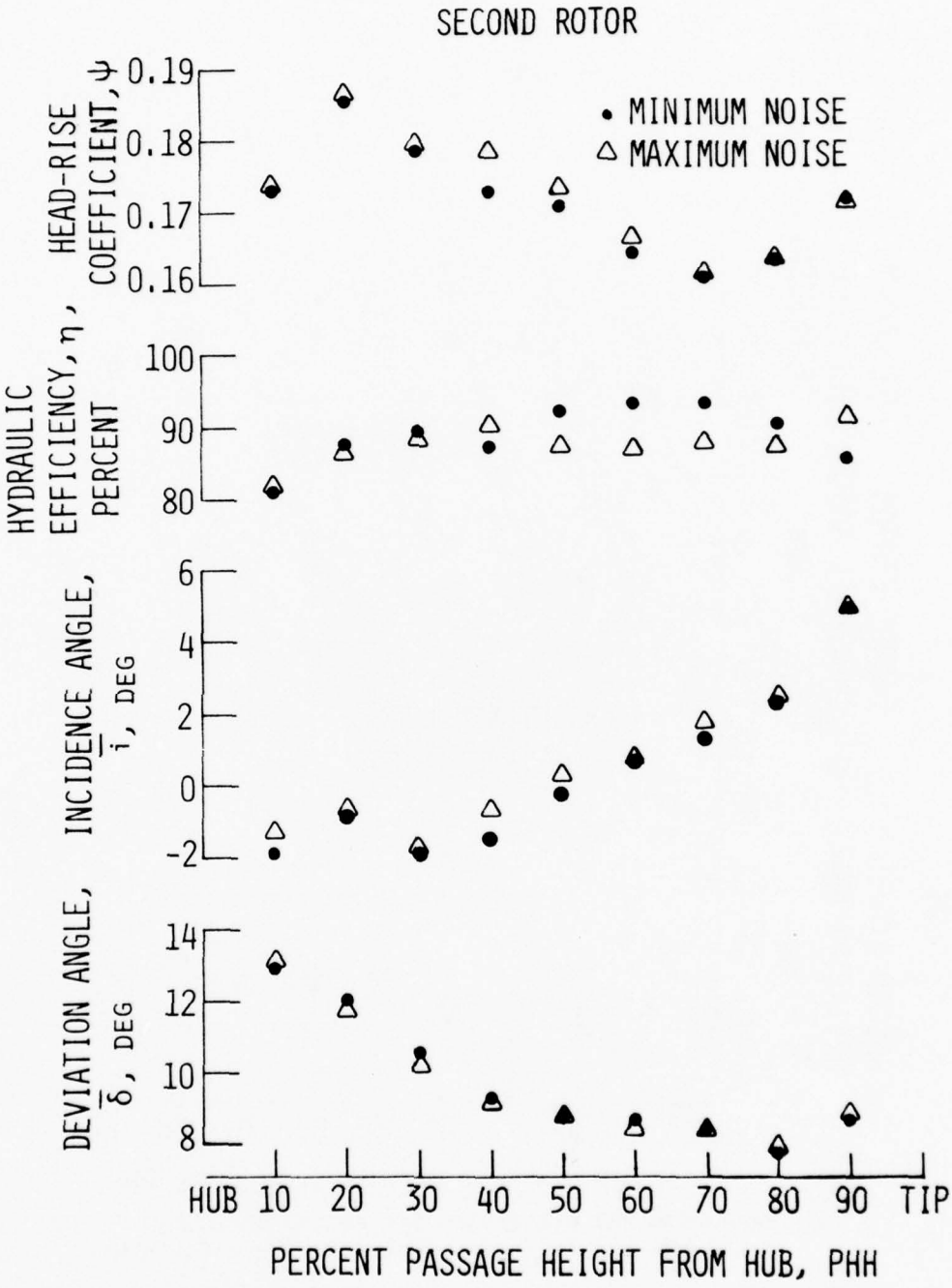
(b) Head-rise, efficiency, and incidence and deviation angles for first rotor.

Figure 5.11. Continued.



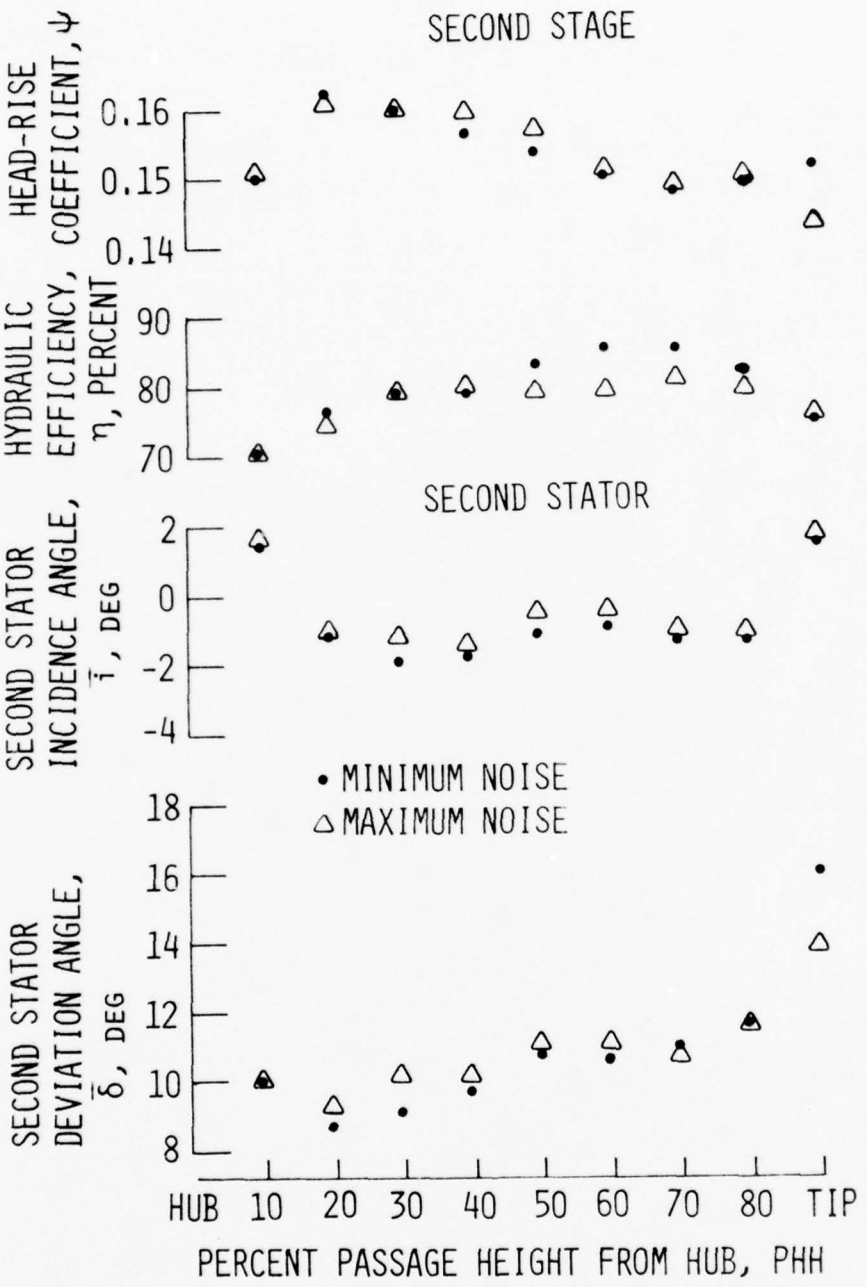
(c) Head-rise and efficiency for first stage and incidence and deviation angles for first stator.

Figure 5.11. Continued.



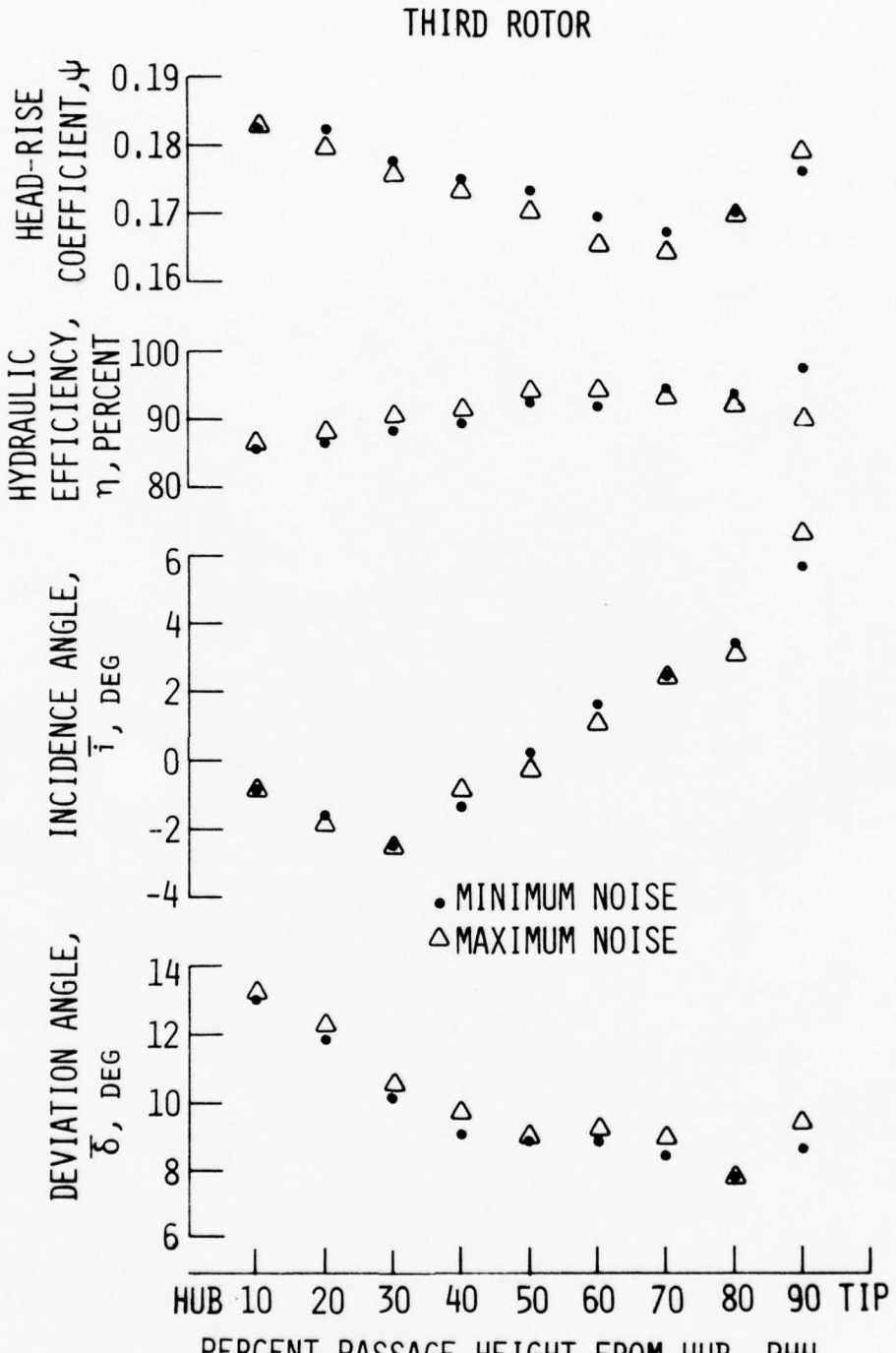
(d) Head-rise, efficiency, and incidence and deviation angles for second rotor.

Figure 5.11. Continued.



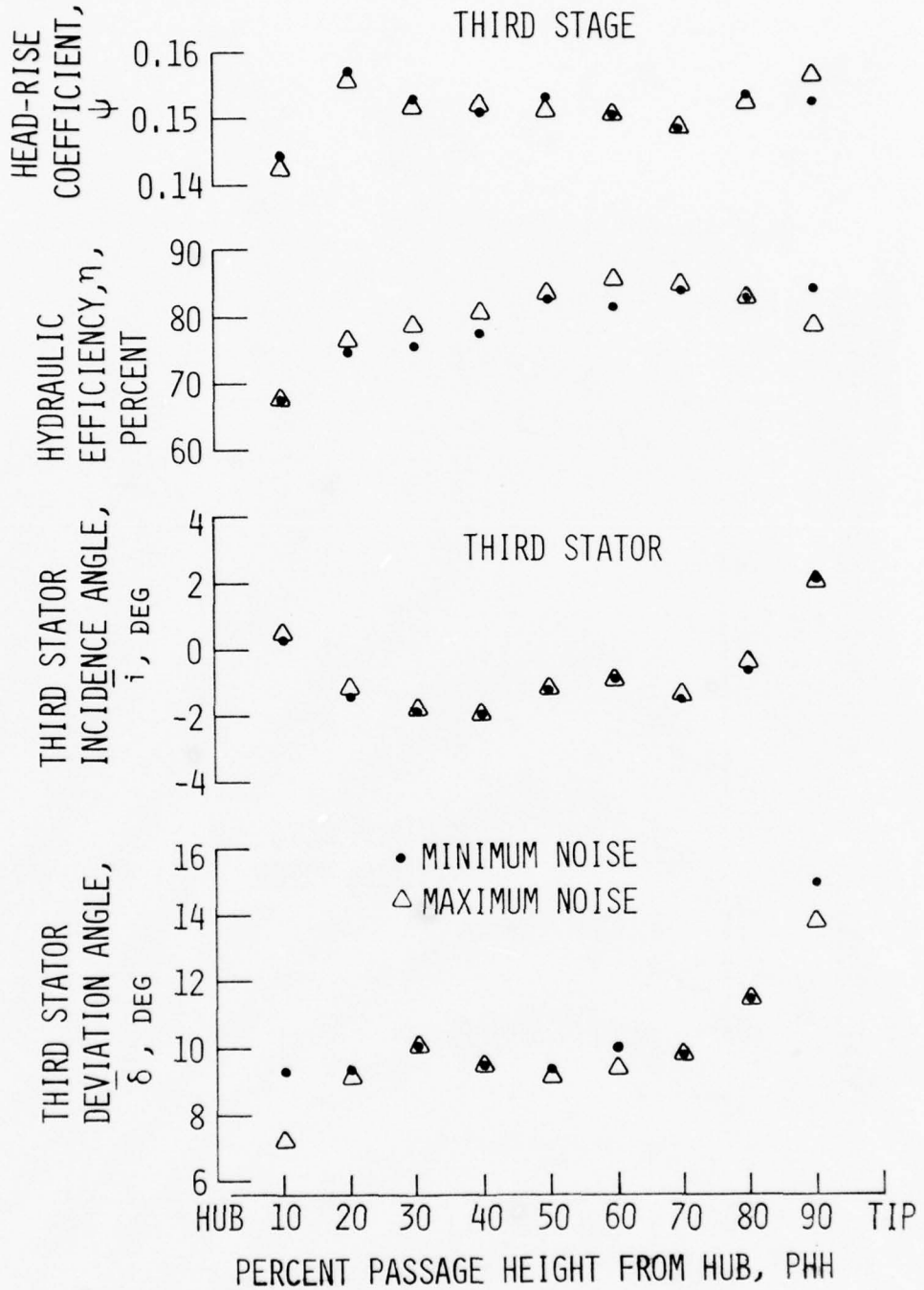
(e) Head-rise and efficiency for second stage and incidence and deviation angles for second stator.

Figure 5.11. Continued.



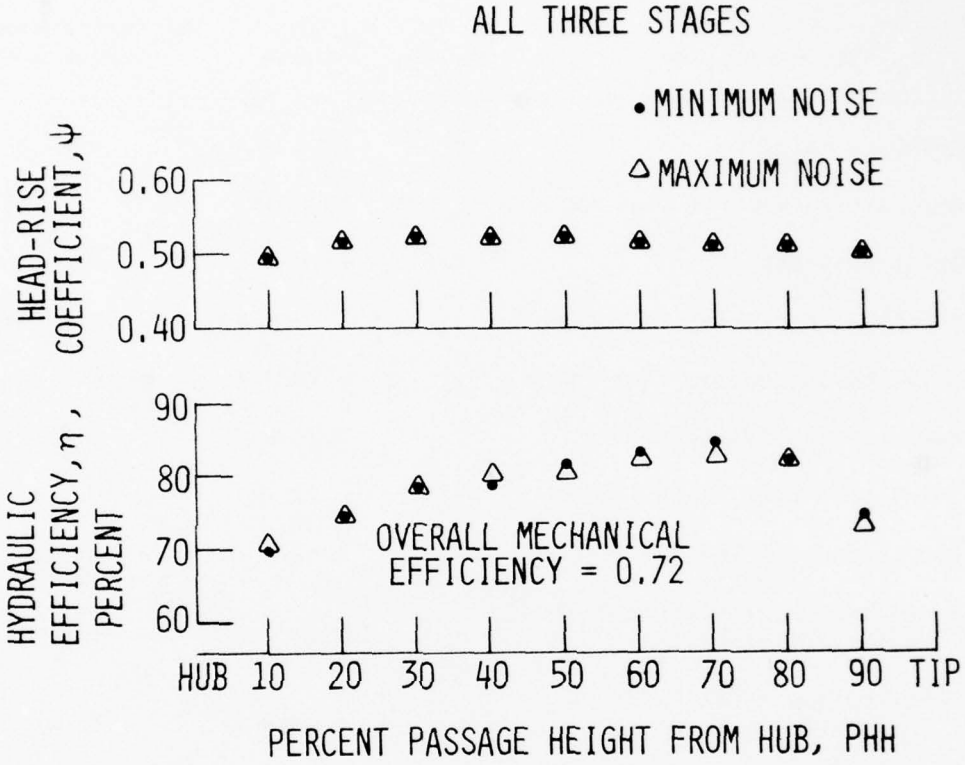
(f) Head-rise, efficiency, and incidence and deviation angles for third rotor.

Figure 5.11. Continued.



(g) Head-rise and efficiency for third stage and incidence and deviation angles for third stator.

Figure 5.11. Continued.



(h) Head-rise and efficiency for overall compressor.

Figure 5.11. Concluded.

Table 5.3. Uncertainty levels of slow-response parameters.

Flow Parameters	Symbol	Typical Values	Estimated Uncertainty (20 to 1 odds)
Absolute velocity	V	20.0 m/s	0.14 m/s
Absolute tangential flow angle	B_y	40.0 deg	0.5 deg
Axial velocity	V_z	14.0 m/s	0.20 m/s
Absolute tangential velocity	V_y	10.0 m/s	0.20 m/s
Relative tangential flow angle	B'_y	45.0 deg	0.5 deg
Head-rise coefficient	Ψ	0.24	0.003
Ideal head-rise coefficient	Ψ_i	0.27	0.006
Hydraulic efficiency	η	0.85	0.05
Stationary row total-head-loss coefficient	ω_S	0.08	0.015
Rotating row total-head-loss coefficient	ω_R	0.08	0.020

pressure, static pressure, and absolute flow angle. The bounds are generally consistent with the random scatter observed in the results. It should be noted that constant radius blade sections were involved in calculating the results instead of blade-elements formed by the intersection of approximate stream surfaces and the blades. The results of the comparison between the integrated flow rate at each station and the venturi flow rate is shown in Table 5.4 for both the minimum and maximum noise conditions. In the calculation of the integrated flow rates for each station, the annulus boundary layer was neglected, causing the integrated values to be greater than the venturi values. The flow rate

Table 5.4. Flow rate comparison between venturi and integrated measurement station flow rates.

Minimum Noise		Maximum Noise	
Station	Flow Rate Comparison Percent	Station	Flow Rate Comparison Percent
1	4.4	1	4.1
2	1.9	2	2.3
3	6.5	3	6.3
4	7.1	4	5.9
5	7.5	5	6.8
6	4.2	6	4.2
7	7.6	7	6.9
8	6.0	8	6.4

comparison values varied a great deal among the eight stations, but values between the same stations for minimum and maximum noise varied less than the axial velocity uncertainty noted in Table 5.3 (1.5%). Although the flow parameter differences between the minimum and maximum noise conditions were difficult to precisely ascertain due to the uncertainty involved, it was possible through careful interpretation of the velocity vector plots and the circumferential-average values to distinguish a few blade-row performance differences over limited regions of the blade span.

A comparison between the minimum and maximum noise values of axial velocity, absolute tangential velocity, and absolute tangential flow angle indicate only small differences (see Figures 5.7, 5.8, and 5.9) over the measured blade span region. However, even small differences in these

parameters could significantly affect the calculated values of blade losses and hydraulic efficiencies. Blade section loss coefficients are shown in Figure 5.10, while head-rise coefficients, hydraulic efficiencies, and blade incidence and deviation angles are presented in Figure 5.11.

Considerable flow losses through the IGV blade row occurred over a large portion of the blade span as made evident by the deep velocity wakes produced by the IGV (see Figures 5.5 and 5.6). These IGV wakes caused the first rotor incidence angle to vary by as much as 20 degrees. Over the region of blade span where the deepest IGV wakes occurred (10% to 50%), the circumferential variation in velocity behind the first rotor was the most pronounced. Since the upstream potential flow effects from the first stator on the first rotor were probably negligible at the blade row spacing involved, there was no reason to expect the performance of the first rotor to be different for minimum and maximum noise conditions. Any differences in blade loss, head-rise coefficient, hydraulic efficiency and flow angles for the first rotor (see Figures 5.10a and 5.11b) were thus interpreted as an indication of the measurement and data reduction precision involved. A significant local difference in first stator blade loss coefficient and first stage head-rise coefficient between the minimum and maximum noise conditions is indicated in Figures 5.10a and 5.11c at 40% passage height from the hub. Figures 5.5d and 5.6d suggest that at this passage height location the first stator exit wake patterns were considerably different. The wake pattern for minimum noise was of the deep "wakes together" type (lower loss), while the wake profile for

maximum noise was of the shallow "wakes apart" type (maximum loss). At 60%, the opposite trend in loss coefficient difference and stator exit flow patterns may be observed. Further, the first stator deviation angle data for the spanwise region from 40% to 70% passage height from the hub indicate that slightly higher (1 degree) deviation angles may be generally related to those instances when the inlet guide vane streets were not in line with the stator blade leading edges ("wakes apart" type profile).

The second stage rotor blade loss coefficients and hydraulic efficiencies (Figures 5.10b and 5.11d) were significantly different for minimum and maximum noise conditions over the blade span range from 40% to 90% passage height from the hub. Over this region, the local blade span hydraulic efficiencies differed by as much as 6% depending on whether the maximum or minimum noise configuration was used. These rotor performance differences were attributed to changes in the second rotor inlet (first stator exit) pattern produced by IGV and first stator wake interaction (see Figures 5.5 and 5.6). Rotor blade section losses were less and efficiencies were greater when the rotor inlet wake pattern was of the shallower "wakes apart" type profile rather than the deeper "wakes together" type. The shallower inlet wake patterns produced less variation in rotor incidence angle and blade loading. The opposite trends in wake pattern shapes at 40% and 60% passage heights for minimum and maximum noise resulted in consistently opposite trends in the loss and efficiency values. The second stage efficiency (Figure 5.11e) was greater for minimum sound over the blade span range from 50% to 80% passage height due to efficiency gains in the second rotor. The local stage efficiency at 90% passage height for minimum and maximum noise was approximately the

same since the second rotor efficiency gain for maximum noise at this location was opposed by the high losses of the 90% span second stator blade section. It is apparent from Figure 5.6i that the high second stator losses were related to secondary flow in this region of the annulus. The second stator deviation angle at this location was about 2 degrees less for maximum sound than for minimum sound. This is one example where improper circumferential placement of the stationary blade rows relative to each other has lead to adverse flow conditions.

The most significant difference in the performance of the third stage rotor occurred at 90% passage height, as indicated in Figures 5.10c and 5.11f. Apparently, losses at 90% rotor blade span for maximum noise were considerably higher due to the large second stator wakes incurred at the rotor inlet. The large positive fluctuations in rotor incidence angle from the inlet flow variation caused a greater tendency for the flow to separate at the rotor suction surface. As indicated by Figure 5.10c, there was no significant third stator performance difference between minimum and maximum noise conditions. For the entire third stage, the efficiency was significantly better for minimum noise at 90% passage height and slightly better for maximum noise at 30%, 40% and 60% passage heights (see Figure 5.11g). As can be seen from Figures 5.5a and 5.6a, a secondary flow region was measured behind the third stator at 10% passage height from the hub. The hub surface at this location was stationary.

No measurable differences in overall hydraulic or mechanical efficiencies (Figure 5.11h) could be detected for the entire compressor.

C. Fast-Response Measurement Results

Fast-response results from three-dimensional hot-wire measurements of the periodic-average flow field between blade rows of the first two stages of the research compressor for the minimum noise condition are discussed in this section. These circumferential survey results are presented in the form of velocity scalar and vector plots. The scalar information includes the blade-to-blade distribution of axial velocity, absolute tangential velocity, radial velocity, absolute tangential angle, and radial angle. The vector plots involve the blade-to-blade plane distribution of individually measured velocities. As defined previously (see Figure 4.12), the radial velocity and radial angle are positive when directed outward toward the annulus outer surface.

The uncertainty and scatter associated with the determination of the fluid velocity and flow angle parameters were estimated and are indicated in Table 5.5. The uncertainty represents the accuracy associated with the flow field parameters, whereas the scatter reflects the point-to-point irregularity of the circumferentially varying parameter distributions. In estimating the uncertainty of each parameter, several factors were considered including: (1) velocity calibration accuracy, (2) calibration drift due to working fluid temperature variation and dirt accumulation on the wire, (3) number of periodic samples N (see Figure 4.7), (4) hot-wire angle alignment accuracy, and (5) comparison with slow-response results. A comparison of the slow-response and fast-response results is shown in Figure 5.12. The six hot-wire periodic-average axial velocity profiles obtained behind the first stator for six different instantaneous positions

Table 5.5. Uncertainty and scatter of periodic-average flow field parameters.

Flow Parameters	Symbol	Typical Values	Estimated Uncertainty (20 to 1 odds)	Estimated Scatter (20 to 1 odds)
Absolute velocity	V	18.0 m/s	0.8 m/s	0.15 m/s
Absolute tangential angle	β_y	40.0 deg	1.5 deg	1.0 deg
Radial angle	β_r	0.0 deg	2.0 deg	1.5 deg
Axial velocity	V_z	13.0 m/s	0.7 m/s	0.3 m/s
Absolute tangential velocity	V_y	12.0 m/s	0.6 m/s	0.4 m/s
Radial velocity	V_r	0.0 m/s	0.5 m/s	0.4 m/s

of the rotor shaft are shown along with the corresponding slow-response circumferential distribution. The figure shows good agreement between the two sets of results with the largest velocity deviation (3%) being within the uncertainty limits set forth in Table 5.5. The predicted values of scatter in Table 5.5 were based on the typical random irregularity of the results and were determined by considering the deviation of the data points about a smooth gradual damped curve formed by the data points.

Hot-wire measurements made behind the first rotor at 50% passage height indicate that the rotor wake exit flow pattern changed dramatically with rotor blade circumferential position due to the influence of the upstream IGV blade row. From the slow-response results, the IGV wake street at the first rotor exit could be identified as a region of lower velocity as shown in Figure 5.13. Points A and B in Figure 5.13 corre-

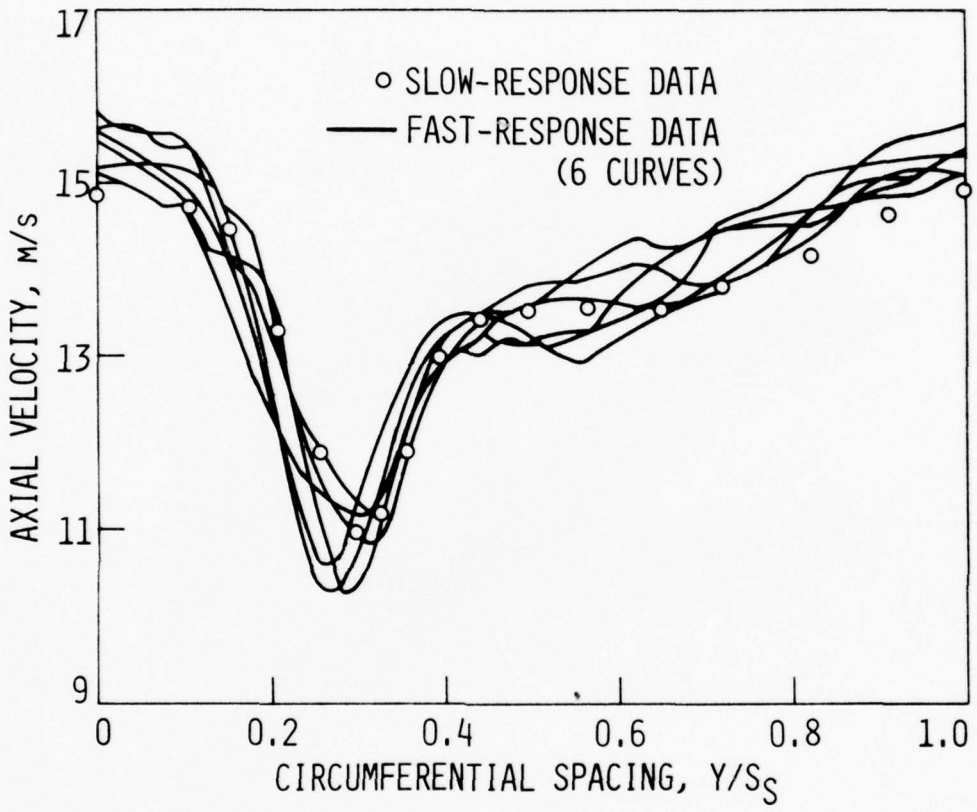


Figure 5.12. Comparison of slow-response and fast-response data behind the first stator.

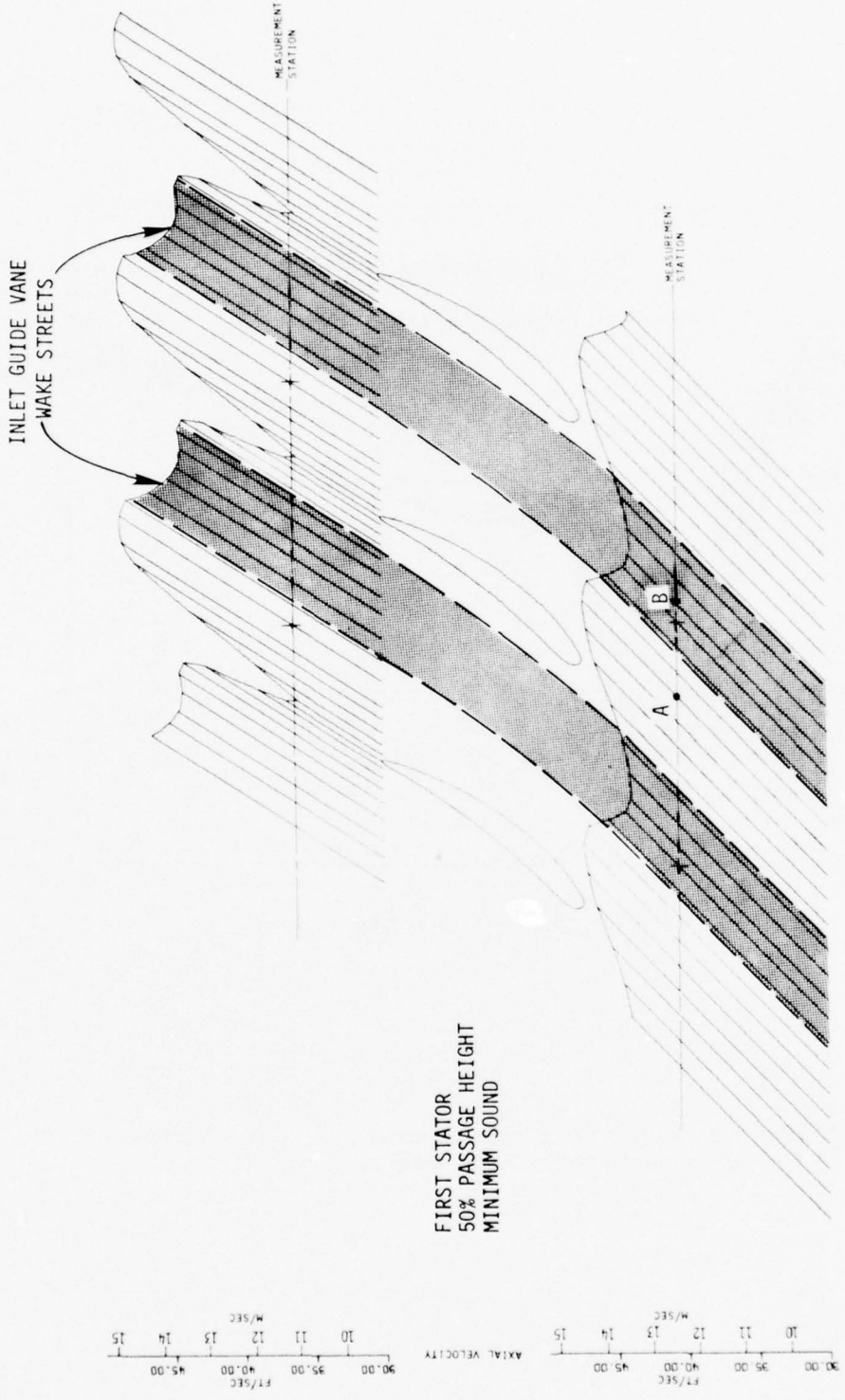


Figure 5.13. Mid-span slow-response instrument averaged velocity vector variation for first stator with inlet guide vane wake streets shown.

spond respectively to positions out of and in the IGV wake street at 50% passage height behind the first rotor. The multiple oscilloscope traces shown in Figures 5.14 and 5.15 represent the first rotor exit flow field at locations A and B. The traces were made using a single hot-wire sensor normal to the radial and average flow directions. The oscilloscope was synchronized to trace the wire signal as the same three rotor blades moved by the sensor. Comparison of the two traces indicate a larger amount of random unsteadiness and deeper rotor wakes in the IGV wake street (location B). The trend related to random unsteadiness is in agreement with the observations of Walker and Oliver (5). However, the deeper rotor wakes related to the IGV wake street noted in the ISU compressor do not agree with the shallower rotor wakes seen in the IGV street region by Walker and Oliver (5).

Three-dimensional periodic-average hot-wire results acquired at locations A and B with the passing rotor-blade flow-field survey method (see page 49) are shown in Figure 5.16. It should be noted that the wake profiles are circumferentially shifted due to the difference in the rotor blade setting position YO_R/S_R corresponding to the two distinct positions of the hot wire. The results clearly contrast the periodic-average first rotor wake profiles in and out of the IGV wake street. The wake produced by the rotor is much deeper, and the variation in absolute tangential flow angle is as much as 6 degrees greater within the IGV wake street (location B). However, the radial velocity and radial angle profiles are similar for both cases with centrifugation occurring in the wake region as expected. The general common trends in circumferential variation of flow quantities indicated by both sets of data in Figure 5.16 are in agreement

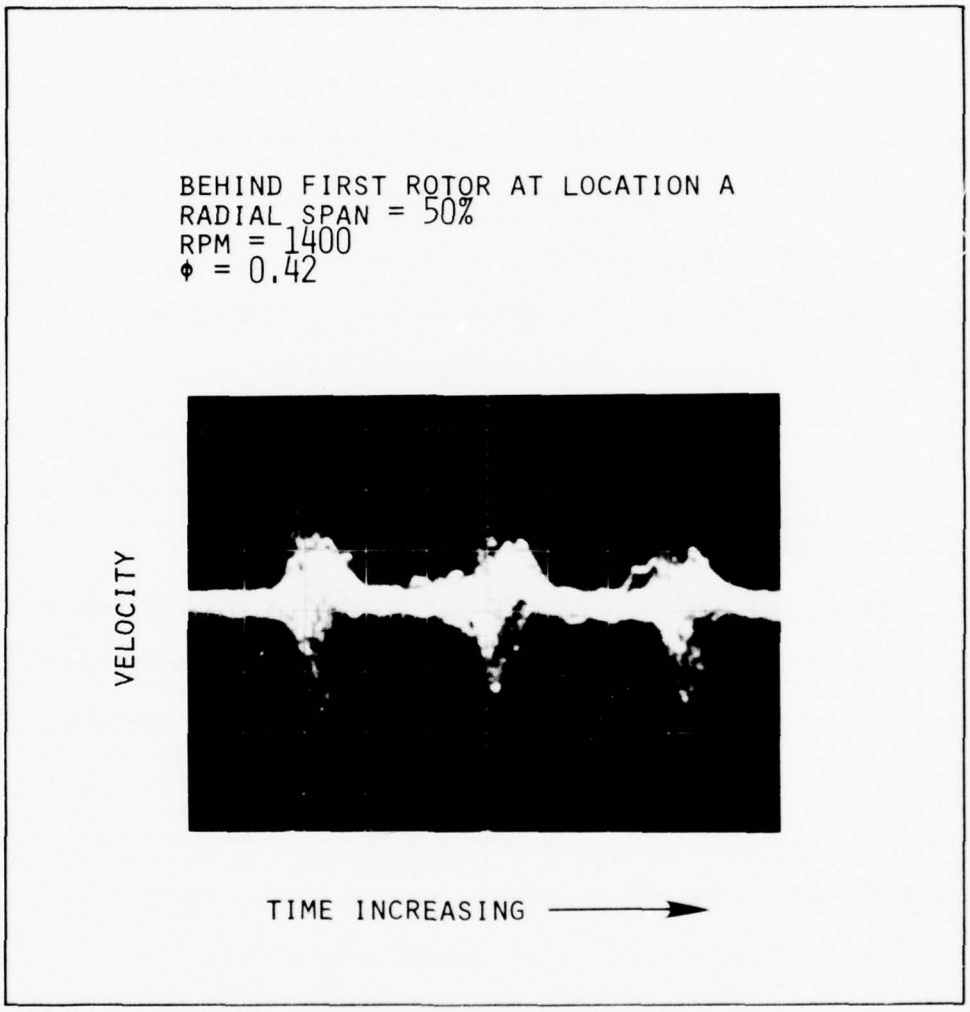


Figure 5.14. Multiple oscilloscope traces of hot-wire signal for location A.

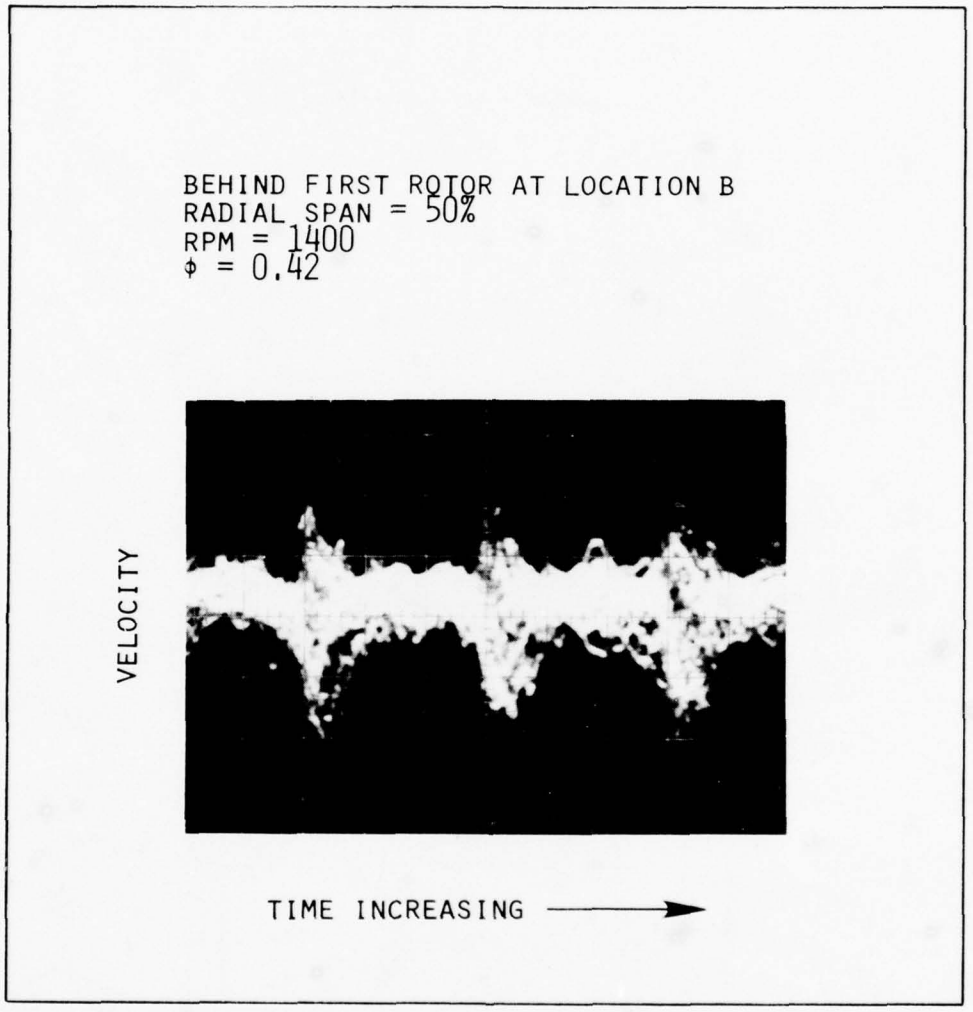


Figure 5.15. Multiple oscilloscope traces of hot-wire signal for location B.

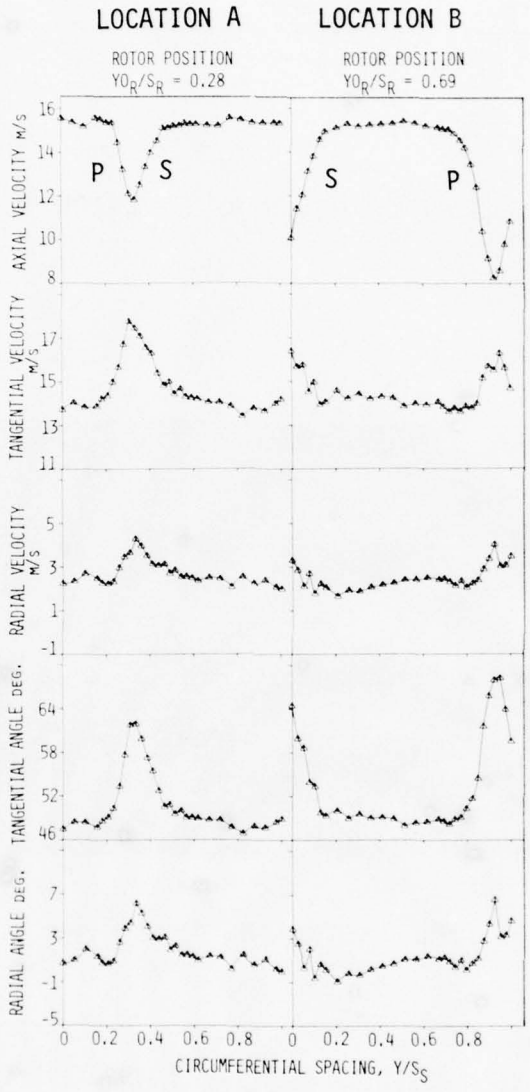
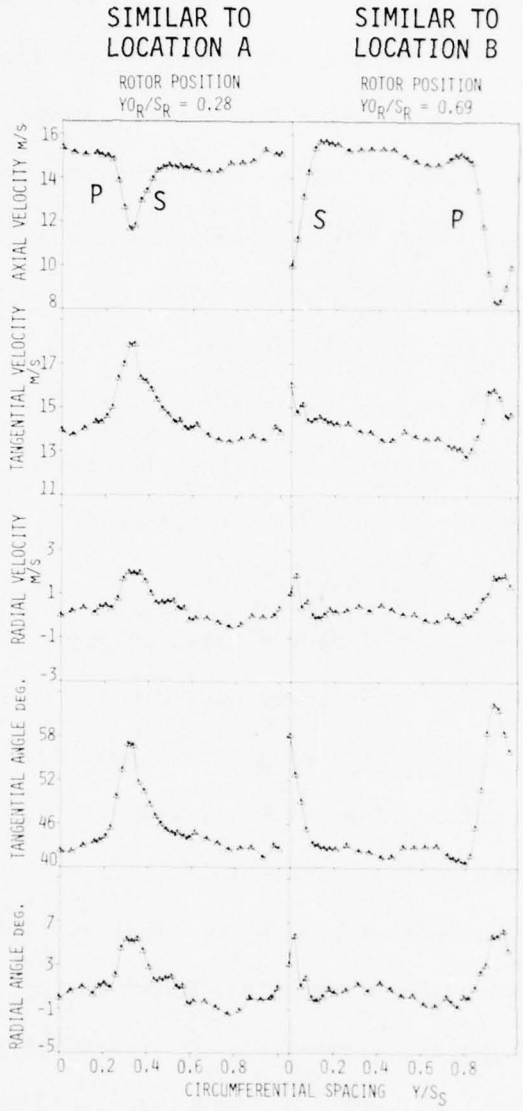


Figure 5.16. Circumferential distribution of periodic-average flow field parameters behind the first rotor at 50% passage height for locations A and B, obtained with passing rotor-blade survey method.

with those observed by others in the past (Hirsch and Kool (20), Raj and Lakshminarayana (13) and Evans (12)).

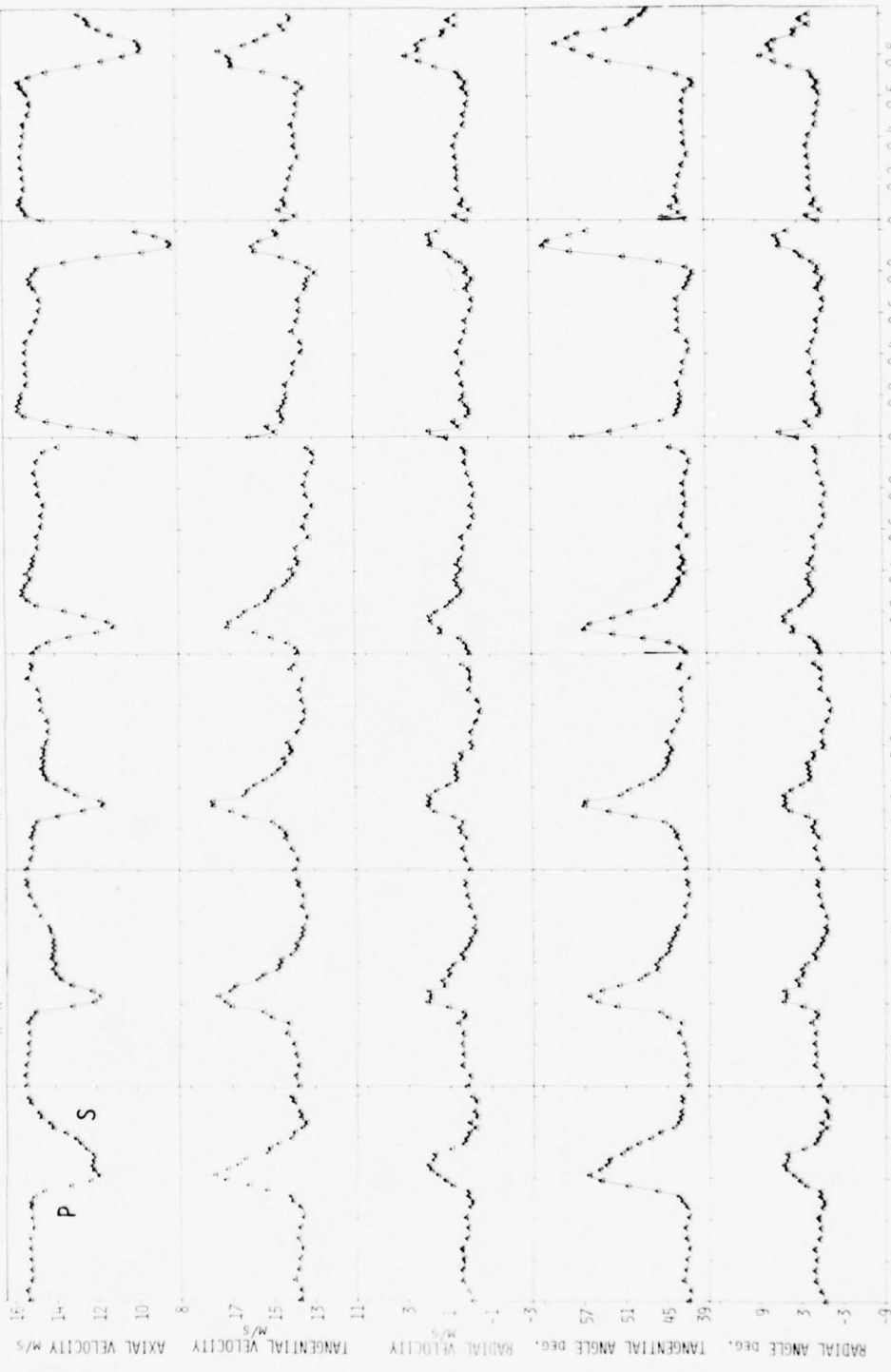
Measurements similar to those in Figure 5.16 behind the first rotor at 50% passage height were obtained using the frozen rotor-blade flow-field survey method (see page 49). The results, shown in Figure 5.17a, were acquired by effectively circumferentially moving the hot wire past the periodically frozen rotor and stationary blade row configuration. With the "frozen" rotor blade section position set at $YO_R/S_R = 0.69$, the rotor wake fell within the IGV wake street. With the rotor position set at $YO_R/S_R = 0.28$, the rotor wake was outside of the IGV wake street. These results are generally similar to those in Figure 5.16. However, the stationary flow pattern from the IGV wake street at the rotor exit is discernible only in the latter case, Figure 5.17a. In Figure 5.17a, the dip in the axial velocity level near a circumferential spacing of about 0.65 reflects the IGV row flow pattern upstream of the rotor. Since the frozen rotor-blade flow-field survey method appeared to provide a more detailed description of the flow field, it was used to obtain all further results as shown in the rest of Figure 5.17.

Data for four additional frozen rotor-blade section positions behind the first rotor at 50% passage height are shown in Figure 5.17b along with the results from the two rotor positions of Figure 5.17a. In general, the depth and width of the rotor wakes at each rotor position varied between the two profiles already discussed and shown in Figure 5.17a. At each rotor position, the slow moving fluid contributing to the IGV wake street can be consistently identified as a velocity deficit region near a circumferential spacing, Y/S_S, of 0.65. Further analysis of the general flow



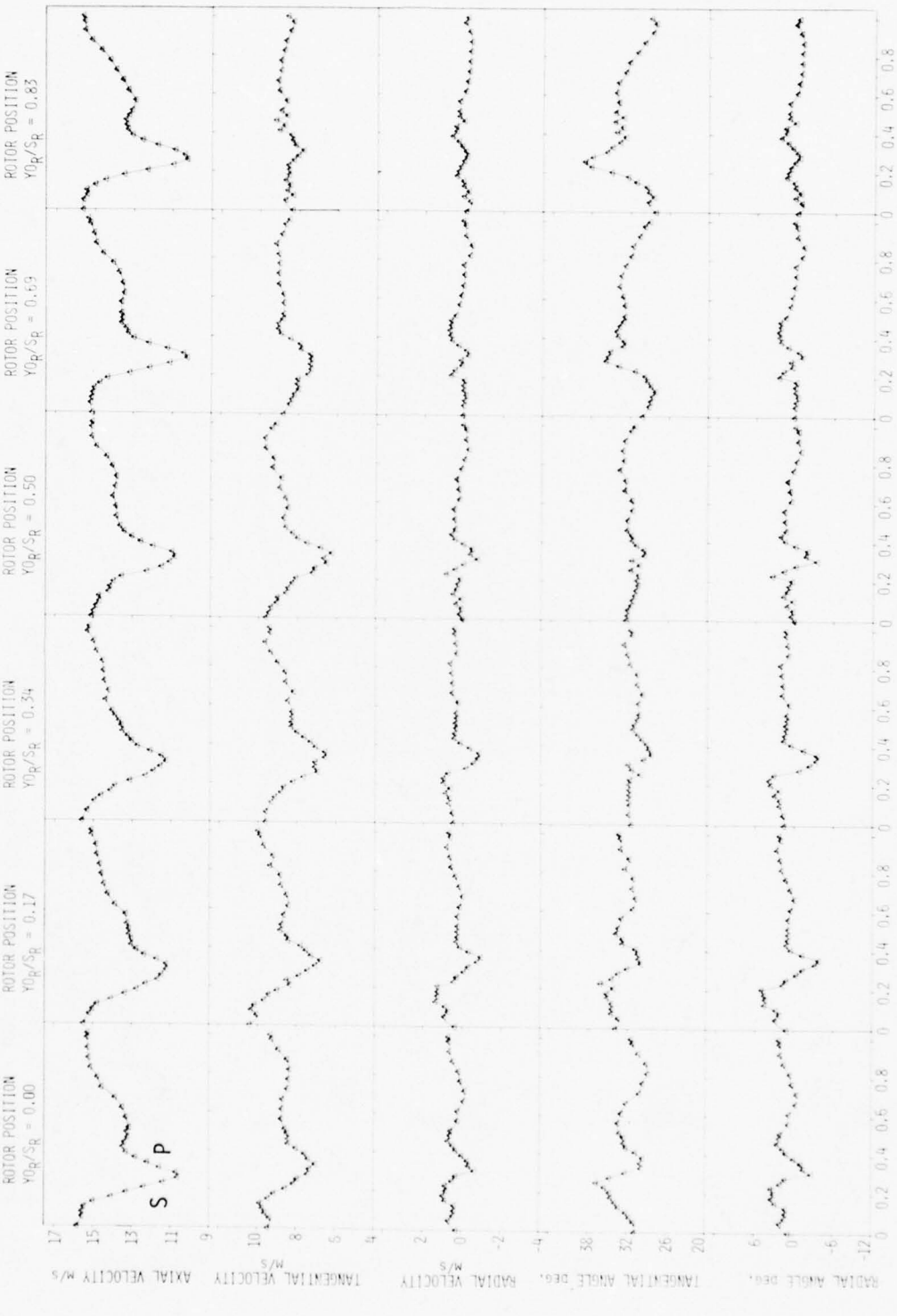
(a) First rotor exit flow at 50% passage height, similar to results in Figure 5.16.

Figure 5.17. Circumferential distribution of periodic-average flow field parameters obtained at different rotor positions with frozen rotor-blade survey method.



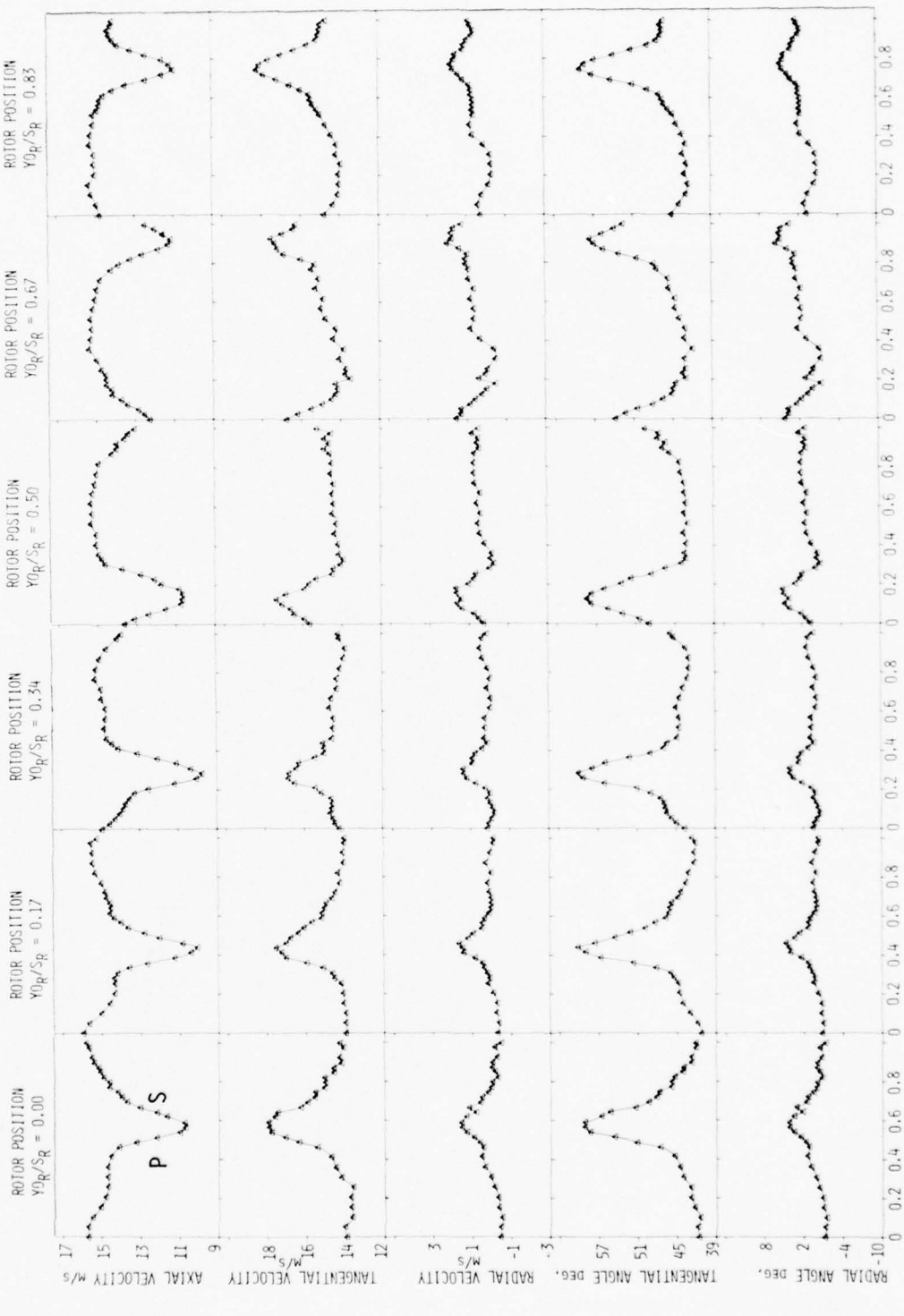
(b) First rotor exit flow at 50% passage height.

Figure 5.17. Continued.



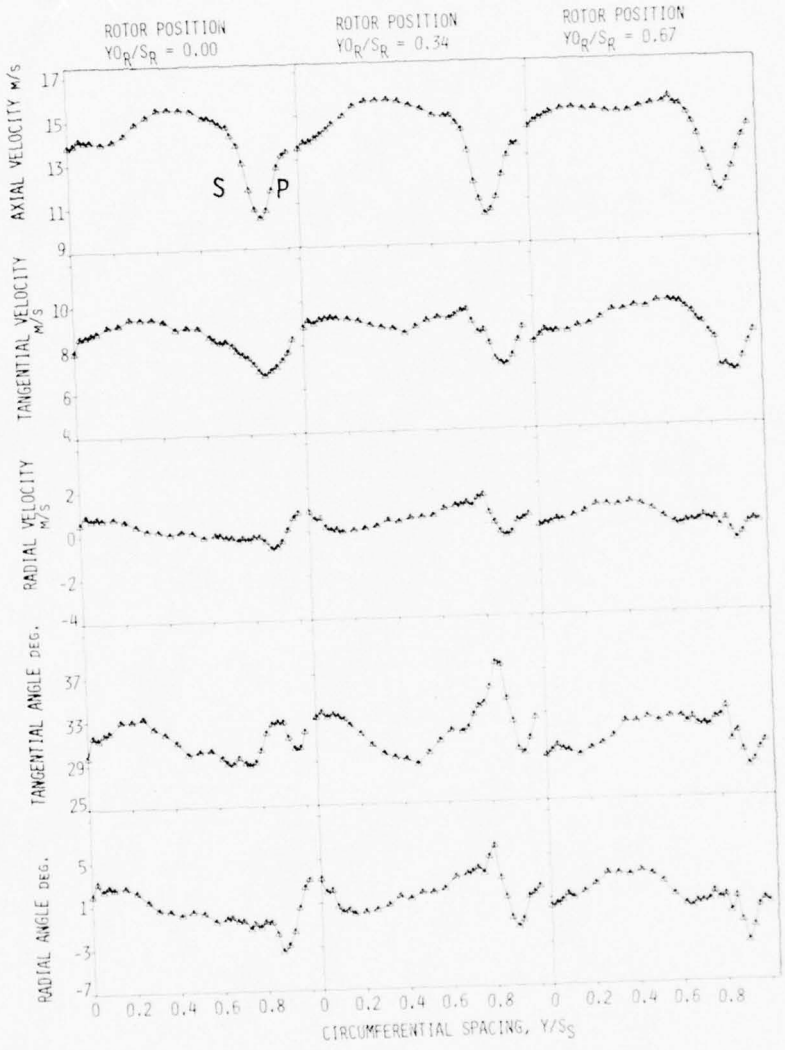
(c) First stator exit flow at 50% passage height.

Figure 5.17. Continued.



(d) Second rotor exit flow at 50% passage height.

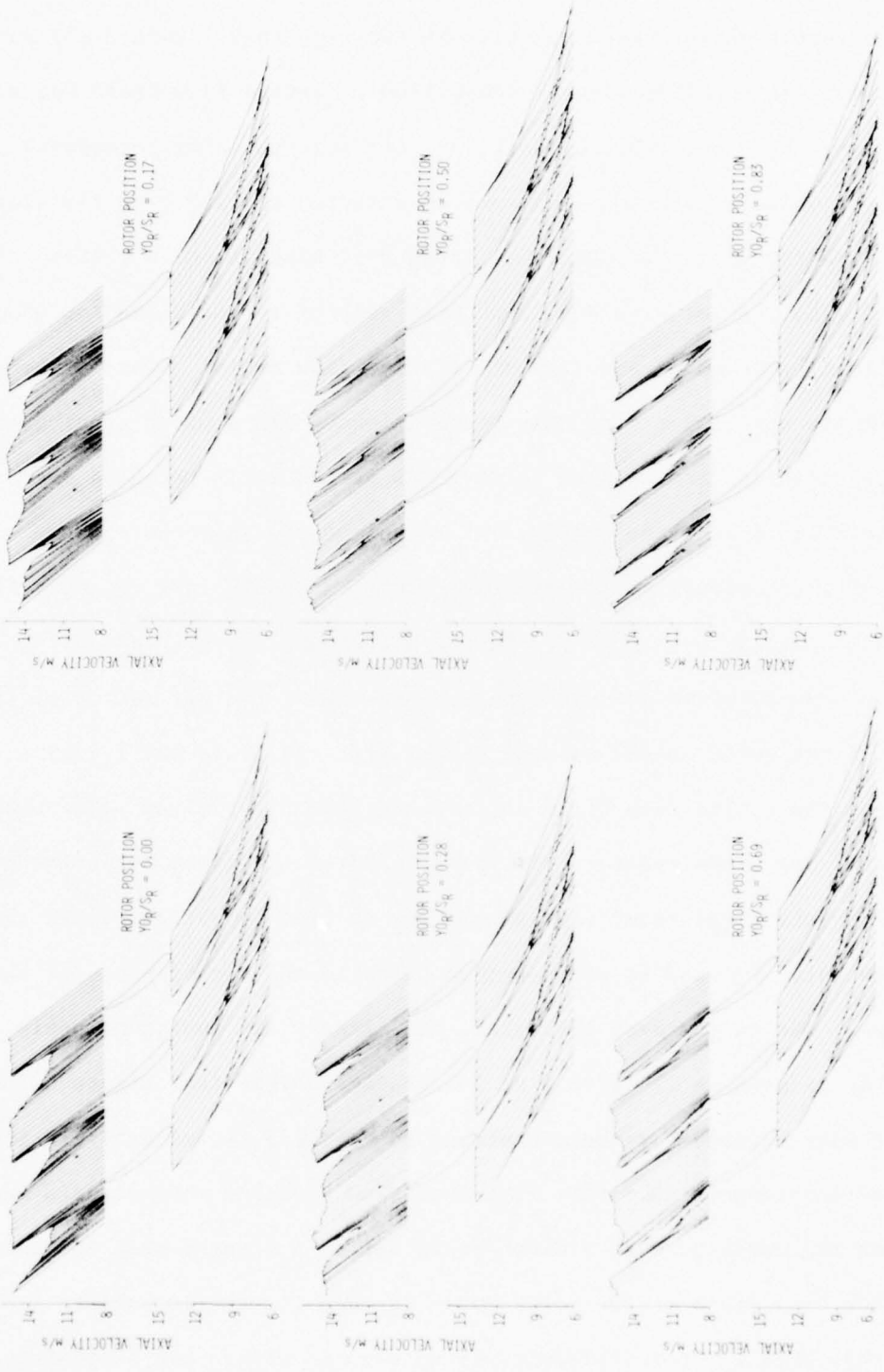
Figure 5.17. Continued.



(e) Second stator exit flow at 50% passage height.

Figure 5.17. Concluded.

pattern development is expedited through the use of blade-to-blade velocity vector plots. Each velocity vector plot (see Figure 5.18) portrays the blade-to-blade view of the periodic-average flow field for a particular frozen rotor-blade position. Although these fast-response instrument velocity vector plots were constructed similarly to the slow-response vector plots, it should be noted that each velocity vector measured with the hot wire was drawn with respect to the blade row shown at the locally measured absolute or relative flow angle. Also, although measurements were taken over only one stationary blade pitch spacing, the circumferentially varying flow pattern was periodically repeated over approximately three blade spacings of the blade row shown to enhance visualization. Actually, the velocity profiles should vary slightly from one blade spacing to another due to the difference in the blade pitch values of the rotating and stationary blade rows. The six vector plots for the first rotor at 50% passage height (Figures 5.18a and 5.18b) represent the cyclic flow field variation as the rotor blade sequentially moves over one blade spacing. The flow field at the inlet measurement station to the first rotor was assumed not to vary appreciably, and slow-response data were used to represent the flow in the vector plots at this location. Due to the deep IGV wakes, the first rotor incidence angle varied by as much as 17 degrees at 50% passage height (see Figure 5.18a). The IGV wake streets have been sketched in Figure 5.18b to help clarify the flow development involved. The locations of these wake streets were based on the corresponding slow-response data. A step-by-step analysis of the rotor flow field as the rotor moves through its cyclic pattern indicates that when the rotor blade trailing edge is within the stationary IGV

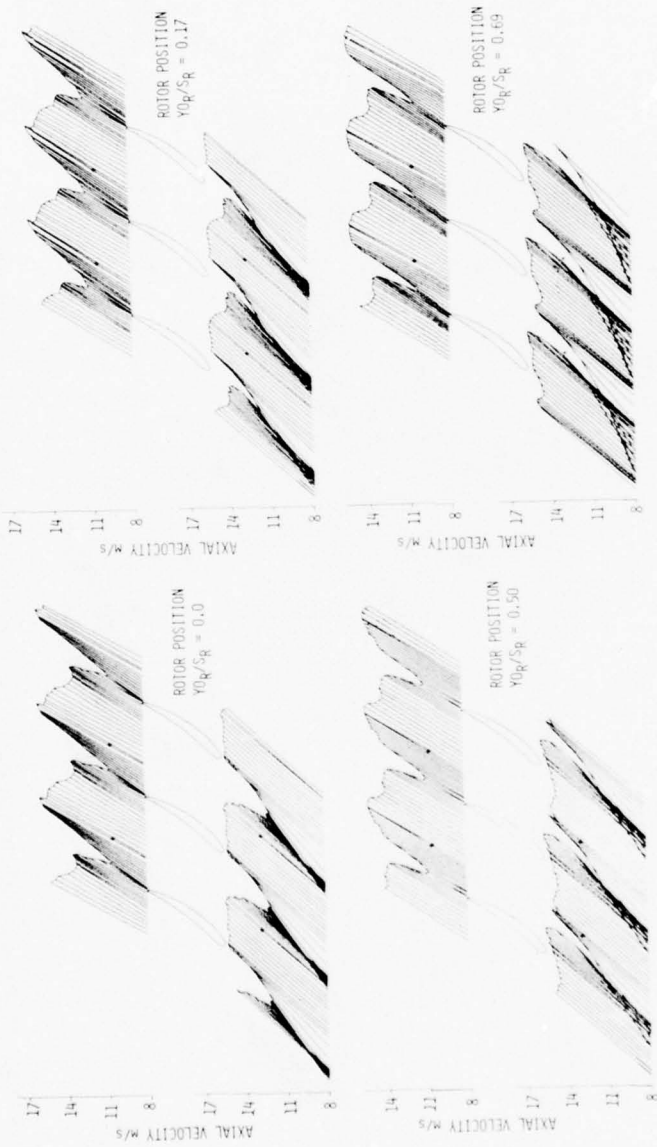


(a) First rotor at 50% passage height.

Figure 5.18. Blade-to-blade velocity vector plots obtained at different rotor positions with frozen rotor-blade survey method.



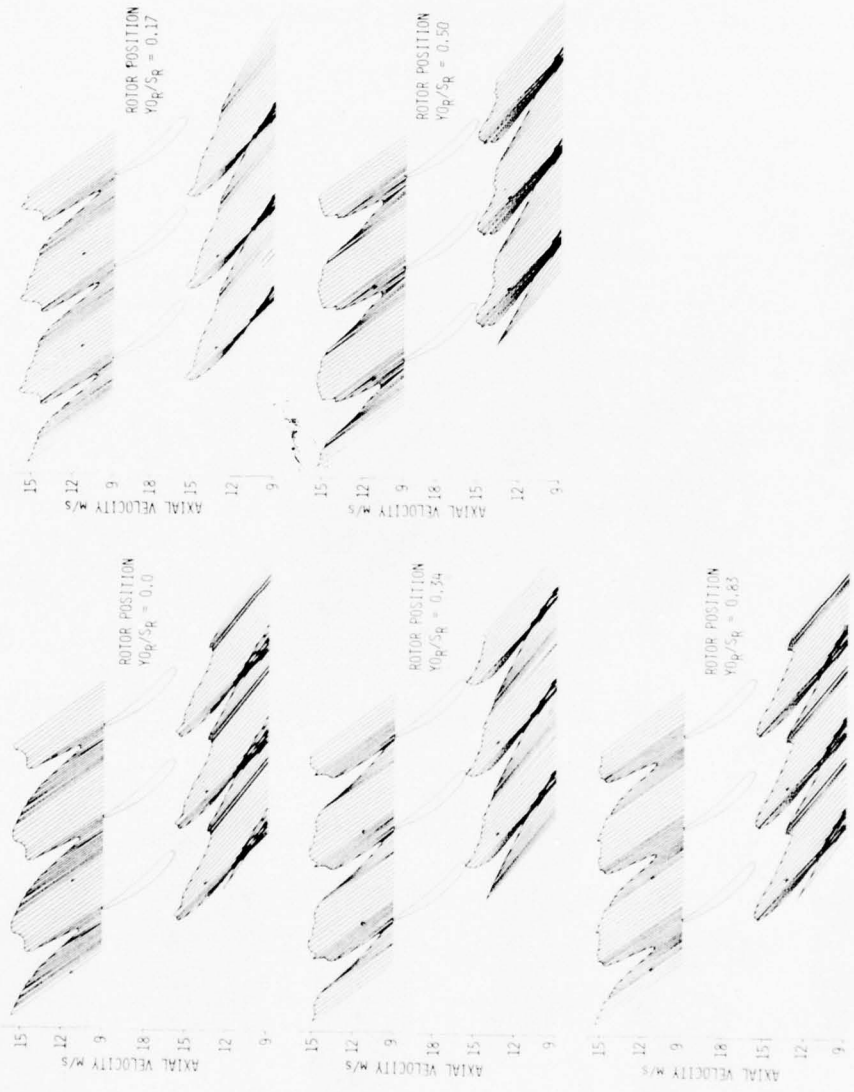
(b) First rotor at 50% passage height with IGV wake streets shown.
Figure 5.18. Continued.



(c) First stator at 50% passage height.
Figure 5.18. Continued.

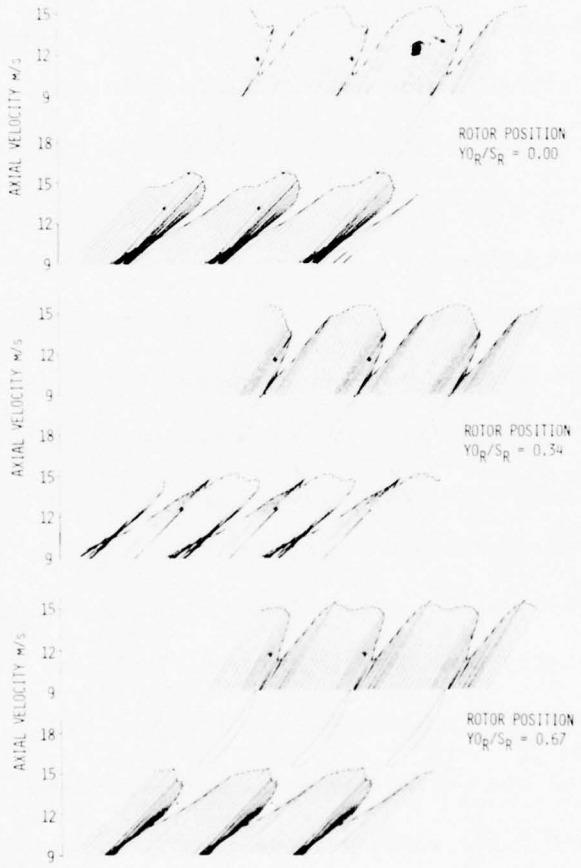


(d) First stator at 50% passage height with IGV wake streets shown. Figure 5.18. Continued.



(e) Second rotor at 50% passage height.

Figure 5.18. Continued.



(f) Second stator at 50% passage height.

Figure 5.18. Concluded.

wake street, the depth and width of the rotor wake increases appreciably. Once the rotor trailing edge has passed beyond the stationary IGV wake street, a normal wake pattern is resumed.

First stator blade section discrete frequency noise is related to the surface pressure fluctuations of that blade section produced by the periodic unsteadiness of the first rotor exit flow. Larger variations in first rotor exit (first stator inlet) periodic unsteadiness (larger rotor wakes) probably result in higher stator noise levels. From the measurements at 50% span, it was observed that larger first rotor wakes occurred in the IGV wake street region. If the effect of the IGV wake street on the rotor is similar over the entire span of the first rotor, then the slow-response data (Figures 5.5 and 5.6) seem to indicate that conditions for maximum noise at most first stator blade sections and conditions for minimum noise at most first stator blade sections were present under maximum and minimum operation, respectively. The first stator fast-response vector plot at 50% passage height for minimum sound (Figure 5.18c) conclusively indicates that the rotor wakes flowing onto the leading edge region of the first stator blade section are smallest.

The results of the periodic-average hot-wire measurements behind the first stator at six rotor positions are shown in scalar form in Figure 5.17c. The rotor wake influence on the stator exit flow can be seen in the sequence of axial velocity profiles. Less obvious is the presence of the stationary IGV wake street influence which is more clearly indicated in the slow-response vector plot (see Figure 5.13). The IGV wake streets can be identified in the axial velocity profile for each rotor position near a circumferential spacing of 0.6, and its position is sketched in the

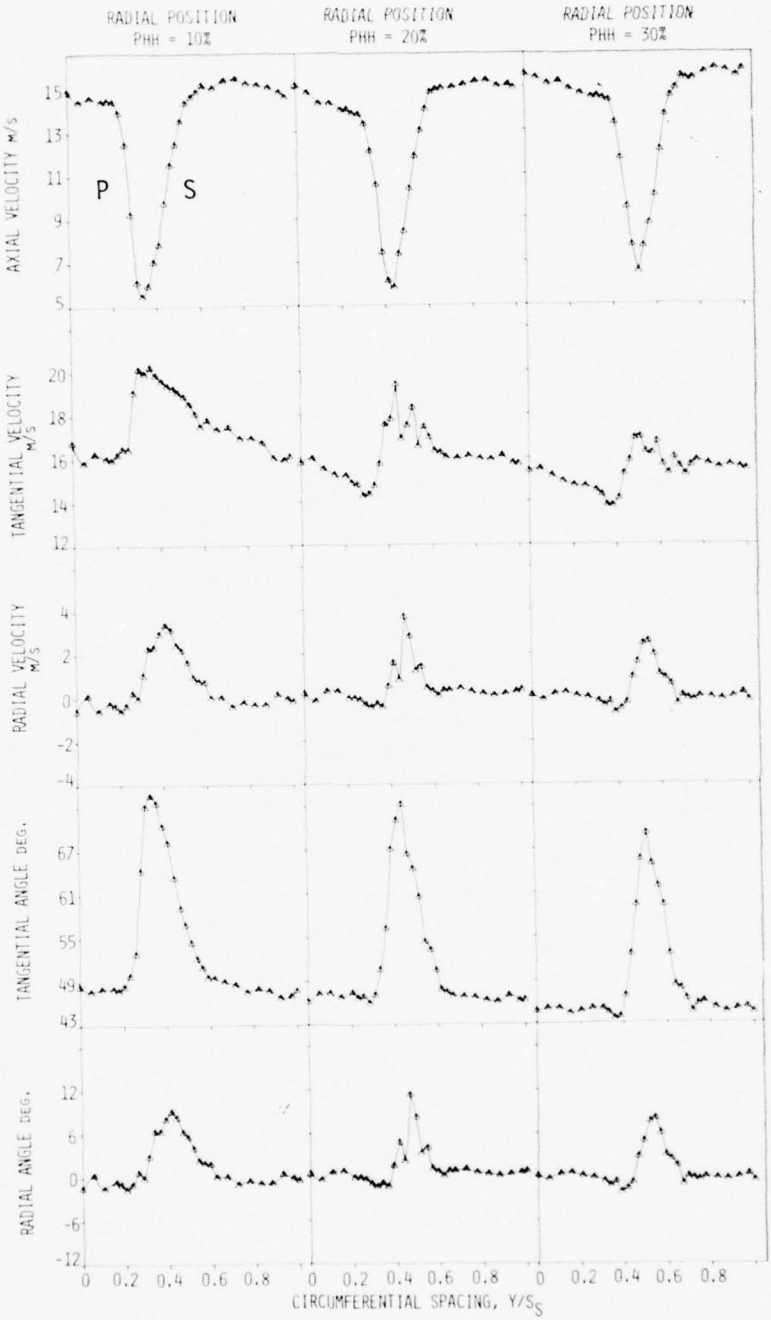
five blade-to-blade vector plots in Figure 5.18d. The absolute tangential velocity and radial velocity blade-to-blade variations are definitely smaller for rotor positions YO_R/S_R = 0.69 and 0.83 (see Figure 5.17c). The tangential angle blade-to-blade differences are notably smaller for rotor positions YO_R/S_R = 0.34 and 0.50. The general expected tendency for the slower moving stator wake fluid to move inward toward the hub is evident. The stator incidence angle varied as much as 20 degrees which is comparable to the range reported by Evans (12) and Hirsch and Kool (20). The velocity vector plots (Figures 5.18c and 5.18d) manifest the wake interaction involved between the IGV, first rotor and first stator. The significant changes in first stator exit flow with frozen rotor position might indicate that second rotor noise due to periodic unsteadiness can be varied with appropriate stator and rotor blade circumferential placement.

Although the second rotor exit flow field changed with rotor position (see Figures 5.17d and 5.18e), the variation was significantly less than that for the first rotor. This observation is consistent with the slow-response data trend indicated in Figure 5.5e and seems reasonable since the second rotor inlet velocity and incidence angle variation at 50% span was less than that for the first rotor. It should be noted that while the first stator wake street is evident, it is less discernible in the second rotor exit flow than that of the IGV wake street in the first rotor exit flow. As expected, centrifugation of the wake fluid is evident in the second rotor exit flow as indicated by the radial angle distributions. In addition, large (20 degrees) circumferential variations in absolute tangential flow angle are apparent at each rotor position while only small circumferential variations in the relative tangential flow angle are

evident in the velocity vector plots. The range of relative tangential flow angles was 33 to 41 degrees. In the case of the first rotor, the range in values of relative tangential flow angle was 32 to 50 degrees. The hot-wire data do not yield conclusive information related to second stator noise.

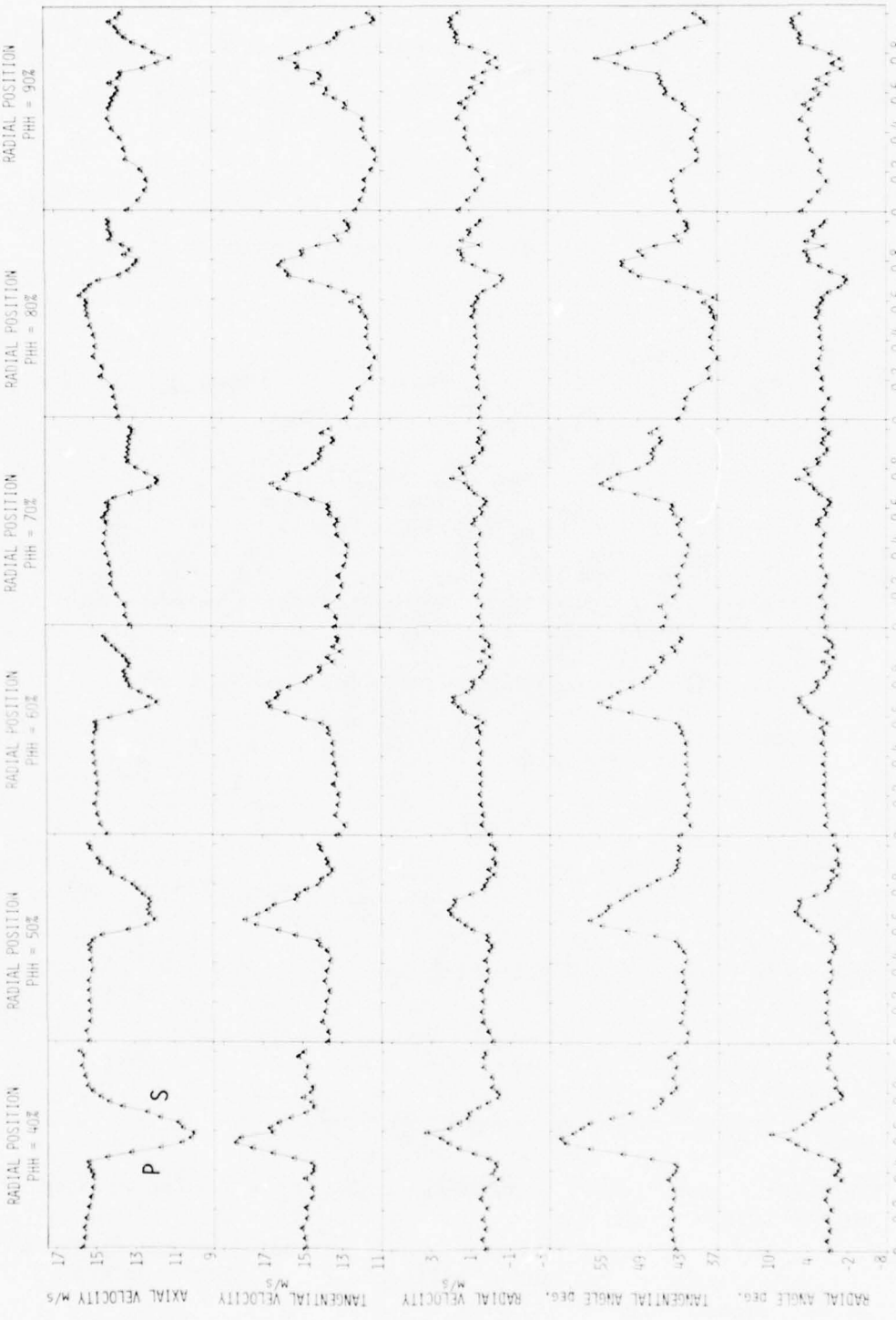
The second stator exit flow distributions at three rotor positions are shown in Figure 5.17e with the corresponding velocity vector plots in Figure 5.18f. There is a marked contrast in the freestream flow region. In addition, the variation of the absolute tangential angle in the region of the stator wake is significantly larger at the rotor position of 0.34. The rotor wake influence on the stator exit flow is noticeable. The first stator wake street is buried within the second stator wake at 50% span as shown in the slow-response data (Figure 5.5e) and therefore is not apparent in the fast-response data. It appears as if third rotor noise can be varied with appropriate stator and rotor blade circumferential placement. The slow-response data indicate an appreciably larger second stator wake at 90% span for the maximum noise condition than for the minimum noise one.

All hot-wire results thus far discussed were obtained at 50% passage height. Results from hot-wire measurements taken behind the first rotor at nine passage height locations (10% to 90% from the hub) and one rotor position (YO_R/S_R = 0.0) are presented in Figures 5.19 and 5.20. Slow-response data were again used to represent the first rotor inlet flow in the vector plots. The performance of the first rotor varied with radial position mainly because of the spanwise variation of inlet flow conditions produced by the IGV blade row. The larger variations in the average first



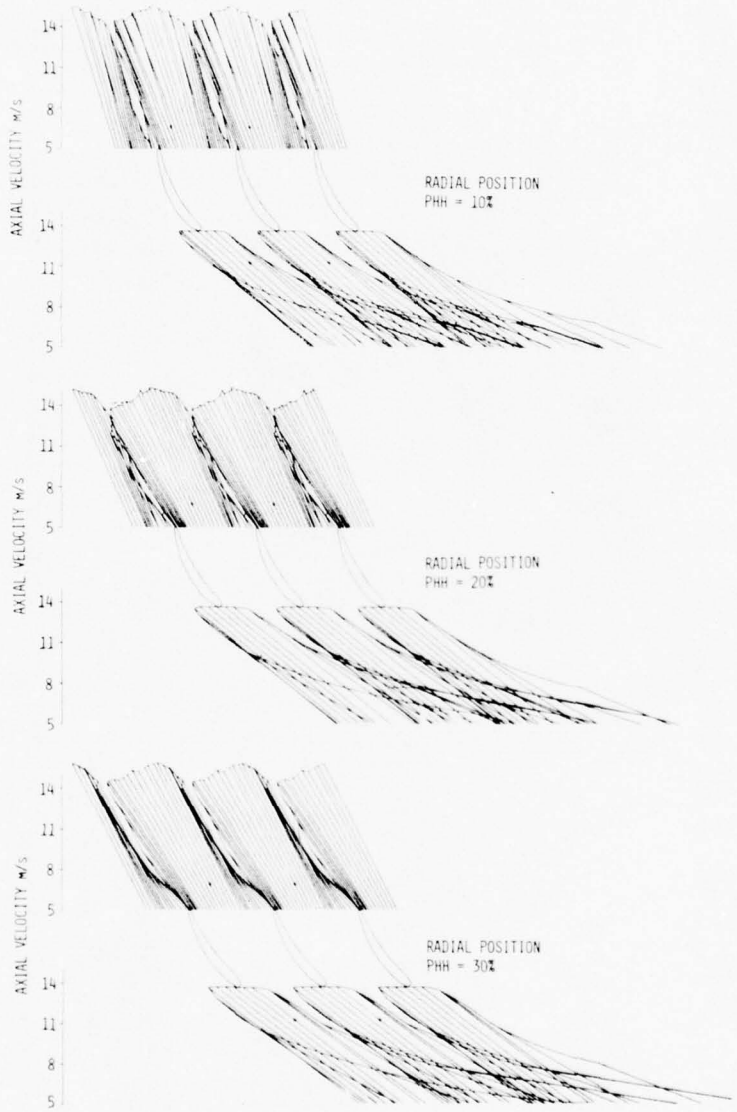
(a) First rotor exit flow at rotor position YO_R/S_R = 0.0 and passage heights 10%, 20%, and 30%.

Figure 5.19. Circumferential distribution of periodic-average flow field parameters obtained at different radial positions with frozen rotor-blade survey method.



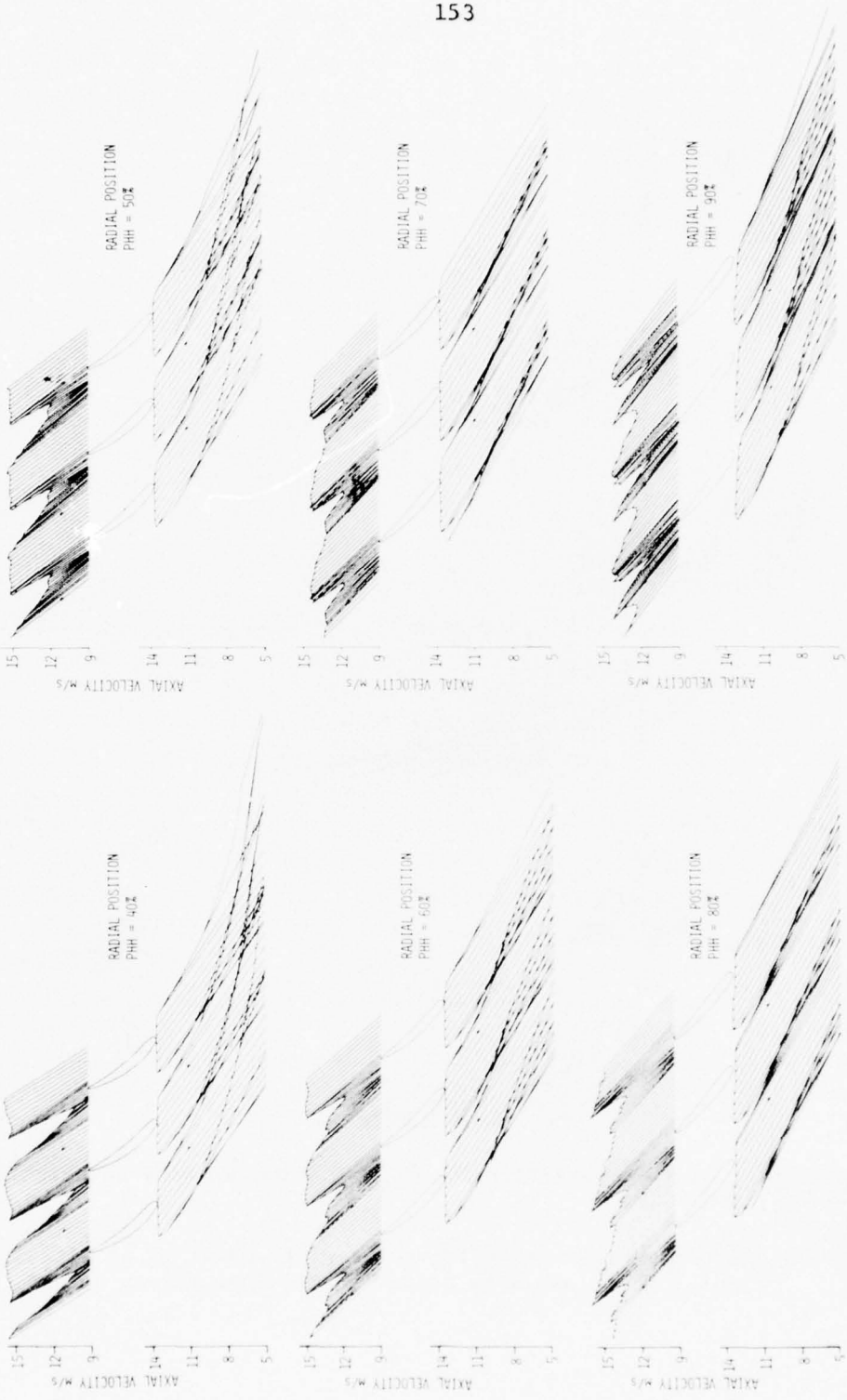
(b) First rotor exit flow at rotor position $YO_R/S_R = 0.0$ and at passage heights 40% through 90%.

Figure 5.19. Concluded.



(a) First rotor at rotor position YO_R/S_R = 0.0 and at passage heights 10%, 20%, and 30%.

Figure 5.20. Blade-to-blade velocity vector plots obtained at different radial positions with frozen rotor-blade survey method.



(b) First rotor at rotor position $YO_R/S_R = 0.0$ and at passage heights 40% through 90%.

Figure 5.20. Concluded.

rotor exit flow field (slow response) and the periodically frozen first rotor-blade exit flow field at different frozen rotor positions (fast response) were related to the larger variation of IGV row exit (first rotor inlet) flow and occurred in the lower half of the annulus. For example, the variation in rotor exit (stator inlet) absolute tangential flow angle was as much as 27 degrees at 10, 20, and 30% of the passage height from the hub. The IGV wake street influence can be observed at each spanwise location. Near the tip (80 and 90% of the span from the hub) appreciable amounts of wake fluid appear to be moving toward the hub.

VI. CONCLUSIONS

Summarized below are the conclusions reached to date. Further data analysis and acquisition are being continued at Iowa State under AFOSR sponsorship.

The level of discrete frequency noise at the inlet of the ISU research compressor could be varied appreciably by relative circumferential positioning of the stationary blade rows when the spinning blade-row interaction pattern speed was above the Tyler and Sofrin (15) "cut-off" value. The details of the fluid flow physics associated with this variation in noise with blade row circumferential positioning are not entirely explainable yet because of insufficient evidence. However, the present detailed flow field data may be interpreted as showing that the pressure fluctuations incurred by the first stator due to wake interaction with the first rotor were generally smaller during minimum noise operation, and generally larger during maximum noise operation. Also, the data suggest that the second and third rotor noise levels might be affected more by stationary blade-row placement than the noise level of the second stator. More specific conclusions about the compressor flow field behavior based on slow- and fast-response instrument data are discussed below.

The stationary flow pattern within the compressor could be changed appreciably in regions of the compressor annulus by varying the circumferential positions of the stationary blade rows relative to each other. Stationary blade row wakes significantly affected the shape of the flow fields of the next rotor and stator rows. Further, the interaction flow pattern formed by two stationary blade rows subsequently influenced the next rotor and stator flow fields. The measured rotor and stator exit

flow fields were found to be periodically and randomly unsteady and dependent on instantaneous rotor blade circumferential position with the extent of variation of exit flow dependent on the intensity of the inlet flow periodic variation. For example, the data indicated that first rotor exit flow periodic and random unsteadiness was greatest in the IGV row wake street region. Because the flow was unsteady in both the absolute and relative reference frames due to the interaction between the rotating and stationary blade rows, the velocity field sensed by a stationary hot-wire behind a rotor blade periodically sampled at different circumferential positions was found to vary from the field sensed by a hot wire traversed circumferentially relative to a rotor blade section periodically frozen at the same circumferential position. The latter method appears to provide more detail and to be a more viable means for measuring unsteady flow phenomena. The amount of influence and location of wake streets varied over the annulus span. In general, the three-dimensional stationary wake streets approached a stator leading edge at an angle relative to the radial direction with two adjacent wake streets intersecting the stator leading edge over the annulus height. Hub to tip distributions of circumferentially averaged (meridional plane) quantities indicated some variation of blade section loss coefficient, head-rise coefficient, hydraulic efficiency, and incidence and deviation angles for a few blade sections with change in stationary blade row placement. However, no difference of overall head-rise coefficient or hydraulic efficiency could be detected between the maximum and minimum noise operation conditions.

It is true that the large variation in ISU research compressor inlet noise with appropriate blade row positioning was possible mainly because the same number of blades was used in each stationary row, and the number of blades in each row allowed the pressure interaction patterns to move forward. However, what is observed about the noise (surface pressure fluctuations) of all the blades in a particular row of the ISU research compressor is probably generally applicable to fewer blades (maybe only one) in a more typical turbomachine. In the latter case reduction of periodic blade lift force variation rather than noise would be important, and the present results may be used to learn more about how the fluctuating lift force pattern for any blade in a practical multistage axial-flow turbomachine depends on factors which include the location of that blade relative to upstream blades and/or other flow distorters in that machine.

VII. RECOMMENDATIONS FOR FUTURE RESEARCH

This research program has established the foundation of a long range program at Iowa State University with the following general technical objectives:

1. To develop a better understanding of the fluid flow physics related to multistage, axial-flow turbomachines. In particular, the details of the production, transport, and interaction of rotor and stator wakes including the effects of main and secondary flows and boundary layers on these wakes will be examined and modeled.
2. To assess the influence of circumferential positioning of the rows of blades in a multistage, axial-flow turbomachine on the aerodynamic performance, acoustic characteristics and aeromechanical interactions involved.
3. To improve turbomachine fluid flow measuring techniques and equipment.
4. To incorporate research results of the above mentioned objectives into turbomachine design procedures.

Several specific suggestions for the continuation of research in this area follow.

Further detailed flow field measurements utilizing the hot-wire anemometry measurement technique developed during the present investigation should be made ahead of and behind each blade row of the research compressor. In order to complement the data already acquired, periodic-average circumferential survey data should be obtained at the same

compressor operating condition at spanwise increments of 10% from hub to tip for several periodic frozen rotor positions. The use of both frozen rotor-blade and passing rotor-blade flow field survey methods should be considered. After a complete set of data has been obtained at the minimum noise condition, further data at the maximum noise condition would be useful for assessing the influence of circumferential positioning of the blade rows.

Continual development in data presentation technique would facilitate data interpretation. Although the velocity vector graph technique is an effective blade-to-blade plane flow visualization technique, three-dimensional display methods similar to those used by Hirsch and Kool (20) and Whitfield, Kelly and Barry (18) should be considered. In addition, the movie sequence approach of Peacock and Overli (34) appears to be an excellent technique for visualizing unsteady rotor and stator wake behavior.

In order to supplement the cobra probe and hot-wire anemometer data, instantaneous and periodic-average total-pressure data obtained with a fast-response total-pressure probe could be used to determine the unsteady loss and static pressure distribution.

The feasibility of determining a minimum noise rotor-row circumferential placement schedule should be considered based on the data related to minimum and maximum noise stationary blade row circumferential placement.

Once a sufficient amount of data has been obtained at the one compressor operating condition, further data at other operating conditions such as near stall or stall would be of value.

The following modifications and additions to the research compressor and related instrumentation would enhance the research capabilities of the facility:

The present scope of the three-dimensional hot-wire anemometer technique should be further developed so that random unsteadiness levels and spectra within the research compressor flow field can be measured.

The probe measurement stations between the blade rows should be modified to allow axial development surveys. This would make possible the study of the development of the flow between the blade rows in the flow direction and permit the individual effects of potential flow and viscous wake interaction to be appreciated.

The mounting of miniature, fast-response, surface pressure transducers on the stator and rotor blade surfaces would allow the acquisition of blade surface fluctuation data (random and periodic) and provide valuable information about the flow within the blade rows.

Finally, in order to further study the compressor blade vibration characteristics, strain gages should be mounted on the rotor blades and measurements made to supplement stator blade strain-gage data.

VIII. BIBLIOGRAPHY

1. Meyer, R. X. "The Effect of Wakes on the Transient Pressure and Velocity Distributions in Turbomachines." Transactions of the ASME 80(1958): 1544-1552.

2. Smith, L. H., Jr. "Wake Dispersion in Turbomachines." Transactions of the ASME 88D (Journal of Basic Engineering) (1966): 688-690.

3. Kerrebrock, J. L. and Mikolajczak, A. A. "Intra-Stator Transport of Rotor Wakes and Its Effect on Compressor Performance." Transactions of the ASME 92A (Journal of Engineering for Power) (1970): 359-368.

4. Parker, R. and Watson, J. F. "Interaction Effects Between Blade Rows in Turbomachines." Heat and Fluid Flow 2 (No. 1) (1972): 33-42.

5. Walker, G. J. and Oliver, A. R. "The Effect of Interaction Between Wakes from Blade Rows in an Axial Flow Compressor on the Noise Generated by Blade Interaction." Transactions of the ASME 94A (Journal of Engineering for Power) (1972): 241-248.

6. Kiock, R. "Turbulence Downstream of Stationary and Rotating Cascades." ASME Paper No. 73-GT-80, 1973.

7. Lockhart, R. C. and Walker, G. J. "The Influence of Viscous Interactions on the Flow Downstream of an Axial Compressor Stage." Proceedings of the 2nd International Symposium on Air Breathing Engines. University of Sheffield, Royal Aeronautical Society, London, 1974.

8. Mikolajczak, A. A. "The Practical Importance of Unsteady Flow." Pratt and Whitney Aircraft, Division of United Technologies. East Hartford, Connecticut, September 1975.

9. Fincher, H. M. "Fan-Noise, the Effect of a Single Upstream Stator." Journal of Sound and Vibration 3 (No. 1) (1966): 100-110.

10. Doak, P. E. and Vaidya, P. G. "A Note on the Relative Importance of Discrete Frequency and Broad Band Noise Generating Mechanisms in Axial Fans." Journal of Sound and Vibration 9 (No. 2) (1969): 192-196.

11. Sofrin, T. G. "Aircraft Turbomachinery Noise, Fan Noise." Notes from the Course in the Fluid Dynamics of Turbomachinery. Iowa State University, Ames, Iowa, 1973.

12. Evans, R. L. "Turbulence and Unsteadiness Measurements Downstream of a Moving Blade Row." Transactions of the ASME 97A (Journal of Engineering for Power) (1975): 131-139.

13. Raj, R. and Lakshminarayana, B. "Three Dimensional Characteristics of Turbulent Wakes Behind Rotors of Axial Flow Turbomachinery." Transactions of the ASME 98A (Journal of Engineering for Power) (1976): 218-228.

14. Horlock, J. H. "Turbomachinery Noise Technology." Transactions of the ASME 97I (Journal of Fluids Engineering) (1975): 283-284.

15. Tyler, J. M. and Sofrin, T. G. "Axial Flow Compressor Noise Studies." Transactions of SAE 70 (1962): 309-332.

16. Okapuu, U. "Some Results from Tests on a High Work Axial Gas Generator Turbine." ASME Paper No. 74-GT-81, 1974.

17. Savell, C. T. and Wells, W. R. "Rotor Design to Attenuate Flow Distortion; Part 1, A Semiactuator Disk Analysis, Part 2, An Unsteady Thin Airfoil Cascade Analysis." Transactions of the ASME 97 (Journal of Engineering for Power) (1975): 11-20 and 37-46.

18. Whitfield, C. E., Kelly, J. C. and Barry, B. "A Three-Dimensional Analysis of Rotor Wakes." The Aeronautical Quarterly 23 (1972): 285-300.

19. Thompkins, W. T., Jr. and Kerrebrock, J. L. "Exit Flow from a Transonic Compressor Rotor." in Unsteady Phenomena in Turbomachinery. AGARD CP177. 1976.

20. Hirsch, Ch. and Kool, P. "Measurement of the Three-Dimensional Flow Field Behind an Axial Compressor Stage." ASME Paper No. 76-GT-18, 1976.

21. Lieblein, S. and Roudebush, W. H. "Low-Speed Wake Characteristics of Two-Dimensional Cascade and Isolated Airfoil Sections." U.S. NACA TN 3771. 1956.

22. Silverstein, A., Katzoff, S. and Bullivant, W. K. "Downwash and Wake Behind Plain and Flapped Airfoils." NACA Report 651. 1939.

23. Pianko, M., ed. Modern Methods of Testing Rotating Components of Turbomachines (Instrumentation). AGARD-AG-207. 1975.

24. Weske, J. R. "An Investigation of the Aerodynamic Characteristics of a Rotating Axial Flow Blade Grid." NACA TN 1128. 1947.

25. Fessler, T. E. and Hartmann, M. J. "Preliminary Survey of Compressor Rotor-Blade Wakes and Other Flow Phenomena with a Hot-Wire Anemometer." NACA RM E56A13. 1956.

26. Lakshminarayana, B. and Poncet, A. "A Method of Measuring Three-Dimensional Rotating Wakes Behind Turbomachinery Rotors." Transactions of the ASME 96I (Journal of Fluids Engineering) (1974): 87-91.

27. Gorton, C. A. and Lakshminarayana, B. "A Method of Measuring the Three Dimensional Mean Flow and Turbulence Quantities Inside a Rotating Turbo-machinery Passage." ASME Paper No. 75-GT-4, 1975.

28. Perkins, J. N., Hardin, L. W., Carta, F. O. and Griffith, W. C. "Transients in Turbocompressors." School of Engineering, North Carolina State University, Raleigh, N.C., EDC-76-1. 1976.

29. Okiishi, T. H., Serovy, G. K., Kavanagh, P. and Junkhan, G. H. "Low Mach Number, Multistage Axial-Flow Research Compressor." ISU-ERI-Ames-74256. December 1974.

30. Hewlett-Packard Model 20 Math Pac. Manual Part No. 09820-70000. Loveland, Colorado: Calculator Products Division, Hewlett Packard, ca. 1970.

31. Scarborough, J. B. Numerical Mathematical Analysis. Baltimore, Maryland: The Johns Hopkins Press, 1955.

32. Champagne, F. H., Sleicher, C. A. and Wehrmann, O. H. "Turbulence Measurements with Inclined Hot-Wires Part 1. Heat Transfer Experiments with Inclined Hot-Wire." Journal of Fluid Mechanics 28 (Part 1) (1967): 153-175.

33. Thermo-Systems Instruction Manual for Model 1072 Linearizer. 2500 N. Cleveland, St. Paul, Minnesota: Thermo Systems Inc., ca. 1972.

34. Peacock, R. E. and Overli, J. "Dynamic Internal Flows in Compressors with Pressure Maldistributed Inlet Conditions." in Unsteady Phenomena in Turbomachinery. ACARD CP 177. 1976.

SYMBOLS AND NOTATION

A	compressor flow passage annulus area, m^2
$\vec{A}$	unit vector along hot-wire sensor axis (Fig. 4.8)
$b_0, b_1, b_2 \ldots b_9$	effective cooling velocity/actual velocity ratio correlation coefficients
c	blade chord length (Fig. 3.3), m
E_ℓ	linearized anemometer bridge voltage, volts
FRC	comparison of integrated and venturi volume flow rates (Eq. 12.46), percent
g	local acceleration of gravity, m/s^2
g_c	gravitational constant, 1.0 kgm/Ns^2
H	total head with respect to barometric pressure (Eq. 12.6), Nm/kg
h	static head with respect to barometric pressure, Nm/kg
h_{hg}	barometric pressure, m of Hg
i	incidence angle (Fig. 12.1; Eqs. 12.24, 12.26, and 12.28), deg
m	constant hot-wire probe turning measurement angle increment (Fig. 4.10), deg
MP	mechanical shaft power (Eq. 12.47), watt
N	number of samples per periodic average
n	random component of hot-wire signal
p	periodic component of hot-wire signal
P_1	cobra probe indicated total pressure with respect to barometric pressure, m of water
P_2	cobra probe side-tube pressure with respect to barometric pressure, m of water
P_3	cobra probe side-tube pressure with respect to barometric pressure, m of water

P_{atm}	barometric pressure (Eq. 12.1), N/m^2
P_s	static pressure with respect to barometric pressure, m of water
P_t	total pressure with respect to barometric pressure, m of water
P_w	annulus-outer surface static wall pressure with respect to barometric pressure, m of water
PHH	percent passage height from hub (Eq. 12.4), percent
Q_a	integrated volume flow rate at probe-traversing measurement stations (Eq. 12.44), m^3/s
Q_v	venturi volume flow rate (Eq. 12.42), m^3/s
R	gas constant, Nm/kg°K
r	radius from compressor axis, m
R_{cb}	cable resistance, ohms
R_{oh}	hot-wire sensor resistance overheat ratio
R_{ph}	probe holder resistance, ohms
R_{pl}	probe lead resistance, ohms
$R_{s,c,d}$	cold resistance read off anemometer resistance deck, ohms
$R_{s,op,d}$	sensor operating resistance anemometer deck setting (Eq. 4.28), ohms
RPM	rotor rotational speed, rpm
R,Y,Z	compressor coordinate system (Fig. 4.12)
S	circumferential space between blades, blade pitch (Fig. 3.3), m or deg
s	general hot-wire signal composed of periodic and random components
SPL	sound-pressure level, decibels
T	period of periodic component of hot-wire signal corresponding to rotor blade passing period, sec
t	time, s; temperature, °K

t_{baro}	barometer ambient temperature, °K
t_{max}	blade section maximum thickness/chord ratio (Fig. 3.3)
U	rotor blade velocity (Eq. 12.14), m/s
V	absolute velocity (Figs. 4.12 or 12.1; Eq. 12.12), m/s
V'	relative velocity (Eqs. 12.21 or 12.59), m/s
V_e	hot-wire effective cooling velocity (Eq. 4.13), m/s
V_r	radial component of fluid velocity (Fig. 4.12; Eq. 12.57), m/s
V_y	tangential component of absolute fluid velocity (Figs. 4.12 or 12.1; Eqs. 12.17 or 12.56), m/s
V'_y	tangential component of relative fluid velocity (Eqs. 12.19 or 12.58), m/s
V_z	axial component of fluid velocity (Figs. 4.12 or 12.1; Eqs. 12.15 or 12.55), m/s
x,y,z	hot-wire probe coordinates fixed to probe (Fig. 4.8)
Y	circumferential traversing position, degree
YO	circumferential blade-row setting position when Y is equal to zero, circumferential distance from probe-traversing measurement stations to blade stacking axis, positive in direction of rotor rotation, degree
WT	torque meter dead weight, kg
α	sensor yaw angle, angle between velocity vector and hot-wire sensor axis (Fig. 4.8; Eq. 4.12), degree
β_{mv}	approximate tangential flow angle (Fig. 4.10), degree
β_r	radial flow angle (Fig. 4.12; Eq. 4.29), degree
β_y	absolute tangential flow angle with respect to axial direction (Figs. 4.12 or 12.1; Eqs. 12.8, 12.9 or 12.53), degree
β'_y	relative tangential flow angle with respect to axial direction (Eqs. 12.23 or 12.60), degree
γ	blade stagger angle (Fig. 3.3; Table 3.1), degree

γ_{H_2O}	specific weight of water manometer fluid (Eq. 12.3), N/m^3
γ_{hg}	specific weight of mercury, N/m^3
ΔP_n	differential pressure between calibration nozzle plenum pressure and atmospheric pressure, m of water
ΔP_{vent}	differential pressure across venturi, m of water
δ	deviation angle (Fig. 12.1; Eqs. 12.25, 12.27, and 12.29), degree
η	hydraulic efficiency (Eqs. 12.37, 12.38, and 12.39)
θ_0	hot-wire sensor angle with respect to a plane normal to the probe axis (Fig. 4.8), degree
θ_{off}	measurement off-set angle (Fig. 4.10), degree
θ_p	probe pitch angle (Figs. 4.2 or 4.8), degree
θ_y	probe yaw angle (Figs. 4.2 or 4.8), degree
κ	blade angle, angle between tangent to blade camber line and axial direction (Fig. 3.3; Table 3.1), degree
ρ	density of air (Eq. 12.2), kg/m^3
σ	standard deviation of periodic-sample averages, m/s
σ_n	standard deviation of random velocity fluctuation, m/s
ϕ	flow coefficient (Eq. 12.30)
ϕ_a	integrated flow coefficient at probe-traversing measurement stations (Eq. 12.45)
ϕ_v	venturi flow coefficient (Eq. 12.43)
Ψ	head-rise coefficient (Eqs. 12.31 through 12.36)
ω	total-head loss coefficient (Eqs. 12.40 and 12.41)

Additional General Subscripts

a	hot-wire probe measurement position a
b	hot-wire probe measurement position b
c	hot-wire probe measurement position c

h	annulus inner surface, hub
i	ideal
IGV	inlet guide vane
me	mechanical
overall	overall compressor
R	rotor
S	stator
stage	stage
t	annulus outer surface, tip
1	blade-row inlet
2	blade-row outlet
1R	first rotor
2R	second rotor
3R	third rotor
1S	first stator
2S	second stator
3S	third stator

Superscripts

$\rightarrow$	vector
'	relative to rotor
$\bar{}$	average; blade-to-blade circumferential average value
~	periodically sampled and averaged
$\underline{\cdot}$	mass-averaged in the radial direction

X. APPENDIX A: PERIODIC-SAMPLING CIRCUIT DESIGN

The periodic-sampling circuit design details including a general block diagram of the logic involved, a circuit diagram of the triggering and sample-and-hold components, and a sketch of the interfacing cable connections are presented in Figures 10.1 through 10.4. The general scheme of circuit operation can be inferred from the block diagram in Figure 10.1. The circuit can be used in two modes of operation. In both cases, a 5 μsec sample of the input analog signal is obtained each time an electric pulse is received from the photoelectric triggering circuit. Switch "A" controls the manner in which the digital voltmeter and calculator interact with the triggering and sample-and-hold circuits. With the switch thrown to "CALC-DVM," the digital voltmeter is read by the calculator independently of the triggering circuit at the moment specified by the calculator. With switch "A" thrown to "interface," the digital voltmeter and calculator are synchronized with the triggering of the sample-and-hold circuit. If the signal averaging circuit is removed, and if the sampling circuit is used in the mode "A," the periodic samples can be individually retained in the calculator memory, and average and RMS values can be calculated. For this investigation, however, the signal averaging circuit was always used, and only the periodic-average signal was obtained. The fluctuating component of the signal was lost in the averaging process.

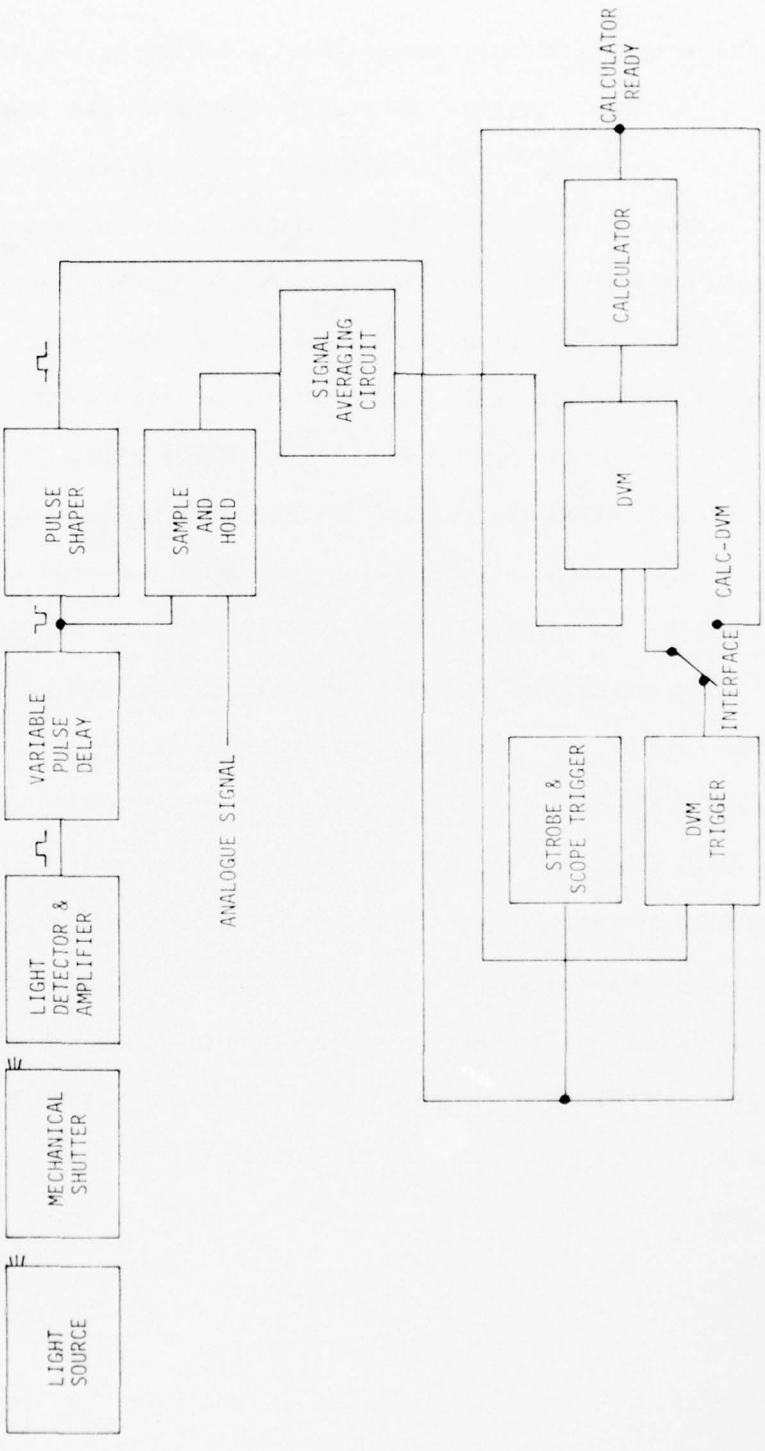


Figure 10.1. Block diagram of periodic-sampling circuit.

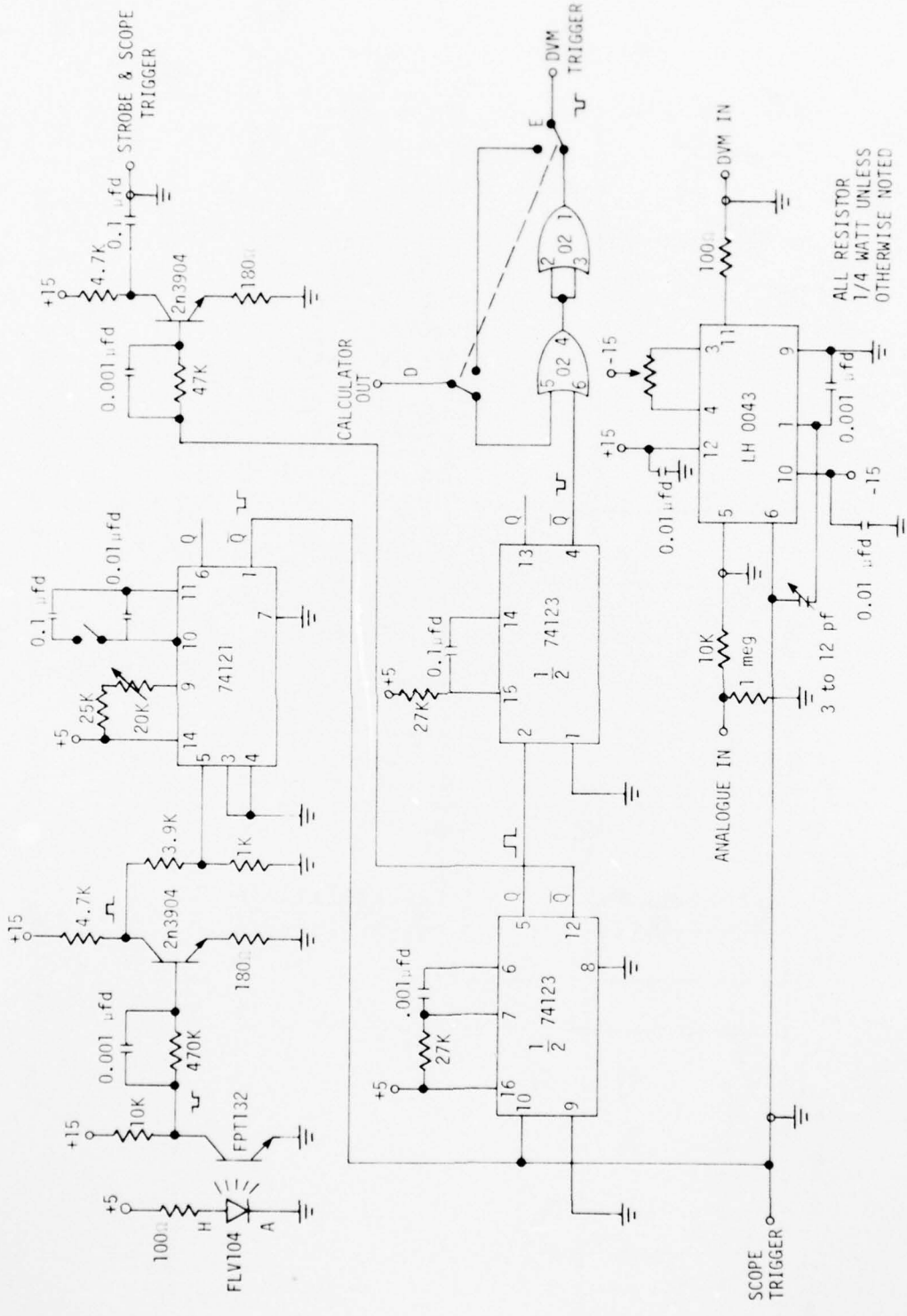


Figure 10.2. Circuit diagram of triggering and sample-and-hold circuits.

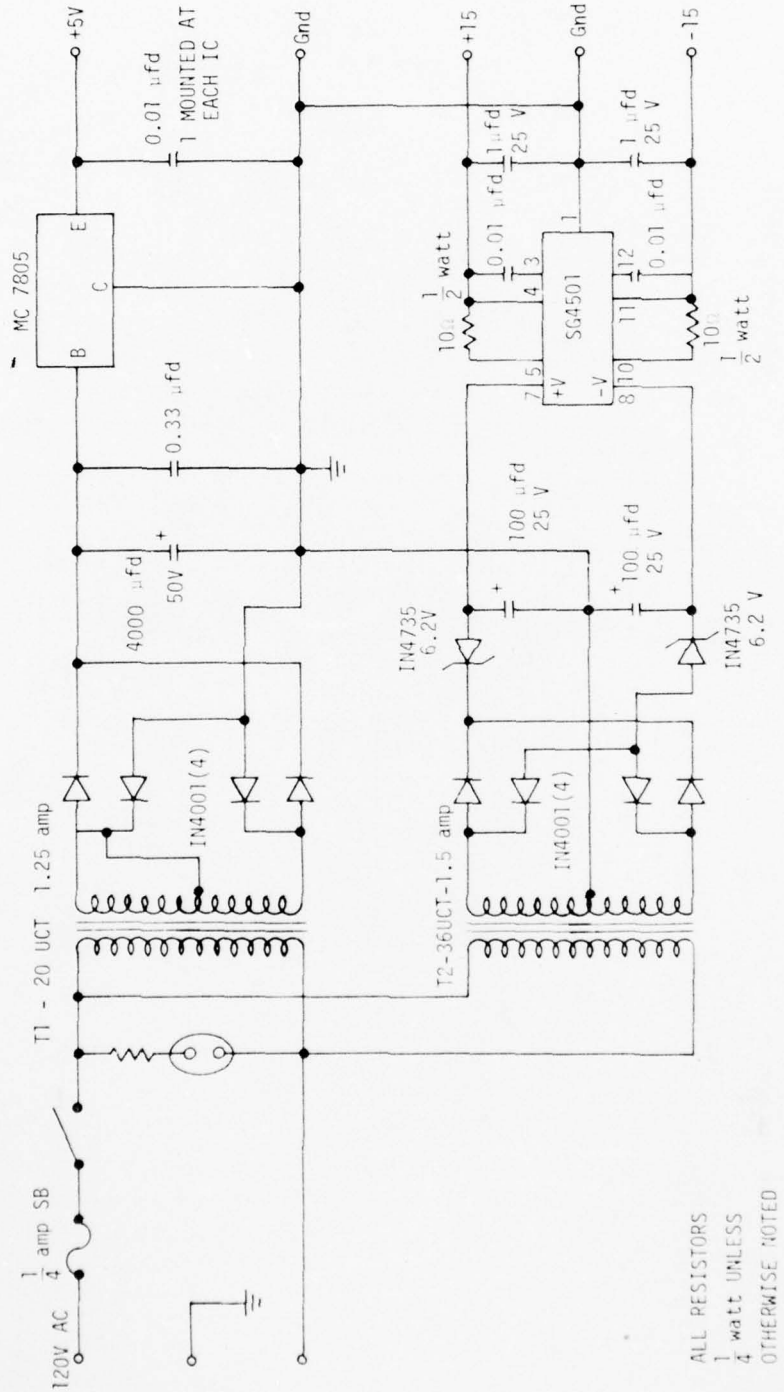


Figure 10.3. Power supply for triggering and sample-and-hold circuits.

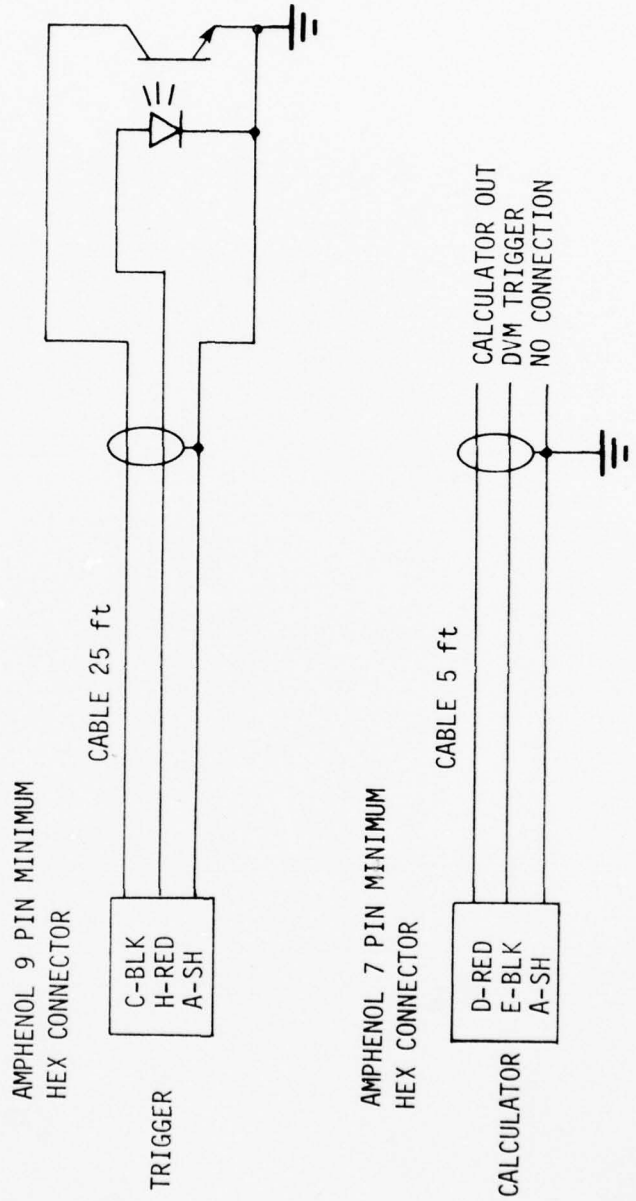


Figure 10.4. Interfacing cable connections.

XI. APPENDIX B: CALCULATOR PROGRAMS AND DATA STORAGE

The data acquisition and reduction calculator programs used in this investigation are listed in this section. These programs and all experimental data are stored on magnetic cassette tapes and are indexed according to cassette and file numbers as specified below. Due to a limitation of available calculator memory space, it was necessary in many cases to subdivide the larger programs and individually store the program parts in separate magnetic tape files.

Flow coefficient program — Calculation of compressor overall flow coefficient from flow rate venturi meter data; cassette 4C, file 16.

Actuator position correlation program — Linear least squares correlation between actuator potentiometer voltage readout and actuator motion for probe and circumferential positioning actuators; cassette 4C, file 3.

Slow-response probe survey acquisition program — Acquisition of slow-response total-pressure and flow-angle circumferential probe survey data; cassette 4C, file 4.

Wall static pressure acquisition program — Acquisition of outer annulus surface static pressure circumferential survey data; cassette 4C, file 76.

Slow-response data reduction program — Complete reduction of slow-response data to obtain point flow-field parameters, average flow-field parameters, and rotor, stator, and stage performance parameters; cassette 4C, files 0-2, 5-15, 18-75.

Slow-response data for minimum sound — Storage of circumferential survey data including probe data, outer annulus surface static-pressure data, and station 8 hub surface static-pressure data; cassette 6, files 1-79, 97-105.

Slow-response data for maximum sound — Storage of circumferential survey data including probe data and outer annulus surface static-pressure data; cassette 7, files 1-79, 97-104.

Hot-wire effective cooling velocity/actual velocity ratio calibration program Calibration of hot wire with respect to sensor yaw angle, pitch angle and velocity for the determination of the ten coefficients in Equation 4.16; consists of two parts: (1) calibration data acquisition and (2) least squares calibration data correlation; cassette 8A, file 8, 9, 11-13; cassette 8B, file 8, 9, 11-13.

Hot-wire linearizer velocity calibration program Velocity calibration to determine the four polynomial coefficients required by the anemometer linearizer through a least squares correlation of calibration data; cassette 11A, files 2-4; cassette 11B, files 2-4.

Hot-wire second order velocity calibration program Velocity calibration to determine the three coefficients in the second order velocity calibration Equation 4.13 through a least squares correlation of calibration data; cassette 11A, file 5; cassette 11B, file 5.

Fast-response hot-wire data acquisition program Acquisition of hot-wire, periodic-average, three-dimensional, circumferential survey data; cassette 11A, files 5-7; cassette 11B, file 5-7.

Fast-response hot-wire data reduction program Reduction of fast-response hot-wire data to obtain three-dimensional point flow-field parameters and circumferential blade-to-blade average flow-field parameters; cassette 11A, files 8-18; cassette 11B, files 8-18.

Fast-response hot-wire data Storage of periodic-average hot-wire data obtained with the single inclined hot-wire sensor in the research compressor; cassette 11A, files 30-52; cassette 11B, files 30-38.

XII. APPENDIX C: PARAMETER EQUATIONS

The equations used in calculating the slow-response and fast-response parameters are presented. The symbols used in the equations are defined in the symbols and notation section and the sign conventions are generally shown in Figures 4.12 and 12.1 for the fast-response and slow-response parameters, respectively. For the fast-response parameters, the sign conventions for the relative velocity, relative tangential velocity, and relative tangential flow angle are similar to those of the slow-response parameters. Parameters averaged circumferentially or radially were obtained using a spline-fit integration technique (Ref. 30).

A. General Parameters

1. Basic fluid properties

Barometric pressure, N/m^2:

$$P_{atm} = h_{hg@t_{baro}} (1.0-0.00018 (t_{baro}-273.15)) \gamma_{hg@273°K} \tag{12.1}$$

Density of air, kg/m^3:

$$\rho = \frac{P_{atm}}{R\ t} \tag{12.2}$$

Specific weight of water, N/m^3:

$$\gamma_{H_2O} = \frac{g}{g_c} \left(996.86224 + 0.1768124\left(\frac{9}{5}\ t - 459.67\right) - 2.64966 \times 10^{-3} \left(\frac{9}{5}\ t - 459.67\right)^2 + 5.00063 \times 10^{-6}\left(\frac{9}{5}\ t - 459.67\right)^3 \right) \tag{12.3}$$

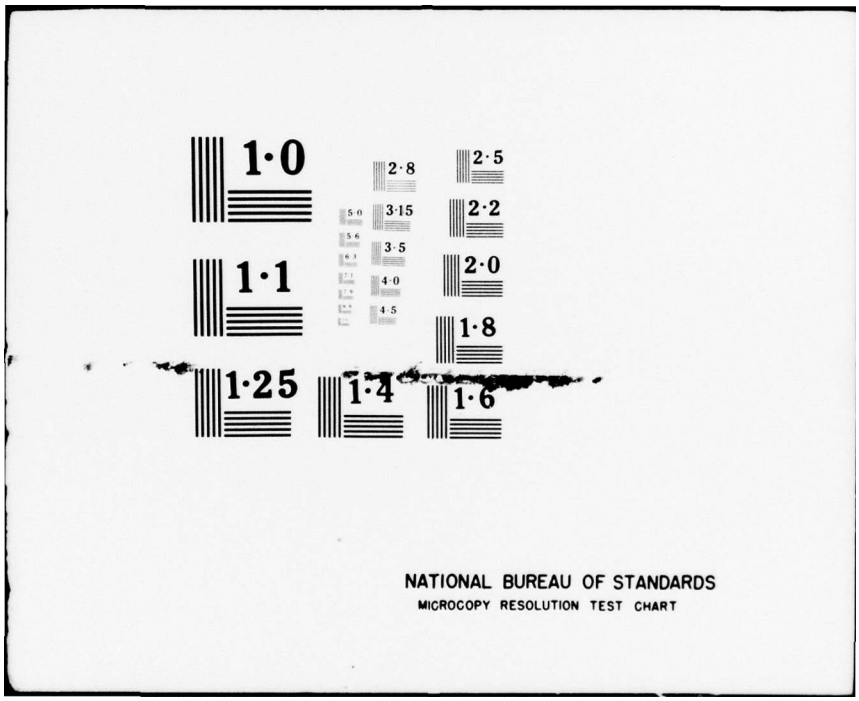
AD-A041 108 IOWA STATE UNIV AMES ENGINEERING RESEARCH INST F/G 13/7
MULTISTAGE AXIAL-FLOW TURBOMACHINERY WAKE PRODUCTION, TRANSPORT--ETC(U)
NOV 76 D P SCHMIDT, T H OKIISHI AF-AFOSR-2916-76
UNCLASSIFIED ISU-ERI-AMES-77130 AFOSR-TR-77-0720 NL

3 OF 3
ADA
041108



END

DATE
FILMED
7-77


1·0
1·1
1·25
1·4
1·6
1·8
2·0
2·2
2·5
2·8
3·15
3·5
4·0
4·5
5·0
5·6
6·3
7·1
8·0
9·0
NATIONAL BUREAU OF STANDARDS
MICROCOPY RESOLUTION TEST CHART

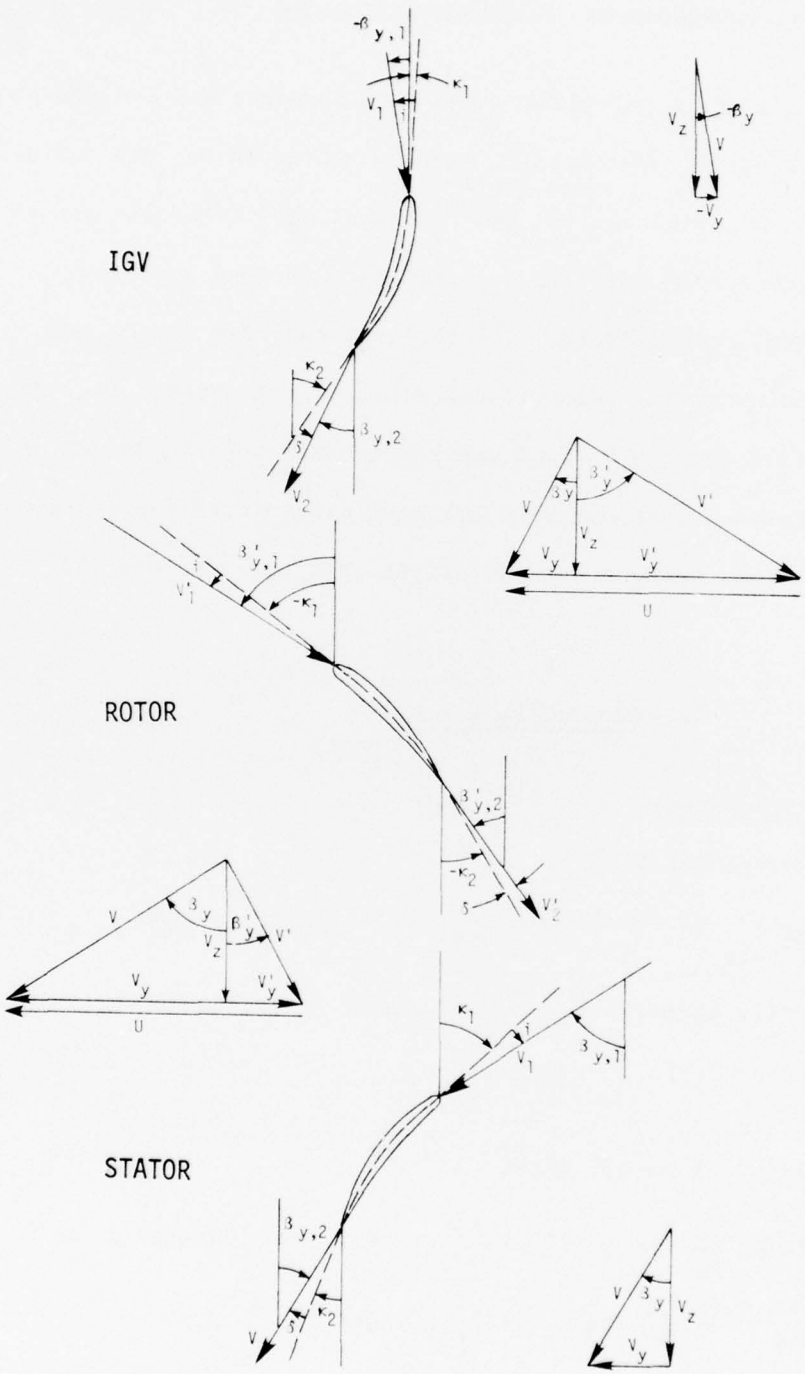


Figure 12.1. Sketch showing nomenclature, sign convention, and velocity triangles for slow-response instrument parameters.

2. Blade-element quantity

Percent passage height from hub:

$$PHH = \left(\frac{r-0.14224}{0.06096}\right) \times 100 \tag{12.4}$$

3. Miscellaneous

Calibration nozzle jet velocity, m/s

$$V = \sqrt{\frac{2g_c\gamma_{H_2O}\Delta P_n}{\rho}} \tag{12.5}$$

B. Slow-Response Instrument Parameters

1. Point and circumferential-average blade-element quantities

Total head, Nm/kg:

$$H = \frac{P_t\gamma_{H_2O}}{\rho} \tag{12.6}$$

and

$$\overline{H} = \frac{1}{S_S}\int_0^{S_S} H\, dY \tag{12.7}$$

Absolute tangential flow angle behind rotors (see Figure 12.1 for sign convention), degrees:

$$\overline{\beta_y} = \frac{1}{S_S}\int_0^{S_S} \beta_y dY \tag{12.8}$$

Absolute tangential flow angle behind stationary blade rows (see Figure 12.1 for sign convention), degrees:

$$\overline{\beta_y} = \frac{1}{Y_{\text{freestream}}}\int_{\substack{\text{across}\\ \text{freestream}}} \beta_y dY \tag{12.9}$$

Annulus outer surface static wall pressure, meters of water:

$$\overline{P_w} = \frac{1}{S_S} \int_0^{S_S} P_w dY \tag{12.10}$$

Static head (radial equilibrium equation), Nm/kg:

$$\frac{d\bar{h}}{dr} = \frac{2 \sin^2 \bar{\beta}_y (\bar{H}-\bar{h})}{r} \tag{12.11}$$

Absolute fluid velocity, m/s:

$$V = \sqrt{2 g_c (H-\bar{h})} \tag{12.12}$$

and

$$\bar{V} = \frac{1}{S_S} \int_0^{S_S} V \, dY \tag{12.13}$$

Blade velocity, m/s:

$$U = \frac{r\pi RPM}{30.0} \tag{12.14}$$

Axial component of fluid velocity, m/s:

$$V_z = V\cos \bar{\beta}_y \tag{12.15}$$

and

$$\bar{V}_z = \bar{V}\cos \bar{\beta}_y \tag{12.16}$$

Tangential component of absolute fluid velocity (see Figure 12.1 for sign convention), m/s:

$$V_y = V\sin \bar{\beta}_y \tag{12.17}$$

and

$$\bar{V}_y = \bar{V}\sin \bar{\beta}_y \tag{12.18}$$

Tangential component of relative fluid velocity (see Figure 12.1 for sign convention), m/s:

$$V'_y = U - V_y \tag{12.19}$$

and

$$\overline{V}'_y = U - \overline{V}_y \tag{12.20}$$

Relative fluid velocity, m/s:

$$V' = \sqrt{(V'_y)^2+(V_z)^2} \tag{12.21}$$

and

$$\overline{V}' = \sqrt{(\overline{V}'_y)^2+(\overline{V}_z)^2} \tag{12.22}$$

Relative tangential flow angle (see Figure 12.1 for sign convention), degrees:

$$\overline{\beta}'_y = \sin^{-1}\left(\frac{\overline{V}'_y}{\overline{V}'}\right) \tag{12.23}$$

Incidence angle for IGV (see Figure 12.1 for sign convention), degrees:

$$\overline{i}_{IGV} = \kappa_{1,IGV} - \overline{\beta}_{y,1,IGV} \tag{12.24}$$

Deviation angle for IGV (see Figure 12.1 for sign convention), degrees:

$$\overline{\delta}_{IGV} = \kappa_{2,IGV} - \overline{\beta}_{y,2,IGV} \tag{12.25}$$

Incidence angle for rotors (see Figure 12.1 for sign convention), degrees:

$$\overline{i}_R = \kappa_{1,R} + \overline{\beta}'_{y,1,R} \tag{12.26}$$

Deviation angle for rotors (see Figure 12.1 for sign convention), degrees:

$$\overline{\delta}_R = \kappa_{2,R} + \overline{\beta}'_{y,2,R} \tag{12.27}$$

Incidence angle for stators (see Figure 12.1 for sign convention), degrees:

$$\overline{i}_S = \overline{\beta}_{y,1,S} - \kappa_{1,S} \tag{12.28}$$

Deviation angle for stators (see Figure 12.1 for sign convention), degrees:

$$\overline{\delta}_S = \overline{\beta}_{y,2,S} - \kappa_{2,S} \tag{12.29}$$

Flow coefficient:

$$\overline{\phi} = \frac{\overline{V}_z}{U_t} \tag{12.30}$$

Actual head-rise coefficient for rotor:

$$\Psi_R = \frac{g_c(\bar{H}_{2,R} - \bar{H}_{1,R})}{U_t^2} \tag{12.31}$$

Actual head-rise coefficient for stage:

$$\Psi_{stage} = \frac{g_c(\bar{H}_{2,S} - \bar{H}_{1,R})}{U_t^2} \tag{12.32}$$

Actual head-rise coefficient for overall compressor:

$$\Psi_{overall} = \frac{g_c(\bar{H}_{2,3S} - \bar{H}_{1,IGV})}{U_t^2} \tag{12.33}$$

Ideal head-rise coefficient for rotor:

$$\Psi_{i,R} = \frac{U(\bar{V}_{y,2,R} - \bar{V}_{y,1,R})}{U_t^2} \tag{12.34}$$

Ideal head-rise coefficient for stage:

$$\Psi_{i,stage} = \frac{U(\bar{V}_{y,1,S} - \bar{V}_{y,1,R})}{U_t^2} \tag{12.35}$$

Ideal head-rise coefficient for overall compressor:

$$\Psi_{i,overall} = \Psi_{i,1R} + \Psi_{i,2R} + \Psi_{i,3R} \tag{12.36}$$

Hydraulic efficiency for rotor:

$$\eta_R = \frac{\Psi_R}{\Psi_{i,R}} \tag{12.37}$$

Hydraulic efficiency for stage:

$$\eta_{stage} = \frac{\Psi_{stage}}{\Psi_{i,stage}} \tag{12.38}$$

Hydraulic efficiency for overall compressor:

$$\eta_{overall} = \frac{\Psi_{overall}}{\Psi_{i,overall}} \tag{12.39}$$

Total-head loss coefficient for rotor:

$$\omega_R = 2(\Psi_{i,R} - \Psi_R) \frac{U_t^2}{(\overline{V}'_{1,R})^2} \tag{12.40}$$

Total-head-loss coefficient for stator:

$$\omega_S = -2g_c \frac{(\overline{H}_{2,S} - \overline{H}_{1,S})}{(\overline{V}_{1,S})^2} \tag{12.41}$$

2. Global parameters

Venturi volume flow rate, m^3/s:

$$Q_v = 0.05229 \sqrt{\frac{2g_c \gamma_{H_2O} \Delta P_{vent}}{\rho}} \tag{12.42}$$

Venturi flow coefficient:

$$\phi_v = \frac{Q_v}{A\ U_t} \tag{12.43}$$

Integrated volume flow rate at probe-traversing measurement stations, m^3/s:

$$Q_a = 2\pi \int_{r_h}^{r_t} \overline{V}_z\ r\ dr \tag{12.44}$$

Integrated flow coefficient at probe-traversing measurement stations:

$$\phi_a = \frac{Q_a}{A\ U_t} \tag{12.45}$$

Integrated and venturi flow-rate comparison, percent:

$$FRC = \frac{Q_a - Q_v}{Q_v} \times 100 \tag{12.46}$$

Mechanical shaft power, watts:

$$MP = 0.2589\ WT \cdot RPM \tag{12.47}$$

General radial mass-average parameter equation (let ξ be any general parameter):

$$\dot{\bar{\xi}} = \frac{\int_{0.148}^{0.197} \xi\ \bar{V}_{z,2}\ r\ dr}{\int_{0.148}^{0.197} \bar{V}_{z,2}\ r\ dr} \tag{12.48}$$

Mechanical efficiency:

$$\eta_{me} = \frac{\rho(\dot{\bar{H}}_{2,3S} - \dot{\bar{H}}_{1,IGV})Q_v}{MP} \tag{12.49}$$

C. Three-Dimensional Fast-Response Hot-Wire Parameters

Effective cooling velocity, m/s:

$$V_e = K_1 + K_2 E_\ell\ K_3 E_\ell^{\,2} \tag{12.50}$$

Sensor yaw angle relationship (see Figure 4.12):

$$\cos\alpha = \cos\theta_0 \cos\theta_p \cos\theta_y + \sin\theta_0 \sin\theta_p \tag{12.51}$$

Effective cooling velocity/actual velocity ratio:

$$\frac{V_e}{V} = b_0 + b_1\alpha + b_2\theta_p + b_3 V + b_4\alpha^2$$
$$b_5\theta_p^{\,2} + b_6 V^2 + b_7\alpha\theta_p + b_8\alpha V + b_9\theta_p V \tag{12.52}$$

Absolute tangential flow angle (see Figure 4.12 for sign convention), degrees:

$$\beta_y = \beta_{mv} + \theta_{a,off} + \theta_y \tag{12.53}$$

Radial flow angle (see Figure 4.12 for sign convention), degrees:

$$\beta_r = -\theta_p \tag{12.54}$$

Axial component of fluid velocity, m/s:

$$V_z = V \cos \beta_r \cos \beta_y \tag{12.55}$$

Tangential component of absolute fluid velocity (see Figure 4.12 for sign convention), m/s:

$$V_y = V \cos \beta_r \sin \beta_y \tag{12.56}$$

Radial component of fluid velocity (see Figure 4.12 for sign convention), m/s:

$$V_r = V \sin \beta_r \tag{12.57}$$

Tangential component of relative fluid velocity (similar to sign convention in Figure 12.1), m/s:

$$V'_y = U - V_y \tag{12.58}$$

Relative fluid velocity, m/s:

$$V' = \sqrt{(V'_y)^2 + (V_z)^2} \tag{12.59}$$

Relative tangential flow angle (similar to sign convention in Figure 12.1), degrees:

$$\beta'_y = \sin^{-1}\left(\frac{V'_y}{V'}\right) \tag{12.60}$$

General blade-to-blade circumferential integrated average (let ξ be any general parameter) for a blade element:

$$\bar{\xi} = \frac{1}{S_S} \int_0^{S_S} \xi \, dY \tag{12.61}$$

XIII. APPENDIX D: LEAST SQUARES EMPIRICAL CORRELATION FOR EFFECTIVE COOLING VELOCITY RATIO

The effective cooling velocity to actual velocity ratio, V_e/V, as a function of sensor yaw angle α, pitch angle θ_p, and velocity V, was predicted with the empirical relationship

$$\frac{V_e}{V} = b_0 + b_1\alpha + b_2\theta_p + b_3V + b_4\alpha^2 + b_5\theta_p^2 + b_6V^2 + b_7\alpha\theta_p + b_8\alpha V + b_9\theta_p V \qquad (13.1)$$

where the coefficients b_0 through b_9 were determined from a least squares fit of effective cooling velocity calibration data

$$((V_e/V)_1,\alpha_1,\theta_{p1},V_1),((V_e/V)_2,\alpha_2,\theta_{p2},V_2), \ldots, ((V_e/V)_n,\alpha_n,\theta_{pn},V_n)$$

where n = the number of calibration data points.

In this section, the least squares technique and related equations required to determine the ten coefficients in Equation 13.1 from the calibration data are developed.

Corresponding to each calibration data point, there are two values of V_e/V: the experimentally measured value $(V_e/V)_{exp}$, and the value predicted by the empirical relation Equation 13.1, $(V_e/V)_{pre}$. The difference between these two values is defined as the deviation, ε

$$\varepsilon = (V_e/V)_{pre} - (V_e/V)_{exp} \qquad (13.2)$$

The method of least squares requires that the sum of squares of the deviations for all calibration data points

$$F = \sum_{i=1}^{i=n} \varepsilon_i^2 \qquad (13.3)$$

be a minimum. This is accomplished by solving the following ten simultaneous equations:

$$\frac{\partial F}{\partial b_0} = 0 \tag{13.4}$$

$$\frac{\partial F}{\partial b_1} = 0 \tag{13.5}$$

$$\frac{\partial F}{\partial b_2} = 0 \tag{13.6}$$

$$\frac{\partial F}{\partial b_3} = 0 \tag{13.7}$$

$$\frac{\partial F}{\partial b_4} = 0 \tag{13.8}$$

$$\frac{\partial F}{\partial b_5} = 0 \tag{13.9}$$

$$\frac{\partial F}{\partial b_6} = 0 \tag{13.10}$$

$$\frac{\partial F}{\partial b_7} = 0 \tag{13.11}$$

$$\frac{\partial F}{\partial b_8} = 0 \tag{13.12}$$

$$\frac{\partial F}{\partial b_9} = 0 \tag{13.13}$$

The ten simultaneous linear equations, which were obtained by carrying out the required partial differentiation, are displayed in matrix form in Equation 13.14. The ten coefficients, b_0 through b_9, in Equation 13.1 can be obtained by solving this matrix set.

Table 13.1. Equation 13.14.

$$
\begin{bmatrix}
n & \Sigma\alpha & \Sigma\theta_p & \Sigma V & \Sigma\alpha^2 & \Sigma\theta_p^2 & \Sigma V^2 & \Sigma\alpha\theta_p & \Sigma\alpha V & \Sigma\theta_p V \\
\Sigma\alpha & \Sigma\alpha^2 & \Sigma\theta_p\alpha & \Sigma V\alpha & \Sigma\alpha^3 & \Sigma\theta_p^2\alpha & \Sigma V^2\alpha & \Sigma\alpha^2\theta_p & \Sigma\alpha^2 V & \Sigma\theta_p V\alpha \\
\Sigma\theta_p & \Sigma\alpha\theta_p & \Sigma\theta_p^2 & \Sigma V\theta_p & \Sigma\alpha^2\theta_p & \Sigma\theta_p^3 & \Sigma V^2\theta_p & \Sigma\alpha\theta_p^2 & \Sigma\alpha V\theta_p & \Sigma\theta_p^2 V \\
\Sigma V & \Sigma\alpha V & \Sigma\theta_p V & \Sigma V^2 & \Sigma\alpha^2 V & \Sigma\theta_p^2 V & \Sigma V^3 & \Sigma\alpha\theta_p V & \Sigma\alpha V^2 & \Sigma\theta_p V^2 \\
\Sigma\alpha^2 & \Sigma\alpha^3 & \Sigma\theta_p\alpha^2 & \Sigma V\alpha^2 & \Sigma\alpha^4 & \Sigma\theta_p^2\alpha^2 & \Sigma V^2\alpha^2 & \Sigma\alpha^3\theta_p & \Sigma\alpha^3 V & \Sigma\theta_p V\alpha^2 \\
\Sigma\theta_p^2 & \Sigma\alpha\theta_p^2 & \Sigma\theta_p^3 & \Sigma V\theta_p^2 & \Sigma\alpha^2\theta_p^2 & \Sigma\theta_p^4 & \Sigma V^2\theta_p^2 & \Sigma\alpha\theta_p^3 & \Sigma\alpha\theta_p^2 V & \Sigma\theta_p^3 V \\
\Sigma V^2 & \Sigma\alpha V^2 & \Sigma\theta_p V^2 & \Sigma V^3 & \Sigma\alpha^2 V^2 & \Sigma\theta_p^2 V^2 & \Sigma V^4 & \Sigma\alpha\theta_p V^2 & \Sigma\alpha V^3 & \Sigma\theta_p V^3 \\
\Sigma\alpha\theta_p & \Sigma\alpha^2\theta_p & \Sigma\theta_p^2\alpha & \Sigma V\alpha\theta_p & \Sigma\alpha^3\theta_p & \Sigma\theta_p^3\alpha & \Sigma V^2\theta_p\alpha & \Sigma\alpha^2\theta_p^2 & \Sigma\alpha^2\theta_p V & \Sigma\theta_p^2 V\alpha \\
\Sigma\alpha V & \Sigma\alpha^2 V & \Sigma\theta_p\alpha V & \Sigma V^2\alpha & \Sigma\alpha^3 V & \Sigma\theta_p^2\alpha V & \Sigma V^3\alpha & \Sigma\alpha^2\theta_p V & \Sigma\alpha^2 V^2 & \Sigma\theta_p V^2\alpha \\
\Sigma\theta_p V & \Sigma\alpha\theta_p V & \Sigma\theta_p^2 V & \Sigma V^2\theta_p & \Sigma\alpha^2\theta_p V & \Sigma\theta_p^3 V & \Sigma V^3\theta_p & \Sigma\alpha\theta_p^2 V & \Sigma\alpha V^2\theta_p & \Sigma\theta_p^2 V^2
\end{bmatrix}
\begin{bmatrix} b_0 \\ b_1 \\ b_2 \\ b_3 \\ b_4 \\ b_5 \\ b_6 \\ b_7 \\ b_8 \\ b_9 \end{bmatrix}
=
\begin{bmatrix} \Sigma V_e/V \\ \Sigma\alpha V_e/V \\ \Sigma\theta_p V_e/V \\ \Sigma V V_e/V \\ \Sigma\alpha^2 V_e/V \\ \Sigma\theta_p^2 V_e/V \\ \Sigma V^2 V_e/V \\ \Sigma\alpha\theta_p V_e/V \\ \Sigma\alpha V V_e/V \\ \Sigma\theta_p V V_e/V \end{bmatrix}
$$

XIV. APPENDIX E: TABULATION OF SLOW-RESPONSE DATA

The slow-response data for minimum and maximum noise conditions obtained at stations ahead of and behind each blade row for each of nine passage height locations are tabulated in this section. All data were obtained at a rotor speed of 1400 rpm and a flow coefficient of 0.42. The measured point-by-point circumferential distributions of total head are listed in Tables 14.1 and 14.2. In Tables 14.3 and 14.4 the blade-to-blade circumferential-average values of total head, static head, absolute tangential flow angle, and incidence and deviation angles are tabulated for each blade span location. Finally, the circumferential-average outer-annulus-surface static head values measured with the outer wall taps are given in Table 14.5 for each measurement station. The axial locations of the measurement stations with respect to the blade rows are depicted in Figure 3.1. Total head and static head are given with respect to atmospheric pressure. The sign conventions for tangential flow angle, incidence angle, and deviation angle are specified in Figure 12.1. The definitions of the Fortran variables used in the computer output listing of Tables 14.1 and 14.2 are listed at the beginning of the two tables. A complete listing of mathematical symbols is presented in the symbols and notation section.

Table 14.1. Point-by-point circumferential distributions of total head for minimum noise condition.

STATION 1

Y/SS	HT N*M/KG	Y/SS	HT N*M/KG	Y/SS	HT N*M/KG	Y/SS	HT N*M/KG	Y/SS	HT N*M/KG
PHH=10.00		PHH=20.00		PHH=30.00		PHH=40.00		PHH=50.00	
HS= -86.95		HS= -86.95		HS= -86.95		HS= -86.95		HS= -86.95	
0.000	0.43	0.000	0.43	0.000	0.00	0.000	0.21	0.000	0.21
0.217	0.43	0.213	0.43	0.217	0.22	0.217	0.21	0.219	0.21
0.428	0.00	0.420	1.08	0.425	0.00	0.425	0.00	0.421	0.21
0.623	0.00	0.622	1.08	0.621	0.00	0.624	0.00	0.633	0.00
0.832	0.43	0.832	1.08	0.834	0.22	0.833	0.00	0.826	0.00
1.000	0.00	1.000	0.43	1.000	0.22	1.000	0.00	1.000	0.00
PHH=60.00		PHH=70.00		PHH=80.00		PHH=90.00			
HS= -86.94		HS= -86.94		HS= -86.94		HS= -86.94			
0.000	-0.00	0.000	-0.00	0.000	-1.72	0.000	-8.63		
0.209	0.22	0.213	-0.00	0.212	-3.23	0.212	-7.55		
0.417	-0.00	0.437	-0.00	0.425	-2.59	0.421	-8.19		
0.631	-0.00	0.629	-0.22	0.625	-2.59	0.626	-8.19		
0.836	-0.00	0.833	-0.00	0.834	-1.94	0.840	-7.55		
1.000	-0.00	1.000	-0.00	1.000	-2.59	1.000	-9.06		

Y/SS = Circumferential spacing, Y/S_S.

HT = Total head with respect to atmospheric pressure, H, N·m/kg.

PHH = Percent passage height from hub, PHH.

HS = Static head with respect to atmospheric pressure, h, N·m/kg.

Table 14.1 Continued.

STATION 2

Y/SS	HT N*M/KG	Y/SS	HT N*M/KG	Y/SS	HT N*M/KG	Y/SS	HT N*M/KG	Y/SS	HT N*M/KG
PHH=10.00		PHH=20.00		PHH=30.00		PHH=40.00		PHH=50.00	
HS=-112.33		HS=-111.03		HS=-109.84		HS=-108.78		HS=-107.84	
0.000	0.00	0.000	-0.43	0.000	-0.00	0.000	0.00	0.000	-0.44
0.107	0.00	0.103	-0.43	0.102	-0.00	0.102	0.00	0.103	-0.44
0.211	0.00	0.206	-0.43	0.207	-0.00	0.206	0.00	0.205	-0.44
0.316	0.00	0.308	-0.43	0.311	-0.00	0.312	0.00	0.309	-0.44
0.412	0.00	0.411	-0.43	0.413	-0.00	0.410	0.00	0.410	-0.44
0.444	-0.43	0.488	-2.59	0.514	-1.08	0.546	-1.08	0.514	-0.44
0.484	-10.86	0.515	-8.64	0.558	-13.41	0.591	-10.82	0.598	-2.17
0.518	-38.03	0.569	-47.52	0.604	-47.14	0.632	-44.37	0.647	-24.28
0.556	-72.14	0.597	-71.28	0.633	-77.85	0.663	-79.01	0.676	-53.06
0.589	-95.83	0.627	-86.40	0.658	-95.15	0.697	-92.00	0.696	-75.79
0.617	-96.92	0.649	-91.80	0.709	-73.53	0.717	-82.25	0.717	-85.54
0.648	-83.66	0.675	-75.60	0.737	-38.93	0.755	-47.62	0.767	-56.31
0.679	-76.05	0.719	-42.12	0.786	-8.22	0.793	-14.07	0.788	-41.14
0.699	-67.36	0.732	-25.92	0.820	-3.89	0.848	-1.73	0.817	-13.43
0.716	-47.81	0.813	-2.16	0.916	-0.43	0.910	-0.43	0.853	-3.90
0.760	-26.07	0.911	-1.08	1.000	-0.43	1.000	0.00	0.923	-1.73
0.802	-10.43	1.000	-0.43					1.000	-0.44
0.847	-1.73								
0.904	-0.43								
0.952	-0.43								
1.000	0.00								
PHH=60.00		PHH=70.00		PHH=80.00		PHH=90.00			
HS=-106.98		HS=-106.18		HS=-105.42		HS=-104.79			
0.000	0.00	0.000	-0.43	0.000	-4.33	0.000	-13.03		
0.104	0.00	0.102	-0.43	0.102	-4.33	0.104	-11.94		
0.210	-0.22	0.208	-0.65	0.206	-4.33	0.208	-10.86		
0.308	-0.22	0.310	-1.08	0.310	-2.60	0.308	-10.86		
0.409	-0.43	0.411	-1.08	0.414	-2.17	0.411	-9.12		
0.514	-0.43	0.514	-0.43	0.516	-2.38	0.516	-8.25		
0.608	-1.08	0.626	-2.16	0.611	-2.60	0.616	-8.69		
0.648	-10.83	0.656	-8.66	0.668	-10.39	0.686	-11.29		
0.680	-34.22	0.688	-31.40	0.701	-33.56	0.708	-26.50		
0.707	-55.23	0.713	-45.48	0.718	-42.22	0.725	-46.04		
0.731	-64.98	0.749	-44.40	0.735	-43.31	0.746	-65.59		
0.771	-48.73	0.764	-42.23	0.751	-32.48	0.773	-72.75		
0.798	-32.40	0.780	-21.66	0.774	-22.73	0.795	-59.72		
0.816	-12.99	0.811	-8.66	0.794	-14.07	0.816	-39.09		
0.863	-2.16	0.833	-4.33	0.812	-7.58	0.831	-36.92		
0.919	-1.08	0.923	-1.08	0.856	-4.33	0.859	-24.97		
1.000	-0.43	1.000	-1.08	0.919	-3.90	0.902	-15.64		
				1.000	-4.33	0.961	-13.47		
						1.000	-11.94		

Table 14.1. Continued.

STATION 3

Y/SS	HT N*M/KG	Y/SS	HT N*M/KG	Y/SS	HT N*M/KG	Y/SS	HT N*M/KG	Y/SS	HT N*M/KG
PHH=10.00		PHH=20.00		PHH=30.00		PHH=40.00		PHH=50.00	
HS= -30.10		HS= -18.61		HS= -8.69		HS= 0.01		HS= 7.77	
0.000	199.94	0.000	208.36	0.000	225.47	0.000	216.71	0.000	196.53
0.103	191.83	0.111	197.84	0.110	221.52	0.105	225.48	0.103	206.85
0.212	185.91	0.205	188.62	0.208	213.84	0.206	225.91	0.209	219.15
0.315	195.25	0.311	182.04	0.314	203.54	0.308	221.53	0.308	222.88
0.410	191.83	0.415	183.14	0.414	191.25	0.411	214.95	0.411	220.03
0.514	199.50	0.513	190.38	0.515	182.48	0.517	204.42	0.514	214.76
0.618	211.56	0.617	202.88	0.619	182.04	0.617	192.58	0.618	204.66
0.723	218.14	0.718	216.04	0.718	196.30	0.724	186.44	0.718	197.63
0.822	215.29	0.823	219.33	0.822	214.51	0.822	193.01	0.823	193.68
0.925	207.17	0.925	215.38	0.925	223.72	0.926	208.37	0.926	193.24
1.000	201.69	1.000	209.46	1.000	225.91	1.000	217.14	1.000	196.53
PHH=60.00		PHH=70.00		PHH=80.00		PHH=90.00			
HS= 14.61		HS= 20.70		HS= 26.20		HS= 31.39			
0.000	197.68	0.000	199.86	0.000	196.52	0.000	195.78		
0.103	195.04	0.104	196.56	0.106	197.61	0.102	193.59		
0.205	198.78	0.205	193.71	0.204	193.66	0.210	195.78		
0.309	210.86	0.315	199.42	0.308	191.03	0.318	192.05		
0.411	217.01	0.413	209.08	0.410	197.17	0.415	191.39		
0.512	216.35	0.512	212.60	0.514	205.95	0.514	193.59		
0.615	210.42	0.617	211.28	0.613	208.59	0.616	197.98		
0.722	202.07	0.719	204.25	0.719	208.59	0.720	203.03		
0.822	197.68	0.822	198.10	0.822	203.10	0.820	202.37		
0.926	197.24	0.924	198.10	0.929	197.61	0.925	196.44		
1.000	195.04	1.000	199.42	1.000	197.61	1.000	192.71		

Table 14.1. Continued.

STATION 4

Y/SS	HT N*M/KG	Y/SS	HT N*M/KG	Y/SS	HT N*M/KG	Y/SS	HT N*M/KG	Y/SS	HT N*M/KG
PHH=10.00		PHH=20.00		PHH=30.00		PHH=40.00		PHH=50.00	
HS=	46.82	HS=	50.17	HS=	53.24	HS=	56.20	HS=	58.95
0.000	173.69	0.000	186.39	0.000	185.23	0.000	206.92	0.000	213.12
0.046	151.76	0.049	173.23	0.073	176.46	0.060	200.36	0.105	212.46
0.083	142.11	0.093	155.69	0.134	157.82	0.147	175.17	0.155	206.56
0.099	141.68	0.129	144.72	0.176	142.48	0.215	145.62	0.210	183.61
0.131	149.57	0.155	139.24	0.215	141.39	0.277	143.42	0.258	158.47
0.171	169.31	0.199	149.11	0.242	153.44	0.315	157.66	0.298	143.82
0.203	180.93	0.251	166.65	0.301	186.32	0.366	179.55	0.327	147.54
0.240	185.98	0.317	180.91	0.361	200.57	0.465	193.79	0.354	157.38
0.309	195.32	0.421	185.29	0.448	206.05	0.565	198.82	0.396	177.49
0.409	181.59	0.508	185.29	0.555	204.95	0.620	203.21	0.439	186.23
0.514	177.64	0.607	184.20	0.665	201.67	0.697	208.02	0.496	187.98
0.616	180.27	0.712	185.29	0.755	200.57	0.805	214.15	0.564	186.89
0.721	189.71	0.807	187.48	0.848	193.99	0.918	214.59	0.651	188.42
0.825	196.28	0.918	188.58	1.000	187.42	1.000	208.02	0.722	192.35
0.925	195.62	1.000	189.67					0.822	200.00
1.000	188.61							0.916	210.27
								1.000	215.95
PHH=60.00		PHH=70.00		PHH=80.00		PHH=90.00			
HS=	61.55	HS=	63.89	HS=	65.99	HS=	67.82		
0.000	198.79	0.000	189.89	0.000	183.85	0.000	172.85		
0.109	207.53	0.111	193.82	0.106	183.19	0.102	167.41		
0.169	209.28	0.212	200.80	0.208	187.11	0.207	167.41		
0.235	197.05	0.262	198.62	0.306	186.67	0.276	165.24		
0.287	174.76	0.313	180.07	0.347	172.97	0.337	159.80		
0.335	149.64	0.342	164.79	0.381	154.04	0.366	150.02		
0.361	150.30	0.373	151.04	0.415	145.33	0.403	132.63		
0.380	157.29	0.398	150.61	0.431	147.51	0.424	129.37		
0.425	184.59	0.424	163.70	0.460	163.61	0.459	143.93		
0.465	196.61	0.467	190.33	0.510	194.07	0.479	159.80		
0.506	198.79	0.501	199.72	0.558	202.33	0.513	176.11		
0.566	196.61	0.563	201.89	0.617	203.42	0.619	187.42		
0.620	194.42	0.616	200.80	0.723	202.33	0.693	195.24		
0.713	190.05	0.719	196.44	0.825	197.55	0.778	196.76		
0.818	188.96	0.824	192.51	0.916	189.72	0.839	193.94		
0.916	192.68	0.915	190.98	1.000	182.76	0.930	182.63		
1.000	198.79	1.000	189.89			1.000	173.94		

Table 14.1. Continued.

STATION 5

Y/SS	HT N*M/KG	Y/SS	HT N*M/KG	Y/SS	HT N*M/KG	Y/SS	HT N*M/KG	Y/SS	HT N*M/KG
PHH=10.00		PHH=20.00		PHH=30.00		PHH=40.00		PHH=50.00	
HS=	87.42	HS=	99.95	HS=	110.92	HS=	120.73	HS=	129.46
0.000	339.23	0.000	337.04	0.000	332.90	0.000	340.44	0.000	349.39
0.101	344.36	0.107	343.46	0.111	332.90	0.112	330.81	0.115	339.74
0.209	344.36	0.208	349.24	0.218	345.74	0.206	329.74	0.211	332.24
0.307	339.23	0.307	352.67	0.310	356.44	0.315	340.44	0.320	329.03
0.412	332.82	0.418	350.53	0.413	361.79	0.421	352.22	0.417	335.45
0.513	324.70	0.512	346.67	0.517	359.65	0.522	357.58	0.520	342.95
0.616	320.43	0.620	342.39	0.618	354.31	0.624	359.72	0.622	348.32
0.724	321.50	0.721	333.83	0.727	346.81	0.725	356.50	0.729	350.46
0.819	328.98	0.821	331.69	0.831	341.46	0.829	350.08	0.826	352.60
0.925	339.23	0.924	335.54	0.928	336.11	0.926	343.66	0.922	352.60
1.000	345.00	1.000	340.68	1.000	333.96	1.000	337.24	1.000	349.39
PHH=60.00		PHH=70.00		PHH=80.00		PHH=90.00			
HS=	137.13	HS=	143.85	HS=	149.93	HS=	155.68		
0.000	342.09	0.000	336.88	0.000	341.40	0.000	333.20		
0.115	342.09	0.107	334.75	0.106	337.12	0.113	328.93		
0.208	337.81	0.207	334.75	0.218	330.70	0.208	321.46		
0.324	329.26	0.323	329.40	0.312	325.35	0.324	317.18		
0.414	328.19	0.418	324.05	0.420	322.14	0.417	319.32		
0.522	337.81	0.523	330.47	0.515	326.42	0.518	325.72		
0.618	341.02	0.628	336.88	0.623	332.84	0.623	330.00		
0.721	339.95	0.719	337.96	0.725	337.12	0.718	331.07		
0.833	337.81	0.824	337.96	0.820	336.05	0.828	331.07		
0.910	338.88	0.934	334.75	0.935	339.26	0.926	333.20		
1.000	341.02	1.000	334.75	1.000	340.33	1.000	333.20		

Table 14.1. Continued.

STATION 6

Y/SS	HT N*M/KG	Y/SS	HT N*M/KG	Y/SS	HT N*M/KG	Y/SS	HT N*M/KG	Y/SS	HT N*M/KG
PHH=10.00		PHH=20.00		PHH=30.00		PHH=40.00		PHH=50.00	
HS= 186.40		HS= 189.75		HS= 192.86		HS= 195.85		HS= 198.60	
0.000	312.87	0.000	330.84	0.000	351.49	0.000	338.32	0.000	320.47
0.109	317.79	0.105	329.77	0.111	349.35	0.112	347.96	0.117	329.04
0.210	325.28	0.208	329.77	0.227	342.92	0.210	352.24	0.222	336.54
0.313	329.56	0.310	330.84	0.310	337.56	0.308	352.24	0.319	340.83
0.423	330.63	0.423	331.91	0.419	333.27	0.413	346.88	0.420	344.05
0.517	324.21	0.529	335.13	0.527	331.13	0.513	341.53	0.523	344.05
0.613	292.11	0.590	330.84	0.640	326.84	0.614	335.11	0.621	341.90
0.655	277.13	0.662	308.36	0.713	300.05	0.667	329.75	0.734	334.40
0.685	274.99	0.712	285.87	0.752	285.05	0.725	311.55	0.794	310.82
0.732	288.90	0.759	281.59	0.778	280.76	0.783	286.93	0.828	288.31
0.782	306.02	0.784	286.95	0.815	290.41	0.832	275.15	0.865	273.31
0.833	312.44	0.845	311.57	0.858	313.98	0.878	289.07	0.894	276.52
0.928	312.44	0.928	327.63	0.929	343.99	0.933	317.98	0.934	296.89
1.000	313.51	1.000	328.70	1.000	350.42	1.000	336.18	1.000	322.61
PHH=60.00		PHH=70.00		PHH=80.00		PHH=90.00			
HS= 201.08		HS= 203.27		HS= 205.28		HS= 207.26			
0.000	315.21	0.000	295.58	0.000	274.93	0.000	258.61		
0.046	325.50	0.028	317.00	0.032	301.24	0.028	277.24		
0.108	327.00	0.050	325.14	0.078	324.13	0.050	295.43		
0.214	328.07	0.088	327.28	0.122	324.77	0.090	311.49		
0.311	332.36	0.198	323.42	0.207	320.50	0.142	309.99		
0.418	337.72	0.314	321.28	0.305	316.64	0.213	307.85		
0.517	339.86	0.412	324.49	0.412	318.36	0.314	307.21		
0.616	338.79	0.507	332.42	0.510	323.49	0.417	310.42		
0.717	336.65	0.611	337.35	0.613	329.91	0.514	318.56		
0.769	331.93	0.708	337.99	0.715	337.61	0.610	323.70		
0.814	318.42	0.765	336.70	0.782	339.11	0.715	330.12		
0.846	303.41	0.827	329.85	0.839	334.83	0.807	319.42		
0.879	281.97	0.867	312.28	0.910	304.24	0.874	304.00		
0.904	273.39	0.911	285.30	0.949	281.34	0.933	286.87		
0.927	274.47	0.946	270.31	0.980	271.29	0.955	277.24		
0.955	286.26	0.965	272.02	1.000	274.28	1.000	266.53		
1.000	313.06	1.000	293.01						

Table 14.1. Continued.

STATION 7

Y/SS	HT N*M/KG	Y/SS	HT N*M/KG	Y/SS	HT N*M/KG	Y/SS	HT N*M/KG	Y/SS	HT N*M/KG
PHH=10.00		PHH=20.00		PHH=30.00		PHH=40.00		PHH=50.00	
HS= 226.90		HS= 239.35		HS= 250.36		HS= 260.21		HS= 268.91	
0.000	483.70	0.000	491.97	0.000	501.34	0.000	492.60	0.000	480.73
0.105	477.29	0.107	490.70	0.095	501.34	0.098	501.75	0.094	488.83
0.209	467.68	0.212	488.14	0.205	495.60	0.200	503.24	0.202	495.67
0.306	462.34	0.308	477.48	0.308	487.50	0.302	498.98	0.304	496.95
0.415	463.41	0.414	468.53	0.403	482.18	0.402	491.11	0.404	492.68
0.511	470.88	0.516	468.95	0.503	478.56	0.502	483.03	0.502	484.99
0.609	478.36	0.606	477.48	0.604	477.29	0.604	477.70	0.600	477.73
0.719	485.19	0.702	487.07	0.718	480.69	0.701	473.45	0.698	470.69
0.823	488.61	0.808	493.47	0.805	485.80	0.799	471.96	0.804	465.35
0.922	485.83	0.901	495.60	0.900	493.89	0.898	477.07	0.900	466.42
1.000	482.20	1.000	496.67	1.000	499.85	1.000	489.83	1.000	475.60
PHH=60.00		PHH=70.00		PHH=80.00		PHH=90.00			
HS= 276.53		HS= 283.17		HS= 289.21		HS= 295.07			
0.000	466.37	0.000	461.22	0.000	467.84	0.000	465.23		
0.100	473.65	0.099	465.49	0.098	468.48	0.101	468.43		
0.203	479.22	0.201	467.20	0.199	471.04	0.205	468.43		
0.303	482.86	0.305	467.63	0.303	467.84	0.310	464.16		
0.406	485.00	0.403	471.90	0.402	464.64	0.402	460.96		
0.500	483.93	0.502	476.60	0.502	470.61	0.505	463.09		
0.606	481.36	0.601	479.37	0.599	475.30	0.610	467.36		
0.705	475.37	0.704	480.86	0.698	478.49	0.702	469.49		
0.799	465.73	0.801	476.16	0.795	478.49	0.800	470.56		
0.898	460.37	0.898	465.92	0.900	471.04	0.909	466.29		
1.000	466.80	1.000	461.65	1.000	465.71	1.000	464.16		

Table 14.1. Concluded.

STATION 8

Y/SS	HT N*M/KG	Y/SS	HT N*M/KG	Y/SS	HT N*M/KG	Y/SS	HT N*M/KG	Y/SS	HT N*M/KG
PHH=10.00		PHH=20.00		PHH=30.00		PHH=40.00		PHH=50.00	
HS= 317.91		HS= 321.35		HS= 324.77		HS= 327.90		HS= 330.59	
0.000	426.97	0.000	470.24	0.000	466.30	0.000	482.30	0.000	485.77
0.105	445.19	0.102	472.88	0.100	466.30	0.103	475.03	0.104	483.12
0.207	462.09	0.205	479.48	0.204	468.94	0.212	466.87	0.206	477.38
0.275	462.75	0.308	479.92	0.306	475.10	0.316	462.46	0.312	468.54
0.318	454.84	0.357	475.08	0.356	477.75	0.431	464.01	0.415	462.58
0.369	434.65	0.432	446.04	0.424	473.34	0.475	458.06	0.513	453.75
0.407	417.52	0.483	422.29	0.492	446.92	0.523	439.76	0.540	442.71
0.421	413.80	0.507	416.79	0.539	426.67	0.568	419.92	0.596	416.21
0.442	413.13	0.531	418.33	0.562	423.15	0.591	415.51	0.624	406.28
0.473	420.38	0.584	439.45	0.587	427.11	0.628	421.02	0.672	417.32
0.524	441.67	0.656	459.68	0.637	457.49	0.679	452.99	0.705	437.19
0.591	456.16	0.687	462.32	0.678	474.44	0.740	482.74	0.813	478.04
0.631	457.70	0.747	462.32	0.730	479.95	0.812	486.05	0.903	484.66
0.686	453.31	0.837	462.98	0.813	477.30	0.900	485.39	1.000	486.87
0.761	443.43	0.918	464.52	0.918	471.14	1.000	480.54		
0.849	432.45	1.000	468.04	1.000	468.50				
0.925	427.62								
1.000	429.82								
PHH=60.00		PHH=70.00		PHH=80.00		PHH=90.00			
HS= 332.98		HS= 335.08		HS= 337.03		HS= 339.05			
0.000	468.35	0.000	455.14	0.000	460.82	0.000	450.91		
0.100	472.77	0.102	457.34	0.111	458.61	0.105	444.28		
0.203	476.08	0.203	461.76	0.205	456.40	0.204	441.63		
0.319	473.88	0.309	466.18	0.310	460.82	0.309	446.49		
0.414	469.45	0.413	470.60	0.406	463.69	0.413	455.78		
0.528	461.72	0.512	471.71	0.508	468.56	0.512	463.07		
0.587	442.95	0.580	467.28	0.577	470.32	0.555	465.28		
0.643	412.02	0.657	433.04	0.640	463.03	0.620	456.44		
0.667	403.18	0.688	413.16	0.697	430.54	0.674	432.79		
0.711	408.70	0.714	402.11	0.739	406.67	0.720	404.94		
0.753	434.11	0.761	412.05	0.758	405.56	0.758	391.23		
0.814	456.20	0.826	450.72	0.774	408.88	0.789	401.84		
0.897	463.93	0.906	454.03	0.813	443.80	0.822	435.88		
1.000	470.56	1.000	456.24	0.843	459.27	0.853	454.89		
				0.903	461.48	0.922	455.33		
				1.000	460.16	1.000	450.91		

Table 14.2. Point-by-point circumferential distribution of total head for maximum noise condition.

STATION 1

Y/SS	HT N*M/KG	Y/SS	HT N*M/KG	Y/SS	HT N*M/KG	Y/SS	HT N*M/KG	Y/SS	HT N*M/KG
PHH=10.00		PHH=20.00		PHH=30.00		PHH=40.00		PHH=50.00	
HS= -86.51		HS= -86.51		HS= -86.51		HS= -86.51		HS= -86.50	
0.000	0.43	0.000	0.43	0.000	-0.00	0.000	0.22	0.000	0.21
0.217	0.43	0.213	0.43	0.217	0.22	0.217	0.22	0.219	0.21
0.428	-0.00	0.420	1.08	0.425	-0.00	0.425	-0.00	0.421	0.43
0.623	-0.00	0.622	1.08	0.621	-0.00	0.624	-0.00	0.633	0.00
0.832	0.43	0.832	1.08	0.834	0.22	0.833	-0.00	0.826	0.00
1.000	-0.00	1.000	0.43	1.000	0.22	1.000	-0.00	1.000	0.00
PHH=60.00		PHH=70.00		PHH=80.00		PHH=90.00			
HS= -86.50		HS= -86.50		HS= -86.50		HS= -86.50			
0.000	-0.00	0.000	0.00	0.000	-1.73	0.000	-8.63		
0.209	0.21	0.213	0.00	0.212	-3.24	0.212	-7.55		
0.417	-0.00	0.437	0.00	0.425	-2.59	0.421	-8.20		
0.631	-0.00	0.629	-0.22	0.625	-2.59	0.626	-8.20		
0.836	-0.00	0.833	0.00	0.834	-1.94	0.840	-7.55		
1.000	-0.00	1.000	0.00	1.000	-2.59	1.000	-9.06		

Y/SS = Circumferential spacing, Y/S_S.

HT = Total head with respect to atmospheric pressure, H, N·m/kg.

PHH = Percent passage height from hub, PHH.

HS = Static head with respect to atmospheric pressure, h, N·m/kg.

Table 14.2. Continued.

STATION 2

Y/SS	HT N*M/KG	Y/SS	HT N*M/KG	Y/SS	HT N*M/KG	Y/SS	HT N*M/KG	Y/SS	HT N*M/KG
PHH=10.00		PHH=20.00		PHH=30.00		PHH=40.00		PHH=50.00	
HS=-111.84		HS=-110.46		HS=-109.25		HS=-108.17		HS=-107.22	
0.000	-0.00	0.000	-0.00	0.000	-0.00	0.000	-0.00	0.000	-0.00
0.109	-0.00	0.108	-0.00	0.108	-0.00	0.106	-0.00	0.104	-0.00
0.212	-0.00	0.212	-0.00	0.214	-0.00	0.207	-0.00	0.208	-0.00
0.325	-0.00	0.321	-0.00	0.320	-0.00	0.315	-0.00	0.324	-0.00
0.465	-2.15	0.420	-0.00	0.431	-0.00	0.412	-0.00	0.417	-0.00
0.497	-9.04	0.487	-1.75	0.522	-1.76	0.559	-1.10	0.519	-0.00
0.540	-47.34	0.513	-6.14	0.558	-11.41	0.632	-36.20	0.616	-6.58
0.578	-75.32	0.559	-31.79	0.616	-52.65	0.665	-66.93	0.643	-20.84
0.610	-79.62	0.610	-72.34	0.651	-75.03	0.690	-81.19	0.679	-53.75
0.653	-85.00	0.632	-85.49	0.675	-87.31	0.737	-61.44	0.714	-76.79
0.681	-75.32	0.680	-70.15	0.704	-74.59	0.774	-32.91	0.759	-61.43
0.734	-37.66	0.741	-24.11	0.738	-35.10	0.827	-4.39	0.826	-13.17
0.779	-19.37	0.773	-7.67	0.783	-7.68	0.933	-0.00	0.860	-3.29
0.838	-4.74	0.827	-1.75	0.828	-1.76	1.000	-0.00	0.916	-0.00
0.928	-1.07	0.942	-0.00	0.932	-0.00			1.000	-0.00
1.000	-0.43	1.000	-0.00	1.000	-0.00				
PHH=60.00		PHH=70.00		PHH=80.00		PHH=90.00			
HS=-106.37		HS=-105.59		HS=-104.86		HS=-104.25			
0.000	0.00	0.000	-0.44	0.000	-3.95	0.000	-10.96		
0.110	0.00	0.152	-0.44	0.162	-4.38	0.158	-8.76		
0.212	0.00	0.320	-0.44	0.315	-2.63	0.317	-8.33		
0.318	0.00	0.481	-0.44	0.462	-2.63	0.479	-7.67		
0.423	0.00	0.616	-1.10	0.619	-2.63	0.626	-6.57		
0.523	0.00	0.653	-8.33	0.662	-5.48	0.698	-12.71		
0.619	-2.19	0.682	-23.03	0.687	-19.74	0.729	-41.63		
0.664	-20.84	0.713	-43.87	0.713	-39.47	0.749	-63.55		
0.691	-40.58	0.722	-47.16	0.737	-43.86	0.768	-72.31		
0.729	-60.32	0.762	-43.43	0.763	-29.60	0.796	-65.74		
0.766	-51.55	0.802	-15.35	0.787	-16.45	0.822	-50.40		
0.826	-12.06	0.819	-7.67	0.810	-7.68	0.866	-21.91		
0.855	-3.29	0.860	-2.63	0.847	-3.95	0.928	-14.24		
1.000	0.00	0.940	-1.10	0.926	-3.29	1.000	-10.96		
		1.000	-0.44	1.000	-3.95				

Table 14.2. Continued.

STATION 3

Y/SS	HT N*M/KG	Y/SS	HT N*M/KG	Y/SS	HT N*M/KG	Y/SS	HT N*M/KG	Y/SS	HT N*M/KG
PHH=10.00		PHH=20.00		PHH=30.00		PHH=40.00		PHH=50.00	
HS= -30.23		HS= -18.65		HS= -8.67		HS= -0.01		HS= 7.72	
0.000	201.94	0.000	211.12	0.000	225.37	0.000	211.38	0.000	191.74
0.097	194.89	0.094	206.20	0.096	224.31	0.099	225.25	0.100	208.81
0.200	187.63	0.203	194.45	0.200	217.90	0.202	227.39	0.200	223.12
0.304	186.98	0.303	186.97	0.307	209.35	0.303	224.61	0.302	225.89
0.400	191.26	0.402	185.47	0.401	197.60	0.401	218.85	0.401	222.05
0.504	201.94	0.505	194.45	0.497	183.29	0.500	209.24	0.495	214.58
0.597	207.72	0.599	196.59	0.596	178.37	0.596	195.36	0.594	208.17
0.693	213.27	0.697	206.20	0.692	182.00	0.694	185.33	0.693	198.56
0.792	211.98	0.794	213.25	0.791	200.38	0.793	184.69	0.789	191.09
0.891	210.49	0.894	216.88	0.894	215.76	0.893	194.72	0.890	186.82
1.000	203.01	1.000	210.48	1.000	226.87	1.000	213.08	1.000	194.29
PHH=60.00		PHH=70.00		PHH=80.00		PHH=90.00			
HS= 14.57		HS= 20.66		HS= 26.15		HS= 31.29			
0.000	191.71	0.000	198.46	0.000	196.63	0.000	194.53		
0.097	192.14	0.097	195.90	0.102	198.77	0.096	193.68		
0.208	203.88	0.198	194.19	0.202	193.01	0.199	195.17		
0.301	215.20	0.301	202.30	0.301	191.51	0.302	194.10		
0.399	218.19	0.404	210.84	0.400	198.34	0.402	191.55		
0.497	215.63	0.497	212.33	0.497	204.73	0.503	193.68		
0.596	210.93	0.595	210.20	0.595	207.30	0.596	197.30		
0.692	202.82	0.692	204.86	0.695	207.30	0.699	201.57		
0.791	194.70	0.791	197.40	0.790	204.31	0.793	201.57		
0.888	192.14	0.886	195.26	0.887	196.20	0.891	199.43		
1.000	191.71	1.000	198.03	1.000	196.63	1.000	191.55		

Table 14.2. Continued.

STATION 4

Y/SS	HT N*M/KG	Y/SS	HT N*M/KG	Y/SS	HT N*M/KG	Y/SS	HT N*M/KG	Y/SS	HT N*M/KG
PHH=10.00		PHH=20.00		PHH=30.00		PHH=40.00		PHH=50.00	
HS=	48.51	HS=	51.82	HS=	54.88	HS=	57.90	HS=	60.59
0.000	180.49	0.000	189.76	0.000	183.68	0.000	198.93	0.000	203.95
0.099	178.31	0.104	192.38	0.099	186.51	0.113	191.51	0.102	213.76
0.199	182.01	0.199	193.03	0.201	192.40	0.206	186.49	0.205	206.78
0.298	190.73	0.301	191.50	0.306	199.60	0.317	185.41	0.302	198.06
0.399	192.91	0.402	189.32	0.403	203.97	0.412	189.33	0.405	189.33
0.497	191.38	0.503	187.58	0.503	205.06	0.511	193.04	0.508	184.97
0.591	180.49	0.607	182.12	0.598	206.15	0.610	198.93	0.608	184.31
0.630	167.41	0.650	176.67	0.648	202.88	0.687	203.95	0.705	188.68
0.661	153.67	0.702	160.32	0.689	197.42	0.754	198.93	0.754	189.77
0.695	140.59	0.750	141.34	0.752	175.61	0.822	174.50	0.795	186.50
0.723	137.33	0.780	136.32	0.808	150.09	0.870	155.31	0.843	171.23
0.754	142.12	0.816	141.77	0.834	145.72	0.895	153.78	0.884	154.43
0.798	161.74	0.871	163.59	0.864	149.43	0.923	163.59	0.913	149.41
0.836	177.65	0.930	178.85	0.922	171.90	0.965	187.59	0.942	155.30
0.872	181.36	1.000	187.14	0.971	180.63	1.000	198.05	0.968	171.88
0.913	182.66			1.000	183.25			1.000	193.70
1.000	183.10								
PHH=60.00		PHH=70.00		PHH=80.00		PHH=90.00			
HS=	63.00	HS=	65.21	HS=	67.19	HS=	69.08		
0.000	183.63	0.000	154.32	0.000	134.04	0.000	134.00		
0.095	208.93	0.046	182.00	0.033	154.74	0.025	137.27		
0.177	212.64	0.108	190.72	0.055	171.09	0.066	165.60		
0.273	213.73	0.205	198.34	0.093	183.08	0.106	173.22		
0.390	207.19	0.301	205.32	0.197	184.16	0.207	169.95		
0.503	199.55	0.403	207.50	0.302	190.70	0.308	171.04		
0.602	193.66	0.500	204.88	0.406	198.33	0.412	173.22		
0.703	188.65	0.600	200.96	0.510	201.60	0.510	176.49		
0.804	182.11	0.703	195.73	0.615	202.69	0.610	188.48		
0.841	170.11	0.801	190.72	0.728	200.51	0.714	198.28		
0.875	154.41	0.853	181.34	0.814	195.06	0.803	196.10		
0.903	142.20	0.899	162.38	0.897	180.90	0.853	191.74		
0.931	135.22	0.931	140.59	0.931	162.37	0.892	181.94		
0.960	141.32	0.962	131.87	0.975	136.22	0.955	150.34		
1.000	168.37	0.991	135.57	0.994	128.59	1.000	124.20		
		1.000	141.24	1.000	129.68				

Table 14.2. Continued.

STATION 5

Y/SS	HT N*M/KG	Y/SS	HT N*M/KG	Y/SS	HT N*M/KG	Y/SS	HT N*M/KG	Y/SS	HT N*M/KG
PHH=10.00		PHH=20.00		PHH=30.00		PHH=40.00		PHH=50.00	
HS= 88.00		HS= 100.59		HS= 111.72		HS= 121.72		HS= 130.58	
0.000	325.73	0.000	352.68	0.000	353.46	0.000	345.12	0.000	349.78
0.097	319.17	0.089	348.96	0.103	357.83	0.091	349.51	0.087	351.97
0.195	316.55	0.193	342.39	0.195	355.64	0.191	352.79	0.192	351.97
0.302	320.26	0.295	337.36	0.292	352.36	0.291	353.89	0.290	349.78
0.394	329.67	0.395	336.49	0.392	349.08	0.390	352.79	0.394	347.59
0.493	339.94	0.490	335.83	0.495	344.70	0.484	348.41	0.488	343.20
0.591	346.49	0.592	339.55	0.595	339.23	0.583	345.12	0.586	337.72
0.688	347.15	0.689	346.11	0.686	338.13	0.684	341.84	0.688	331.14
0.791	342.13	0.786	352.24	0.779	340.32	0.783	340.74	0.784	331.14
0.887	336.66	0.887	354.87	0.883	345.79	0.885	341.84	0.883	339.91
1.000	327.91	1.000	353.99	1.000	354.55	1.000	347.31	1.000	351.97
PHH=60.00		PHH=70.00		PHH=80.00		PHH=90.00			
HS= 138.41		HS= 145.26		HS= 151.37		HS= 157.15			
0.000	337.69	0.000	318.91	0.000	324.62	0.000	326.52		
0.084	345.36	0.087	323.30	0.099	323.52	0.097	324.32		
0.188	347.56	0.188	328.78	0.203	326.82	0.205	325.86		
0.291	349.75	0.291	334.26	0.298	326.82	0.308	324.76		
0.393	351.95	0.391	340.83	0.402	326.38	0.409	322.57		
0.486	349.75	0.487	347.41	0.499	333.40	0.495	321.47		
0.587	344.27	0.585	348.50	0.596	341.73	0.596	326.96		
0.687	333.30	0.681	344.12	0.694	345.46	0.697	333.98		
0.784	322.34	0.782	334.26	0.795	345.46	0.795	335.74		
0.886	323.44	0.878	323.30	0.894	335.59	0.898	334.64		
1.000	337.69	1.000	318.91	1.000	324.18	1.000	328.06		

Table 14.2. Continued.

STATION 6

Y/SS	HT N*M/KG	Y/SS	HT N*M/KG	Y/SS	HT N*M/KG	Y/SS	HT N*M/KG	Y/SS	HT N*M/KG
PHH=10.00		PHH=20.00		PHH=30.00		PHH=40.00		PHH=50.00	
HS= 185.12		HS= 188.55		HS= 191.83		HS= 194.98		HS= 197.81	
0.000	101.28	0.000	325.01	0.000	336.75	0.000	341.73	0.000	347.18
0.027	289.03	0.048	305.31	0.052	325.15	0.062	337.35	0.111	342.80
0.058	276.57	0.102	281.24	0.108	302.16	0.108	328.15	0.194	320.89
0.094	271.11	0.137	274.67	0.161	280.26	0.162	304.93	0.253	290.23
0.123	276.57	0.167	278.40	0.186	276.98	0.209	282.15	0.285	279.28
0.164	294.06	0.236	306.85	0.220	283.55	0.249	276.01	0.340	289.13
0.209	309.37	0.306	326.11	0.272	307.63	0.279	283.68	0.400	317.61
0.254	313.08	0.367	331.58	0.313	325.15	0.333	312.16	0.425	320.89
0.311	312.21	0.429	333.77	0.364	335.44	0.393	329.68	0.528	326.37
0.410	312.21	0.508	334.86	0.433	340.47	0.444	334.06	0.623	332.94
0.507	314.83	0.612	334.86	0.504	344.85	0.520	338.44	0.720	341.70
0.602	319.64	0.703	333.77	0.604	347.70	0.620	343.92	0.823	348.27
0.700	323.57	0.802	333.11	0.702	349.89	0.720	347.87	0.929	348.27
0.798	327.95	0.900	332.67	0.800	347.04	0.822	347.87	1.000	347.18
0.903	329.70	1.000	328.29	0.900	343.32	0.922	345.02		
0.954	324.67			1.000	337.63	1.000	341.73		
1.000	312.21								
PHH=60.00		PHH=70.00		PHH=80.00		PHH=90.00			
HS= 200.39		HS= 202.64		HS= 204.66		HS= 206.53			
0.000	340.54	0.000	319.34	0.000	319.37	0.000	304.26		
0.113	344.92	0.103	324.17	0.110	315.43	0.108	297.25		
0.203	342.72	0.207	332.49	0.206	317.18	0.214	284.56		
0.256	335.21	0.246	331.17	0.267	316.52	0.282	270.33		
0.304	296.74	0.288	319.78	0.294	311.05	0.351	258.29		
0.334	283.60	0.329	300.07	0.331	296.81	0.384	251.29		
0.382	294.55	0.359	286.49	0.367	277.75	0.422	262.67		
0.423	319.73	0.381	281.45	0.397	271.62	0.459	295.06		
0.457	326.30	0.407	290.87	0.430	284.32	0.498	321.77		
0.521	324.11	0.449	324.17	0.464	314.33	0.566	327.90		
0.624	321.92	0.484	337.75	0.514	337.77	0.622	332.27		
0.729	324.11	0.541	339.50	0.599	340.62	0.716	330.53		
0.831	331.78	0.615	335.12	0.703	339.52	0.812	323.96		
0.928	338.35	0.714	328.11	0.814	332.95	0.913	311.92		
1.000	340.54	0.816	321.54	0.915	324.19	1.000	303.82		
		0.917	318.69	1.000	320.25				
		1.000	320.88						

Table 14.2. Continued.

STATION 7

Y/SS	HT N*M/KG	Y/SS	HT N*M/KG	Y/SS	HT N*M/KG	Y/SS	HT N*M/KG	Y/SS	HT N*M/KG
PHH=10.00		PHH=20.00		PHH=30.00		PHH=40.00		PHH=50.00	
HS= 227.81		HS= 240.18		HS= 251.14		HS= 260.92		HS= 269.49	
0.000	479.15	0.000	477.36	0.000	472.78	0.000	474.01	0.000	483.23
0.105	486.09	0.102	486.48	0.100	472.78	0.103	467.05	0.100	473.01
0.205	487.18	0.203	491.91	0.204	479.96	0.205	465.31	0.202	464.31
0.303	485.67	0.303	494.09	0.301	490.17	0.306	474.01	0.306	463.22
0.400	481.32	0.404	493.43	0.403	499.52	0.407	484.88	0.401	470.19
0.500	473.07	0.499	490.39	0.499	502.56	0.498	495.75	0.501	481.06
0.600	464.40	0.597	483.87	0.599	499.95	0.597	502.27	0.596	491.06
0.696	459.62	0.699	474.54	0.697	491.26	0.695	501.84	0.693	495.85
0.795	462.23	0.794	466.94	0.794	483.00	0.795	495.31	0.793	497.59
0.891	469.82	0.895	465.85	0.895	478.21	0.891	483.79	0.892	492.58
1.000	479.15	1.000	472.37	1.000	473.43	1.000	472.27	1.000	483.23
PHH=60.00		PHH=70.00		PHH=80.00		PHH=90.00			
HS= 277.03		HS= 283.60		HS= 289.64		HS= 295.48			
0.000	492.84	0.000	470.84	0.000	475.28	0.000	462.12		
0.099	478.49	0.102	470.84	0.101	470.28	0.104	453.42		
0.201	471.53	0.204	469.75	0.205	467.23	0.205	449.07		
0.303	462.83	0.300	464.31	0.303	462.23	0.307	453.42		
0.400	460.65	0.402	458.44	0.400	458.97	0.403	461.03		
0.501	468.05	0.501	465.40	0.498	465.92	0.505	470.82		
0.598	473.05	0.596	471.92	0.596	477.46	0.600	471.90		
0.700	478.49	0.695	472.36	0.694	478.54	0.698	468.65		
0.794	491.75	0.793	473.01	0.791	478.54	0.791	467.56		
0.896	483.27	0.890	471.49	0.889	478.54	0.895	468.65		
1.000	492.40	1.000	468.66	1.000	473.76	1.000	463.21		

Table 14.2. Concluded.

STATION 8

Y/SS	HT N*M/KG	Y/SS	HT N*M/KG	Y/SS	HT N*M/KG	Y/SS	HT N*M/KG	Y/SS	HT N*M/KG
PHH=10.00		PHH=20.00		PHH=30.00		PHH=40.00		PHH=50.00	
HS= 317.69		HS= 320.91		HS= 324.33		HS= 327.47		HS= 330.14	
0.000	427.74	0.000	456.55	0.000	486.41	0.000	473.43	0.000	456.56
0.036	414.71	0.051	434.81	0.039	480.97	0.097	476.69	0.107	461.99
0.060	413.63	0.100	414.16	0.105	455.94	0.142	464.72	0.143	458.73
0.103	423.83	0.109	410.89	0.160	429.82	0.190	440.78	0.176	448.94
0.148	444.03	0.168	417.42	0.197	424.38	0.210	432.07	0.226	427.20
0.215	458.14	0.220	438.07	0.223	432.65	0.240	427.72	0.250	418.51
0.214	459.23	0.300	457.64	0.259	446.58	0.274	436.43	0.259	416.34
0.255	458.14	0.365	463.07	0.290	458.77	0.322	466.90	0.301	422.86
0.315	451.62	0.458	468.51	0.329	463.12	0.390	481.05	0.339	447.86
0.423	434.25	0.569	472.86	0.409	462.47	0.487	475.61	0.410	482.64
0.498	423.40	0.668	477.20	0.513	463.56	0.586	469.07	0.448	485.90
0.653	425.57	0.771	479.38	0.611	466.82	0.692	461.46	0.524	484.81
0.763	444.03	0.871	478.29	0.711	472.26	0.790	460.37	0.614	481.56
0.839	452.71	0.931	475.03	0.808	480.53	0.886	464.72	0.716	475.04
0.884	454.88	1.000	464.16	0.909	486.41	1.000	474.52	0.816	466.34
0.941	448.37			1.000	488.58			0.925	460.90
1.000	428.83							1.000	459.81
PHH=60.00		PHH=70.00		PHH=80.00		PHH=90.00			
HS= 332.48		HS= 334.55		HS= 336.51		HS= 338.46			
0.000	463.63	0.000	466.08	0.000	463.99	0.000	451.98		
0.101	459.29	0.093	462.18	0.106	460.52	0.100	450.90		
0.150	456.03	0.162	457.84	0.217	454.01	0.187	446.99		
0.190	448.43	0.205	451.33	0.258	443.81	0.243	432.47		
0.246	423.03	0.265	424.86	0.315	413.43	0.281	409.71		
0.288	406.09	0.306	404.03	0.351	398.24	0.340	377.19		
0.317	405.65	0.344	394.48	0.377	398.24	0.365	371.77		
0.340	414.77	0.375	406.85	0.405	414.08	0.396	381.10		
0.378	442.57	0.407	430.72	0.435	443.81	0.433	417.30		
0.411	462.55	0.447	453.50	0.469	459.00	0.460	446.56		
0.455	471.67	0.508	461.09	0.522	463.99	0.507	451.98		
0.511	475.14	0.611	466.52	0.617	469.20	0.606	456.32		
0.607	478.19	0.702	468.69	0.714	470.94	0.708	461.74		
0.721	476.66	0.812	468.69	0.822	472.02	0.806	461.31		
0.819	473.41	0.913	467.60	0.923	467.68	0.907	456.32		
0.915	469.06	1.000	465.43	1.000	463.99	1.000	451.98		
1.000	464.29								

Table 14.3. Blade-to-blade circumferential-average values of total head, static head, tangential flow angle, and incidence and deviation angles for minimum noise condition.

	Percent Pass.Ht. From Hub	H N·m/kg	h N·m/kg	β_y degrees	i degrees	δ degrees
Station 1	10.00	0.23	-86.95	-0.01		0.01
	20.00	0.83	-86.95	0.07		-0.07
	30.00	0.11	-86.95	-0.37		0.37
	40.00	0.07	-86.95	-0.65		0.65
	50.00	0.16	-86.95	-0.88		0.88
	60.00	0.05	-86.94	-1.12		1.12
	70.00	-0.04	-86.94	-0.66		0.66
	80.00	-2.54	-86.94	-1.05		1.05
	90.00	-7.99	-86.94	-1.08		1.08
Station 2	10.00	-18.32	-112.33	24.75	8.03	16.02
	20.00	-13.85	-111.03	23.81	6.78	15.66
	30.00	-13.10	-109.34	22.96	6.75	15.27
	40.00	-11.87	-108.78	22.00	6.74	15.08
	50.00	-10.89	-107.84	21.29	6.91	14.76
	60.00	- 7.82	-106.98	20.34	6.61	14.69
	70.00	- 5.72	-106.18	20.30	6.24	13.64
	80.00	- 6.93	-105.43	19.43	6.49	13.49
	90.00	-17.16	-104.79	18.91	8.36	13.19
Station 3	10.00	200.61	-30.10	53.92	0.44	16.31
	20.00	200.21	-18.61	51.77	-0.60	16.15
	30.00	205.10	- 8.69	48.89	-2.54	14.42
	40.00	208.85	0.01	47.27	-2.98	12.33
	50.00	207.30	7.77	45.96	-2.60	11.26
	60.00	204.39	14.61	44.76	-2.37	10.47
	70.00	202.25	20.70	44.14	-2.51	9.57
	80.00	200.15	26.20	43.17	-3.19	9.00
	90.00	196.12	31.39	45.99	0.40	9.57
Station 4	10.00	180.39	46.82	35.26	-1.99	9.59
	20.00	178.24	50.17	33.78	-0.84	9.10
	30.00	188.52	53.24	33.26	-1.86	9.52
	40.00	192.44	56.20	32.03	-1.41	9.26
	50.00	191.17	58.95	32.62	-0.29	10.90
	60.00	191.18	61.55	31.87	0.63	11.11
	70.00	190.61	63.89	31.10	1.33	11.09
	80.00	187.43	65.99	30.14	2.35	10.79
	90.00	174.24	67.82	30.63	4.99	12.02

Table 14.3. Concluded.

	Percent Pass.Ht. From Hub	H N·m/kg	h N·m/kg	β_y degrees	i degrees	δ degrees
Station 5	10.00	333.54	87.42	54.89	1.41	12.92
	20.00	342.63	99.95	51.22	-1.14	12.11
	30.00	347.08	110.92	49.56	-1.87	10.45
	40.00	346.04	120.74	48.57	-1.69	9.36
	50.00	343.01	129.46	47.51	-1.04	8.80
	60.00	337.45	137.13	46.30	-0.84	8.72
	70.00	333.65	143.85	45.40	-1.25	8.27
	80.00	332.57	149.93	45.14	-1.23	7.76
	90.00	326.94	155.68	47.19	1.60	8.71
Station 6	10.00	313.91	186.40	35.71	-0.88	10.04
	20.00	322.40	189.75	33.44	-1.61	8.76
	30.00	330.58	192.86	32.92	-2.23	9.18
	40.00	331.64	195.85	32.50	-1.38	9.73
	50.00	327.85	198.60	32.56	0.23	10.84
	60.00	325.09	201.08	31.42	1.62	10.66
	70.00	322.35	203.26	31.05	2.59	11.03
	80.00	319.86	205.28	31.07	3.41	11.73
	90.00	309.44	207.27	34.80	5.79	16.18
Station 7	10.00	476.12	226.90	53.75	0.27	13.01
	20.00	484.20	239.35	50.96	-1.41	11.88
	30.00	488.29	250.37	49.49	-1.94	10.19
	40.00	487.02	260.21	48.33	-1.93	9.18
	50.00	481.82	268.91	47.43	-1.12	8.92
	60.00	475.43	276.53	46.27	-0.86	8.94
	70.00	471.28	283.17	45.11	-1.54	8.54
	80.00	471.30	289.21	45.65	-0.71	7.85
	90.00	466.43	295.07	47.71	2.12	8.76
Station 8	10.00	442.10	317.91	35.03		9.37
	20.00	461.52	321.35	34.08		9.40
	30.00	466.03	324.77	33.84		10.10
	40.00	465.42	327.90	32.33		9.55
	50.00	464.35	330.59	31.15		9.43
	60.00	458.73	332.98	30.85		10.10
	70.00	454.27	335.08	29.88		9.87
	80.00	455.80	337.03	30.93		11.59
	90.00	444.97	339.05	33.66		15.04

Table 14.4. Blade-to-blade circumferential-average values of total head, static head, tangential flow angle, and incidence and deviation angles for maximum noise condition.

	Percent Pass.Ht. From Hub	H N·m/kg	h N·m/kg	β_y degrees	i degrees	δ degrees
Station 1	10.00	0.23	-86.51	-0.01	0.01	
	20.00	0.83	-86.51	0.07	-0.07	
	30.00	0.11	-86.51	-0.37	0.37	
	40.00	0.07	-86.51	-0.65	0.65	
	50.00	0.16	-86.50	-0.88	0.88	
	60.00	0.05	-86.50	-1.12	1.12	
	70.00	-0.04	-86.50	-0.66	0.66	
	80.00	-2.54	-86.50	-1.05	1.05	
	90.00	-7.99	-86.50	-1.08	1.08	
Station 2	10.00	-17.22	-111.85	25.66	7.70	15.11
	20.00	-12.87	-110.47	24.25	6.58	15.22
	30.00	-11.55	-109.25	22.99	6.42	15.23
	40.00	-10.39	-108.17	22.24	6.43	14.83
	50.00	-10.02	-107.22	21.03	6.83	15.02
	60.00	- 7.20	-106.37	20.34	6.60	14.68
	70.00	- 5.87	-105.59	19.84	6.41	14.09
	80.00	- 6.87	-104.86	19.46	6.57	13.46
	90.00	-15.95	-104.25	17.96	8.34	14.14
Station 3	10.00	200.79	-30.24	53.98	0.50	16.21
	20.00	201.18	-18.66	51.94	-0.42	15.88
	30.00	203.81	- 8.67	49.11	-2.31	14.61
	40.00	207.85	- 0.01	47.19	-3.06	12.52
	50.00	207.08	7.72	46.02	-2.54	11.29
	60.00	203.45	14.57	44.92	-2.21	10.62
	70.00	201.96	20.66	44.16	-2.48	9.60
	80.00	199.71	26.15	43.03	-3.33	9.06
	90.00	196.13	31.29	45.72	0.13	9.53
Station 4	10.00	178.04	48.51	35.87	-1.30	10.20
	20.00	179.62	51.82	33.50	-0.72	8.83
	30.00	188.69	54.88	33.79	-1.70	10.05
	40.00	188.47	57.90	33.13	-0.72	10.36
	50.00	189.63	60.59	31.73	0.28	10.01
	60.00	192.12	63.00	30.91	0.88	10.16
	70.00	190.33	65.21	30.14	1.73	10.13
	80.00	187.62	67.19	29.68	2.57	10.34
	90.00	175.69	69.08	32.65	4.97	14.03

Table 14.4. Concluded.

	Percent Pass.Ht. From Hub	H N·m/kg	h N·m/kg	β_y degrees	i degrees	δ degrees
Station 5	10.00	332.45	88.00	55.10	1.63	13.12
	20.00	344.77	100.59	51.36	-1.01	11.80
	30.00	347.79	111.72	50.28	-1.15	10.22
	40.00	347.22	121.72	48.97	-1.29	9.22
	50.00	343.50	130.58	48.15	-0.40	8.81
	60.00	340.32	138.41	46.86	-0.27	8.44
	70.00	334.16	145.26	45.75	-0.90	8.43
	80.00	332.95	151.37	45.44	-0.92	7.93
	90.00	327.87	157.15	47.44	1.85	8.83
Station 6	10.00	312.48	185.12	35.76	-0.85	10.09
	20.00	322.44	188.55	34.04	-1.89	9.36
	30.00	331.20	191.83	33.95	-2.62	10.21
	40.00	330.43	194.98	33.01	-1.41	10.24
	50.00	329.57	197.81	32.85	-0.21	11.13
	60.00	326.93	200.39	31.95	1.13	11.20
	70.00	322.75	202.64	30.89	2.38	10.88
	80.00	320.84	204.66	31.08	3.18	11.73
	90.00	303.31	206.53	32.55	6.77	13.93
Station 7	10.00	474.94	227.81	53.89	0.41	13.30
	20.00	482.18	240.18	51.13	-1.23	12.27
	30.00	486.92	251.14	49.73	-1.70	10.46
	40.00	484.07	260.92	48.32	-1.93	9.77
	50.00	481.16	269.49	47.32	-1.23	9.14
	60.00	474.10	277.03	46.22	-0.91	9.23
	70.00	468.73	283.60	45.32	-1.33	9.00
	80.00	471.29	289.64	46.02	-0.34	7.94
	90.00	462.62	295.48	47.64	2.05	9.43
Station 8	10.00	438.72	317.69	32.95		7.28
	20.00	460.48	320.91	33.78		9.10
	30.00	466.08	324.33	33.88		10.14
	40.00	465.12	327.47	32.33		9.56
	50.00	463.67	330.14	30.86		9.14
	60.00	460.24	332.48	30.19		9.43
	70.00	454.25	334.55	29.88		9.87
	80.00	456.04	336.51	30.81		11.47
	90.00	442.30	338.46	32.48		13.87

Table 14.5. Circumferential-average outer-annulus-surface static head for minimum and maximum noise conditions.

Minimum Noise		Maximum Noise	
Measurement Station	Outer Wall Static Head N·m/kg	Measurement Station	Outer Wall Static Head N·m/kg
1	- 86.94	1	- 86.50
2	-104.23	2	-103.67
3	36.82	3	36.85
4	69.20	4	70.78
5	161.53	5	162.75
6	208.96	6	207.94
7	300.68	7	301.17
8	340.67	8	340.04

XV. APPENDIX F: TABULATION OF FAST-RESPONSE HOT-WIRE DATA

The fast-response, hot-wire, circumferential survey data obtained over the first two stages of the compressor for the minimum noise condition are tabulated in this section. This data were obtained at a rotor speed of 1400 rpm and a flow coefficient of 0.42. The periodic-average three-dimensional velocity vector at each flow-field measurement point is completely specified by the listing of velocity magnitude, tangential flow angle, and radial flow angle. Frozen rotor-blade survey data for various rotor blade positions are tabulated in Table 15.1. Passing rotor-blade survey data are listed in Table 15.2. The sign convention for the tangential and radial flow angles is given in Figure 4.12. The definitions of the computer output variables used in the table headings are as follows:

Y/SS = circumferential spacing, Y/S_S

V = absolute velocity, V, m/s

BETA Y = absolute tangential flow angle, β_y, degrees

BETA R = radial flow angle, β_r, degrees

PHH = percent passage height from hub, PHH

YOR/SR = circumferential rotor blade position, YO_R/S_R

Table 15.1. Fast-response circumferential survey data obtained with frozen rotor-blade survey method at minimum noise condition.

STATION 3

Y/SS	V M/S	BETA Y DEG	BETA R DEG	Y/SS	V M/S	BETA Y DEG	BETA R DEG	Y/SS	V M/S	BETA Y DEG	BETA R DEG
PHH=10.00 YOR/SR=0.00				PHH=20.00 YOR/SR=0.00				PHH=30.00 YOR/SR=0.00			
0.000	22.434	48.357	-1.516	-0.000	21.859	46.198	0.468	0.000	21.896	44.665	0.159
0.052	21.401	47.655	0.285	0.052	21.793	47.243	-0.434	0.052	21.844	45.111	-0.315
0.103	21.838	48.022	-1.579	0.103	21.092	47.329	0.717	0.106	21.440	45.089	0.376
0.155	21.547	48.032	-0.664	0.154	20.887	46.855	0.865	0.155	21.337	44.336	0.525
0.180	21.523	47.736	-0.990	0.205	20.686	47.423	-0.083	0.207	20.943	44.656	0.081
0.206	21.678	48.329	-1.649	0.231	20.444	46.687	-0.075	0.257	20.754	44.993	-0.153
0.231	21.528	49.825	-0.971	0.257	20.256	46.893	-0.291	0.309	20.487	44.939	-0.658
0.258	20.587	52.875	0.678	0.284	19.862	45.973	-0.934	0.334	20.379	44.423	-1.216
0.283	21.161	64.197	-0.101	0.309	19.590	47.089	-1.333	0.360	19.956	43.661	-0.673
0.309	21.037	73.123	2.867	0.334	19.060	50.587	-0.855	0.385	19.896	43.835	-2.127
0.334	20.775	74.613	6.373	0.360	18.946	56.196	-1.366	0.411	19.398	46.703	-1.622
0.360	21.221	73.560	6.359	0.387	19.056	67.059	1.493	0.436	19.210	52.485	-0.842
0.385	21.279	70.402	8.026	0.412	18.878	71.036	4.769	0.464	18.475	59.189	2.717
0.411	21.369	68.136	9.089	0.437	20.240	73.273	2.228	0.488	18.611	65.479	4.847
0.437	21.906	63.272	8.259	0.462	18.763	66.486	11.327	0.515	18.271	69.002	7.557
0.465	22.538	59.094	6.194	0.489	19.613	64.424	8.206	0.539	18.111	64.796	7.963
0.488	22.862	56.834	5.526	0.514	21.090	60.541	3.303	0.566	18.445	61.698	5.903
0.514	23.255	54.365	4.036	0.541	20.397	54.389	3.972	0.591	19.464	59.124	2.901
0.539	23.431	52.212	2.321	0.565	21.782	53.256	1.099	0.617	19.766	52.419	2.339
0.565	23.244	50.976	1.949	0.592	21.996	50.422	0.729	0.642	20.475	48.125	1.492
0.592	22.945	49.632	1.859	0.617	22.019	47.819	0.119	0.669	21.593	47.691	-1.050
0.620	23.381	49.545	0.043	0.643	22.050	47.429	0.819	0.693	21.507	46.252	0.068
0.668	22.965	49.049	0.088	0.668	21.933	46.949	0.805	0.720	21.656	44.527	-0.259
0.720	23.264	48.597	-0.995	0.719	21.907	46.795	1.029	0.745	21.868	45.550	-0.466
0.772	22.913	47.569	-0.525	0.771	22.054	46.767	0.592	0.771	22.054	45.884	-0.065
0.824	22.768	48.002	-0.833	0.823	22.075	46.328	0.377	0.826	22.123	45.078	-0.196
0.875	22.544	47.754	-0.783	0.874	22.078	46.121	0.139	0.875	22.138	44.468	-0.348
0.925	21.967	46.798	0.435	0.926	22.029	46.952	0.359	0.926	22.154	44.872	-0.076
0.975	21.759	47.002	-0.116	0.976	21.811	46.182	0.593	0.973	21.890	45.128	0.380
1.000	21.712	47.737	-0.455	1.000	21.665	46.393	0.808	1.000	22.052	44.382	-0.532

Table 15.1. Continued.

STATION 3

Y/SS	V M/S	BETA Y DEG	BETA R DEG	Y/SS	V M/S	BETA Y DEG	BETA R DEG	Y/SS	V M/S	BETA Y DEG	BETA R DEG
PHH=40.00 YOR/SR=0.00				PHH=50.00 YOR/SR=0.00				PHH=50.00 YOR/SR=0.17			
0.000	21.618	43.466	0.551	0.001	20.545	41.928	-0.362	-0.000	20.640	41.854	0.527
0.052	21.531	43.769	1.048	0.052	20.605	41.579	0.210	0.051	20.775	42.147	0.060
0.103	21.629	44.011	0.567	0.103	20.658	42.662	1.026	0.103	20.621	41.897	1.113
0.154	21.384	43.726	0.994	0.154	20.532	42.241	1.096	0.155	20.659	42.375	1.025
0.210	21.317	44.094	0.288	0.206	20.502	42.096	0.849	0.206	20.717	42.564	1.206
0.260	21.024	43.648	1.241	0.257	20.418	41.704	1.172	0.257	20.924	43.312	0.982
0.308	20.930	43.764	0.812	0.308	20.591	42.208	0.457	0.309	20.940	42.964	1.737
0.360	21.190	44.569	-1.263	0.359	20.383	42.321	0.272	0.334	21.383	44.971	0.843
0.386	20.980	43.710	-0.199	0.411	20.339	41.778	0.636	0.359	21.521	46.045	0.964
0.411	21.019	43.234	-0.777	0.462	20.468	42.098	0.009	0.387	21.562	52.351	2.908
0.437	21.111	43.397	-0.863	0.489	20.738	42.760	-0.378	0.411	21.244	55.069	5.689
0.463	21.073	47.026	0.150	0.515	20.665	43.288	0.324	0.439	21.359	56.332	5.192
0.489	21.101	51.439	2.128	0.540	21.151	46.413	0.256	0.463	21.083	54.470	5.593
0.515	21.094	56.351	4.295	0.565	20.937	50.680	2.399	0.489	21.433	51.967	3.301
0.540	21.300	59.996	5.622	0.592	21.273	54.557	3.285	0.516	20.938	49.017	3.785
0.566	20.882	60.776	6.781	0.617	21.533	56.387	4.269	0.539	20.840	48.037	2.818
0.592	19.515	58.864	9.523	0.643	21.186	54.781	5.259	0.565	20.469	46.377	3.005
0.617	19.814	57.657	5.956	0.668	20.833	53.780	5.707	0.592	20.267	46.579	2.371
0.643	19.494	56.421	4.608	0.694	20.501	53.400	5.073	0.617	20.366	45.950	0.842
0.669	19.505	53.141	3.300	0.723	19.620	51.545	5.204	0.642	19.937	45.034	1.262
0.694	19.317	50.227	3.066	0.746	19.702	50.597	2.766	0.669	19.744	44.626	0.561
0.722	19.795	46.637	1.678	0.773	19.526	49.196	1.031	0.694	19.756	44.615	0.045
0.745	20.372	45.534	0.253	0.797	19.222	47.457	0.668	0.719	19.647	44.051	-0.093
0.771	20.972	45.543	-1.218	0.825	19.446	46.023	0.253	0.745	19.638	43.716	-0.757
0.798	20.974	43.957	-1.105	0.848	19.601	43.997	-0.696	0.771	19.685	43.507	-0.499
0.823	21.081	43.259	-0.295	0.874	19.572	43.295	0.209	0.822	19.814	42.314	-0.701
0.874	21.453	43.776	-0.283	0.899	20.076	43.048	-0.887	0.875	20.191	42.288	-0.010
0.925	21.483	43.252	0.869	0.925	20.169	42.929	-0.490	0.925	20.316	41.693	0.334
0.976	21.747	44.413	0.814	0.977	20.660	42.783	-0.818	0.976	20.586	41.949	0.594
1.000	21.691	43.417	0.535	1.000	20.803	42.814	-0.176	1.000	20.633	42.030	0.595

Table 15.1. Continued.

STATION 3

Y/SS	V M/S	BETA Y DEG	BETA R DEG	Y/SS	V M/S	BETA Y DEG	BETA R DEG	Y/SS	V M/S	BETA Y DEG	BETA R DEG
PHH=50.00 YOR/SR=0.28				PHH=50.00 YOR/SR=0.50				PHH=50.00 YOR/SR=0.69			
0.000	20.775	42.225	-0.014	-0.000	20.408	42.426	-0.007	0.000	18.903	58.122	3.134
0.053	20.483	42.192	0.622	0.027	20.244	43.054	0.260	0.025	18.610	52.747	5.717
0.104	20.607	43.004	1.027	0.053	20.174	44.873	0.554	0.052	20.051	49.021	1.049
0.156	20.884	43.469	0.307	0.077	20.066	48.476	1.299	0.077	20.264	45.230	1.849
0.180	20.775	43.644	1.077	0.103	19.850	52.872	4.041	0.105	21.053	43.229	0.016
0.206	20.953	44.193	1.304	0.129	20.469	57.066	3.848	0.127	21.388	42.955	-0.273
0.231	21.085	45.268	0.814	0.156	20.587	56.147	5.168	0.154	21.269	42.613	0.144
0.258	21.417	49.642	2.073	0.181	20.823	52.813	5.199	0.180	21.122	42.566	0.849
0.283	21.243	53.349	4.534	0.205	21.192	50.312	4.264	0.207	21.057	42.519	0.462
0.309	21.409	56.844	5.357	0.231	21.609	46.565	2.799	0.257	20.898	43.138	0.773
0.335	21.512	56.574	5.140	0.257	21.546	44.921	2.205	0.311	20.673	42.271	1.309
0.361	20.952	51.562	5.391	0.283	21.634	44.207	1.303	0.360	20.666	42.157	0.609
0.385	21.070	50.371	4.304	0.309	21.481	43.863	0.785	0.414	20.419	41.392	1.399
0.411	21.120	48.571	2.797	0.334	20.998	43.070	1.433	0.463	20.400	41.511	0.830
0.436	21.013	46.936	1.585	0.360	20.699	43.132	1.753	0.514	20.482	42.924	0.254
0.463	20.799	45.868	1.674	0.385	20.676	42.127	1.470	0.565	20.125	42.845	0.302
0.488	20.696	45.105	1.768	0.411	20.645	43.017	0.904	0.617	19.940	42.932	-0.545
0.515	20.396	44.653	1.983	0.437	20.341	42.314	1.675	0.668	19.955	43.038	-0.704
0.539	20.516	44.755	1.007	0.463	20.374	42.587	1.156	0.720	19.869	41.750	0.144
0.566	20.174	44.198	1.113	0.514	20.234	43.100	0.731	0.745	20.019	41.346	-0.319
0.591	20.212	44.013	-0.517	0.565	19.819	41.603	1.028	0.771	19.991	41.068	-0.864
0.618	20.213	44.758	-0.294	0.617	19.847	42.653	-0.169	0.797	19.577	40.603	0.149
0.669	19.802	43.889	-0.310	0.668	19.724	42.319	-0.664	0.822	19.664	41.661	-0.071
0.720	19.693	43.305	-0.865	0.719	19.435	41.886	-0.322	0.848	19.151	45.519	0.906
0.771	19.909	42.483	-1.427	0.771	19.843	42.087	-0.810	0.874	18.615	50.776	2.352
0.824	20.015	42.698	-1.075	0.822	19.946	42.144	-0.453	0.899	18.445	58.471	3.029
0.874	20.151	42.777	0.118	0.874	19.954	41.598	0.094	0.925	17.924	62.382	5.659
0.926	20.416	41.378	-0.097	0.930	19.654	41.140	0.453	0.950	17.627	61.672	5.633
0.976	20.671	43.078	0.073	0.976	19.423	41.885	0.299	0.977	17.229	58.443	6.193
1.000	20.508	42.559	0.968	1.000	19.091	43.919	0.661	1.000	17.802	56.018	4.394

Table 15.1. Continued.

STATION 3

Y/SS	V M/S	BETA Y DEG	BETA R DEG	Y/SS	V M/S	BETA Y DEG	BETA R DEG	Y/SS	V M/S	BETA Y DEG	BETA R DEG
PHH=50.00 YOR/SR=0.83				PHH=60.00 YOR/SR=0.00				PHH=70.00 YOR/SR=0.00			
0.000	20.311	44.803	0.019	0.000	19.474	42.731	0.001	-0.000	18.682	45.370	1.031
0.026	20.446	42.048	1.548	0.053	19.470	41.080	1.220	0.051	18.797	44.717	1.488
0.051	21.115	43.497	-0.549	0.102	19.906	41.881	0.992	0.103	19.133	45.666	0.986
0.077	21.014	42.356	0.708	0.154	19.916	41.348	1.332	0.154	19.022	43.541	1.864
0.103	21.049	42.803	0.246	0.205	19.816	41.495	1.476	0.209	19.109	42.540	1.195
0.154	20.813	42.676	1.131	0.258	19.976	42.151	1.318	0.257	19.236	42.959	0.839
0.206	20.765	42.361	1.092	0.308	19.917	41.593	1.337	0.309	19.102	42.134	1.620
0.257	20.729	41.968	1.189	0.360	20.075	41.767	1.532	0.360	19.142	41.593	1.726
0.308	20.543	41.271	1.332	0.411	20.149	41.805	1.249	0.411	19.207	41.257	1.771
0.361	20.635	41.801	1.520	0.465	20.144	41.793	1.760	0.464	19.501	42.508	1.165
0.411	20.550	41.904	1.124	0.514	20.244	42.419	1.306	0.515	19.499	42.848	2.310
0.464	20.655	42.122	0.151	0.541	20.179	42.611	1.875	0.541	19.554	42.161	1.957
0.514	20.320	42.206	0.153	0.566	20.483	43.159	0.816	0.565	19.707	43.438	0.866
0.565	20.277	42.222	-0.190	0.591	20.549	46.336	1.849	0.594	19.662	43.846	1.146
0.617	20.396	41.895	-0.389	0.618	20.557	50.222	3.660	0.617	19.724	43.588	0.365
0.642	20.348	40.777	0.279	0.643	20.683	53.504	4.284	0.642	20.038	46.013	0.553
0.670	20.620	41.063	-0.228	0.668	20.521	54.843	5.101	0.668	20.039	49.147	1.914
0.694	20.626	43.204	0.523	0.694	20.382	53.253	5.165	0.694	20.206	52.979	2.646
0.719	20.841	46.921	0.960	0.720	20.579	52.000	3.137	0.720	20.285	54.491	3.278
0.745	21.033	52.991	3.862	0.745	20.447	50.048	2.363	0.745	19.782	53.295	5.397
0.771	20.466	55.522	6.073	0.773	19.916	48.185	2.543	0.771	19.969	51.841	3.506
0.797	20.073	58.235	8.193	0.797	19.793	47.507	1.304	0.796	19.581	48.979	4.161
0.822	20.010	60.944	6.328	0.822	19.464	46.331	0.936	0.824	19.521	47.251	2.147
0.849	18.989	59.089	6.947	0.848	19.294	46.982	0.447	0.848	19.338	46.544	2.295
0.873	18.518	57.721	6.089	0.874	18.846	45.299	1.608	0.875	19.301	46.761	1.165
0.900	18.724	53.690	3.248	0.899	19.185	45.496	-0.183	0.899	19.207	46.501	0.730
0.925	18.359	50.415	3.191	0.926	18.922	43.288	1.030	0.928	18.809	45.441	1.588
0.951	18.835	49.814	1.160	0.950	19.359	43.800	-0.013	0.951	18.752	45.437	1.361
0.976	18.561	48.556	2.435	0.978	19.379	42.552	0.410	0.976	19.064	47.042	0.475
1.000	18.886	47.864	1.156	1.000	19.553	42.380	1.159	1.000	18.846	45.877	1.353

Table 15.1. Continued.

STATION 3

Y/SS	V M/S	BETA Y DEG	BETA R DEG	Y/SS	V M/S	BETA Y DEG	BETA R DEG
PHH=80.00 YOR/SR=0.00				PHH=90.00 YOR/SR=0.00			
0.000	18.746	42.866	1.436	0.000	18.138	42.709	4.794
0.053	18.585	41.873	1.401	0.053	17.487	43.307	3.417
0.104	18.682	41.695	0.508	0.102	17.083	43.671	2.132
0.154	18.522	40.803	1.725	0.154	17.032	43.759	0.819
0.207	18.578	38.048	1.647	0.205	17.021	42.244	1.997
0.257	18.557	38.353	2.366	0.257	17.448	40.010	1.665
0.309	18.746	36.803	2.019	0.309	17.590	40.074	3.251
0.360	18.885	37.818	1.754	0.365	18.050	40.822	3.820
0.415	19.014	37.948	1.976	0.411	18.455	40.295	3.577
0.463	19.142	37.551	1.956	0.463	18.602	39.740	4.879
0.514	19.277	37.354	2.541	0.516	19.145	42.014	3.415
0.539	19.472	37.792	2.001	0.540	19.025	42.097	4.379
0.566	19.521	37.966	2.389	0.567	19.334	43.466	3.129
0.591	19.785	39.069	1.720	0.591	19.511	44.928	1.942
0.617	19.794	37.408	1.626	0.617	19.387	44.743	2.700
0.642	20.026	39.659	0.689	0.642	20.206	45.465	0.704
0.668	20.352	41.758	-0.953	0.669	19.609	45.664	2.273
0.693	20.667	44.450	-1.904	0.696	19.574	45.907	0.706
0.720	20.774	48.731	-1.781	0.719	19.637	50.651	-1.454
0.745	20.550	49.966	0.407	0.746	19.230	52.272	0.033
0.774	20.642	51.274	2.019	0.771	19.472	55.354	-1.240
0.796	20.398	51.296	3.630	0.797	19.325	51.823	0.330
0.823	20.092	47.932	3.742	0.827	19.153	49.597	2.653
0.848	19.916	48.760	4.216	0.848	18.877	46.345	4.836
0.874	19.558	46.282	1.172	0.875	18.919	44.662	5.069
0.899	19.312	42.556	4.019	0.899	19.034	43.823	4.909
0.926	19.331	43.338	2.782	0.926	18.663	41.724	5.748
0.950	19.028	41.569	2.989	0.951	18.305	38.748	6.110
0.976	18.931	41.408	1.691	0.975	17.946	39.372	6.083
1.000	19.124	41.762	1.045	1.000	17.936	40.510	4.845

Table 15.1. Continued.

STATION 4

Y/SS	V M/S	BETA Y DEG	BETA R DEG	Y/SS	V M/S	BETA Y DEG	BETA R DEG	Y/SS	V M/S	BETA Y DEG	BETA R DEG
PHH=50.00 YOR/SR=0.00				PHH=50.00 YOR/SR=0.17				PHH=50.00 YOR/SR=0.34			
0.000	18.428	30.844	0.760	-0.000	18.666	33.919	1.107	0.000	18.335	31.660	1.573
0.052	18.166	30.994	2.038	0.052	18.237	33.508	2.882	0.053	18.092	32.041	1.711
0.077	18.289	31.621	1.301	0.077	18.251	34.585	2.253	0.102	17.647	31.938	2.301
0.102	18.270	32.181	1.199	0.102	17.969	34.492	2.780	0.129	17.265	32.012	2.228
0.129	17.952	33.318	1.132	0.129	17.125	34.522	4.598	0.155	16.685	31.951	3.045
0.154	16.954	33.843	2.827	0.158	16.396	35.255	4.447	0.181	16.400	31.996	2.208
0.180	16.149	34.538	3.346	0.180	15.661	35.250	4.614	0.207	15.514	32.006	3.642
0.205	15.055	34.670	2.977	0.207	14.897	34.204	4.964	0.232	14.544	31.916	3.877
0.232	14.014	35.489	3.405	0.232	14.440	36.212	1.719	0.258	13.801	30.235	3.109
0.257	13.269	36.724	2.018	0.257	13.909	34.527	1.192	0.282	13.554	31.601	-0.742
0.282	13.010	34.661	1.268	0.285	13.458	33.536	-0.361	0.308	13.299	32.131	-2.383
0.308	13.695	32.306	-2.798	0.309	13.252	32.157	-1.299	0.334	13.248	29.711	-3.385
0.335	14.054	29.845	-1.520	0.335	13.547	30.022	-3.245	0.361	13.760	28.533	-3.516
0.360	14.768	29.945	-1.185	0.360	14.369	30.440	-3.837	0.385	14.545	29.009	-1.439
0.386	15.281	29.585	-0.044	0.387	14.828	30.536	-1.253	0.411	14.936	29.302	0.479
0.413	15.654	30.749	1.094	0.411	15.190	30.890	0.495	0.437	15.299	30.012	1.634
0.438	15.783	32.189	1.644	0.437	15.526	32.913	1.178	0.462	15.733	30.661	1.470
0.462	15.644	32.548	2.508	0.462	15.677	32.936	0.953	0.489	15.908	31.447	1.219
0.491	15.718	32.542	2.154	0.489	15.850	33.934	0.892	0.514	16.002	31.183	1.352
0.514	15.674	33.191	2.032	0.517	15.898	33.567	0.885	0.540	16.163	30.742	1.092
0.566	15.909	33.426	0.754	0.567	15.889	33.093	0.899	0.565	16.306	30.456	1.193
0.617	16.051	32.936	0.713	0.617	16.229	31.323	0.509	0.621	16.708	30.550	0.778
0.668	16.358	32.164	-0.366	0.672	16.608	30.934	-0.034	0.669	16.414	29.916	1.894
0.721	16.826	30.134	-0.516	0.721	16.937	31.420	0.613	0.720	16.816	30.779	1.759
0.771	16.982	29.645	0.278	0.774	17.060	31.276	1.279	0.772	16.876	30.747	1.939
0.822	17.272	28.898	0.546	0.822	17.424	32.624	1.954	0.822	17.108	31.835	2.154
0.873	17.414	29.128	1.537	0.874	17.467	31.900	2.160	0.873	17.533	32.271	0.975
0.925	17.688	30.355	2.055	0.925	17.774	33.262	2.634	0.925	17.832	32.798	1.130
0.977	17.900	31.239	2.143	0.977	18.070	33.317	2.032	0.974	17.971	31.526	1.324
1.001	17.910	31.450	2.232	1.000	18.134	33.550	2.276	1.000	17.904	31.793	1.328

Table 15.1. Continued.

STATION 4

Y/SS	V M/S	BETA Y DEG	BETA R DEG	Y/SS	V M/S	BETA Y DEG	BETA R DEG	Y/SS	V M/S	BETA Y DEG	BETA R DEG
PHH=50.00 YOR/SR=0.50				PHH=50.00 YOR/SR=0.69				PHH=50.00 YOR/SR=0.83			
0.000	17.929	32.512	0.055	-0.000	17.500	30.148	0.199	0.000	17.711	28.130	-0.276
0.026	17.751	32.260	0.561	0.051	17.411	29.114	0.101	0.051	17.875	29.204	-0.859
0.053	17.593	32.231	0.264	0.077	17.309	28.880	-0.036	0.077	17.504	28.385	0.146
0.077	17.291	31.687	1.187	0.103	17.187	28.556	-0.320	0.103	17.686	29.155	-0.702
0.104	17.293	31.519	0.215	0.129	17.015	28.068	0.064	0.130	17.219	29.492	0.151
0.129	16.630	31.137	1.706	0.155	16.797	28.761	0.083	0.155	16.862	31.052	0.273
0.154	16.529	30.985	1.095	0.181	16.436	29.310	-0.095	0.181	15.971	32.370	1.495
0.180	16.255	30.639	0.910	0.205	15.202	29.702	2.528	0.205	14.973	34.887	1.206
0.206	15.798	30.830	0.426	0.232	14.232	31.226	1.866	0.231	13.921	38.004	0.839
0.231	14.274	30.539	3.433	0.259	13.375	33.704	0.517	0.260	13.175	38.981	0.183
0.258	13.539	31.752	1.643	0.285	12.605	35.756	0.773	0.283	13.133	37.813	-0.505
0.283	12.861	30.405	-0.166	0.308	12.781	35.379	-1.014	0.308	13.366	35.606	-0.163
0.308	12.727	31.645	-3.390	0.334	13.742	35.060	-0.445	0.334	14.335	34.815	0.541
0.334	12.631	29.663	-1.697	0.360	14.564	33.035	1.152	0.359	15.060	33.618	1.268
0.362	13.771	29.748	-1.985	0.387	15.491	32.965	2.291	0.386	15.556	32.760	2.343
0.386	14.666	30.894	-0.099	0.412	16.012	33.874	2.533	0.413	16.086	34.124	1.557
0.411	15.305	31.564	1.509	0.437	16.188	34.107	2.631	0.437	15.999	33.195	1.646
0.437	15.798	31.632	2.151	0.463	16.389	33.606	2.325	0.464	16.282	34.433	0.073
0.463	16.161	32.325	1.398	0.489	16.208	33.057	2.392	0.488	15.812	33.039	1.047
0.513	16.379	32.230	1.530	0.514	16.224	32.821	1.523	0.513	15.866	34.265	1.028
0.566	16.281	31.503	1.633	0.571	16.218	32.827	0.838	0.566	15.556	33.784	1.005
0.617	16.479	31.600	0.639	0.617	16.099	33.127	0.533	0.617	16.060	34.162	-0.118
0.668	16.527	32.725	0.797	0.668	16.296	33.668	0.170	0.668	16.327	33.812	-0.459
0.720	16.423	32.572	1.192	0.723	16.456	33.338	-0.005	0.721	16.539	32.717	-0.778
0.774	16.864	33.507	0.301	0.774	16.691	32.684	0.095	0.772	16.814	32.155	-0.825
0.822	17.062	32.783	-0.200	0.822	17.162	31.843	-0.962	0.824	17.104	30.884	-0.915
0.874	17.739	32.996	-0.869	0.875	17.550	31.546	-1.238	0.874	17.481	29.800	-1.024
0.925	17.949	32.633	-0.464	0.925	17.473	30.496	-0.258	0.926	17.671	28.524	-0.709
0.976	17.796	31.688	-0.518	0.975	17.557	29.746	-0.204	0.973	17.636	28.067	0.006
1.000	17.631	31.112	0.016	1.000	17.543	28.975	0.197	1.000	17.831	28.789	-0.433

Table 15.1. Continued.

STATION 5

Y/SS	V M/S	BETA Y DEG	BETA R DEG	Y/SS	V M/S	BETA Y DEG	BETA R DEG	Y/SS	V M/S	BETA Y DEG	BETA R DEG
PHH=50.00 YOR/SR=0.00				PHH=50.00 YOR/SR=0.17				PHH=50.00 YOR/SR=0.34			
0.001	20.980	41.615	-1.271	-0.000	21.175	41.210	-0.836	-0.000	20.566	43.660	0.423
0.054	21.025	41.810	-1.315	0.053	20.943	41.751	-1.090	0.027	20.436	44.891	0.158
0.102	20.672	41.457	-1.440	0.104	20.451	42.890	-0.825	0.051	20.303	45.640	-0.295
0.155	20.378	42.297	-1.029	0.154	20.202	43.982	-0.930	0.078	20.239	46.449	-0.634
0.205	20.189	42.813	-0.972	0.206	20.054	44.552	-0.330	0.103	20.080	46.583	-0.373
0.258	19.997	42.762	-0.430	0.256	20.120	44.741	0.459	0.129	19.965	46.800	-0.041
0.309	20.432	44.034	0.100	0.284	20.387	45.401	0.195	0.154	19.872	47.359	0.431
0.361	20.639	44.570	0.955	0.308	20.343	45.882	0.556	0.181	20.100	48.875	0.038
0.415	20.700	45.383	1.441	0.335	20.280	48.081	0.994	0.205	19.870	50.965	0.715
0.463	20.906	47.557	1.148	0.360	20.310	51.590	1.211	0.232	19.922	55.913	2.126
0.488	21.042	51.074	1.649	0.387	20.339	56.570	2.255	0.258	19.611	59.190	3.448
0.514	20.961	54.512	2.433	0.415	20.117	58.886	3.950	0.283	19.419	59.873	3.957
0.540	20.917	58.314	3.482	0.439	20.237	60.131	4.146	0.308	19.406	57.838	4.064
0.566	20.925	59.115	4.198	0.462	20.181	57.519	4.645	0.336	19.703	55.817	2.632
0.591	20.969	59.091	4.229	0.490	20.623	54.407	3.258	0.362	19.605	52.095	2.643
0.623	21.127	56.518	3.480	0.514	20.743	52.036	2.505	0.386	19.883	48.881	2.169
0.643	21.267	55.168	2.109	0.540	21.030	49.746	1.221	0.411	20.531	46.828	1.104
0.668	20.845	51.304	3.134	0.567	20.954	48.264	1.173	0.438	20.786	46.307	0.300
0.695	20.979	49.307	1.542	0.591	20.831	46.642	0.874	0.463	20.634	44.825	0.853
0.721	20.885	48.097	1.308	0.617	20.984	46.148	0.233	0.515	20.710	44.478	0.693
0.745	21.003	47.621	0.452	0.644	20.840	45.978	-0.061	0.566	20.659	44.573	0.785
0.772	20.947	45.843	0.014	0.668	20.834	45.803	-0.023	0.618	20.793	45.006	-0.025
0.798	20.952	45.778	-0.088	0.694	20.768	44.782	-0.021	0.668	20.851	44.393	-0.141
0.822	21.185	45.320	-0.864	0.725	20.687	44.345	0.261	0.719	20.623	43.840	0.386
0.851	20.958	44.058	-0.517	0.771	20.651	43.494	0.429	0.771	20.857	43.251	-0.010
0.873	21.010	43.915	-0.065	0.823	20.948	43.081	-0.119	0.822	20.758	43.028	0.384
0.899	20.898	42.676	-0.166	0.874	20.824	42.259	0.662	0.874	20.493	42.990	1.087
0.926	21.042	42.655	-0.824	0.927	20.916	42.350	0.166	0.926	20.163	43.465	1.409
0.976	20.993	41.975	-0.506	0.976	20.916	42.046	-0.332	0.978	19.956	45.245	1.097
1.000	21.239	42.106	-1.340	1.001	20.655	42.626	-0.397	1.000	19.833	45.812	0.358

Table 15.1. Continued.

STATION 5

Y/SS	V M/S	BETA Y DEG	BETA R DEG	Y/SS	V M/S	BETA Y DEG	BETA R DEG	Y/SS	V M/S	BETA Y DEG	BETA R DEG
PHH=50.00 YOR/SR=0.50				PHH=50.00 YOR/SR=0.67				PHH=50.00 YOR/SR=0.83			
0.001	20.756	48.928	0.672	-0.000	20.828	53.858	4.288	0.000	20.907	45.008	0.753
0.025	20.635	50.475	1.388	0.028	20.495	52.266	3.649	0.052	20.702	43.795	1.079
0.052	20.605	53.021	2.073	0.051	20.134	50.369	3.702	0.104	20.703	42.784	0.541
0.078	20.287	55.263	3.843	0.077	20.050	48.117	2.418	0.156	20.780	42.433	-0.423
0.103	20.234	57.824	4.570	0.103	19.935	46.518	1.665	0.207	20.573	43.068	-0.759
0.128	20.420	58.409	3.860	0.128	20.101	45.117	0.671	0.259	20.538	42.706	-0.727
0.155	20.005	57.756	4.655	0.154	20.024	44.894	-0.038	0.308	20.687	43.273	-0.653
0.180	19.301	55.800	4.932	0.181	20.310	44.547	-1.393	0.360	20.812	42.749	0.274
0.205	19.630	53.191	2.991	0.208	19.774	42.924	1.117	0.411	20.950	43.399	1.808
0.231	19.532	51.689	2.229	0.231	19.959	43.497	0.173	0.463	21.121	44.293	2.194
0.257	19.343	48.564	1.923	0.256	20.113	43.019	-0.144	0.515	21.320	44.773	1.696
0.285	19.915	46.389	-0.207	0.308	20.543	43.227	-1.218	0.539	21.259	45.484	1.823
0.308	20.266	43.883	-0.911	0.360	20.685	41.931	-1.028	0.566	21.325	46.082	1.705
0.334	20.269	43.271	-0.303	0.411	20.980	43.234	0.928	0.591	21.383	46.341	1.680
0.359	20.570	43.455	-0.492	0.463	20.841	43.056	2.240	0.618	21.299	46.799	1.913
0.411	20.704	43.213	0.551	0.515	21.228	43.960	1.694	0.642	21.296	48.570	1.898
0.462	20.847	43.642	1.229	0.566	21.344	44.681	1.800	0.668	21.284	50.892	2.205
0.514	20.985	42.939	1.430	0.617	21.184	44.620	2.272	0.694	21.223	54.223	3.081
0.565	21.050	43.481	1.036	0.669	21.392	45.565	1.718	0.720	21.299	57.128	3.681
0.618	21.038	43.152	1.021	0.720	21.139	45.603	2.463	0.746	21.305	58.971	4.432
0.669	21.035	43.515	1.150	0.771	21.015	47.428	2.439	0.771	21.301	58.324	4.759
0.720	20.930	43.535	1.908	0.797	20.637	47.841	2.909	0.796	21.144	56.745	4.299
0.771	20.959	44.038	1.975	0.822	20.773	50.396	2.939	0.822	21.086	53.848	4.155
0.824	20.811	44.149	1.924	0.848	21.070	53.216	2.584	0.848	20.963	51.066	3.064
0.874	20.378	45.650	1.860	0.874	20.874	55.578	3.823	0.873	20.871	48.530	2.928
0.899	20.404	46.792	1.199	0.901	20.756	56.953	5.528	0.899	20.689	47.180	2.587
0.926	20.259	46.222	1.526	0.925	20.836	57.599	4.808	0.927	20.750	46.566	1.865
0.951	20.140	47.537	1.317	0.952	20.584	55.753	4.993	0.952	20.768	46.272	1.592
0.976	19.753	47.303	2.340	0.977	20.333	53.850	4.704	0.977	20.606	46.560	2.023
1.000	20.078	49.427	1.344	1.000	20.516	52.520	3.477	1.000	20.344	46.118	2.298

Table 15.1. Concluded.

STATION 6

Y/SS	V M/S	BETA Y DEG	BETA R DEG	Y/SS	V M/S	BETA Y DEG	BETA R DEG	Y/SS	V M/S	BETA Y DEG	BETA R DEG
PHH=50.00 YOR/SR=0.00				PHH=50.00 YOR/SR=0.34				PHH=50.00 YOR/SR=0.67			
0.000	15.915	29.685	1.917	0.001	16.143	33.095	3.219	-0.000	16.364	29.078	0.264
0.026	16.348	31.563	3.090	0.026	16.552	33.527	1.981	0.027	16.703	29.543	0.463
0.052	16.555	31.291	2.394	0.052	16.488	33.076	2.138	0.051	16.951	30.046	0.723
0.078	16.510	31.777	2.758	0.077	16.736	33.313	0.650	0.077	17.016	29.589	1.279
0.103	16.583	31.977	2.526	0.102	16.892	33.122	0.160	0.102	17.146	29.459	0.912
0.154	16.652	32.997	2.658	0.129	17.100	32.877	0.294	0.155	17.239	29.071	1.512
0.206	16.778	32.969	2.171	0.154	17.275	32.268	-0.085	0.205	17.393	29.685	2.189
0.258	17.137	33.232	1.314	0.205	17.564	31.461	0.095	0.258	17.369	30.084	3.190
0.308	17.523	32.258	0.560	0.257	17.867	30.482	0.307	0.308	17.558	30.774	3.107
0.359	17.788	31.753	0.444	0.309	17.960	29.646	0.710	0.360	17.608	32.079	2.926
0.413	17.991	30.957	0.036	0.360	17.948	29.258	1.512	0.411	17.564	32.008	3.350
0.463	17.838	29.825	0.382	0.411	17.923	29.054	1.212	0.462	17.652	32.426	3.002
0.516	17.824	30.081	0.171	0.462	17.724	28.528	1.759	0.515	17.786	31.968	2.257
0.567	17.756	30.151	-0.587	0.515	17.706	29.630	1.810	0.565	18.021	32.454	1.032
0.620	17.260	29.497	-0.253	0.566	17.690	30.707	2.077	0.618	18.070	32.393	0.145
0.642	17.176	29.007	-0.160	0.617	17.530	31.611	3.088	0.645	18.235	31.838	-0.166
0.670	16.996	28.941	-0.575	0.669	17.469	31.442	3.383	0.668	17.952	32.291	0.347
0.694	16.883	29.443	-0.587	0.694	17.544	31.783	3.536	0.694	17.791	31.661	0.387
0.725	16.703	28.962	-1.286	0.720	17.365	32.993	3.908	0.724	17.318	31.713	0.479
0.745	16.214	28.775	-0.773	0.745	17.127	33.763	3.379	0.747	16.773	31.511	1.216
0.771	15.695	29.067	-1.140	0.771	16.033	33.984	4.920	0.773	16.229	32.244	0.602
0.796	14.929	30.155	-0.651	0.796	14.580	35.504	5.941	0.797	15.298	32.369	0.837
0.823	13.727	31.721	-0.714	0.823	13.954	37.744	2.961	0.824	14.466	33.176	-0.664
0.848	12.815	32.545	-1.769	0.848	13.036	37.526	1.185	0.848	13.120	30.118	0.694
0.873	12.384	32.710	-3.346	0.874	12.801	34.397	-0.781	0.874	12.921	30.941	-1.538
0.900	12.775	32.727	-2.822	0.899	13.159	32.266	-1.557	0.900	13.270	29.159	-3.442
0.925	13.642	31.290	-1.595	0.925	13.991	29.756	-0.953	0.926	13.791	27.743	-2.052
0.952	14.684	30.245	0.554	0.951	14.894	29.371	1.196	0.951	14.789	28.238	-0.120
0.977	15.343	30.273	2.401	0.976	15.707	30.717	1.532	0.976	15.649	29.358	0.468
1.000	15.809	31.749	3.159	1.000	16.038	32.613	2.060	1.000	16.355	30.041	0.126

Table 15.2. Fast-response circumferential survey data obtained with passing rotor-blade survey method at minimum noise condition.

STATION 3

Y/SS	V M/S	BETA Y DEG	BETA R DEG	Y/SS	V M/S	BETA Y DEG	BETA R DEG
PHH=50.00 YOR/SR=0.28				PHH=50.00 YOR/SR=0.69			
0.001	20.746	41.440	0.694	0.000	19.283	58.427	3.854
0.052	20.835	42.444	0.990	0.025	19.408	53.960	2.512
0.103	20.553	42.383	1.980	0.052	19.832	52.618	0.301
0.157	20.868	41.722	1.317	0.078	19.578	47.910	2.045
0.181	21.030	42.573	0.738	0.103	20.359	47.332	-0.646
0.208	21.027	43.120	0.657	0.130	20.163	43.748	0.637
0.231	21.447	44.325	0.873	0.154	20.508	43.290	0.147
0.258	21.311	47.334	2.608	0.207	20.987	43.998	-0.948
0.283	21.348	51.664	3.907	0.257	20.863	42.924	-0.208
0.308	21.557	55.780	4.424	0.308	20.915	43.580	-0.342
0.335	21.193	55.900	6.206	0.359	20.812	42.987	0.175
0.359	21.256	53.846	5.307	0.412	20.912	43.120	0.486
0.386	21.312	51.222	4.080	0.464	20.896	42.913	0.707
0.411	21.491	49.415	3.036	0.514	20.701	41.944	1.104
0.437	21.175	46.709	2.927	0.566	20.708	42.373	1.127
0.465	21.177	44.516	3.091	0.617	20.596	42.509	1.394
0.489	21.287	44.814	1.911	0.670	20.643	42.889	1.121
0.514	20.963	43.528	2.314	0.693	20.431	42.567	1.284
0.542	21.139	44.010	1.476	0.720	20.271	42.142	0.877
0.565	20.964	43.072	1.539	0.745	20.232	42.838	0.368
0.591	20.902	43.083	1.349	0.772	19.910	43.112	1.039
0.619	20.857	42.959	0.997	0.796	19.813	44.326	0.125
0.669	20.712	42.752	1.400	0.823	19.224	45.700	0.716
0.720	20.690	42.768	1.277	0.849	18.663	48.441	1.166
0.772	20.832	41.739	0.200	0.875	18.355	55.603	2.786
0.823	20.463	40.922	1.548	0.900	18.199	59.785	4.327
0.876	20.589	41.944	0.655	0.925	17.661	61.999	6.576
0.925	20.509	41.709	1.144	0.953	18.404	62.249	3.171
0.976	20.748	42.442	0.244	0.976	18.428	57.939	3.320
1.001	20.851	42.865	-0.022	1.000	18.271	53.554	4.611